

AN ABSTRACT OF THE THESIS OF

Sarah Ashley Bromley for the degree of Master of Science in Geology presented on June 7, 2011.

Title: Evolution and Inheritance of Cascadia Sub-arc Mantle Reservoirs

Abstract approved:

Anita L. Grunder

Inheritance from pre-existing mantle domains and fluid and melt contributions from active subduction together produce the geochemical signatures of mantle-derived arc basalts. In this context, this work evaluates the evolution of Cascadia mantle sources by documenting the isotopic and compositional characteristics of primitive basalts along a transect across the Eocene-Oligocene Proto-Cascadia (EOPC) arc at ~44.5-45.5° N.

Primitive EOPC flows, dikes, and sills are exposed across a ~300 km transect that includes the Oregon Coast Range in the Cascadia forearc, the Western Cascades, flanking the modern arc, and the John Day and Eastern Clarno formations east of the Cascades. Like the modern arc, EOPC was built upon accreted terranes of western North America and within the Columbia embayment, which is lithosphere of oceanic affinity that crops out as the Siletzia terrane in the forearc and extends beneath the arc to the backarc. Potential mantle source reservoirs for EOPC magmas include contributions from mantle domains related to pre-existing underlying terranes, distinct North America lithosphere, and depleted Pacific-like upper mantle. In addition, the geochemical characteristics of EOPC magmas have likely been overprinted by subduction processes.

Major, trace element, and isotopic data from the EOPC reveal a heterogeneous mantle source that was variably influenced by subduction processes. In the forearc,

the high field strength (HFSE) enriched basalts of the Oregon Coast Range represent low degree partial melts of a relatively enriched mantle source. Despite this enriched character, there is little evidence in the trace element or isotopic data to suggest that the OCR (Oregon Coast Range) samples have been strongly influenced by either a crustal or subduction component. Their distinctive $^{206}\text{Pb}/^{204}\text{Pb}$ enrichment (as compared to $^{207}\text{Pb}/^{204}\text{Pb}$) distinguishes the forearc magmas from the arc and backarc magmas and also from a hypothetical Cascadia subduction component. Forearc EOPC magmas share a mantle source with the accreted Siletzia terrane, as evidenced by their shared $^{206}\text{Pb}/^{204}\text{Pb}$ enrichment.

At the apparent arc axis, the Western Cascades produced a diversity of primitive magmas that are, for the most part, interpreted to result from higher degrees of partial melting of a less enriched source. Fluid fluxing appears to have facilitated mantle melting beneath the Western Cascades. Additionally, the mantle beneath the arc may be slightly influenced by the $^{206}\text{Pb}/^{204}\text{Pb}$ enriched source underlying the forearc. Though this effect is difficult to resolve, the Western Cascades samples appear to be slightly more variable in $^{206}\text{Pb}/^{204}\text{Pb}$ (and generally higher in $^{206}\text{Pb}/^{204}\text{Pb}$ at a given $^{207}\text{Pb}/^{204}\text{Pb}$) than their backarc counterparts, suggesting such an influence.

Both trace element and isotopic data suggest a significant subduction contribution to EOPC backarc primitive magmas. The EOPC backarc magmas appear to have originated from a heterogeneous mantle and are variably influenced by a subduction component. Though this subduction influence could be an inherited feature, the affinity between John Day and Eastern Clarno magmas and a modern Cascadia sediment source suggest that this is at least a relatively young feature. Taken together, these results demonstrate the heterogeneity of source and process across the Eocene-Oligocene arc. Apparent subduction contribution increases from the geographic forearc to backarc, perhaps indicating a wider arc than is typically envisioned at the time. The distinct $^{206}\text{Pb}/^{204}\text{Pb}$ enrichment associated with the Siletzia mantle and apparent in the forearc appears to wane in influence to the east, having at most a minor influence on the Western Cascade arc magmas.

As with the Siletzia mantle domain in EOPC arc and backarc, mantle domains associated with the Western Cascades and John Day/Eastern Clarno magmas do not persist in the High Cascades or High Lava Plains. Beneath and behind the arc, mantle reservoirs appear to have been largely replaced since the Eocene-Oligocene. However, the High Lava Plains basalts appear to carry a paleo-enrichment signature that may be an inherited feature from advected mantle. If this enriched mantle was advected from beneath North America, it may explain the observation that High Lava Plains basalts are more enriched to the east.

© Copyright by Sarah Ashley Bromley

June 7, 2011

All Rights Reserved

Evolution and Inheritance of Cascadia Sub-arc Mantle Reservoirs

by

Sarah Ashley Bromley

A THESIS

submitted to

Oregon State University

in partial fulfillment of
the requirements for the
degree of

Master of Science

Presented June 7, 2011

Commencement June 2012

Master of Science thesis of Sarah Ashley Bromley presented on June 7, 2011.

APPROVED:

Major Professor, representing Geology

Chair of the Department of Geosciences

Dean of the Graduate School

I understand that my thesis will become part of the permanent collection of Oregon State University libraries. My signature below authorizes release of my thesis to any reader upon request.

Sarah Ashley Bromley, Author

ACKNOWLEDGEMENTS

I am indebted foremost to my advisor, Anita Grunder, for her unfailing patience and support throughout this project. Thanks, Anita, not only for your insight into all things geological, but also for sharing your vision and appreciation of the good life. I feel lucky to have had an advisor who so fully supported my endeavors, scientific and otherwise. I want to thank Bob Duncan, Adam Kent, and Armin Stuedlein for serving on my committee. I am especially grateful to Adam and Armin for their willingness to step in at the last minute. Bob provided invaluable assistance in acquiring and interpreting age data, and both Bob and Adam provided thoughtful feedback for which I am grateful.

John Dilles, Ashley Hatfield, Jeremiah Oxford, and Kevin Urbanczyk all supplied me with samples. Jeremiah was particularly generous in sharing his data, rocks, and expertise. Doug Pyle shared his unpublished data on the Sieltzia terrane. Dave Sherrod and Bob Duncan provided guidance on sampling in the Western Cascades, and Mark Ferns and Jason McClaughry were kind enough to lead me straight to primitive basalts.

Dale Burns provided instruction and assistance on the electron microprobe and was a total champ when I needed even more instruction and assistance in the middle of the night. Thanks again, Dale. John Huard provided assistance in the collection and reduction of age data. Alison Koleszar and Justin Millard both prepped samples for me, a favor I hope to repay to both down the road. Rick Carlson was a patient teacher in the lab and contributed greatly to my understanding of radiogenic isotopes and the geology of the western U.S. I could not have asked for a better surrogate advisor during my two stints doing lab work at Carnegie. I also want to thank Mark Ford for showing me the ropes on many, many lab related things and also for his discussions about the HLP, radiogenic isotopes, and geology, more generally.

I want to thank all the VIPER students and faculty for making OSU such a great place to study and work. I have to thank my cohort, in particular, for being

alongside me in the trenches those first couple of terms. I am convinced it was teamwork and beer that got us through Winter 2010. I cannot express how much I lucked out in getting Alison Koleszar and Erin Lieuallen as officemates. They have put up with my messy desk and emotional rollercoasters the whole way. I am very, very grateful to have been stuck in the basement with them both. Thanks also to Matt Loewen for being my comrade in all things geologic and union related. I should also thank Alison, Joe, Erin, Rocco, Matt, Caitlin, and Dennis for coordinating snacks at my defense when I was too rushed and frazzled to do it myself (and for knowing me well enough to anticipate that I would be). Thanks also to Stacey and Melinda for their humor and help through it all.

I have to thank Dennis Dugan for being a field assistant, cheerleader, and, occasionally, a punching bag through much of this process. Dennis accompanied me in the field to collect last minute samples (including a detour on his birthday), dropped me off for 2AM shuttles, and fielded countless texts, calls, and late night emails about the angst of writing. This thesis could not have been completed without his many late night deliveries of burritos, Blow Pops, and Coke Mexicos. And I'm sure I wouldn't have arrived here sanely if he had not been willing to play so much and so hard along the way. Thanks again, DD.

I also want to thank everyone from the Coalition of Graduate Employees (CGE, Local 6069) for fighting the good fight and for keeping me engaged in something more immediate than the Oligocene. Solidarity Forever.

Finally, I'm so thankful for my big, messy family. Through the ups and downs of this crazy year, I have been reminded again of the gift I was given by being born into a team. I cannot imagine weathering life without the love, support, and unique humor of each one of my siblings. Mleeka, Willem, Abbey, Fleda, and Bo—I hope you know how much I love and appreciate each one of you. Same goes for you, Daryl and Andy. I am also so thankful to my older siblings for sharing their amazing, gifted children. Lennie, Finn, Ori, and Beckett are each fascinating little individuals that I love watching grow into themselves. I want to thank my mom for being the

insanely strong and stubborn woman she is, for most of the millions of ways I'm like her, and for her help in staying up many nights. I'm grateful to my Poppa for his constant support, love, and understanding and for not giving me too hard of a time when I'm slow to return his calls.

TABLE OF CONTENTS

	<u>Page</u>
1 Introduction.....	2
2 Geologic Setting.....	5
2.1 Overview	5
2.2 Siletzia Terrane Forearc Basement.....	8
2.3 Eocene-Oligocene Coast Range Intrusive and Volcanic Units	10
2.3.1 Alkaline Intrusions	10
2.3.2 Gabbroic Intrusions.....	11
2.3.3 Yachats Basalt.....	12
2.3.4 Cascade Head Basalt.....	13
2.4 Western Cascades.....	14
2.5 Eastern Clarno and John Day Formations.....	16
2.6 Younger Cascadia Volcanism	18
2.6.1 High Cascades.....	18
2.6.2 High Lava Plains	21
3 Methods of Investigation	23
3.1 Sample Selection	23
3.2 $^{40}\text{Ar}/^{39}\text{Ar}$ Geochronology	24
3.2.1 Sample Preparation	24
3.2.2 Analytical Techniques.....	25

TABLE OF CONTENTS (Continued)

	<u>Page</u>
3.2.3 Age Determination.....	25
3.3 Whole Rock Composition by XRF and ICP-MS Analysis	25
3.4 Electron Microprobe Analysis of Phenocryst Phases.....	27
3.5 Radiogenic Isotopes by ICP-MS and TIMS.....	28
4 Eocene-Oligocene Proto-Cascadia Mantle	31
4.1 Age Data and Timing of Eocene-Oligocene Magmatism	31
4.1.1 Oregon Coast Range Intrusive and Volcanic Rocks	31
4.1.2 Western Cascades	32
4.1.3 Eastern Clarno and John Day Formations.....	33
4.2 Primitive Magmatism of Eocene-Oligocene Proto-Cascadia.....	37
4.3 Insights from Major and Trace Element Chemistry	39
4.3.1 Primitive Magma Types.....	41
4.3.2 Comparing Primitive Magmas Across the Arc	42
4.4 Insights from Radiogenic Isotopes	69
4.5 Heterogeneity of the Eocene-Oligocene Proto-Cascadia Mantle	80
5 Temporal Evolution of Cascadia Mantle Reservoirs	82
5.1 Comparison of the Eocene-Oligocene to Older and Younger Mantle Domains	82
5.1.1 Comparison with the Siletz River Volcanics	82
5.1.2 Comparison with the High Cascades	94
5.1.3 Comparison with the High Lava Plains	107

TABLE OF CONTENTS (Continued)

	<u>Page</u>
5.2 Implications for the Persistence and Modification of Sub-arc Mantle Domains	108
6 Conclusions	112
Bibliography.....	114
Appendixes.....	124

LIST OF FIGURES

<u>Figure</u>	<u>Page</u>
1.1 Map of the field area showing relevant magmatic provinces	4
2.1 Generalized compilation of Pacific Northwest magmatism focused on activity across present day latitude of central Cascades	7
4.1 Olivine compositions from Eocene-Oligocene Proto-Cascadia primitive samples.	38
4.2 MgO vs. SiO ₂ for primitive basalts from the Eocene-Oligocene transect	59
4.3 Map of the field area showing relevant magmatic provinces	59
4.4 Ba vs. Nb for primitive basalts from the Eocene-Oligocene transect	62
4.5 Ba/Zr vs. Nb/Zr for primitive basalts from the Eocene-Oligocene transect	62
4.6 Ba/ Nb vs. Nb/Zr for primitive basalts from the Eocene-Oligocene transect	64
4.7 Ba/Ce vs. Nb/Zr for primitive basalts from the Eocene-Oligocene transect.....	65
4.8 Simplified model of the effect of mantle partial melting on Ba/Ce, Ce/Yb, and La/Y ratios	67
4.9 Ba/Ce vs. Ce/Yb for primitive basalts from the Eocene-Oligocene transect.....	68
4.10 ¹⁴³ Nd/ ¹⁴⁴ Nd vs. ⁸⁷ Sr/ ⁸⁶ Sr for EOPC primitive magmas.....	76

LIST OF FIGURES (Continued)

<u>Figure</u>	<u>Page</u>
4.11 $^{87}\text{Sr}/^{86}\text{Sr}$ vs. Sr concentration for EOPC primitive magmas	78
4.12 $^{143}\text{Nd}/^{144}\text{Nd}$ vs. $^{206}\text{Pb}/^{204}\text{Pb}$ for EOPC primitive magmas	80
4.13 $^{207}\text{Pb}/^{204}\text{Pb}$ vs. $^{206}\text{Pb}/^{204}\text{Pb}$ for EOPC primitive magmas	81
4.14 $^{176}\text{Hf}/^{177}\text{Hf}$ vs. $^{206}\text{Pb}/^{204}\text{Pb}$ for EOPC primitive magmas	83
4.15 $^{176}\text{Hf}/^{177}\text{Hf}$ vs. $^{143}\text{Nd}/^{144}\text{Nd}$ for EOPC primitive magmas	84
5.1 MgO vs. SiO ₂ for primitive basalts from the Siletz River Volcanics	88
5.2 Nb/Zr vs. FeO*/MgO for primitive basalts from the Siletz River Volcanics.	90
5.3 Ba vs. Nb for primitive basalts from the Siletz River Volcanics	91
5.4 Ba/Zr vs. Nb/Zr for primitive basalts from the Siletz River Volcanics	92
5.5 Ba/Ce vs. La/Y for primitive basalts from the Siletz River Volcanics	94
5.6 $^{143}\text{Nd}/^{144}\text{Nd}$ vs. $^{87}\text{Sr}/^{86}\text{Sr}$ for primitive magmas from the Siletz River Volcanics.	95
5.7 $^{87}\text{Sr}/^{86}\text{Sr}$ vs. Sr concentration for primitive magmas from the Siletz River Volcanics	96

LIST OF FIGURES (Continued)

<u>Figure</u>	<u>Page</u>
5.8 $Z^{143}\text{Nd}/^{144}\text{Nd}$ vs. $^{206}\text{Pb}/^{204}\text{Pb}$ for primitive magmas from the Siletz River Volcanics	97
5.9 $^{207}\text{Pb}/^{204}\text{Pb}$ vs. $^{206}\text{Pb}/^{204}\text{Pb}$ for primitive magmas from the Siletz River Volcanics	98
5.10 MgO vs. SiO ₂ for primitive basalts from the High Cascades and High Lava Plains.	100
5.11 Nb/Zr vs. FeO*/MgO for primitive basalts from MgO vs. SiO ₂ for primitive basalts from the High Cascades and High Lava Plains	101
5.12 Ba vs. Nb for primitive basalts from the High Cascades and High Lava Plains	102
5.13 Ba/Zr vs. Nb/Zr the High Cascades and High Lava Plains.....	104
5.14 Ba/Ce vs. La/Y for primitive basalts from the High Cascades and High Lava Plains.....	105
5.15 Ba/Ce vs. Ce/Yb for primitive basalts from the High Cascades and High Lava Plains.....	106
5.16 $^{143}\text{Nd}/^{144}\text{Nd}$ vs. $^{87}\text{Sr}/^{86}\text{Sr}$ for primitive magmas from the High Cascades and High Lava Plains	107
5.17 $^{87}\text{Sr}/^{86}\text{Sr}$ vs. Sr concentration for primitive magmas from the High Cascades and High Lava Plains.....	108
5.18 $^{143}\text{Nd}/^{144}\text{Nd}$ vs. $^{206}\text{Pb}/^{204}\text{Pb}$ for primitive magmas from the High Cascades and High Lava Plains.....	110

LIST OF FIGURES (Continued)

<u>Figure</u>	<u>Page</u>
5.19 $^{207}\text{Pb}/^{204}\text{Pb}$ vs. $^{206}\text{Pb}/^{204}\text{Pb}$ for primitive magmas from the High Cascades and High Lava Plains	111
5.20 Schematic cartoon of Cascadia during the Eocene-Oligocene and Recent.....	116

LIST OF TABLES

<u>Table</u>	<u>Page</u>
2.1 Acronyms used in this text and the igneous provinces and units they denote	6
4.1 Summary of $^{40}\text{Ar}/^{39}\text{Ar}$ dating results.....	36
4.2 Primitive magma characterization scheme.....	40
4.3 Major and trace element chemistry for the Eocene-Oligocene mantle transect..	43
4.4 Isotope compositions for the Eocene-Oligocene mantle transect.....	71
4.5 External error of standards used for isotopic analyses	75

LIST OF APPENDICES

<u>Table</u>	<u>Page</u>
A $^{40}\text{Ar}/^{39}\text{Ar}$ Geochronology	129
B Phenocryst Compositions from Electron Microprobe (EMP) Analysis	166
C Complete Geochemistry of Samples Analyzed for this Study	182

Evolution and Inheritance of Cascadia Sub-arc Mantle Reservoirs

1 – Introduction

The aim of this work is to further the understanding of the heterogeneity of mantle source of magmas erupted and emplaced across the Eocene-Oligocene arc that is ancestral to the Cascades, herein called Eocene-Oligocene Proto-Cascadia (EOPC). The Eocene-Oligocene transition ($\sim 35 \pm 5$ Ma) corresponds to the onset of Cascadia magmatism and represents an important and understudied period in the evolution of Cascadia (e.g. du Bray et al., 2006; Priest, 1990). This work establishes the first EOPC mantle transect to determine the nature and scale of mantle heterogeneity. Through geochemical characterization of primitive, basaltic Eocene-Oligocene ($\sim 35 \pm 5$ Ma) rocks exposed in an across-arc transect, the spatial relationship between different mantle domains of Proto-Cascadia may be resolved. These results are then placed within the context of the broader evolution of the Cascadia subduction system by comparison to inferred mantle domains of the modern High Cascades and High Lava Plains, as well as older, Paleocene accreted oceanic lithosphere, the Siletzia terrane.

While the Cascade Arc has been widely studied and its modern isotopic heterogeneity well documented (see compilations of Schmidt et al., 2008; Hildreth, 2007), little work has focused on the extent to which this heterogeneity is inherited versus acquired in the modern arc configuration. The hypothesis is that geochemical mantle signatures may be inherited from earlier magmatic or tectonic episodes as well as being acquired via active subduction processes. To test the idea, this work characterizes the major element, trace element, and isotopic chemistry of primitive melts in a transect across the Cascadia arc in the past to evaluate the ancient distribution of mantle reservoirs and compare the past to pre-existing mantle domains and to the present arc. The persistence, change, or loss of sub-arc mantle domains in time has implications for how Cascadia in particular, but also how other subduction zones, recycle or replace mantle.

Late Eocene to early Oligocene mafic volcanic rocks related to the Proto-Cascadia forearc, arc, and backarc are exposed over a present-day distance of more than 300 km, providing a geological “window” into the underlying mantle (Figure 1.1). Accretion of the Paleocene Siletzia terrane at ~42 Ma (Duncan, 1982; Magill et al., 1981) and protracted subduction since ~42 Ma (Lux, 1981; Wells et al. 1984; Verplanck and Duncan, 1987; du Bray et al., 2006) have resulted in the accretion of lithospheric mantle, the flux of fluids from the subducting slab, and the extraction of magmas. Together, these processes have likely produced a heterogeneous mantle source underlying Cascadia. Moreover, the Eocene-Oligocene transect can be compared to the present day compositional and isotopic variability of basalt that is reasonably well established along the arc (e.g., Bacon et al. 1997; and see compilations by Schmidt et al., 2008 and Hildreth, 2007) and also across the arc (southern Washington- Leeman et al., 1990; 2004; Jicha et al., 2009, Gunn et al., 1996; central Oregon- Rowe et al. 2006, 2008; Schmidt et al., 2007, northern California- Grove et al., 1982, 2002; Kinzler and Grove, 2000). The isotopic characterization of the Paleocene Siletzia terrane has also been reported and may be used for comparison as well (Pyle et al., 2009; Pyle, personal communication).

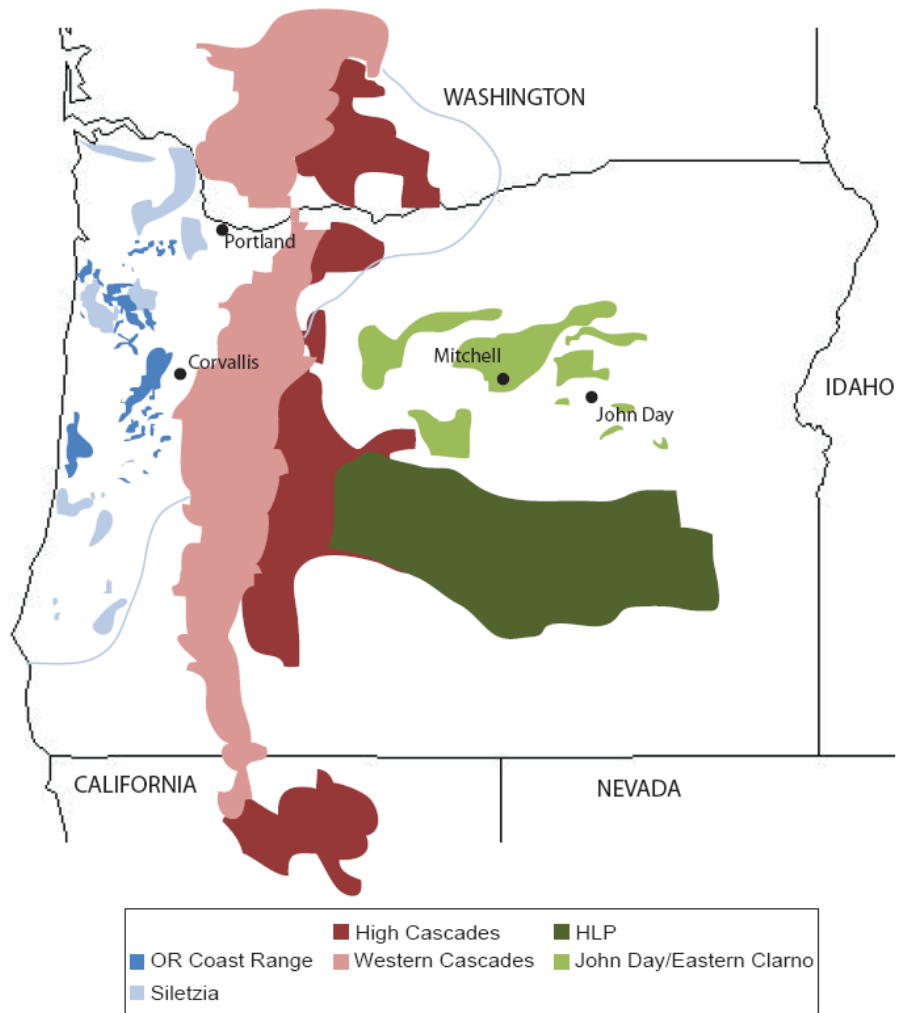


Figure 1.1: Map of the transect showing relevant magmatic provinces. Locations are after Oxford (2006) for the Paleocene-Eocene Siletzia and Eocene- Oligocene Oregon Coast Range; du Bray et al. (2006) for the Eocene-Miocene Western Cascades and Miocene-Quaternary High Cascades; Robinson et al. (1984) for the Eocene-Miocene John Day Formation; and Urbanczyk (1994) for the Eocene Eastern Clarno Formation. The transect was taken through central Oregon and is schematically outlined by the black box. The inferred extent of the Siletzia terrane is shown by the blue line. Lighter shades denote younger provinces.

2 – Geologic Setting

2.1 Overview

The Late Eocene to Early Oligocene witnessed a fundamental change in the dynamics and style of subduction at the margin of the North American continent. Broad, enigmatic Paleocene to Eocene volcanism that extended from British Columbia to South Dakota gave way to the early Cascadia arc at ~42 Ma (Lux, 1981; Wells et al. 1984; Verplanck and Duncan, 1987; du Bray et al., 2006). Largely intermediate composition volcanic rocks and intrusions of the deeply eroded Western Cascades flank the modern High Cascades and represent the remains of the original, more westerly axis of the arc that was active between ~42-10 Ma (du Bray et al., 2006). Coeval magmatism east of (behind) the arc axis is preserved within the John Day and Eastern Clarno Formations as silicic air fall and ash flow tuffs, tuffaceous sedimentary rocks, and sparse mafic flows and dikes (Appel, 2001; Urbanczyk, 1994; Walker, 1990; Robinson et al., 1984; Taylor, 1981). Magmatism in the Proto-Cascadia forearc is now preserved as numerous mafic dikes and sills in the Oregon Coast Range (Snively and Wagner, 1961; Oxford, 2006; Walker and MacLeod, 1991) and as the Yachats and Cascade Head Basalt flows. Tertiary forearc magmatism appears to be the result of localized extension, possibly related to tectonic rotation and dextral transtension of the Coast Range block (e.g., Plumley et al., 1997; Wells et al., 1998; Oxford, 2006) and is expressed as gabbros, alkali basalts, camptonite plus minor differentiated products including nepheline syenite (Oxford, 2006).

The Oregon Coast Range Intrusions (OCRI) and related Tertiary magmatic provinces are underlain by the Siletz River Volcanics (SRV), which are mostly mafic submarine volcanics formed between 56-50 Ma and appear to have been rapidly accreted to the North American continent (Pyle et al., 2009; Duncan, 1982). Subsequent forearc magmatism is restricted to areas underlain by the Siletzia terrane, suggesting that Siletzia is the mantle source for much of the forearc magma. The

Siletzia terrane also extends beneath the Western and, perhaps, the High Cascades and may influence magmatism beneath the arc as well (Schmidt et al., 2008; Trehu et al., 1994).

Western Cascades magmatism gave way to magmatism along the arc of the modern High Cascades at ~10 Ma (du Bray et al., 2006). The High Cascades, while more focused than the older arc (Sherrod and Smith, 2000; Priest, 1990), remains a broad arc with abundant forearc and backarc magmatism (Figure 2.1). Diffuse mafic volcanism is common especially in the extended central Cascades (Hildreth, 2007; Sherrod and Smith, 1990). Bimodal High Lava Plains magmatism in the backarc began ~12 Ma and continues until recent (e.g. Jordan, 2004). Taken together, these provinces provide a record of ~60 My of magmatism preserved in Cascadia (Figure 2.1). Each of these provinces and units are considered in greater detail to provide a framework for considering the mantle evolution recorded by their primitive magmas.

Table 2.1: Acronyms used in this text and the igneous units and provinces they denote.

Acronym	Igneous Unit or Province
EOPC	Eocene-Oligocene Proto-Cascadia
OCR	Oregon Coast Range
OCRI	Oregon Coast Range Intrusions
YB	Yachats Basalt
CHB	Cascade Head Basalt
JD/EC	John Day and Eastern Clarno formations
SRV	Siletz River Volcanics
HLP	High Lava Plains

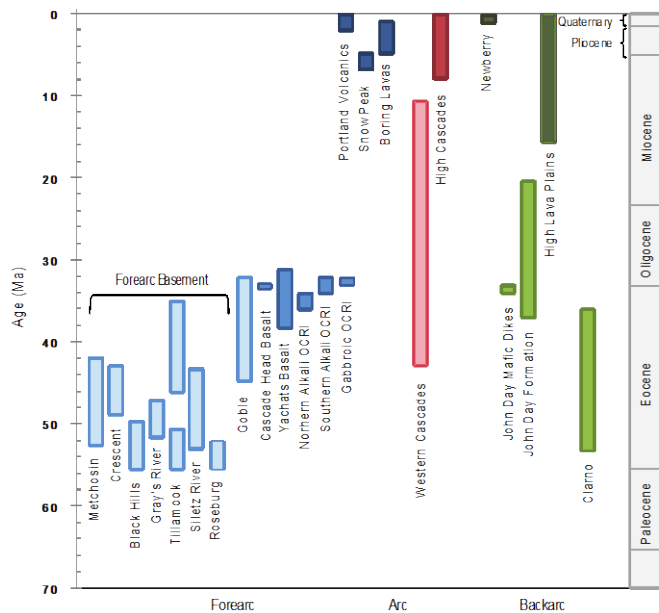


Figure 2.1: Generalized compilation of Pacific Northwest magmatism focused on activity across present day latitude of central Cascades. Localities and ages taken from: Siletzia (Metchoshin, Crescent, Black Hills, Gray's River, Siletz River, Roseburg), Duncan (1982); Tillamook, Magill et al. (1981) and Wells et al. (1994); Goble, Beck and Burr (1979); Yachats basalt and the Cascade Head Basalt, Davis et al. (1995); OCRI, Oxford (2006); Portland Volcanics and Boring lavas, Allen (1975); Snow Peak, Hatfield (2008); Quartzville basalt, Rowe (2006); Western Cascades and High Cascades, Christiansen et al. (1992); Newberry, (Sherrod et al. (1997); The Clarno and John Day Formations, Walker and Robinson (1990) and Urbanczyk (1994); John Day Mafic Dikes, Appel (2001); High Lava Plains, Jordan (2001).

2.2 Siletzia Terrane Forearc Basement

The Paleocene-Eocene (~56-50 Ma) Siletz River Volcanics (SRV) include the separately named basalts of the Metchosin Formation (Vancouver, B.C.), Crescent Formation (Washington), Siletz River Volcanics (Central Oregon), and Roseburg Formation (Southern Oregon) (Duncan et al., 1982; Pyle et al, 2009). These submarine and subaerially erupted basalts, along with interbedded sediments, constitute the upper portion of the allocthonous Siletzia terrane (Christiansen et al., 1992). Siletzia has been interpreted as a fossil oceanic plateau that was tectonically emplaced onto the North American margin and now forms the basement beneath much of the Cascadia forearc (Trehu et al., 1994). The Siletzia terrane constitutes the largest block of the Columbia Embayment, a lithospheric terrane defined by negative gravity anomalies (Couch and Riddihough, 1982) and inferred to be of oceanic affinity (Miller et al., 1989; Burchfiel et al., 1992). The eastern extent of the Siletzia terrane is not well defined, but may lie beneath the Western Cascades or as far east as the axis of the High Cascades (Schmidt et al., 2008; Trehu et al., 1994).

Siletzia ranges from ~10-15 km thick in southern Washington to more than 30 km thick beneath Central Oregon (Stanley et al, 1990; Trehu et al, 1994; Parsons et al, 1999). Based on seismic imaging, Pyle et al. (2009) estimated the total volume of Siletzia to be ~2.6 million km³ in original volume. A more modest estimate of ~250,000 km³ still makes Siletzia the most voluminous volcanic unit in the Pacific Northwest (Duncan, 1992).

Recent ⁴⁰Ar/³⁹Ar dating has refined the timing of Siletzia volcanism and constrained the majority of the activity to between ~56-50 Ma (Pyle et al., 2009). Previous K/Ar and ⁴⁰Ar/³⁹Ar dating found that volcanism migrated from the northern and southern extremities of the province to the center with time (Duncan, 1982). However, refined dating and reclassification of some units has led to the more recent

interpretation that volcanism began in the south (56-53 Ma) and swept north (54-50 Ma). Taken together, the volume, short duration (high volume flux), and age progression of Siletzia volcanism have been interpreted as evidence that Siletzia is a large igneous province (LIP) resulting from a mantle plume (Pyle et al., 2009; Duncan, 1982).

Specifically, Pyle et al. (2009) and Duncan (1982) have identified Siletzia as an early expression of the Yellowstone hotspot. Duncan (1982) further argued that Siletzia resulted from the interaction of the Yellowstone hotspot and the Kula-Farallon ridge. This model explained the early observation that ages increased symmetrically from a central location (Duncan, 1982), but may not agree as well with more recent dating (Pyle et al., 2009). Plate reconstructions place the Yellowstone hotspot just offshore during the initiation of Siletzia magmatism (Wells et al., 1984). Moreover, elevated $^3\text{He}/^4\text{He}$ ratios and HIMU-like Pb isotopic compositions for SRV lavas support a mantle plume origin for Siletzia (Pyle et al., 2009). The location of Eocene-Oligocene Oregon Coast Range forearc magmatism also coincides with the proposed track of the Yellowstone hotspot (Duncan, 1982), perhaps suggesting a Yellowstone hotspot influence for these small volume forearc units.

Others have argued that Siletzia is the product of asthenospheric upwelling around a slab window created as the Kula-Farallon ridge was subducted beneath the North American margin (Babcock et al., 1992). Haeussler et al. (2003) suggest that Siletzia is actually the product of a slab window from the subduction of the Farallon-Resurrection ridge and that the ocean island basalt (OIB)-like chemistry of the upper SRV is suggestive of an origin via a slab window. The involvement of a slab window also explains the range of compositions from MORB to OIB present from the lower to upper SRV, but may not adequately account for the large volume of the SRV. Though the precise origin of Siletzia has not been agreed upon, most authors appeal to either a mantle plume or slab window to account for the rapid emplacement of such a voluminous and compositionally diverse LIP.

Cascadia forearc magmatism has been restricted to areas underlain by the Siletzia basement and associated mantle since the accretion of the Siletzia terrane. Siletzia mantle may have provided a fertile source for subsequent magmatism in the forearc or along the arc. Comparison of younger magmas to the SRV will allow for the identification of a possible common mantle source and suggest the longevity of the accreted Siletzia mantle domain.

2.3 Eocene-Oligocene Coast Range Intrusive and Volcanic Units

2.3.1 Alkaline Intrusions

Alkaline rocks (including lamprophyres, nepheline syenites, camptonites, and alkali basalts) constitute less than 5 percent of the total volume of exposed Oregon Coast Range Intrusions (OCRI) (Oxford, 2006; Snavely and Wagner, 1961). Alkaline intrusions tend to crop out as small dikes, sills, stocks, and other intrusive bodies and are generally found farther west than, and never in contact with, gabbroic intrusions (Snavely and Wagner, 1961). Alkaline intrusions were emplaced between ~36-32 Ma and overlap in age with both gabbroic intrusions and the Yachats Basalt (YB) and Cascade Head Basalt (CHB) forearc volcanic centers (Oxford, 2006; Davis et al., 1995).

The camptonite intrusions are the most silica undersaturated rocks in the OCRI (Oregon Coast Range Intrusions) suite and appear to represent the most primitive magmas (MacLeod and Snavely, 1973). Camptonites are basaltic to basanitic in composition with silica contents ranging from 40.4% to 49.8%. Textural and major element evidence for crystal fractionation precludes these magmas from being primary melts (Oxford, 2006). However, there is no evidence of extensive assimilation, so that both radiogenic isotopes and incompatible trace element pairs may serve as good indicators of mantle source.

Broadly speaking, camptonites and alkaline basalts have incompatible element compositions similar to those of OIBs (Oxford, 2006; Sun, 1980). They tend to be highly enriched in the highly incompatible elements (e.g. Ba, Rb, Zr, Nb), displaying a greater degree of enrichment than typical OIB magmas (Oxford, 2006; Sun, 1980). Oxford (2006) interpreted these trace element enrichments to suggest that the alkaline OCRI originated from small degrees of partial melting of an enriched source. Oxford (2006) also preferred a deep source (sub-slab) to impart a garnet signature (low La/Y) upon the alkaline OCRI. Oxford (2006) postulated that the petrogenesis of the OCRI may have involved an interaction between asthenospheric and metasomatized lithospheric mantle sources. Though trace element comparisons could not conclusively link the SRV and alkaline intrusions, a shared mantle source is suggested for the two (Oxford, 2006). Other authors have appealed to the spatial and temporal association of the alkaline and gabbroic intrusions to suggest a common mantle source (Snively and Wagner, 1961). Alternately, authors have suggested that the geochemical affinity and proximity between the alkaline OCRI and YB and CHB suggest a shared mantle source (Oxford, 2006; Davis et al., 1995; MacLeod and Snively, 1973). The general affinity among SRV and Eocene-Oligocene forearc intrusions and volcanic centers suggests the possibility of a shared mantle source for all of these forearc units.

2.3.2 *Gabbroic Intrusions*

Gabbroic intrusions represent a more wide-spread, short lived pulse of magmatism than do the alkaline OCRI. Gabbroic magmatism only lasted from ~33-32 Ma (Oxford, 2006), but MacLeod (1981) estimates that more than 5,000 km² of the central Oregon Coast Range is covered by gabbroic sills. These sills tend to be thick (on average 120-170m) and are often strongly differentiated (Snively and Wagner, 1961). Gabbros typically lie along a tholeiitic differentiation path but are generally more enriched in alkalis than other tholeiites (Oxford, 2006).

Gabbroic intrusions are less enriched in incompatible elements than the alkaline OCRI, but have signatures suggestive of a subduction influence (Oxford, 2006). The closer proximity of gabbroic intrusions to the Western Cascades may provide a source for this signature. Oxford (2006) suggests that gabbroic magmas resulted from Eocene-Oligocene forearc extension with some subduction flux from the arc.

Though Oxford (2006) selected gabbroic dikes that did not appear to have undergone significant *in situ* fractionation, gabbros sampled are basaltic andesites in composition and do not represent mantle melts. Gabbroic OCRI samples are not considered in this work because no samples were found that were sufficiently mafic to pass the filter for primitive compositions (See Section 4.2). Oxford (2006) suggests that the gabbroic and alkaline OCRI have separate mantle sources and that the gabbroic OCRI are therefore not related to accreted Siletzia lithospheric mantle, but originate from a deeper asthenospheric source.

2.3.3 *Yachats Basalt*

The Yachats Basalt (YB) erupted between ~37-34 Ma (Davis et al., 1995), overlapping in age with the alkaline OCRI (Oxford, 2006). The YB consists primarily of subaerial flows and pyroclastic units. Less common pillow basalts and other subaqueous deposits suggest that the YB formed low lying near shore islands (Snively and MacLeod, 1974, Barnes and Barnes, 1992). Eruptive products were primarily tholeiitic basalts with smaller volumes of more differentiated products. Additionally, small volume alkaline basalts are also present in the eruptive sequence, with the alkaline character more pronounced in the later stages (Davis et al., 1995). Trends within the YB can be explained largely by crystal fractionation (Davis et al., 1995), and primary melts do not appear to be present in the YB sequence. Magmas are believed to have stalled and differentiated en route to the surface in shallow crustal chambers. This view is argued for based on the porphyritic nature of many of the

volcanic rocks and the lack of a true primary magma (Snively and MacLeod, 1974; Davis et al., 1995). However, reasonably primitive magmas (MgO wt.% ~7) can be found and do not appear to have undergone significant crustal contamination.

The YB lies above Eocene sedimentary sequences that are underlain by Siletzia basement (Davis et al., 1995). The YB has chemical affinities with the alkalic OCRI and SRV and could possibly share a Siletzia mantle source.

2.3.4 *Cascade Head Basalt*

The Cascade Head Basalt (CHB), like the Yachats Basalt, was erupted over a narrow time interval (~34-33.5 Ma). While also basaltic in composition, the CHB has a more alkaline character than the YB, with ~75% of the CHB consisting of alkali basalt, hawaiite, ankaramitic basalt, and trachyandesite (Barnes and Barnes, 1992). While many CHB samples have high MgO (>7 wt.%), these samples are often the result of the accumulation of clinopyroxene phenocrysts, and are not primitive mantle melt compositions. However, flows from the youngest phase of the CHB, the Cannery Hills, extend to >9 wt.% MgO, and provide reasonable proxies for mantle melts (Davis et al., 1995). As with the YB, most CHB magmas are believed to have fractionated in shallow crustal reservoirs (Barnes and Barnes, 1992) before making it the surface. Both YB and CHB share geochemical characteristics with intraplate, OIB type magmas (Davis et al., 1995; Barnes and Barnes, 1992). LREE, HFSE, and LILE enrichments suggest an enriched source, similar to that of the alkaline OCRI. These CHB and YB may have derived from low degree partial melts of the Siletzia mantle before stalling and fractionating in the crust (Davis et al., 1995), or they may be deep source melts from beneath a slab window. Barnes and Barnes (1992) argue for the latter, suggesting that the Siletzia mantle could not have been hot enough at the depth of the slab to induce melting. Along with the alkaline OCRI, the YB and CHB will be evaluated to determine the potential for a shared mantle source with the SRV.

2.4 Western Cascades

The Late Eocene to Early Oligocene witnessed a shift in the location of subduction at the margin of the North American continent. Magmatism along the broad, poorly understood Challis arc, which extended from British Columbia to South Dakota, gave way to the early Cascadia arc at ~ 42 Ma (Lux, 1981; Wells et al., 1984; Verplanck and Duncan, 1987; du Bray et al., 2006). The Western Cascades were active between ~42-10 Ma. Western Cascade magmas are now exposed as the deeply eroded flanks of the modern High Cascades. Eruptive products range from rhyolitic to basaltic compositions defining both calc-alkaline and tholeiitic trends (du Bray et al., 2006; Verplanck, 1985). Trace-element compositions of the tholeiitic series are consistent with that of an island arc, and coupled with evidence for voluminous silicic magmatism, document the early stages of continental arc formation (Priest and Vogt, 1983).

The early phase of Western Cascades magmatism (~42-18 Ma) consisted of local andesitic volcanoes, tholeiitic olivine basalt and basaltic andesite lavas, and voluminous andesitic to dacitic ash flow tuffs (Priest, 1990; Verplanck and Duncan, 1987; Verplanck, 1985). An erosional unconformity is observed by some authors between ~19-17 Ma (Priest, 1990; Priest and Vogt, 1983) and is inferred to represent an episode of uplift where early Western Cascade units were tilted and deformed. Other authors have argued for nearly continuous magmatism between 42-10 Ma (Verplanck and Duncan, 1987). Later Western Cascades volcanism (~18-9 Ma) is preserved as andesitic-basaltic lava flows interbedded with volcanoclastic rocks (Verplanck and Duncan, 1987; Verplanck, 1985). Volcanic strata of the Western Cascades have a shallow regional eastward dip (~3-10°), with younger units dipping more gently. Owing to this regional dip and later erosion, older Western Cascades units are generally exposed farther west with the age of exposures decreasing eastward (Verplanck and Duncan, 1987).

Other authors have also argued that this apparent age progression reflects an eastward migration of the arc axis during the last 35 My (Priest 1990). Priest (1990) appeals to a flattening of the shallow slab (<100 km depth) to explain the migration of the arc. Lithospheric thinning from thermal erosion and extension is suggested as a cause for a more shallow dip for the hot, buoyant subducting plate (Priest, 1990). The apparent eastward migration of the arc axis is also complicated by the interpretation of the ash flow tuffs of the John Day Formation. While early authors interpreted these voluminous silicic units to be distal products of the Western Cascades (Robinson, 1984), more recent mapping has suggested that some of these tuffs may be products of local caldera systems well to the east of the assumed axis of the Western Cascades (McCloughry et al., 2009). These authors (ibid.) suggest that the arc during this time was much broader than traditionally assumed and stretched to the modern day backarc. Though such ash flow units may be considered part of the Western Cascades, the term Western Cascades is used in this text as in du Bray et al. (2006) to denote Tertiary volcanic rocks exposed west of the present High Cascades crest. These volcanic rocks make up the geographic expression of the arc during the Eocene-Oligocene, though the arc influence may extend further east. Local mafic dikes and flows of the John Day and Eastern Clarno Formations are considered separately and are denoted as geographically backarc.

Priest (1990) also observes a narrowing of the volcanic belt through time, even without considering the possible eastern extent of the arc suggested by the work of McCloughry et al. (2009). This narrowing has been attributed to decreasing convergence rates leading to a shallower loss of volatiles and decreasing degrees of partial melting at depth, thus narrowing the zone of melting within the mantle wedge (Verplanck and Duncan, 1987; Taylor, 1990). These observations agree with the decreased convergence rate surmised by Verplanck and Duncan (1987) based on calculated eruption rates from inferred volumes of Western Cascade volcanics. The narrowing of the volcanic belt has alternately been attributed to the steepening of the deep slab (>100 km) through time (Priest, 1990).

The Western Cascades represent the onset of Cascadian subduction. The extent and configuration of the Western Cascade arc remains unclear, and it is possible that the Western Cascades represented a wide, diffuse arc. A comparison of Western Cascade magmas to those from the geographic fore- and backarc will further inform our understanding of Western Cascade magmas and the mantle sources of magmas from across the arc.

2.5 Eastern Clarno and John Day Formations

The Clarno Formation of eastern Oregon is composed of Tertiary volcanic and volcanoclastic rocks (e.g. Walker and Robinson, 1990). The Clarno is dominantly andesitic in composition and has a calcalkaline differentiation trend and LILE enrichment that has lead many authors to surmise an arc affinity. The Clarno Formation has been lumped with a number of Eocene calcalkaline volcanic provinces as part of the Challis arc (Armstrong, 1978). The Challis arc has traditionally been interpreted to result from flat slab subduction producing a very broad magmatic belt (Lipman, 1992; Lipman and Glazner, 1991; Noblett, 1981). Other authors have attributed Challis volcanism to lithospheric extension (e.g. Hiza, 1999; Hooper et al, 1995; Norman and Mertzman, 1991), sometimes associated with a slab window (e.g. Loewen, 2008; Madsen et al., 2006; Dostal et al., 2003).

Large Clarno Formation outcrops south of Prineville, OR extend northward and have been most thoroughly studied. However, scattered outcrops of similar composition are clustered north of John Day, OR and make up the Eastern Clarno Formation (Urbanczyk, 1994). The Eastern Clarno Formation extends to younger ages (43.5-33 Ma) and has been found to overlap in age with the base of the John Day Formation at ~39.7 Ma (Retallack et al., 2000; Bestland and Retallack, 1994). The overlap in ages between the Western Cascades and Eastern Clarno argue against the traditional explanation that the Clarno formed as part of the Challis arc that was active before the westward jump of the subduction zone at ~42 Ma (Urbanczyk, 1994). The

Eastern Clarno may be explained as a backarc expression of Western Cascades subduction. However, if the EC is related to extension, an explanation must be offered for the apparent arc signature in these magmas. Urbanczyk (1994) argues that such a signature may result from paleo-enrichment from earlier subduction events. If the lithospheric mantle beneath the EC was previously altered by subduction events, these signatures may persist in magmas produced by or interacting with the lithospheric mantle. Such a paleo-subduction influence is difficult to distinguish from a modern subduction influence unless significant time has passed for isotopic signatures to evolve.

The John Day Formation (JD) of north-central Oregon extends ~200 km east from the Cascade arc and is generally considered to lie stratigraphically between the Eocene Clarno Formation and the Miocene Columbia River Basalts (Robinson et al., 1984). This stratigraphy breaks down where the Eastern Clarno and John Day Formations are believed to overlap in age. Unlike the Clarno, the John Day Formation is a dominantly andesitic to dacitic pyroclastic sequence (Robinson et al., 1984). The JD ranges in age from ~39.7-19 Ma and consists of andesitic to dacitic tuffaceous claystones and air fall tuffs. These are interlayered with more rhyolitic ash flow sheets. Additionally, rhyolite, trachyandesite, and basalt lava flows occur early in the JD.

Robinson et al. (1984) interpreted the air fall tuffs of the JD as distal records of early Western Cascade volcanism based on differences in thickness and stratigraphy between the three geographically separate facies (Eastern, Southern, and Western). Trachyandesite and alkali-olivine basalts and dikes represent local magmatism within the JD (Robinson et al., 1984; Taylor, 1981). While Robinson et al. (1984) appeal to a far distal (130-160 km) source for air fall tuffs, they interpret ash flow tuffs as slightly more proximal in source. Rhyolite domes at the far western extent of the JD Formation (Powell Buttes, Grizzly Mountain, and Juniper Butte) are suggested as sources for the more silicic ash flow tuffs. Ash flow tuffs and local lava flows disappear from the JD by about ~25 Ma, after which only apparently distal sources

continued to erupt. The end of the John Day time at ~19 Ma corresponds with a likely hiatus in Cascade volcanism at ~20-19 Ma (McBirney et al., 1974).

Recent work has suggested a more proximal source for ash flow and air fall tuffs within the JD Formation. McClaughry et al. (2009) describe the presence of at least 5 large Eocene-early Miocene calderas in southwest Oregon, some of which were recognized previously by Robinson et al. (1984). These calderas are suggested to be more likely sources for the tuffs of the John Day Formation. Therefore, the relationship between the Western Cascades and both the John Day and Eastern Clarno Formations remains unclear. These relationships, and especially the possibility of shared mantle sources may be illuminated through examination of the trace element and isotopic characteristics of these contemporaneous magmatic provinces.

2.6 Younger Cascadia Volcanism

2.6.1 High Cascades

Though the High Cascades are most readily associated with the large andesitic-dacitic stratovolcanoes that make up the irregular arc axis running from Mount Baker to Mount Lassen, 2,339 Quaternary volcanoes have been identified in the Cascade arc proper (Hildreth, 2007). These range in composition from rhyolitic domes to primitive basaltic cinder cones and spatter cones. The onset of High Cascade volcanism is variably cited as between 10-2 Ma, such that the Quaternary volcanoes may represent only the more recent stage of High Cascade volcanism (du Bray et al., 2006). While some authors have suggested that a pronounced discontinuity exists between Western Cascades and High Cascades magmatism (Callaghan, 1933), field work has demonstrated that such an unconformity is not present for much of the length of the arc (du Bray et al, 2006). Owing to this and the presence of common forearc magmatic centers of the High Cascades, the Western Cascades and High Cascades may overlap somewhat in both time and space.

The High Cascades arc is broad, and what is considered spatially the arc front does not represent the full extent of magmatism. Both geographic fore- and backarc magmatic centers are common and may share a subduction influence, making the exact distinction of an arc difficult (Hildreth, 2007). The broad nature of the High Cascades arc has been attributed to the young, hot, and relatively flat (at shallow depths, 5-20°C, but steepens beneath the axis of the arc) nature of the subducting Juan de Fuca plate and associated microplates and their slow convergence (35-45 mm/yr) beneath North America (Schmidt et al, 2008; Hildreth, 2007). These features lead to the continuous loss of fluid beneath the forearc, arc, and backarc of the High Cascades axis, thus promoting fluid flux melting over a wide swath. Leeman and others (1990, 2004, 2005) concluded that in Southern Washington there was very little slab contribution beneath the arc axis volcanoes, citing the loss of Li and B in the forearc. However, it has been observed that the majority of plate dehydration commonly occurs beneath the forearc (Peacock, 1993; Schmidt and Poli, 1998; Bostock and others, 2002; Hacker and others, 2003; Hyndman and Peacock, 2003; Brocher and others, 2003), but that enough water makes it deep enough to facilitate melting beneath arc axes.

Additionally, the arc character of the Cascades is within the range observed in other arcs, suggesting that the subduction component may be reduced by early devolatilization of a young, hot slab, but that the slab still makes important fluid contributions to melt generation beneath the High Cascades arc (Hildreth, 2007). The broad nature of the arc and presence of apparently arc-like volcanics in the fore- and backarc suggest that hydrous mantle melting conditions are met in a broad 25-160 km east-west belt beneath the arc (Hildreth, 2007). Basaltic magmas ascend from a wide across-arc region of partially molten sub-arc mantle reservoirs that are inferred to be heterogeneous based on the close distribution of distinct primitive magma types (Hildreth, 2007; Bacon et al., 1997; Conrey et al., 1997). The subduction component, thermal structure, and mantle domains must vary on small spatial scales to produce

closely spaced (temporally and spatially) magmas of different character (Hildreth, 2007).

Schmidt et al. (2008) use the distribution of High Cascades volcanic centers along with the trace element and Nd and Sr isotopic character of primitive magmas to divide the arc into four segments. These segments are distinguished by tectonic setting, distinct mantle domains, and variable melting conditions at depth. From north to south, they are 1) the North Segment from Mt. Meager to Glacier Peak; 2) the Columbia Segment from Mt. Ranier to Mt. Jefferson; 3) the Central Segment from the Three Sisters to Medicine Lake, and 4) the South Segment from Mt. Shasta to Lassen Peak (Schmidt et al., 2008).

The Eocene-Oligocene Proto-Cascadia (EOPC) mantle transect presented in this study brackets the geomorphic and isotopic domain boundary between the Central and Columbia segments of the modern arc (Schmidt et al., 2008), and the character of these segments is most closely considered for comparison with earlier mantle domains. The central Oregon Cascades within the Columbia and Central segments are especially notable for abundant and broadly distributed mafic volcanism. These mafic magmas are typically low potassium tholeiites (LKT), and their presence traces the northward sweep of the intra-arc rift between 8-0 Ma (Schmidt et al., 2008; Conrey et al., 2004; Sherrod and Smith, 1990; Hughes and Taylor, 1986). Clockwise rotation of the Siletz forearc block, which underlies the arc in Southern Washington and Northern Oregon, has been observed and explains the northward propagation of the intra-arc rift (Wells et al., 1998; Wells et al., 1994).

Of the five primitive magma types recognized by Schmidt et al. (2008), calcalkaline basalts (CABs), low K tholeiites (LKTs), and high field strength element enriched basalts are most abundant in the Columbia and Central segments. High Mg andesites and absarokites are much less common. Workers have identified at least three distinct mantle domains responsible for producing these three most common primitive magma types in the Cascades (Rowe et al., 2009; Bacon et al., 1997; Conrey

et al., 1997). These same magma types are recognized across the EOPC arc and can be used for comparison of mantle domain longevity.

2.6.2 *High Lava Plains*

The High Lava Plains province (HLP) comprises a suite of strongly bimodal Late Tertiary to Quaternary volcanic rocks exposed across central and southeastern Oregon (e.g. Jordan et al., 2004; Walker, 1974). The HLP is located at the northward termination of the Basin and Range province where faulting transitions to the northwest striking Brothers Fault Zone (Scarberry et al., 2010; Jordan et al., 2004, Lawrence, 1976). Silicic volcanism of the HLP is expressed as numerous dome complexes and three major, voluminous ash flow tuffs (Prater Creek, Devine Canyon, and Rattlesnake Tuffs), among many smaller tuffs. Silicic rocks are mainly metaluminous to mildly peralkaline high silica rhyolites. HLP rhyolites are time transgressive with age decreasing to the west (Ford et al., 2009; Jordan et al., 2004; Walker, 1974; MacLeod et al., 1975; McKee and Walker, 1976).

Numerous models have been suggested to explain the time transgressive nature of HLP silicic magmatism. The HLP trend has been suggested to have resulted from the accommodation of the termination of Basin and Range extension through a propagating shear zone (Christiansen et al., 2002; Christiansen and McKee, 1978). Subduction induced mantle flow in the backarc has also been suggested to create the westward younging of silicic centers (Druken et al., in submission; Long et al., 2009). Others have suggested that the HLP trend is an expression of the Yellowstone Hot Spot, and particularly of the flow of plume head material (Jordan et al., 2004; Humphreys et al., 2000; Draper, 1991).

In addition to age progressive silicic volcanism, the HLP experienced voluminous basaltic volcanism between ~12 Ma and present. Basalts of the province are dominantly tholeiitic (corresponding to the LKTs of the High Cascades). Calcalkaline basaltic andesites also occur (Jordan et al., 2004). While the basalts of

the HLP do not follow a westward younging trend, other trends in ages are apparent. Episodes of province-wide basaltic volcanism appear to have occurred at ~7.8-7.5, 5.9-5.3, and 3-2 Ma (Jordan et al., 2004). The timing of this earliest widespread event corresponds closely with the onset of High Cascades volcanism (7.4 Ma according to Priest, 1990).

The current focus of the HLP trend has been suggested to be at Newberry Volcano (Humphreys et al. 2000). Newberry may therefore represent the intersection of the High Cascades arc and HLP. The HLP generally overlap the footprint of Eocene-Oligocene backarc magma (though displaced south), and comparison among these provinces may suggest the longevity of the mantle source beneath these regions and perhaps influence the interpretation of the HLP.

3 – Methods of Investigation

3.1 Sample Selection

A total of 31 new samples were collected from a transect across central Oregon, and 13 previously dated or chemically characterized samples were also chosen for isotopic analysis. Samples were selected to provide the least obstructed view of the mantle possible, so the most primitive and least altered samples were targeted. As this work aims to characterize the mantle within a narrow time frame, samples from units previously dated or stratigraphically constrained to $\sim 35 \pm 5$ Ma were also targeted. Samples from the Oregon Coast Range were provided by Jeremiah Oxford. Oxford (2006) characterized the major and trace element chemistry of Coast Range intrusive rocks from central Oregon and dated many of these units. Existing geochemistry and dating allowed for the selection of the most primitive samples possible and guaranteed that samples fell within the desired age range. Further sampling from the forearc focused on the Yachats Basalt (YB). Samples from the YB have been dated by the K/Ar method and have major element chemistry determined by Davis et al. (1995). Sampling from localities described by Davis et al. (1995) allowed for sampling of the most primitive parts of the YB and constrained the ages of samples taken.

One Western Cascade sample was provided by Ashley Hatfield. Hatfield (2009) determined a precise $^{40}\text{Ar}/^{39}\text{Ar}$ age and characterized the major and trace element chemistry of this sample. Sampling of other Western Cascade localities was guided by the work of Verplanck (1985) for the purpose of resampling primitive samples of appropriate age. Mark Ferns and Jason McClaughry of DOGAMI provided field expertise that allowed for the location of additional suitable samples within the Western Cascades.

In the geographic backarc, samples were taken from both the John Day and Eastern Clarno Formations. Samples from the John Day Formation of known or

stratigraphically constrained age were provided by John Dilles and Ed Taylor. Additional samples were collected from the John Day Formation based on previous dating of John Day mafic dikes by Taylor (1981) and Appel (2001). Samples from Eastern Clarno were provided by Kevin Urbanczyk. Previous XRF major element characterization and dating of these samples allowed for the selection of the most primitive samples believed to be of similar age to the desired transect.

Where available, samples with established ages and composition were preferred to guarantee that isotopic analyses were focused on the mantle-derived samples of similar age. For newly collected samples believed to be most primitive based on mineralogy, isotopic analyses were performed before whole-rock chemical and age data could be obtained.

3.2 $^{40}\text{Ar}/^{39}\text{Ar}$ Dating

3.2.1 Sample Preparation

Seven samples from the central Oregon transect were dated using $^{40}\text{Ar}/^{39}\text{Ar}$ incremental heating techniques at the Noble Gas Mass Spectrometry Lab located in the College of Oceanic and Atmospheric Sciences at Oregon State University following the methods of Koppers et al. (2003). Small hand samples of material from each sample were crushed using a steel hammer and plate. Chips were then fed through a small jaw crusher and sieved to a grain size of ~300-500 μm . The resulting material was rinsed and put through an ultrasonic bath in distilled water. Samples were then dried in an oven and put through a Franz magnetic separator to remove magnetic phases. The remaining fraction was cleaned in an ultrasonic bath of 5% (by volume) HNO_3 then rinsed thoroughly with deionized water and dried. Fresh groundmass pieces were then hand-picked under a binocular microscope prior to irradiation and analysis. Approximately 70 mg of each sample was wrapped in Cu-foil and loaded in quartz tubes for irradiation at Oregon State University's TRIGA

experimental reactor for 6 hours at 1 MW power.

3.2.2 Analytical Techniques

Incremental heating $^{40}\text{Ar}/^{39}\text{Ar}$ age determinations were performed on crystalline groundmass separates using a CO_2 laserprobe combined with a MAP-215/50 mass spectrometer. The mass spectrometer is a 90° sector instrument with a Nier-type source with an all metal extraction system. The system is equipped with a Merchantek integrated CO_2 laser gas extraction system connected to an ultra-clean gas cleanup line. Following irradiation, samples were placed within the sample chamber and degassed at 400°C for 15 minutes. Each sample was incrementally heated in $75\text{--}125^\circ\text{C}$ steps; step size was chosen to control the amount of Ar gas liberated from each heating step. The resultant ion beam currents were measured with the electron multiplier at $m/z=35, 36, 37, 38, 39, 40$ and at baselines between these peaks. The electron multiplier operates at 2050 Volt with a sensitivity of $\sim 1 \times 10^{-13}$ mol/volt. Peak heights for each isotope of Ar are monitored through each analysis and typically follow first- or second-order polynomial decay patterns.

3.2.3 Age Determinations

All new argon ages were measured relative to the flux monitor standard FCT-3 biotite (28.04 ± 0.18 Ma (1σ); Renne et al., 1994); estimated uncertainties for the J-values are between 0.3–0.5% (1σ). The decay constant of $5.530 \pm 0.097 \times 10^{-10} \text{ yr}^{-1}$ (2σ), as reported by Min et al. (2000), is used to calculate ages. Incremental heating plateau ages and argon-isotope isochron ages were calculated using the ArArCALC v2.2 software (Koppers, 2002). Plateau ages were generally preferred over the isochron ages because the slope of the isochron is not well controlled by the closely grouped concordant heating steps. Plateau ages consist of at least three consecutive, concordant steps comprising at least 50% of the total ^{39}Ar released and have a MSWD

<2. In the absence of such a plateau, pseudo-plateau ages were preferred if there was evidence for excess Ar or Ar loss and when the plateau age overlapped within uncertainty with the isochron ages. For samples with release patterns suggestive of Ar recoil, plateau (or pseudo-plateau) ages containing the middle steps were chosen as the best estimate of crystallization age.

3.3 Whole-rock Composition by XRF and ICP-MS Analysis

Thirty-three samples collected from across the central Oregon Proto-Cascadia transect were selected for whole-rock major element analysis by X-ray fluorescence (XRF). Along with samples collected as part of this study, five additional primitive samples whose major element chemistry was characterized as part of older studies (Urbanczyk, 1994; Oxford, 2006) were further analyzed for trace element chemistry by inductively coupled plasma mass spectrometry (ICP-MS).

Analyses were performed at the GeoAnalytical Laboratory at Washington State University (Pullman, Washington) using the XRF method of Johnson et al. (1999) and ICP-MS method of Knaack et al. (1994). Appendix B contains the complete results from XRF and ICP-MS analysis, and selected geochemical data are included in Table 4.3 and discussed in Chapter 4 of this text. Hand samples were crushed to chips with either a hydraulic press or a hammer and steel plate; chips were carefully picked for freshness. Powdering for XRF and ICP-MS analysis was done at Oregon State University, Washington State University, and the Carnegie Institute's Department of Terrestrial Magnetism using either a tungsten carbide (WC) or agate bowl in a shatter box. For XRF analysis, a dilithium tetraborate ($\text{Li}_2\text{B}_4\text{O}_7$) flux was added to a portion of the rock powder (at a 2:1 ratio) and then fused into a glass bead. Following re-grinding in a WC bowl in a shatter box, the samples were again fused, and the resulting bead was polished for analysis. Following sample preparation, XRF analysis was completed by technicians at the GeoAnalytical lab according to the method detailed by Johnson et al. (1999). ICP-MS powders were mixed with an equal

amount of lithium tetraborate flux and fused to a glass bead. Following fusion, the bead was reground in a WC shatter box and dissolved and analyzed as described by Knaack et al. (1994).

Along with major element oxide concentrations, a suite of trace elements (Ni, Cr, Sc, V, Ba, Rb, Sr, Zr, Y, Nb, Ga, Cu, Zn, Pb, La, Ce, Th, Nd, and U) were analyzed by XRF. Results were reproducible to within 1% error for all major elements and all trace elements excluding Cr, Rb, Nb, Ga, Zn, Pb, La, Ce, Th, U. Of these, Ga and Pb were reproducible to within 10% error, and La was reproducible to within 20% error. Both Th and U were near or below detection limits and were not significantly resolved. ICP-MS analyses returned concentrations for the La, Ce, Pr, Nd, Sm, Eu, Gd, Tb, Dy, Ho, Er, Tm, Yb, Lu, Ba, Th, Nb, Y, Hf, Ta, U, Pb, Rb, Cs, Sr, Sc, and Zr. Precision is generally better than 5% (RSD) for the rare earth elements and 10% for all others (Knaack et al. 1994). For elements analyzed by both methods, ICP-MS analysis is preferred and reported where available.

3.4 Electron Microprobe Analysis of Phenocryst Phases

Eight samples from the Western Cascades segment of the central Oregon Proto-Cascadia transect were analyzed by electron microprobe (EMP) at Oregon State University using the Cameca SX-100 Electron Microprobe equipped with wavelength dispersive spectrometers. These samples were chosen to supplement existing data on the phenocryst compositions of samples from the Oregon Coast Range and Eastern Clarno (Oxford, 2006; Urbanczyk, 1994). Mafic mineral phases (olivine, clinopyroxene, and orthopyroxene) were targeted for analysis to determine whether primitive samples were in or near equilibrium with mantle compositions. All thin sections were carbon-coated prior to analysis to generate a uniform charge across the thin section surface. Olivine and pyroxene grains were analyzed with a focused 1 μm beam, 15 kV accelerating voltage, and 30 nA beam current. Back-scattered electron images were also taken to evaluate internal zoning. Grain interiors were primarily

targeted, as they are most likely to preserve compositions in equilibrium with the mantle. Appendix C includes analyzed elements, counting times, detection limits, and standards information for all EMP analyses, and selected results are discussed in Chapter 4.

3.5 Radiogenic Isotopes by ICP-MS and TIMS

Sr, Nd, and Pb isotopic analyses for 24 samples and Hf isotopic analyses for 18 samples were performed at the Carnegie Institute of Washington's Department of Terrestrial Magnetism (DTM) using the methods outlined by Carlson et al. (2006) and summarized here. Results and relevant analytical details, including measured standard values, are reported in Tables 4.4 and 4.5.

Samples were powdered at DTM using an agate shatter box. Between 50-100 mg of sample powder were dissolved for Sr, Nd, Pb, and, in some cases, Hf isotopic analysis. Each sample was dissolved in approximately 3ml concentrated HF and 1 ml concentrated HNO₃ then subjected to microwave digestion. Following evaporation to dryness, samples were treated with 1 ml of concentrated HNO₃ and dried, and the process was repeated. After the addition of 2 ml 0.5N HBr and drying, the remaining sample was dissolved in 3 ml 0.5 HBr and loaded into columns (0.04 ml) containing AG1-X8 anion-exchange resin. Elution of matrix elements in 0.5N HBr was followed by elution of Pb in 0.5N HNO₃. The collected Pb was dried, taken up in 0.5N HBr and subjected to a second pass through the Pb column to purify the split.

After drying, the solution containing the matrix elements eluted from the Pb column was oxidized by the addition of 1ml of water and 1 ml of concentrated HNO₃. The solution was dried, redissolved in 4N HCl, and then dried again. The remaining sample was then taken up in 5ml 1N HCl-0.1 N HF and loaded on a 0.6 X 20 cm column of AG50W-X8 cation-exchange resin. Hf was collected by adding an additional 5ml 1N HCl-0.1 N HF to the solution loaded on the column. Rb and U and then Sr were collected by adding 2.5N HCl and collecting the specified volumes from

the columns. The eluent was then switched to 4N HCl, and the REE were collected as a group. The Hf split was loaded in 3N HCl onto a 1 ml column of LN-spec resin followed by washes in 3N HCl, 6N HCl, H₂O, and a solution of 0.09N citric acid-0.45N HNO₃-1wt%H₂O₂ to remove Ti. Finally, 6N HCl-0.06N HF was used to wash the column and remove Zr. Hf was then eluted from the column using 6N HCl-0.4N HF.

From the REE split, Sm, Nd, and heavy REE were separated using a 0.2 X 20 cm column filled with AG50-X8 resin. The REE split from each sample was loaded in 0.04 ml 0.1N HCl and eluted in α -hydroxyisobutyric acid. The heavy REE split was loaded in 0.05 ml 0.25N HCl onto a 4mm X 70 mm column filled with LN-spec resin. The column was then rinsed with 33ml of 2.5N HCL. The U and Rb cut was separated using a .25ml column of TRU resin. Following loading in 1.5 mL of 2N HNO₃, Rb was collected from the initial loading solution and also from a wash of 4ml of 2N HNO₃. Elution with 4ml of 0.1N HCL-0.3N HF liberated U from the column.

Pb isotopic compositions were measured by multi-collector ICP-MS using the DTM VG-P54 for the six initial samples (April 2009) and then by Nu high-resolution multi-collector ICP-MS for the second round of analyses (April-May 2010). Mass fractionation corrections are made by comparing average measured standard Pb values to the isotopic composition of NBS 981 reported by Todt et al. (1996). Hf isotopic compositions were measured on the DTM VG-P54 multi-collector ICP-MS and while monitoring potential interferences from Yb, Lu, Ta and W. Data are fractionation corrected to $^{178}\text{Hf}/^{177}\text{Hf} = 0.7215$ and normalized to the average $^{176}\text{Hf}/^{177}\text{Hf}$ value obtained from measurements of the JMC-475 Hf standard. Standard measurements are interspersed with sample analyses during each session. All data are reported relative to the accepted value of $^{176}\text{Hf}/^{177}\text{Hf} = 0.282160$ for the JMC-475 standard.

Sr isotopic composition was determined from samples loaded onto single Re filaments in DTM's Thermo-Finnigan Triton thermal ionization mass spectrometer (TIMS) while monitoring all Sr isotopes and ^{85}Rb . Fractionation corrections were made using the constant $^{86}\text{Sr}/^{88}\text{Sr} = 0.1194$. Nd isotopic compositions were measured

on the DTM Triton using double Re filaments. Ce and Sm were monitored for interferences and fractionation was corrected to the constant $^{146}\text{Nd}/^{144}\text{Nd} = 0.7219$.

4 – Eocene-Oligocene Cascadia Mantle

4.1 Age Data and Timing of Eocene-Oligocene Proto-Cascadia Magmatism

Seven new $^{40}\text{Ar}/^{39}\text{Ar}$ dates were determined to better constrain the timing of Proto-Cascadia Eocene-Oligocene magmatism and to provide precise ages for the correction of initial radiogenic isotope ratios. Careful and thorough dating of the forearc Oregon Coast Range by Oxford (2006) alleviated the necessity for further dating in that region. Four samples from the Western Cascades, two samples from the Eastern Clarno formation (Urbanczyk, 2004), and one sample from the John Day formation, all believed to fall within the appropriate age range of ~30-37 Ma, were dated (See Figure 2.1). One Western Cascade sample (AB09-07) returned an age of 23.52 ± 0.30 Ma, which placed it outside of the age range of consideration. The three remaining Western Cascade samples produced ages of 29.78-32.41 Ma. The sample from the John Day formation returned a similar age of 32.90 ± 0.32 Ma. Samples from the Eastern Clarno produced unexpectedly old ages of 41.09 ± 0.42 and 40.64 ± 0.31 Ma. These ages are more completely presented and discussed within the larger context of the timing of Eocene-Oligocene Proto-Cascadia (EOPC) magmatism below.

4.1.1 *Oregon Coast Range Intrusive and Volcanic Rocks*

Alkaline and gabbroic Oregon Coast Range intrusive units (OCRI; Oxford, 2006) as well as the Yachats and Cascade Head Basalts fall within a narrow age range of ~30-36 Ma allowing for the evaluation of the forearc Eocene-Oligocene mantle of central Oregon at this time. The OCRI range from ~32-36 Ma (Oxford, 2006), and the Yachats Basalt returns ages between 30.7 and 36.5 Ma, with $^{40}\text{Ar}/^{39}\text{Ar}$ ages slightly older than those returned by K/Ar dating (Davis et al., 1995). Cascade Head Basalt samples were dated to between 30.5 and 34.0 Ma (Davis et al., 1995). The slightly older $^{40}\text{Ar}/^{39}\text{Ar}$ age of 34.0 Ma is preferred for the Cascade Head Basalt as it

conforms to the age constraint determined from a ~34 Ma dike that cuts some flows (Davis et al., 1995).

4.1.2 *Western Cascades*

Protracted magmatism (~42-10 Ma) in the Western Cascades (WC) includes the age range of Eocene-Oligocene magmatism in the forearc. Localities of basaltic samples previously dated to be within this range were resampled for evaluation as part of the Eocene-Oligocene transect. One sample from a rock quarry outside of Lebanon, OR and samples from further south in the Western Cascades, near Springfield, OR, were also collected and dated as part of this study (Figure 1.1).

Samples AB09-19, AB09-20A, and AB09-21 were collected from localities near Springfield, OR previously dated to be within the desired age range and returned ages of 29.78- 32.41 Ma. AB09-19 was collected from a rock quarry on Mt. Tom and returned a plateau age of 29.78 ± 0.39 Ma. While the age spectrum suggests slight Ar recoil effects, owing to the fine grain size of the sample, the plateau spans the middle of this gas release pattern, effectively minimizing this effect. The plateau age is preferred here (and generally) over the isochron age because the slope of the isochron is not well controlled due to the closely grouped concordant heating steps. Sample AB09-20A, a lava flow, returned an age of 32.13 ± 0.39 Ma. A slightly high MSWD (2.71) suggests that this plateau does not meet rigorous standards of statistical significance. Though the total fusion and plateau ages are the same within error, the plateau age is preferred as the choice of the middle heading steps best overcomes the effect of recoil. Sample AB09-21 was collected from a large (>0.5 km in length) dike that crops out as a spine across Horse Mountain. Incremental heating failed to produce a statistically acceptable plateau. However, the six consecutive, concordant heating steps comprise 65% of the total ^{39}Ar released. The pseudo-plateau age of 32.41 ± 0.42 is the preferred age. This age overlaps within uncertainty with both the normal and inverse isochron ages but is considered more precise. The total fusion age

is affected by Ar loss in the low temperature heating steps. Despite some uncertainty for age in this sample, all three samples collected in the Western Cascades near Springfield, OR fit within the desired time frame and allow for a comparison of mantle in the geographic forearc and arc of Eocene-Oligocene Cascadia within a restricted time interval.

Sample AB09-07 was taken from a previously undated rock quarry near Lebanon, OR. The 23.52 Ma age returned by this sample is significantly younger than the time transect, and this sample will not be considered as part of the Eocene-Oligocene transect. AB09-07 returned a 23.52 ± 0.30 Ma plateau age indistinguishable within uncertainty from the total fusion and isochron ages. As with AB09-19 and AB09-20A, AB09-07 appears to have experienced Ar recoil, but the selection of the plateau through the middle of this pattern minimized the effect, and the plateau age is again preferred as the best estimate of the crystallization age.

4.1.3 *Eastern Clarno and John Day Formations*

Mafic dikes and lava flows of mafic composition make up a small volume of the John Day (JD) Formation and a somewhat larger, though still minor, volume of the Eastern Clarno (EC) Formation (Appel, 2001; Robinson et al., 1984; Taylor, 1981). The Eastern Clarno Formation has been dated by Urbanczyk (1994) to overlap in age with the oldest John Day aged units. Urbanczyk constrained the ages of olivine basalts from the Eastern Clarno Formation to between 37.6 and 33.6 Ma with total fusion $^{40}\text{Ar}/^{39}\text{Ar}$ dates on samples that gave stratigraphic control on the entire upper sequence of the EC. Because the EC has not been widely reported to extend to ages as young as 33.6 Ma and because an incremental heating approach could be used to improve upon the dates reported by Urbanczyk, two EC samples were dated by the incremental heating $^{40}\text{Ar}/^{39}\text{Ar}$ method. Samples K90-367 and K90-328 were provided by Kevin Urbanczyk from the Magone Lake section of the Eastern Clarno Formation. Both samples are from the upper olivine basalt unit believed to fall within the 37.6-

33.6 Ma age range. K90-367 produced a robust plateau age of 40.64 ± 0.31 Ma that overlaps with both the total fusion and isochron ages. Sample K90-328 produced a similar, though less robust (MSWD = 4.24), plateau age of 41.09 ± 0.42 . The plateau age is indistinguishable within uncertainty from the total fusion and isochron ages. The plateau is comprised of 4 heating steps representing 72% of total ^{39}Ar released, but fails to meet statistical significance with an MSWD of 4.24. The plateau age is, nonetheless, preferred, as the total fusion age would return an erroneously young age owing to Ar loss in the low temperature heating steps. The plateau age is considered robust despite evidence for Ar recoil because the plateau spans the middle of the recoil pattern, although the true age may be slightly older since the low temperature heating steps appear to truncate the recoil pattern due to Ar loss. These new ages from the Eastern Clarno Formation suggest that the EC may not extend to ages as young as those suggested by Urbanczyk (1994). While the olivine basalts of the EC have older ages than expected, they are included in the Eocene-Oligocene transect to provide greater coverage of the geographic backarc mantle during this time slice.

A single sample from the John Day Formation was also dated. Mafic dikes from the JD were determined to have K-Ar ages of 29.3-33.4 Ma (Taylor, 1981; Enlows and Parker, 1972) based on the dating of 3 mafic dikes. Sample EMT-117, a mafic dike from the JD used in the isotopic transect was dated by Appel (2001) to be 34 Ma. An additional sample from the JD was dated as part of this study. The dated sample, JDM-293, was collected by John Dilles from a basaltic lava flow near the base of the John Day Formation and is believed to be of an appropriate age for inclusion in the Eocene-Oligocene transect. Incremental heating of JDM-293 produced a robust plateau age of 32.90 ± 0.32 that overlaps within uncertainty with total fusion and isochron ages. The agreement between K-Ar ages of JDF mafic dikes and the $^{40}\text{Ar}/^{39}\text{Ar}$ age of Appel (2001) is taken to suggest that mafic dikes from JD are of an appropriate age to be included in the transect. Additionally, dating from the basal lava flow demonstrates that it falls within the desired age range for this study. Previous and new dating of samples from across central Oregon Proto-Cascadia demonstrate the

existence of roughly coeval magmatism across the arc at a narrow age range ($\sim 35 \pm 5$ Ma), allowing for the assessment of mantle heterogeneity during the Eocene-Oligocene transition.

Table 4.1: Summary of $^{40}\text{Ar}/^{39}\text{Ar}$ dating results. Samples were irradiated at Oregon State University's TRIGA reactor for 6 hours at 1 MW power. Neutron flux was measured using the FCT-3 biotite monitor (28.030 ± 0.003 Ma (1σ), Renne et al. 1998). Ages were calculated using a decay constant of $5.530 \pm 0.097 \times 10^{-10}$ 1/yr (2σ), as reported by Min et al. (2000) and the ArArCALC v2.2 software package (Koppers, 2002). Preferred ages are shown in bold.

Sample	Rock Type	Material Dated	J	Weighted Plateau Age			Total Fusion Age			
				Age (Ma)	Error (2σ)	Heating Steps (n)	^{39}Ar (%)	MSWD	Age (Ma)	Error (2σ)
AB09-07	B	Groundmass	0.0015404	23.52	± 0.30	4	56.86	2.36	22.11	± 0.22
AB09-19	B	Groundmass	0.0014809	29.78	± 0.39	5	68.85	2.32	29.28	± 0.34
AB09-20A	B	Groundmass	0.0015013	32.13	± 0.39	4	56.70	2.71	32.21	± 0.32
AB09-21	B	Groundmass	0.0015996	32.41	± 0.42	6	64.75	2.72	31.12	± 0.31
JDM 293	B	Groundmass	0.0015615	32.90	± 0.32	9	95.39	0.11	32.69	± 0.38
K90-328	B	Groundmass	0.0015211	41.09	± 0.42	4	72.23	4.24	40.76	± 0.36
K90-367	B	Groundmass	0.0015798	40.64	± 0.31	10	95.18	1.36	40.30	± 0.31

Sample	Rock Type	Material Dated	J	Normal Isochron Age			Inverse Isochron Age				
				Age (Ma)	Error (2σ)	Intercept	Age (Ma)	Error (2σ)	Intercept	MSWD	
AB09-07	B	Groundmass	0.0015404	23.35	± 0.60	306.09	3.48	23.43	± 0.59	0.00331	3.24
AB09-19	B	Groundmass	0.0014809	29.56	± 0.39	302.17	1.20	29.57	± 0.39	0.00331	1.15
AB09-20A	B	Groundmass	0.0015013	31.18	± 1.39	532.24	1.18	31.14	± 1.38	0.00181	1.19
AB09-21	B	Groundmass	0.0015996	31.65	± 1.18	311.20	2.36	31.71	± 1.19	0.00322	2.39
JDM 293	Basalt	Groundmass	0.0015615	32.97	± 0.42	294.79	0.09	32.97	± 0.42	0.00339	0.09
K90-328	Basalt	Groundmass	0.0015211	40.55	± 0.73	359.49	2.48	40.57	± 0.74	0.00279	2.49
K90-367	Basalt	Groundmass	0.0015798	40.64	± 0.34	295.42	1.49	40.64	± 0.34	0.00339	1.54

4.2 Primitive Magmatism of Eocene-Oligocene Cascadia

Few arc magmas make their way through the crust without some crustal modification, making most arc basalts imperfect records of the mantle from which they are derived. The extent to which magmas experience modification after mantle segregation may depend on the thickness of the crust, local structural features, the thermal state of the crust, the flux of mantle magmas, and other factors. For this reason, magmas from across a single arc are likely to experience different degrees of modification, producing basalts that provide variably obscured records of their mantle source. Despite this limitation, arc basalts provide important clues as to the nature of the mantle beneath arcs and how these source characteristics influence arc magmatism and are recorded in magmatic products.

To best remove the influence of crustal modification, samples chosen were the least evolved samples available from the transect (Figure 1.1). While none of the samples chosen represent perfectly primitive, purely mantle-derived magmas, they provide the closest possible look at the Cascadian Eocene-Oligocene mantle. Samples were screened to have >6 wt.% MgO and >45 ppm Ni, and, where available, less evolved samples were favored. Isotopic analyses were obtained for samples that were later determined to not meet these criteria. Those data are included in figures as open symbols and in Tables 4.3 and 4.4. While this filter is not strict enough to isolate only primitive magmas, it is the most thorough filter that may be applied given the range of compositions exposed across the arc. These least evolved samples that have passed the filter are hereafter referred to as primitive, though they are not true primitive compositions.

Electron microprobe analysis of mafic phenocryst phases (olivine, clinopyroxene, and orthopyroxene) shows these mineral phases to be out of equilibrium with mantle compositions (Appendix B). Olivine compositions of Mg# ~0.88 – 0.93 are considered to be in equilibrium with the mantle (Yogodzinski et al., 2007; Arai, 1994), and clinopyroxene compositions with Mg# ~0.86-0.92 would be in

equilibrium with these mantle olivines (Yogodzinski et al 2007). Olivines from the EOPC arc have a compositional range from Mg# ~0.6-0.81, and backarc olivines range from Mg# ~0.72-0.87. The Mg# and NiO content of olivines from samples from the arc and backarc segment of the Cascadia transect fall below values defined by the mantle array defined by Takahashi (1986). It is clear from Figure 4.1 that even olivines from the more primitive samples from the backarc region do not approach true mantle compositions. Additionally, clinopyroxenes from studied samples range from Mg# ~0.53-0.80 and therefore did not grow in equilibrium with mantle olivine.

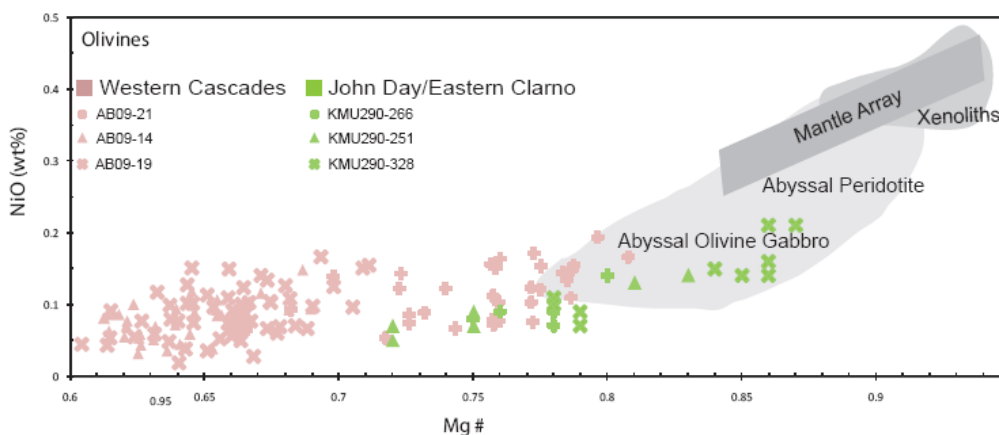


Figure 4.1: Olivine compositions from Eocene-Oligocene Proto-Cascadia primitive samples. Figure and after Keiko et al. (2010). Mantle array defined by Takahashi (1986). Western Cascade samples data from this study. John Day/ Eastern Clarno olivine data from Urbanczyk (1994).

Difficulty in locating truly primitive samples, especially in the arc and forearc region, mean that the view of the Proto-Cascadian mantle is necessarily obscured by post-mantle processing and that all results should be viewed in light of this. Although both mineral and whole rock chemistry suggest that the samples studied do not represent unmodified mantle compositions, the lack of correlation between either incompatible element concentrations (e.g. Zr) or MgO content and initial isotope values ($^{87/86}\text{Sr}_i$, e.g.), suggests that the isotopic variability is not controlled by

assimilation or mixing. If post-mantle modification is dominated by closed-system fractional crystallization, evolving magmas will retain their initial isotopic signature. Though mineral and whole rock data demonstrate that samples do not provide an unobscured window to the mantle, a lack of evidence for abundant assimilation or mixing suggests that isotopic values may still provide a valuable record.

4.3 The Eocene-Oligocene Proto-Cascadia Mantle: Insights from Major and Trace Element Chemistry

Schmidt et al. (2008) recognized five distinct primitive magma types in the modern Cascades, three of which are also present in Eocene-Oligocene Proto-Cascadia (EOPC). The complete compilation of whole-rock geochemical data from this study as well as complementary data from the literature are in Appendix B. Major element, trace element, and isotopic compositions for primitive samples comprising the EOPC mantle transect are given in Tables 4.3 and 4.4. Each primitive basalt sample was classified following the criteria of Schmidt et al. (2008) (see Table 4.2 for slight modifications).

Table 4.2: Primitive magma characterization scheme. The scheme follows Schmidt et al. (2008), with minor changes in compositional ranges to accommodate the compositions of all samples considered.

	MgO	Al ₂ O ₃ / TiO ₂	K ₂ O	Sr	P	Nb	Ce	Ce/Sm	Ce/Yb
	wt%	wt%	ppm	ppm	ppm	ppm	ppm		
CAB	6-13.5	8-26	0.4-3.6	290- 1330	520- 3700	2-26	9-81	4.5-10	5-43
LKT	7-12	10.5-32	<0.6	190-500	215- 1450	1-10	4-26	2.5-7.5	2-13.5
HFSE-rich	5.5-10.0	2-11	0.6-3.6	380- 1000	1300- 7050	>17.5	35-79	6.0-10.5	17-45

4.3.1 *Primitive Magma Types*

Calc-alkaline basalts (CABs) are the most prevalent basalt type in the Eocene-Oligocene Proto-Cascadia (EOPC) arc and backarc but are absent from the forearc. CABs are distinguished from tholeiitic basalts by higher CaO, Na₂O, and K₂O concentrations and lower FeO*/MgO (Schmidt, 2008; Miyashiro, 1974). CABs are common in subduction environments and are enriched in the fluid-mobile, large ion lithophile elements (LILEs), owing to the addition of fluid and sediments (\pm melt) to the mantle wedge from the subducting slab (e.g. Plank and Langmuir, 1993; Saunders et al., 1991).

Low K tholeiites (LKTs) were sampled in the EOPC arc but are absent from the forearc and backarc. LKTs generally have lower concentrations of incompatible elements compared to other primitive basalt types and are lower in K₂O and higher in Al₂O₃, FeO, and TiO₂ (Schmidt et al., 2008; Hart et al., 1984). LKTs are similar to MORB but are distinguished from N-MORB by modest enrichment in LILEs. Taken together, these features suggest that LKTs are dry, decompression-induced melts of depleted mantle that has been previously modified by subduction fluids (Till et al., 2010; Borg et al., 2000; Bacon et al., 1997; Conrey et al., 1997; Hart et al., 1997; Bartels et al., 1991).

High field strength element (HFSE)-rich basalts comprise all of the primitive basalts of the EOPC forearc and are present as minor constituents in the arc and backarc. These basalts, referred to as OIB type (Bacon et al., 1997; Conrey et al., 1997) or intraplate type (Hildreth, 2007) are distinguished primarily by their high HFSE contents relative to most arc magmas, which are characterized by depletions in HFSE relative to elements of comparable compatibility in MORB. HFSE-rich basalts also tend to be low in MgO at a given SiO₂ content and have lower Al₂O₃/TiO₂ (Schmidt et al., 2008).

4.3.2 *Comparing Primitive Magmas Across the Arc*

Eocene-Oligocene Proto-Cascadia (EOPC) primitive magmas range from ~45-56 wt. % SiO₂ and ~14-6 wt. % MgO (Figure 4.2). Forearc samples are suppressed in MgO at a given SiO₂ content, distinguishing them from the compositional trend shared by the arc and backarc samples. Many of the forearc samples represent alkaline compositions that extend to lower SiO₂ and are undersaturated with respect to silica. Backarc samples span a wider compositional range than do the more restricted arc samples and extend to the most primitive compositions.

Ratios of highly incompatible elements (e.g. Nb/Zr) may be used as a proxy for mantle source as they should not be sensitive to the effects of variable degrees of partial melting (except at very low degrees) or differentiation. Although some overlap occurs, the ranges of Nb/Zr values for each region are largely distinct, and may suggest discrete mantle domains beneath the EOPC margin (Figure 4.3).

While arc samples from the Western Cascades have a relatively uniform Nb/Zr (~0.05-0.08), the fore- and backarc display greater variation in Nb/Zr (~0.08-0.28 and ~0.08-0.18, respectively). This variability may be attributed to a number of causes. A variable Nb/Zr ratio could merely reflect a heterogeneous mantle being tapped in these regions. Alternatively, this variability may suggest that Nb and Zr were decoupled during partial melting due to the slightly greater incompatibility of Nb (e.g. Hildreth, 2007; Neal et al., 1997); this effect would be most pronounced at low degrees of partial melting. The variability in both the fore- and backarc is mostly present in the HFSE-rich samples. HFSE-rich basalts in the Cascades, Oregon Coast Range, and elsewhere have been attributed to low degrees of partial melting (Rowe et al., 2009; Schmidt et al., 2008; Oxford, 2006; Reiners et al., 2000; Davis et al., 1995). If HFSE-rich basalts from the backarc result from lower degrees of partial melting, this would explain why they do not share the more narrow range of Nb/Zr that is defined by the CABs from the same region.

Table 4.3: Major and trace element chemistry for the Eocene-Oligocene mantle transect. Where a reference is given, XRF and ICP-MS data not marked with an asterisk (*) are from the literature. Those data marked with an asterisk and data from all other samples without a reference are from this study.. Major element data has been normalized to 100% volatile free. FeO* indicates all Fe calculated as FeO. Major elements reported as oxide wt. %; trace elements are reported as ppm.

Sample Name	8_12_1	8_23_2	8_31_8	9_14_2	AB10-24	AB10-26	S91-14	SR83-94	SR61-5
Unit	OCR	OCR	OCR	OCR	Yachats	Yachats	YB	CHB	CHB
Reference	Oxford (2006)	Oxford (2006)	Oxford (2006)	Oxford (2006)			Davis et al. (1995)	Davis et al. (1995)	Davis et al. (1995)
Magma Type	HFSE	HFSE	HFSE	Non-Prim	HFSE	Non-Prim	HFSE	HFSE	HFSE
<u>Normalized XRF Results</u>									
SiO ₂	43.62	40.37	43.00	53.04	46.77	48.62	47.02	47.51	48.99
TiO ₂	4.56	4.91	4.24	3.26	3.37	3.27	4.22	3.42	2.93
Al ₂ O ₃	12.53	11.62	13.88	14.12	14.76	16.03	11.75	14.44	17.17
FeO*	14.71	16.70	13.87	13.28	13.46	12.42	9.97	9.80	9.52
MnO	0.23	0.27	0.17	0.22	0.18	0.14	0.25	0.20	0.24
MgO	7.67	7.84	6.45	3.71	8.01	5.35	7.01	8.31	6.07
CaO	10.17	11.02	9.03	7.78	9.34	10.36	14.39	10.67	8.90
Na ₂ O	3.32	3.73	7.77	2.99	2.67	2.92	2.59	3.32	3.45
K ₂ O	1.86	1.92	0.41	1.23	0.95	0.43	2.01	1.35	1.57
P ₂ O ₅	1.32	1.61	1.16	0.36	0.49	0.45	0.79	0.97	1.15
Total before Normalization	95.13	94.23	93.33	95.59	96.62	96.06	98.10	99.90	100.00
Ni	135	55	69	9	131	99			
Cr	126	36	22	30	67	96			
V	277	219	164	365	266	300			
Ga	27	26	29	22	23	23			
Cu	74	22	29	28	68	100			
Zn	175	200	226	139	128	113			

Table 4.3 (cont.): Major and trace element chemistry for the Eocene-Oligocene mantle transect. Where a reference is given, XRF and ICP-MS data not marked with an asterisk (*) are from the literature. Those data marked with an asterisks and data from all other samples without a reference are from this study.. Major element data has been normalized to 100% volatile free. FeO* indicates all Fe calculated as FeO. Major elements reported as oxide wt. %; trace elements are reported as ppm.

Sample Name	S84-112	S91-10	SH64-1C	SH64-1D	SH64-1E	SR83-160	SR87-23	S87-83	SR83-48
Unit	CHB								
Reference	Davis et al. (1995)								
Magma Type	HFSE								
<u>Normalized XRF Results</u>									
SiO ₂	47.05	47.71	45.54	44.92	45.15	45.19	46.94	46.07	50.32
TiO ₂	3.68	3.57	3.64	3.75	3.91	4.65	3.93	3.90	3.27
Al ₂ O ₃	12.35	15.59	14.35	14.38	14.59	14.55	13.26	13.92	13.09
FeO*	10.73	10.31	11.75	11.84	11.86	10.64	11.32	10.41	10.51
MnO	0.19	0.19	0.19	0.19	0.21	0.24	0.20	0.22	0.20
MgO	9.89	6.75	9.36	9.17	9.09	8.99	9.13	8.56	7.64
CaO	12.03	10.95	10.61	11.36	11.45	11.49	11.23	12.73	11.16
Na ₂ O	2.22	3.00	2.60	2.40	2.11	1.75	2.32	2.23	2.44
K ₂ O	1.08	1.28	1.14	1.25	0.79	1.52	1.01	1.17	0.88
P ₂ O ₅	0.78	0.64	0.83	0.73	0.85	0.98	0.66	0.80	0.49
Total before Normalization	99.30	99.70	99.80	99.90	100.00	98.40	98.50	98.30	100.20
Ni									
Cr									
V									
Ga									
Cu									
Zn									

Table 4.3 (cont.): Major and trace element chemistry for the Eocene-Oligocene mantle transect. Where a reference is given, XRF and ICP-MS data not marked with an asterisk (*) are from the literature. Those data marked with an asterisk and data from all other samples without a reference are from this study.. Major element data has been normalized to 100% volatile free. FeO* indicates all Fe calculated as FeO. Major elements reported as oxide wt. %; trace elements are reported as ppm.

Sample Name	SR83-27	CH-58	H-1	AB09-14	AB09-17	AB09-18	AB09-19	AB09-20B
Unit Reference	CHB Davis et al. (1995)	CHB Barnes & Barnes (1992)	CHB Barnes & Barnes (1992)	WC	WC	WC	WC	AB09-20A WC
Magma Type	HFSE	HFSE	HFSE	CAB	CAB	HFSE	LKT	CAB
Normalized XRF Results	HFSE	HFSE	HFSE	CAB	CAB	HFSE	LKT	CAB
SiO ₂	49.52	48.41	47.43	51.06	51.85	50.08	49.46	49.79
TiO ₂	3.40	3.33	3.73	1.27	1.15	1.69	1.59	1.59
Al ₂ O ₃	14.15	13.06	13.83	17.55	16.84	16.40	16.87	16.55
FeO*	9.19	10.71	10.31	8.93	9.10	11.14	10.77	10.45
MnO	0.41	0.20	0.32	0.16	0.16	0.21	0.18	0.18
MgO	7.16	8.56	7.46	7.22	6.89	6.49	8.13	6.68
CaO	11.90	11.28	12.40	9.91	10.62	10.00	9.92	11.36
Na ₂ O	2.41	2.55	2.57	3.17	2.49	2.71	2.47	2.47
K ₂ O	1.23	1.20	1.24	0.46	0.67	0.75	0.38	0.53
P ₂ O ₅	0.63	0.70	0.71	0.28	0.23	0.54	0.23	0.41
Total before Normalization	99.30	—	—	100.47	99.71	99.26	98.70	98.30
Ni				93	52	68	100	46
Cr				210	124	147	340	132
V				222	262	245	261	293
Ga				19	18	20	18	20
Cu				31	157	54	34	83
Zn				80	84	111	84	95

Table 4.3 (cont.): Major and trace element chemistry for the Eocene-Oligocene mantle transect. Where a reference is given, XRF and ICP-MS data not marked with an asterisk (*) are from the literature. Those data marked with an asterisks and data from all other samples without a reference are from this study.. Major element data has been normalized to 100% volatile free. FeO* indicates all Fe calculated as FeO. Major elements reported as oxide wt. %; trace elements are reported as ppm.

Sample Name	AB09-21	AB09-22	AH-SP06-2	JDM-293	EMT-117	K89-130	K90-247	K90-251	K90-260
Unit	WC	WC	WC	JD	JD	EC	EC	EC	EC1
Reference			Hatfield (2009)			Urbanczyk (1994)	Urbanczyk (1994)	Urbanczyk (1994)	Urbanczyk (1994)
Magma Type	LKT	LKT	Non-Prim	Non-Prim	Non-Prim	CAB	HFSE	CAB	HFSE
<u>Normalized XRF Results</u>									
SiO ₂	51.98	49.30	51.50	51.92	52.95	48.22*	55.23	46.96	55.04
TiO ₂	0.98	1.34	1.60	3.15	3.02	1.31*	1.15	1.29	1.14
Al ₂ O ₃	17.19	17.23	19.26	14.44	13.96	13.85*	16.47	14.20	16.33
FeO*	9.04	10.11	9.67	12.43	13.81	9.32*	7.28	8.82	7.27
MnO	0.16	0.17	0.19	0.21	0.23	0.16*	0.13	0.17	0.12
MgO	6.97	8.04	3.39	2.31	3.78	13.51*	6.07	11.99	6.35
CaO	11.02	10.94	10.52	12.27	8.02	10.24*	8.41	12.86	8.53
Na ₂ O	2.27	2.32	3.01	2.47	3.18	2.14*	1.39	0.70	1.35
K ₂ O	0.27	0.32	0.58	0.39	0.66	0.82*	3.57	2.31	3.58
P ₂ O ₅	0.12	0.23	0.28	0.42	0.39	0.42*	0.30	0.70	0.29
Total before Normalization	99.21	97.43	99.24	94.15	100.06	96.55*	—	—	—
Ni	40	56	14	1	11	317*	105	187	101
Cr	122	153	32	1	23	749*	212	553	221
V	279	285	283	2	337	237*	176	275	197
Ga	18	19	19	28	23	18*	15	15	17
Cu	125	103	83	10	35	91*	93	97	87
Zn	77	84	87	271	139	76*	65	83	66

Table 4.3 (cont.): Major and trace element chemistry for the Eocene-Oligocene mantle transect. Where a reference is given, XRF and ICP-MS data not marked with an asterisk (*) are from the literature. Those data marked with an asterisk and data from all other samples without a reference are from this study.. Major element data has been normalized to 100% volatile free. FeO* indicates all Fe calculated as FeO. Major elements reported as oxide wt. %; trace elements are reported as ppm.

Sample Name	K90-266	K90-326	K90-327	K90-328	K90-366	K90-367	K90-392	K90-395	K90-397
Unit	EC								
Reference	Urbanczyk (1994)								
Magma Type	CAB								
<u>Normalized XRF Results</u>									
SiO ₂	45.82	48.52	48.50	48.60	49.39	49.29	48.45	50.09	55.78
TiO ₂	1.39	1.52	1.53	1.37	1.40	1.41	1.57	1.35	1.07
Al ₂ O ₃	13.82	17.45	17.45	15.01	16.77	16.78	15.43	17.71	17.50
FeO*	9.48	9.43	9.45	8.84	9.12	9.16	9.55	8.97	7.72
MnO	0.18	0.16	0.16	0.16	0.17	0.17	0.16	0.16	0.14
MgO	12.64	7.78	7.91	9.19	7.78	7.77	9.17	7.96	6.20
CaO	12.84	11.55	11.32	12.99	11.12	11.15	11.07	9.55	8.98
Na ₂ O	1.10	0.57	0.51	0.97	0.96	0.96	1.05	0.63	0.79
K ₂ O	1.88	2.77	2.90	2.41	2.90	2.89	2.99	3.40	3.61
P ₂ O ₅	0.85	0.26	0.27	0.45	0.40	0.41	0.56	0.21	0.22
Total before Normalization	—	—	—	—	—	—	—	—	—
Ni	221	79	77	95	57	58	136	103	56
Cr	541	138	144	330	74	75	302	223	226
V	269	241	248	296	265	258	235	205	179
Ga	15	16	15	19	17	18	15	15	16
Cu	104	78	78	148	81	75	116	88	41
Zn	84	70	73	75	77	75	84	65	70

Table 4.3 (cont.): Major and trace element chemistry for the Eocene-Oligocene mantle transect. Where a reference is given, XRF and ICP-MS data not marked with an asterisk (*) are from the literature. Those data marked with an asterisks and data from all other samples without a reference are from this study.. Major element data has been normalized to 100% volatile free. FeO* indicates all Fe calculated as FeO. Major elements reported as oxide wt. %; trace elements are reported as ppm.

Sample Name	8_12_1	8_23_2	8_31_8	9_14_2	AB10-24	AB10-26	S91-14	SR83-94	SR61-5
La	90.66	119.20	90.42*	21.78	32.99	31.99			
Ce	189.92	252.13	196.98*	48.80	70.28	69.01			
Pr	23.56	31.44	23.84*	6.59	8.97	8.84			
Sm	94.07	127.38	95.82*	28.97	37.79	36.38			
Nd	19.24	25.78	19.71*	7.61	8.74	8.14			
Eu	5.94	7.91	6.31*	2.38	2.91	2.71			
Gd	16.48	21.92	15.68*	8.18	8.27	7.47			
Tb	2.20	2.96	1.99*	1.38	1.23	1.14			
Dy	10.78	15.05	9.02*	8.48	6.88	6.36			
Ho	1.74	2.56	1.25*	1.72	1.24	1.19			
Er	3.76	5.74	2.35*	4.57	2.96	2.90			
Tm	0.44	0.70	0.24*	0.66	0.38	0.38			
Yb	2.26	3.73	1.18*	4.00	2.14	2.21			
Lu	0.30	0.52	0.14*	0.61	0.31	0.32			
Ba	661	724	441*	365	245	172			
T	9.38	10.85	9.63*	3.94	3.42	3.21			
Nb	83.0	140.1	106.2*	17.9	43.2	40.9			
Y	42.85	61.12	30.32*	43.25	30.20	28.85			
Hf	11.05	17.12	13.94*	6.01	6.09	5.78			
Ta	4.59	8.93	6.75*	1.22	2.81	2.66			
U	2.49	2.94	2.68*	1.22	0.82	0.94			
Pb	4.31	4.62	5.49*	8.97	1.81	1.65			
Rb	40.7	41.2	13.6*	35.7	19.5	2.3			
C	2.03	3.45	0.13*	1.37	0.28	0.01			
Sr	928	1427	1092*	223	499	537			
Sc	22.4	22.0	8.5*	42.6	23.4	24.4			
Zr	467	711	664*	226	248	235			

Table 4.3 (cont.): Major and trace element chemistry for the Eocene-Oligocene mantle transect. Where a reference is given, XRF and ICP-MS data not marked with an asterisk (*) are from the literature. Those data marked with an asterisk and data from all other samples without a reference are from this study.. Major element data has been normalized to 100% volatile free. FeO* indicates all Fe calculated as FeO. Major elements reported as oxide wt. %; trace elements are reported as ppm.

Sample Name	S84-112	S91-10	SH64-1C	SH64-1D	SH64-1E	SR83-160	SR87-23	S87-83	SR83-48
La									
Ce									
Pr									
Sm									
Nd									
Eu									
Gd									
Tb							47.30		25.00
Dy							98.20		50.00
Ho							600.00		430.00
Er							43.00		27.00
Tm									
Yb									
Lu									
Ba									
T									
Nb							4.7		3.8
Y									
Hf									
Ta									
U									
Pb							280		255
Rb									
C							58.00		58.00
Sr							23.00		28.00
Sc									
Zr									

Table 4.3 (cont.): Major and trace element chemistry for the Eocene-Oligocene mantle transect. Where a reference is given, XRF and ICP-MS data not marked with an asterisk (*) are from the literature. Those data marked with an asterisk and data from all other samples without a reference are from this study.. Major element data has been normalized to 100% volatile free. FeO* indicates all Fe calculated as FeO. Major elements reported as oxide wt. %; trace elements are reported as ppm.

Sample Name	SR83-27	CH-58	H-1	AB09-14	AB09-17	AB09-18	AB09-19	AB09-20A	AB09-20B
La		52.60	57.10	11.59	12.42	19.47	8.22	17.82	19.34
Ce		119.00	138.00	24.86	27.58	44.24	19.01	40.26	43.85
Pr		694.00	657.00	3.81	3.76	6.01	2.68	5.44	5.94
Sm		62.00	73.00	17.25	16.41	25.89	12.28	23.46	25.70
Nd				4.23	3.92	6.18	3.19	5.57	6.07
Eu				1.62	1.34	1.96	1.30	1.81	1.96
Gd				4.61	3.91	6.23	3.46	5.60	6.08
Tb				0.76	0.64	1.00	0.58	0.90	0.98
Dy				4.62	3.90	5.94	3.59	5.47	5.91
Ho		5.96	6.47	0.96	0.77	1.20	0.72	1.09	1.16
Er				2.56	2.05	3.11	1.91	2.81	3.10
Tm				0.37	0.29	0.44	0.27	0.40	0.43
Yb				2.25	1.76	2.68	1.67	2.45	2.64
Lu				0.36	0.27	0.41	0.26	0.38	0.41
Ba		378	355	209	162	212	112	201	211
T				0.71	1.52	1.53	0.69	1.65	1.51
Nb		79.0	88.0	5.0	7.7	15.9	7.0	14.0	15.7
Y		27.00	32.00	24.28	19.20	29.46	17.59	26.85	29.04
Hf				2.51	2.59	4.34	2.11	3.85	4.27
Ta				0.31	0.47	0.93	0.46	0.82	0.92
U				0.23	0.47	0.54	0.24	0.51	0.52
Pb				2.10	3.32	3.27	1.51	3.32	3.27
Rb		26.0	20.0	4.9	9.4	8.4	6.5	3.2	8.3
C				0.05	0.33	0.10	0.22	0.06	0.09
Sr				619	494	444	319	441	441
Sc				28.0	32.1	34.3	32.3	37.2	35.9
Zr		289	317	96	101	193	81	170	191

Table 4.3 (cont.): Major and trace element chemistry for the Eocene-Oligocene mantle transect. Where a reference is given, XRF and ICP-MS data not marked with an asterisk (*) are from the literature. Those data marked with an asterisks and data from all other samples without a reference are from this study.. Major element data has been normalized to 100% volatile free. FeO* indicates all Fe calculated as FeO. Major elements reported as oxide wt. %; trace elements are reported as ppm.

Sample Name	AB09-21	AB09-22	AH-SP06-2	JDM-293	EMT-117	K89-130	K90-247	K90-251	K90-260
La	7.32	11.81	13.33	21.57	21.04	25.70*		50.86*	
Ce	16.03	25.87	29.85	48.48	47.56	52.72*		104.47*	
Pr	2.20	3.51	4.15	6.57	6.49	6.91*		12.56*	
Sm	9.78	15.50	18.91	29.27	28.53	28.73*		49.10*	
Nd	2.55	3.85	5.13	7.65	7.60	6.24*		9.14*	
Eu	0.96	1.34	1.82	2.36	2.38	1.86*		2.45*	
Gd	2.61	3.95	5.52	8.31	8.21	5.23*		6.76*	
Tb	0.44	0.65	0.92	1.39	1.40	0.76*		0.89*	
Dy	2.69	3.97	5.65	8.61	8.51	4.20*		4.80*	
Ho	0.55	0.80	1.14	1.73	1.71	0.79*		0.89*	
Er	1.48	2.09	3.06	4.57	4.54	2.06*		2.29*	
Tm	0.21	0.29	0.44	0.65	0.64	0.28*		0.32*	
Yb	1.26	1.77	2.69	3.99	3.89	1.68*		1.95*	
Lu	0.20	0.27	0.42	0.61	0.60	0.25*		0.30*	
Ba	112	124	214	207	341	358*	420	660*	396
T	1.62	1.09	2.19	3.73	3.52	4.92*		10.24*	
Nb	3.5	7.6	7.2	17.3	17.2	11.2*	22.1	12.9*	22.2
Y	13.61	19.86	27.69	43.31	42.66	20.01*	23.00	22.18*	22.00
Hf	1.51	2.44	2.96	5.65	5.64	3.03*		3.63*	
Ta	0.22	0.46	0.47	1.18	1.17	0.67*		0.73*	
U	0.77	0.25	0.65	1.22	1.13	1.22*		2.28*	
Pb	5.83	2.42	3.20	4.84	4.95	4.07*		7.36*	
Rb	2.9	4.0	8.4	8.3	35.0	25.6*	51.0	19.6*	48.0
C	0.31	0.34	0.21	0.43	2.09	0.66*		0.74*	
Sr	465	406	370	284	249	568*	385	1151*	384
Sc	36.3	36.7	30.6	36.9	40.4	32.1*	22.0	39.6*	25.0
Zr	53	94	107	221	217	120*	144	144*	146

Table 4.3 (cont.): Major and trace element chemistry for the Eocene-Oligocene mantle transect. Where a reference is given, XRF and ICP-MS data not marked with an asterisk (*) are from the literature. Those data marked with an asterisk and data from all other samples without a reference are from this study.. Major element data has been normalized to 100% volatile free. FeO* indicates all Fe calculated as FeO. Major elements reported as oxide wt. %; trace elements are reported as ppm.

Sample Name	K90-266	K90-326	K90-327	K90-328	K90-366	K90-367	K90-392	K90-395	K90-397
La	61.37*		14.40	28.33*	25.97*	25.76*	40.70	12.10	
Ce	127.17*		32.10	58.28*	55.29*	54.78*	78.90	24.50	
Pr	15.25*			7.64*	7.30*	7.20*			
Sm	59.75*		17.80	31.43*	30.55*	30.04*	37.10	12.70	
Nd	10.95*		4.46	6.43*	6.52*	6.33*	6.44	3.37	
Eu	2.92*		1.48	1.90*	2.01*	2.00*	1.96	1.23	
Gd	7.70*			5.22*	5.61*	5.50*			
Tb	0.99*			0.74*	0.84*	0.83*			
Dy	5.08*			4.09*	4.77*	4.70*			
Ho	0.88*			0.75*	0.91*	0.91*			
Er	2.22*			1.94*	2.38*	2.39*			
Tm	0.30*			0.25*	0.32*	0.32*			
Yb	1.79*		2.72	1.55*	1.96*	1.93*	1.84	2.16	
Lu	0.29*		0.39	0.23*	0.30*	0.30*	0.22	0.43	
Ba	870*	189	463	440*	437*	186*	478	206	305
T	11.30*		2.10	5.80*	4.68*	4.60*	7.06	1.44	
Nb	16.0*	14.8	8.4	10.8*	10.9*	14.6*	17.5	18.4	11.0
Y	22.33*	25.00	18.83	22.87*	22.62*	26.00*	19.00	23.00	23.00
Hf	3.97*		2.81	2.83*	3.17*	3.16*	3.32	2.43	
Ta	0.90*		0.80	0.48*	0.65*	0.66*	1.09	1.40	
U	2.57*			1.34*	1.15*	1.19*			
Pb	7.76*			4.84*	3.94*	3.82*			
Rb	26.9*	10.0	20.1	21.1*	20.9*	7.0*	21.0	14.0	20.0
C	0.81*		0.54	0.25*	0.26*				
Sr	1451*	551	826	717*	715*	482*	1066	415	462
Sc	35.9*	38.0	37.2	32.8*	32.1*	37.0*	26.0	26.0	25.0
Zr	53*	94	107	221*	217*	120*	144	144	146

Table 4.3 (cont.): Major and trace element chemistry for the Eocene-Oligocene mantle transect. Where a reference is given, XRF and ICP-MS data not marked with an asterisk (*) are from the literature. Those data marked with an asterisk and data from all other samples without a reference are from this study.. Major element data has been normalized to 100% volatile free. FeO* indicates all Fe calculated as FeO. Major elements reported as oxide wt. %; trace elements are reported as ppm.

Sample Name	8_12_1	8_23_2	8_31_8	9_14_2	AB10-24	AB10-26	S91-14	SR83-94	SR61-5
Al ₂ O ₃ /TiO ₂	2.75	2.37	3.27	4.33	4.38	4.90	2.78	4.22	5.86
FeO*/MgO	1.92	2.13	2.15	3.58	1.68	2.32	1.42	1.18	1.57
Ce/Sm	9.87	9.78	9.99	6.41	8.04	8.48			
Ce/Yb	83.94	67.51	167.37	12.20	32.85	31.26			
Nb/Zr	0.18	0.20	0.16	0.08	0.17	0.17			
Zr/Nb	5.63	5.07	6.25	12.62	5.75	5.76			
Ba/Nb	7.96	5.17	4.15	20.39	5.67	4.21			
Ba/Zr	1.41	1.02	0.66	1.62	0.99	0.73			
Ba/Ce	3.48	2.87	2.24	7.49	3.48	2.49			

Table 4.3 (cont.): Major and trace element chemistry for the Eocene-Oligocene mantle transect. Where a reference is given, XRF and ICP-MS data not marked with an asterisk (*) are from the literature. Those data marked with an asterisk and data from all other samples without a reference are from this study.. Major element data has been normalized to 100% volatile free. FeO* indicates all Fe calculated as FeO. Major elements reported as oxide wt. %; trace elements are reported as ppm.

Sample Name	S84-112	S91-10	SH64-1C	SH64-1D	SH64-1E	SR83-160	SR87-23	S87-83	SR83-48
Al ₂ O ₃ /TiO ₂	3.36	4.37	3.94	3.83	3.73	3.13	3.37	3.57	4.00
FeO*/MgO	1.08	1.53	1.26	1.29	1.30	1.18	1.24	1.22	1.38
Ce/Sm									
Ce/Yb							0.21		0.24
Nb/Zr							4.74		4.14
Zr/Nb							4.83		4.40
Ba/Nb							1.02		1.06
Ba/Zr							2.85		5.10

Table 4.3 (cont.): Major and trace element chemistry for the Eocene-Oligocene mantle transect. Where a reference is given, XRF and ICP-MS data not marked with an asterisk (*) are from the literature. Those data marked with an asterisk and data from all other samples without a reference are from this study.. Major element data has been normalized to 100% volatile free. FeO* indicates all Fe calculated as FeO. Major elements reported as oxide wt. %; trace elements are reported as ppm.

Sample Name	AB09-									
	SR83-27	CH-58	H-1	AB09-14	AB09-17	AB09-18	AB09-19	20A	AB09-20B	
Al ₂ O ₃ /TiO ₂	4.16	3.92	3.71	13.81	14.68	9.71	10.64	10.43	9.96	
FeO*/MgO	1.28	1.25	1.38	1.24	1.32	1.72	1.32	1.56	1.70	
Ce/Sm				5.88	7.04	7.16	5.96	7.23	7.22	
Ce/Yb				11.07	15.65	16.53	11.42	16.46	16.62	
Nb/Zr		0.27	0.28	0.05	0.08	0.08	0.09	0.08	0.08	
Zr/Nb		3.66	3.60	19.22	13.09	12.12	11.63	12.16	12.17	
Ba/Nb		4.78	4.03	41.81	21.08	13.35	15.99	14.37	13.45	
Ba/Zr		1.31	1.12	2.18	1.61	1.10	1.37	1.18	1.11	
Ba/Ce		3.18	2.57	8.42	5.87	4.79	5.89	5.00	4.82	

Table 4.3 (cont.): Major and trace element chemistry for the Eocene-Oligocene mantle transect. Where a reference is given, XRF and ICP-MS data not marked with an asterisk (*) are from the literature. Those data marked with an asterisk and data from all other samples without a reference are from this study.. Major element data has been normalized to 100% volatile free. FeO* indicates all Fe calculated as FeO. Major elements reported as oxide wt. %; trace elements are reported as ppm.

Sample Name	AB09-									
	SR83-27	CH-58	H-1	AB09-14	AB09-17	AB09-18	AB09-19	20A	AB09-20B	
Al ₂ O ₃ /TiO ₂	4.16	3.92	3.71	13.81	14.68	9.71	10.64	10.43	9.96	
FeO*/MgO	1.28	1.25	1.38	1.24	1.32	1.72	1.32	1.56	1.70	
Ce/Sm				5.88	7.04	7.16	5.96	7.23	7.22	
Ce/Yb				11.07	15.65	16.53	11.42	16.46	16.62	
Nb/Zr		0.27	0.28	0.05	0.08	0.08	0.09	0.08	0.08	
Zr/Nb		3.66	3.60	19.22	13.09	12.12	11.63	12.16	12.17	
Ba/Nb		4.78	4.03	41.81	21.08	13.35	15.99	14.37	13.45	
Ba/Zr		1.31	1.12	2.18	1.61	1.10	1.37	1.18	1.11	
Ba/Ce		3.18	2.57	8.42	5.87	4.79	5.89	5.00	4.82	

Table 4.3 (cont.): Major and trace element chemistry for the Eocene-Oligocene mantle transect. Where a reference is given, XRF and ICP-MS data not marked with an asterisk (*) are from the literature. Those data marked with an asterisks and data from all other samples without a reference are from this study.. Major element data has been normalized to 100% volatile free. FeO* indicates all Fe calculated as FeO. Major elements reported as oxide wt. %; trace elements are reported as ppm.

Sample Name	AB09-21	AB09-22	AHSP06-2	JDM-293	EMT-117	K89-130	K90-247	K90-251	K90-260
Al ₂ O ₃ /TiO ₂	17.47	12.87	12.04	4.59	4.62	10.60	14.28	11.05	14.35
FeO*/MgO	1.30	1.26	2.85	5.39	3.66	0.69	1.20	0.74	1.14
Ce/Sm	6.28	6.71	5.82	6.33	6.26	8.45		11.43	
Ce/Yb	12.68	14.63	11.10	12.16	12.21	31.42		53.59	
Nb/Zr	0.07	0.08	0.07	0.08	0.08	0.09	0.15	0.09	0.15
Zr/Nb	15.07	12.37	14.78	12.79	12.67	10.76	6.52	11.12	6.58
Ba/Nb	31.55	16.30	29.54	11.98	19.89	31.97	19.00	51.13	17.84
Ba/Zr	2.09	1.32	2.00	0.94	1.57	2.97	2.92	4.60	2.71
Ba/Ce	6.97	4.81	7.16	4.27	7.17	6.79		6.32	

Table 4.3 (cont.): Major and trace element chemistry for the Eocene-Oligocene mantle transect. Where a reference is given, XRF and ICP-MS data not marked with an asterisk (*) are from the literature. Those data marked with an asterisks and data from all other samples without a reference are from this study.. Major element data has been normalized to 100% volatile free. FeO* indicates all Fe calculated as FeO. Major elements reported as oxide wt. %; trace elements are reported as ppm.

Sample Name	K90-266	K90-326	K90-327	K90-328	K90-366	K90-367	K90-392	K90-395	K90-397
Al ₂ O ₃ /TiO ₂	9.97	11.48	11.39	10.92	11.99	11.93	9.85	13.13	16.36
FeO*/MgO	0.75	1.21	1.19	0.96	1.17	1.18	1.04	1.13	1.25
Ce/Sm	11.61		7.20	9.06	8.48	8.66	12.25	7.27	
Ce/Yb	71.23		11.80	37.71	28.23	28.44	42.88	11.34	
Nb/Zr	0.10	0.13	0.08	0.09	0.09	0.12	0.11	0.18	0.10
Zr/Nb	10.09	7.97	12.50	11.02	10.86	8.22	8.74	5.54	10.27
Ba/Nb	54.49	12.77	55.29	40.83	40.15	12.74	27.31	11.20	27.73
Ba/Zr	5.40	1.60	4.42	3.70	3.70	1.55	3.12	2.02	2.70
Ba/Ce	6.84		14.43	7.56	7.90	3.40	6.06	8.41	

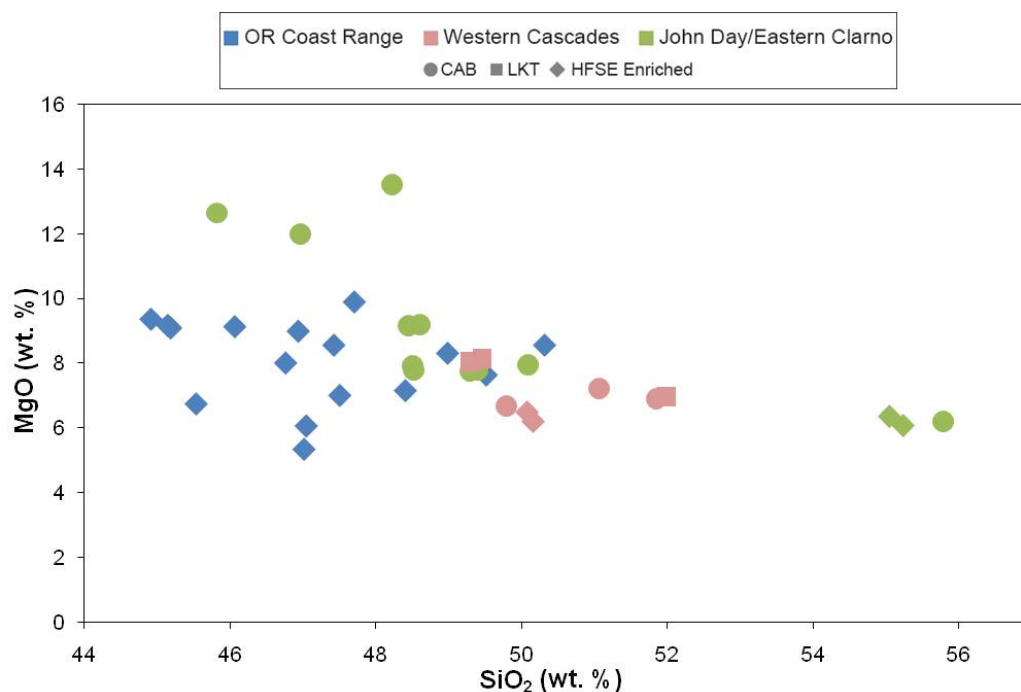


Figure 4.2: MgO vs. SiO₂ for primitive basalts from the Eocene-Oligocene transect. Data are from this and other studies as outlined in Table 4.3.

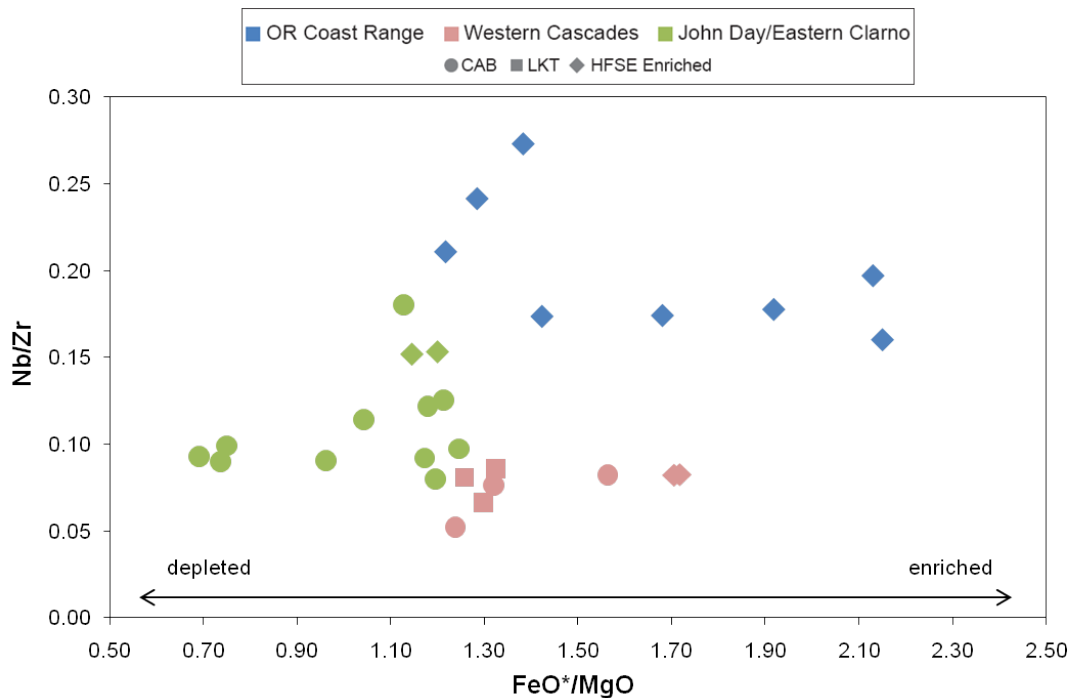


Figure 4.3: Nb/Zr vs. FeO*/MgO for primitive basalts from the Eocene-Oligocene transect. Data are from this and other studies as outlined in Table 4.3.

This interpretation is supported by higher FeO^*/MgO among the samples with variable Nb/Zr , which may indicate a less depleted source. Finally, it is also possible that the subducting slab carried sediments with Nb/Zr distinct from that of the backarc mantle and that this sediment signature overprinted the mantle source signature during fluid (and sediment) flux melting.

If FeO^*/MgO is taken as a proxy for mantle fertility, the backarc appears to be tapping a less fertile mantle source than the arc. The forearc spans a range of apparent fertility with the alkaline intrusions appearing to have a more fertile source while samples from the Tertiary volcanic centers (Yachats and Cascade Head Basalts) are from a more depleted source. This agrees with the interpretation of Davis et al. (1995) that the alkaline intrusions are lower degree partial melts of a similar mantle source as the YB and CHB. However, if magmas stalled in the crust and fractionated (as indicated by their not perfectly primitive nature), FeO^*/Mg may not be a reliable proxy for source enrichment, but may instead reflect the fractionation of Mg-rich phases, or even the effect of partial melting.

The common enrichment of Ba and other fluid mobile LILEs in arc basalts is interpreted to represent the influence of fluids and subduction-derived sediments in melting beneath subduction zones (e.g. Schmidt et al. 2008; Gill, 1980). Niobium, while similarly incompatible, is a fluid immobile HFSE and thus not expected to be enriched by the fluxing of fluid and sediments. The forearc samples are enriched in HFSE and also have high concentrations of Ba (Figure 4.4). This enrichment in incompatible elements lends further support to the interpretation that the HFSE-rich basalts of the forearc are low degree partial melts of a relatively fertile source. In contrast, both the arc and backarc are generally lower in Nb. The arc is lower in both Nb and Ba, perhaps suggesting a more depleted source, or, as suggested by their uniform Nb/Zr , a higher degree of partial melting. While the backarc has generally low Nb, elevated Ba suggests a subducted slab influence.

Ba/Zr provides a better proxy for subduction influence than Ba concentration alone. As Ba and Zr are similarly incompatible, their ratio should not be affected by differing

degrees of partial melting. However, their different mobilities will lead Ba to be preferentially concentrated in subduction fluids and sediments. Therefore, elevated Ba/Zr (and likewise Ba/Nb and Ba/Ce) provides a tool for assessing slab influence (Figure 4.5). While a few samples from both the arc and backarc fall along the mantle array described by Leeman et al. (1990 and references therein; see Figure 4.5 caption) and could be explained by melting of a heterogeneous mantle source, the preponderance of samples from both the arc and backarc lie above the mantle array with elevated Ba/Zr. These samples trend upward from the mantle array toward a pelagic sediment source (Leeman et al., 1990; Hole et al., 1983). As many of the backarc samples extend to higher Ba/Zr than the upper crust (Leeman et al., 1990; Taylor and McLennan, 1985), their Ba/Zr signature cannot be explained by crustal contamination alone, and must involve the influence of subducted sediments and fluids. Samples from the arc do not trend toward an upper crustal signature, but rather toward the pelagic sediment source, which illustrates the influence of subducted sediments and fluids in the formation of the Western Cascade arc basalts. The variability of apparent arc component among the arc and backarc samples suggests that mantle processes were variable both temporally and spatially.

HFSE-rich basalts from the arc and backarc tend to be in the lower range of Ba/Zr values for their respective regions, and in the arc, they entirely overlap with the mantle array. Other LILE (e.g. Sr, Rb, K) are also depleted relative to HFSE in the forearc magmas. HFSE-rich basalts from these regions therefore appear to have experienced less subduction influence. Samples from the forearc actually fall below the mantle array. As they appear to be low degree partial melts, Ba, Nb and Zr may have decoupled during melting resulting in anomalous Ba/Zr and Nb/Zr ratios that fall off of the mantle array. Nevertheless, the mantle source of these magmas must have either been enriched in the HFSE without the concomitant enrichment in fluid mobile incompatible elements or have subsequently lost LILE. Metasomatism of the hydrated and serpentized forearc may offer a mechanism by which LILE were removed from

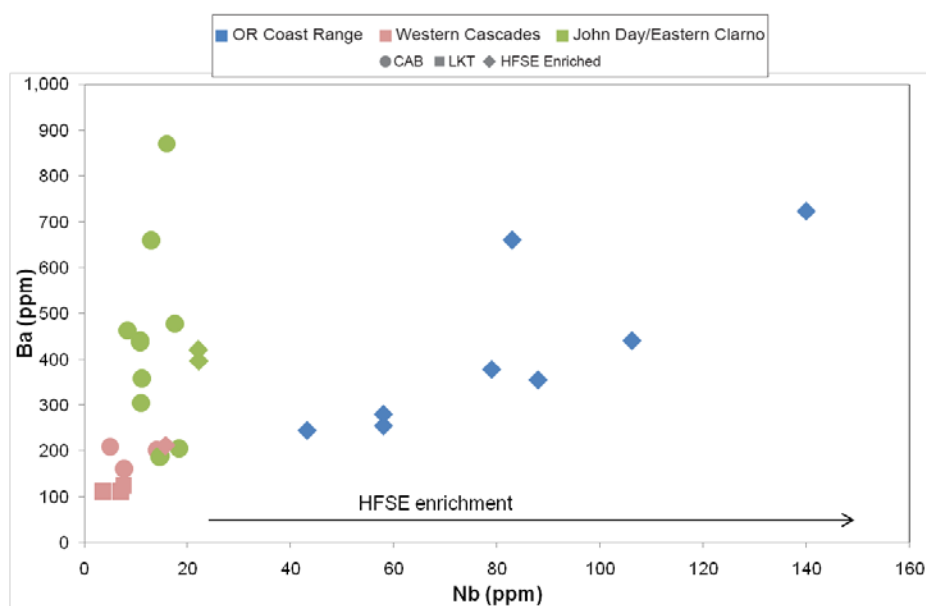


Figure 4.4: Ba vs. Nb for primitive basalts from the Eocene-Oligocene transect. Data are from this and other studies as outlined in Table 4.3.

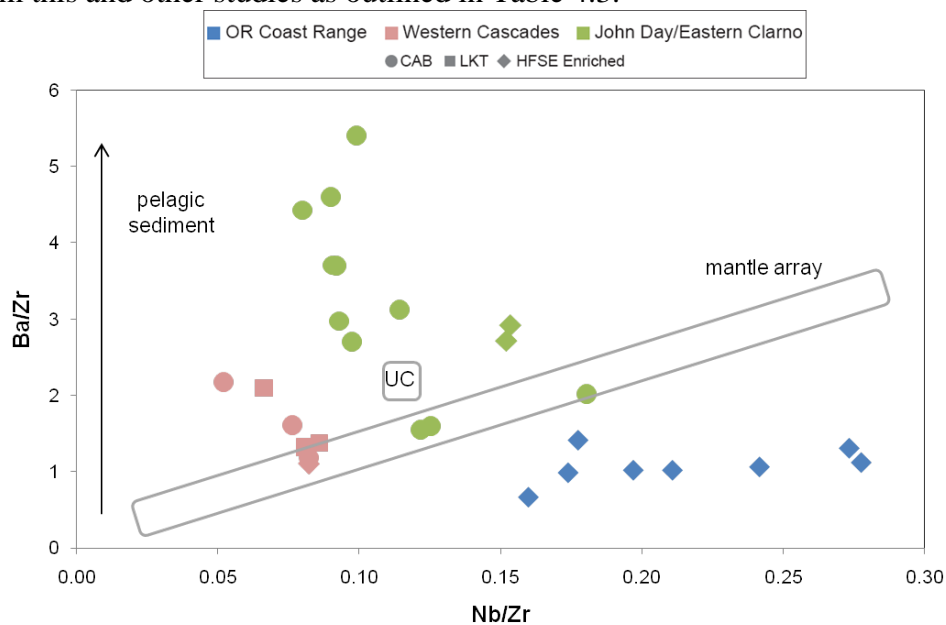


Figure 4.5: Ba/Zr vs. Nb/Zr for primitive basalts from the Eocene-Oligocene transect. Data are from this and other studies as outlined in Table 4.3. UC represents an average upper crustal composition and is reported by Taylor and McLennan, 1985. The mantle array is defined by Tristan de Cunha (Weaver et al., 1987), BHVO-1 Hawaiian tholeiite (Govindaraju, 1984), N-MORB (Le Roex et al., 1983) and the unpublished data and literature compilation of W.P. Leeman given as a field in Leeman et al., 1990). Pelagic sediment composition is from Hole et al. (1984).

some mantle domains. Metasomatism would act to concentrate LILE, thus depleting much of mantle of these fluid mobile elements.

Plots of Ba/Nb and Ba/Ce vs. Nb/Zr (Figures 4.6 and 4.7) support the conclusions drawn above that both the arc and backarc have considerable sediment and fluid contributions from the subducting slab, while the forearc is little overprinted by active subduction processes. The relative contribution of the slab beneath the arc vs. beneath the backarc is difficult to determine from trace element chemistry. As incompatible element ratios (Nb/Zr) are variable in these samples, the apparent enrichment in Ba varies depending on the HFSE used for comparison. Additionally, Ce data are less complete than Nb or Zr, and some of the backarc samples with greater apparent subduction signatures are not shown in the Ba/Ce plot. Nonetheless, incompatible trace element data support the conclusion that the geographic backarc experienced fluxing from subduction that was at least comparable to that experienced coevally at the axis of the arc. These observations lend credence to interpretations of field relations and geochemical data that require that the arc was broad at the time of the Western Cascades and extended much farther east than is commonly accepted (McCloughry et al., 2009).

In Figure 4.9, Ba/Ce is again used as a proxy for fluid addition while Ce/Yb quantifies the steepness of the REE pattern. In general, a steeper REE pattern with enriched LREE (light rare earth elements, that is high Ce/Yb) suggests a lower degree of partial melting (as LREE tend to be more incompatible than HREE). In contrast, a flatter pattern (lower Ce/Yb) denotes a higher degree of partial melting as the LREE are more incompatible than the HREE during mantle melting (Figure 4.8). The elevated Ce/Yb of all forearc and most backarc samples supports earlier suppositions that these may represent lower degree partial melts. In contrast, the lower Ce/Yb of the arc samples suggests a higher degree of melting of the mantle source. Alternately, Ce/Yb would be increased by the presence of residual garnet in the source rock. This affect can be demonstrated through simple batch melt modeling (Figure 4.8). However, the variability in Ce/Yb is here interpreted as

resulting from varying degrees of partial melting because garnet would require that the source of the magmas be >80 km deep. This seems unlikely, as it would require a source below the slab. Instead, high Ce/Yb values are interpreted as evidence of low degrees of partial melting, which is consistent with other geochemical indicators, especially in the forearc, where values are most extreme. These elevated Ce/Yb are not accompanied by elevated Ba/Ce, as predicted by the model for a partial melting influence. This is likely explained by the choice of starting mineral assemblage chosen for the partial melting modeling. As the partition coefficient for Ba varies by three orders of magnitude among olivine, orthopyroxene, and clinopyroxene, it is apparent that Ba/Ce would be sensitive to the percentages of each mineral assumed in the source rock.

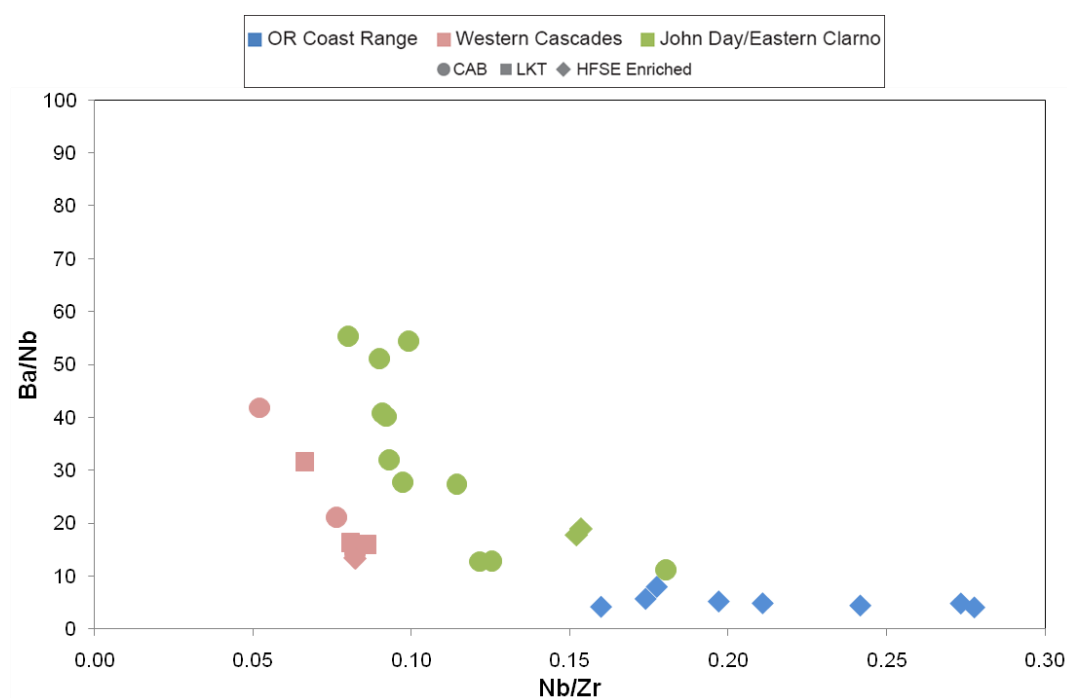


Figure 4.6: Ba/ Nb vs. Nb/Zr for primitive basalts from the Eocene-Oligocene transect. Data are from this and other studies as outlined in Table 4.3.

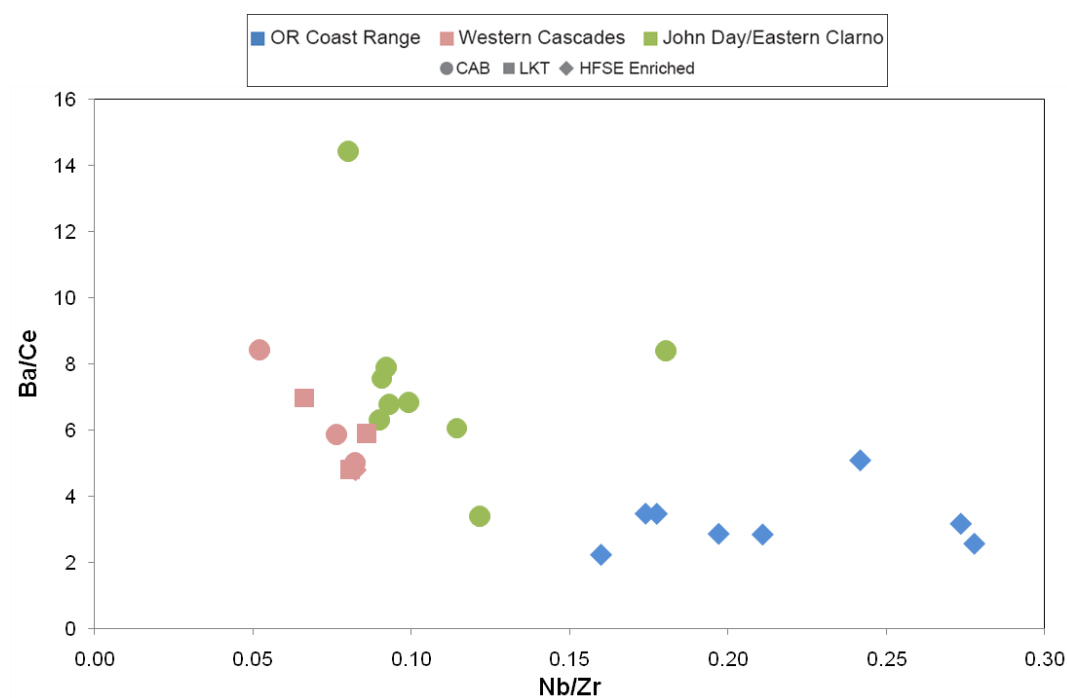


Figure 4.7: Ba/Ce vs. Nb/Zr for primitive basalts from the Eocene-Oligocene transect. Data are from this and other studies as outlined in Table 4.3

As these samples do not represent true primitive mantle melts, it is likely that their olivine content is overestimated by the lherzolite mineral assemblages. For this reason, the high Ba/Ce at low degrees of partial melting may be greatly exaggerated. In this work, variable Ce/Yb is interpreted as resulting from varying degrees of partial melting, however, it must be noted that this trend could also be explained by residual garnet in the source, though this explanation is not favored due to the geologic implausibility.

Taken together, observations of the major and trace element chemistry of the Eocene-Oligocene Proto-Cascadia (EOPC) suggest a heterogeneous mantle that was variably influenced by subduction. In the forearc, HFSE-rich basalts appear to have been formed by low degrees of partial melting of a relatively enriched mantle source, with little demonstrable subduction influence. CABs, LKTs, and HFSE-rich basalts were produced in the Western Cascades and likely resulted from higher degrees of

partial melting of a less enriched source, with the HFSE-basalts tending to have a slightly more enriched signature. Fluid fluxing beneath the Western Cascades facilitated melting and is recorded in the geochemistry of the CABs and LKTs, especially. Behind the geographic arc, the backarc appears to have experienced considerable material flux from the subducting slab. Backarc samples are predominately CABs and demonstrate characteristics typical of arc basalts (elevated Ba/Zr, e.g.). The backarc mantle may have been more heterogeneous, as the CABs and HFSE-rich basalts appear to have more distinct histories as products of variably fertile mantles and different degrees of partial melting. Additionally, the apparent subduction signature of the backarc could be a signature of paleo-enrichment and not actively acquired in the Eocene-Oligocene.

While major and trace element compositions can inform interpretations of mantle source, these signatures may be overprinted by fractional crystallization and may be subject to the effects of decoupling nominally similar element pairs (such as Nb and Zr) during partial melting or crystallization of trace phases. Radiogenic isotopes may provide a more faithful record of mantle heterogeneity as they are unaffected by partial melting and fractional crystallization.

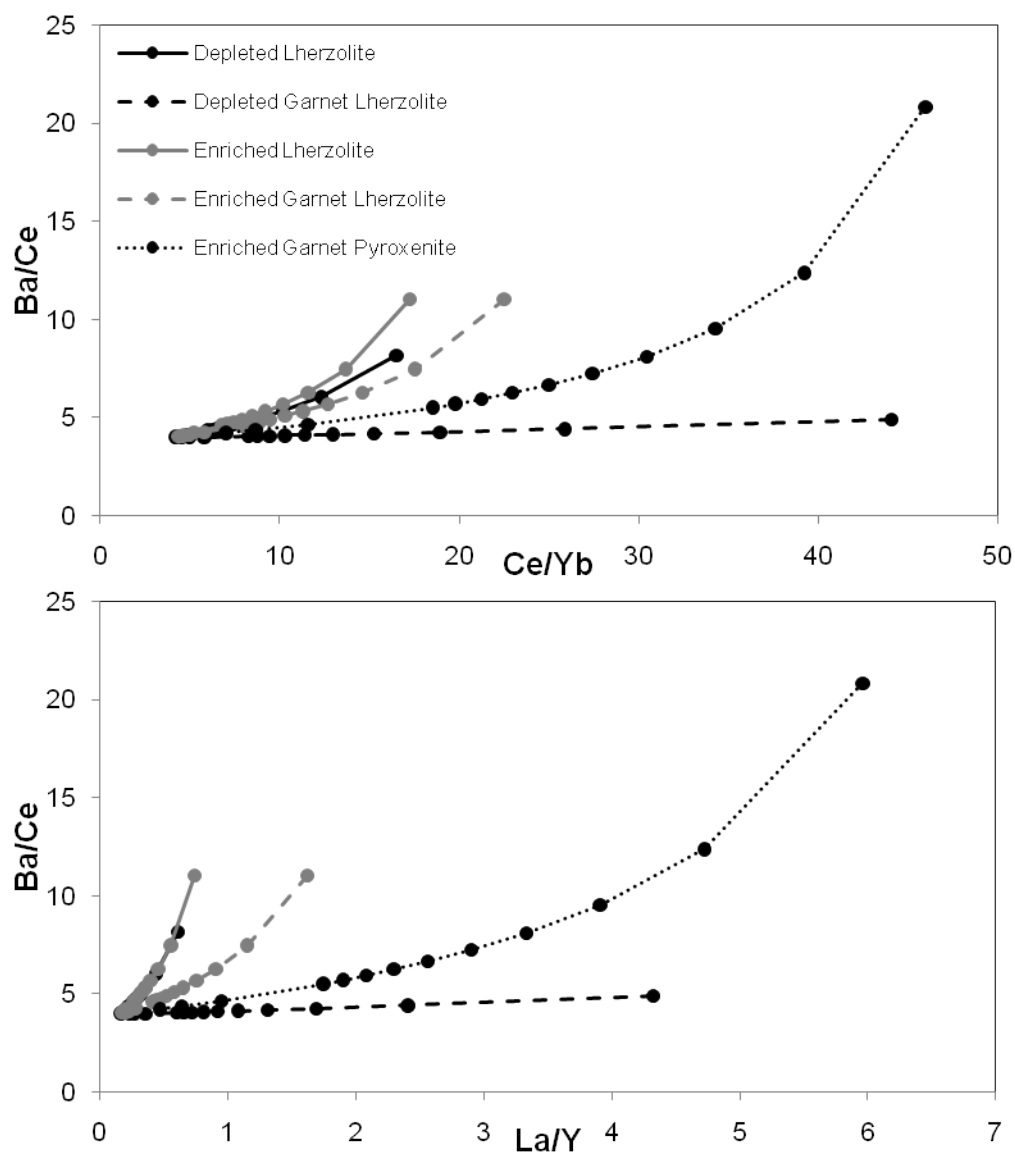


Figure 4.8: Simplified model of the effect of mantle partial melting on Ba/Ce, Ce/Yb, and La/Y ratios. Batch melting modeling was performed using starting Ba, Ce, Yb, and La, and Y concentrations of primitive mantle ('pyrolite' from McDonough and Sun, 1995). The mineralogy of each mantle composition was taken from Oxford (2006). Partition coefficients were taken from Halliday et al., 1995; LaTourette et al., 1995; Jenner et al., 1994; and Rollinson, 1993. Melting proceeds from right to left in 1% melt increments through 10%, then in 10% melt increments through 40%.

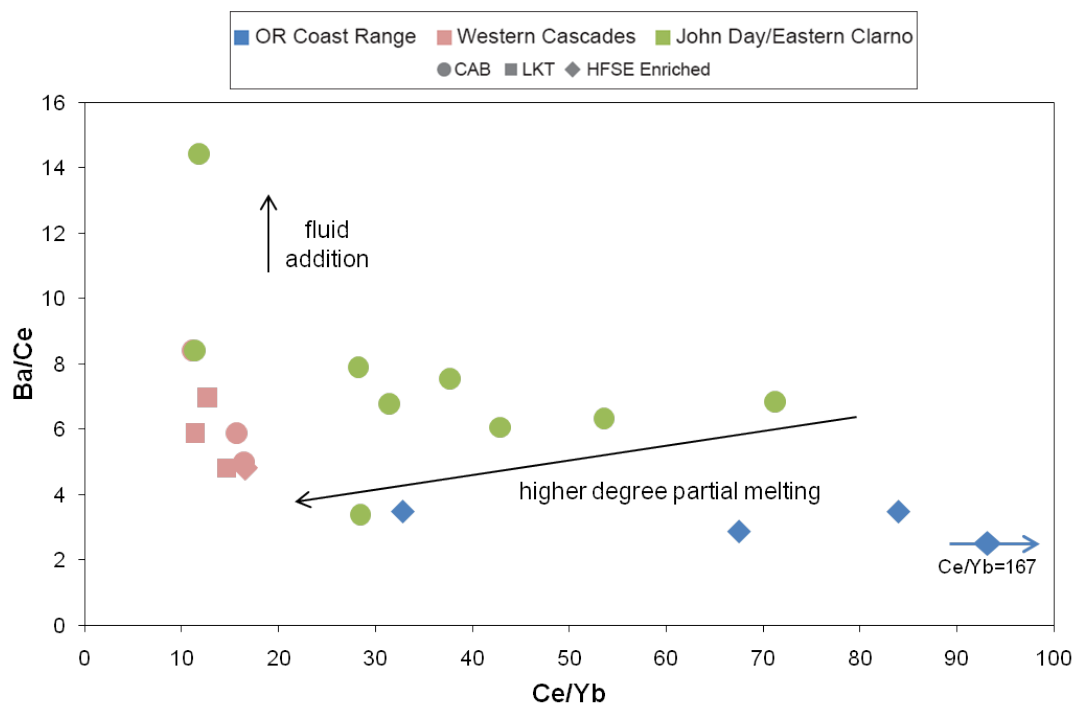


Figure 4.9: Ba/Ce vs. Ce/Yb for primitive basalts from the Eocene-Oligocene transect. Data are from this and other studies as outlined in Table 4.3.

4.4 Insights from Radiogenic Isotopes

The Sr, Nd, and Pb isotopic compositions of 24 Eocene-Oligocene Proto-Cascadia (EOPC) samples were measured at the Carnegie Institution of Washington Department of Terrestrial Magnetism as described in Section 3.5. A subset of 18 of these samples was also analyzed for Hf isotopes. Of the 24 total samples, one failed to return Pb data and 5 were determined to be non-primitive. Isotopic ratios of non-primitive samples are shown in figures (as open symbols) for reference but should not be interpreted as indicative of mantle character. Two of the 24 samples were determined to be outside of the age range of EOPC considered here and are not shown in any figures (see Appendix B for characterization). Sr, Nd, and Pb isotopic compositions from two additional samples from the forearc Yachats Basalt and Cascade Head Basalt are reported from the unpublished data of Doug Pyle (personal communication, 2009). All isotopes have been age corrected (to either radiometric or stratigraphically constrained ages) and are shown in all figures as initial ratios. This section considers the initial isotopic character of the 17 primitive samples to build upon the interpretation of mantle heterogeneity derived from the investigation of major and trace element chemistry.

The isotopic signature of a magma may be affected by a number of processes including the assimilation of continental crust by primitive magmas, the addition of a subduction component (fluid \pm sediment \pm melt) from the slab, and isotopic heterogeneity within the mantle wedge (e.g. Borg et al., 2002). Consideration of each of the isotopic trends discussed in this section should be viewed in light of the interplay among these influences.

All EOPC samples fall along the mantle array of Sr-Nd isotopic ratios but are more isotopically evolved than Pacific MORB (Figure 4.10). Both the arc and backarc primitive samples follow a linear trend in $^{143}\text{Nd}/^{144}\text{Nd}$ vs. $^{87}\text{Sr}/^{86}\text{Sr}$, but the two isotope ratios appear less strongly coupled in the forearc Oregon Coast Range (OCR) samples.

Non-primitive samples, excepting one, are more isotopically evolved than primitive samples from the same region, suggesting that they interacted with continental crust.

Table 4.4: Isotope compositions for the Eocene-Oligocene mantle transect. All isotope data are from this study. Ages are from this study for samples from Table 4.2 and from the references listed in Table 4.3 for the remaining samples. Because in-run precision was greater than the external reproducibility of the standards, data are assigned the external errors given in Table 4.5.

Sample Name	8_12_1	8_23_2	8_31_8	9_14_2	AB10-24	AB10-26
Age (Ma)	36.84	33.64	36	32.6	33	33
$^{87}\text{Rb}/^{86}\text{Sr}$	0.0354	0.0847	0.036	0.4798	0.1129	0.0124
$^{87}\text{Sr}/^{86}\text{Sr}$ (m)	0.703525	0.703504	0.703193	0.704376	0.703249	0.703340
$^{87}\text{Sr}/^{86}\text{Sr}$ (i)	0.703507	0.703464	0.703175	0.704154	0.703196	0.703335
$^{147}\text{Sm}/^{144}\text{Nd}$	0.1237	0.1224	0.1589	0.1588	0.1399	0.1352
$^{143}\text{Nd}/^{144}\text{Nd}$ (m)	0.512943	0.512930	0.512915	0.512866	0.512954	0.512924
$^{143}\text{Nd}/^{144}\text{Nd}$ (i)	0.512913	0.512903	0.512877	0.512832	0.512924	0.512895
ϵNd (i)	6.44	6.05	5.73	4.64	6.55	5.99
$^{176}\text{Lu}/^{177}\text{Hf}$	0.00385		0.00143		0.00723	0.00786
$^{176}\text{Hf}/^{177}\text{Hf}$ (m)	0.283037		0.283034		0.282856	0.282868
$^{176}\text{Hf}/^{177}\text{Hf}$ (i)	0.283035		0.283033		0.282852	0.282863
ϵHf (i)	9.65		9.57		3.09	3.48
$^{238}\text{U}/^{204}\text{Pb}$	37.4	41.77	31.54	8.68	29.39	36.67
$^{206}\text{Pb}/^{204}\text{Pb}$ (m)	19.597	20.152	19.524	19.007	19.463	19.575
$^{207}\text{Pb}/^{204}\text{Pb}$ (m)	15.594	15.629	15.593	15.613	15.604	15.602
$^{208}\text{Pb}/^{204}\text{Pb}$ (m)	39.25	39.72	39.19	38.73	39.20	39.23
$^{206}\text{Pb}/^{204}\text{Pb}$ (i)	19.382	19.934	19.347	18.963	19.312	19.387
$^{207}\text{Pb}/^{204}\text{Pb}$ (i)	15.584	15.618	15.585	15.611	15.597	15.593
$^{208}\text{Pb}/^{204}\text{Pb}$ (i)	38.19	38.11	38.50	38.63	37.41	36.79

Table 4.4: Isotope compositions for the Eocene-Oligocene mantle transect. All isotope data are from this study. Ages are from this study for samples from Table 4.2 and from the references listed in Table 4.3 for the remaining samples. Because in-run precision was greater than the external reproducibility of the standards, data are assigned the external errors given in Table 4.5.

Sample Name	AB09-14	AB09-17	AB09-18	AB09-19	AB09-20A	AB09-21
Age (Ma)	32	31.4	31.4	29.78	32.13	32.41
$^{87}\text{Rb}/^{86}\text{Sr}$	0.0234	0.0589	0.0803	0.0641	0.0257	0.0187
$^{87}\text{Sr}/^{86}\text{Sr}$ (m)	0.703193	0.703240	0.703201	0.703610	0.703313	0.703436
$^{87}\text{Sr}/^{86}\text{Sr}$ (i)	0.703182	0.703214	0.703165	0.703583	0.703301	0.703427
$^{147}\text{Sm}/^{144}\text{Nd}$	0.1482	0.1444	0.1443	0.1570	0.1435	0.1576
$^{143}\text{Nd}/^{144}\text{Nd}$ (m)	0.512953	0.512940	0.512951	0.512911	0.512921	0.512922
$^{143}\text{Nd}/^{144}\text{Nd}$ (i)	0.512922	0.512911	0.512921	0.512880	0.512891	0.512889
ϵNd (i)	6.5	6.26	6.46	5.62	5.9	5.86
$^{176}\text{Lu}/^{177}\text{Hf}$	0.02006	0.01495	0.01350	0.01727	0.01399	0.01854
$^{176}\text{Hf}/^{177}\text{Hf}$ (m)	0.283098	0.283064	0.283072	0.283053	0.283082	0.283027
$^{176}\text{Hf}/^{177}\text{Hf}$ (i)	0.283086	0.283056	0.283064	0.283043	0.283073	0.283016
ϵHf (i)	11.37	10.26	10.56	9.78	10.91	8.89
$^{238}\text{U}/^{204}\text{Pb}$	6.93	8.97	10.46	10.15	9.75	8.39
$^{206}\text{Pb}/^{204}\text{Pb}$ (m)	18.771	18.867	18.850	19.095	18.916	18.915
$^{207}\text{Pb}/^{204}\text{Pb}$ (m)	15.570	15.559	15.562	15.610	15.573	15.585
$^{208}\text{Pb}/^{204}\text{Pb}$ (m)	38.38	38.44	38.42	38.72	38.52	38.57
$^{206}\text{Pb}/^{204}\text{Pb}$ (i)	18.736	18.823	18.799	19.048	18.867	18.872
$^{207}\text{Pb}/^{204}\text{Pb}$ (i)	15.569	15.557	15.559	15.608	15.570	15.583
$^{208}\text{Pb}/^{204}\text{Pb}$ (i)	38.03	38.17	38.09	38.06	38.21	38.42

Table 4.4: Isotope compositions for of the Eocene-Oligocene mantle transect. All isotope data are from this study. Ages are from this study for samples from Table 4.2 and from the references listed in Table 4.3 for the remaining samples. Because in-run precision was greater than the external reproducibility of the standards, data are assigned the external errors given in Table 4.5.

Sample Name	AB09-22	AHSP06-2	JDM-293	EMT-117	K89-130	K90-251
Age (Ma)	35	32.75	32.9	34.2	35.3	38
$^{87}\text{Rb}/^{86}\text{Sr}$	0.0355	0.0657	0.0943	0.406	0.1303	0.0494
$^{87}\text{Sr}/^{86}\text{Sr}$ (m)	0.703174	0.703626	0.704950	0.704141	0.703482	0.703988
$^{87}\text{Sr}/^{86}\text{Sr}$ (i)	0.703157	0.703595	0.704906	0.703944	0.703416	0.703961
$^{147}\text{Sm}/^{144}\text{Nd}$	0.1502	0.1632	0.1708	0.1610	0.1313	0.1126
$^{143}\text{Nd}/^{144}\text{Nd}$ (m)	0.512954	0.512895	0.512856	0.512865	0.512911	0.512809
$^{143}\text{Nd}/^{144}\text{Nd}$ (i)	0.512919	0.512860	0.512819	0.512829	0.512881	0.512781
ϵNd (i)	6.52	5.19	4.4	4.62	5.77	3.9
$^{176}\text{Lu}/^{177}\text{Hf}$	0.01595					0.01173
$^{176}\text{Hf}/^{177}\text{Hf}$ (m)	0.283082					0.282991
$^{176}\text{Hf}/^{177}\text{Hf}$ (i)	0.283071					0.282983
ϵHf (i)	10.91					7.85
$^{238}\text{U}/^{204}\text{Pb}$	6.54	43.25	128.15	14.58	19.09	19.70
$^{206}\text{Pb}/^{204}\text{Pb}$ (m)	18.841	19.015	19.180	19.166	18.893	18.934
$^{207}\text{Pb}/^{204}\text{Pb}$ (m)	15.551	15.603	15.629	15.626	15.579	15.590
$^{208}\text{Pb}/^{204}\text{Pb}$ (m)	38.41	38.72	38.87	38.85	38.52	38.62
$^{206}\text{Pb}/^{204}\text{Pb}$ (i)	18.806	18.795	18.524	19.089	18.788	18.817
$^{207}\text{Pb}/^{204}\text{Pb}$ (i)	15.549	15.593	15.598	15.622	15.574	15.585
$^{208}\text{Pb}/^{204}\text{Pb}$ (i)	38.10	37.26	31.91	38.52	37.98	38.29

Table 4.4: Isotope compositions for the Eocene-Oligocene mantle transect. All isotope data are from this study. Ages are from this study for samples from Table 4.2 and from the references listed in Table 4.3 for the remaining samples. Because in-run precision was greater than the external reproducibility of the standards, data are assigned the external errors given in Table 4.5.

Sample Name	K90-266	K90-328	K90-366	K90-367
Age (Ma)	38	41.09	40.64	40.64
$^{87}\text{Rb}/^{86}\text{Sr}$	0.0537	0.0704	0.0853	0.0846
$^{87}\text{Sr}/^{86}\text{Sr}$ (m)	0.703918	0.703573	0.703589	0.703570
$^{87}\text{Sr}/^{86}\text{Sr}$ (i)	0.703889	0.703532	0.703540	0.703521
$^{147}\text{Sm}/^{144}\text{Nd}$	0.1108	0.1237	0.1291	0.1273
$^{143}\text{Nd}/^{144}\text{Nd}$ (m)	0.512823	0.512892	0.512931	0.512926
$^{143}\text{Nd}/^{144}\text{Nd}$ (i)	0.512795	0.512859	0.512896	0.512892
ϵNd (i)	4.17	5.5	6.21	6.13
$^{176}\text{Lu}/^{177}\text{Hf}$	0.01037	0.01154	0.01343	0.01348
$^{176}\text{Hf}/^{177}\text{Hf}$ (m)	0.283026	0.283057	0.283072	0.283079
$^{176}\text{Hf}/^{177}\text{Hf}$ (i)	0.283018	0.283048	0.283062	0.283068
ϵHf (i)	9.1	10.22	10.7	10.92
$^{238}\text{U}/^{204}\text{Pb}$	21.11	17.60	18.51	19.79
$^{206}\text{Pb}/^{204}\text{Pb}$ (m)	18.959	18.888	18.909	18.922
$^{207}\text{Pb}/^{204}\text{Pb}$ (m)	15.592	15.582	15.576	15.574
$^{208}\text{Pb}/^{204}\text{Pb}$ (m)	38.63	38.54	38.53	38.53
$^{206}\text{Pb}/^{204}\text{Pb}$ (i)	18.834	18.775	18.792	18.797
$^{207}\text{Pb}/^{204}\text{Pb}$ (i)	15.586	15.577	15.570	15.568
$^{208}\text{Pb}/^{204}\text{Pb}$ (i)	38.29	38.05	37.91	37.84

Table 4.5: External error of standards used for isotopic analyses. Each error is given as a 2σ mean errors. As in-run precision was greater than external reproducibility, the errors for each ratio below are assigned for all data given in Table 4.4, respectively.

Standard	Ratio	Reported	Measured	2σ Mean Error (\pm)	n
NBS 987	$^{87}\text{Sr}/^{86}\text{Sr}$	0.710250	0.710254	0.000004	4
JNdi	$^{143}\text{Nd}/^{144}\text{Nd}$	0.512115	0.512109	0.0000029	4
JMC-475	$^{176}\text{Hf}/^{177}\text{Hf}$	0.282160	0.282145	0.000003	4
NBS 981	$^{206}\text{Pb}/^{204}\text{Pb}$	36.7006	36.687	0.014	4
NBS 981	$^{207}\text{Pb}/^{204}\text{Pb}$	15.4891	15.487	0.004	4
NBS 981	$^{208}\text{Pb}/^{204}\text{Pb}$	16.9356	16.933	0.005	4

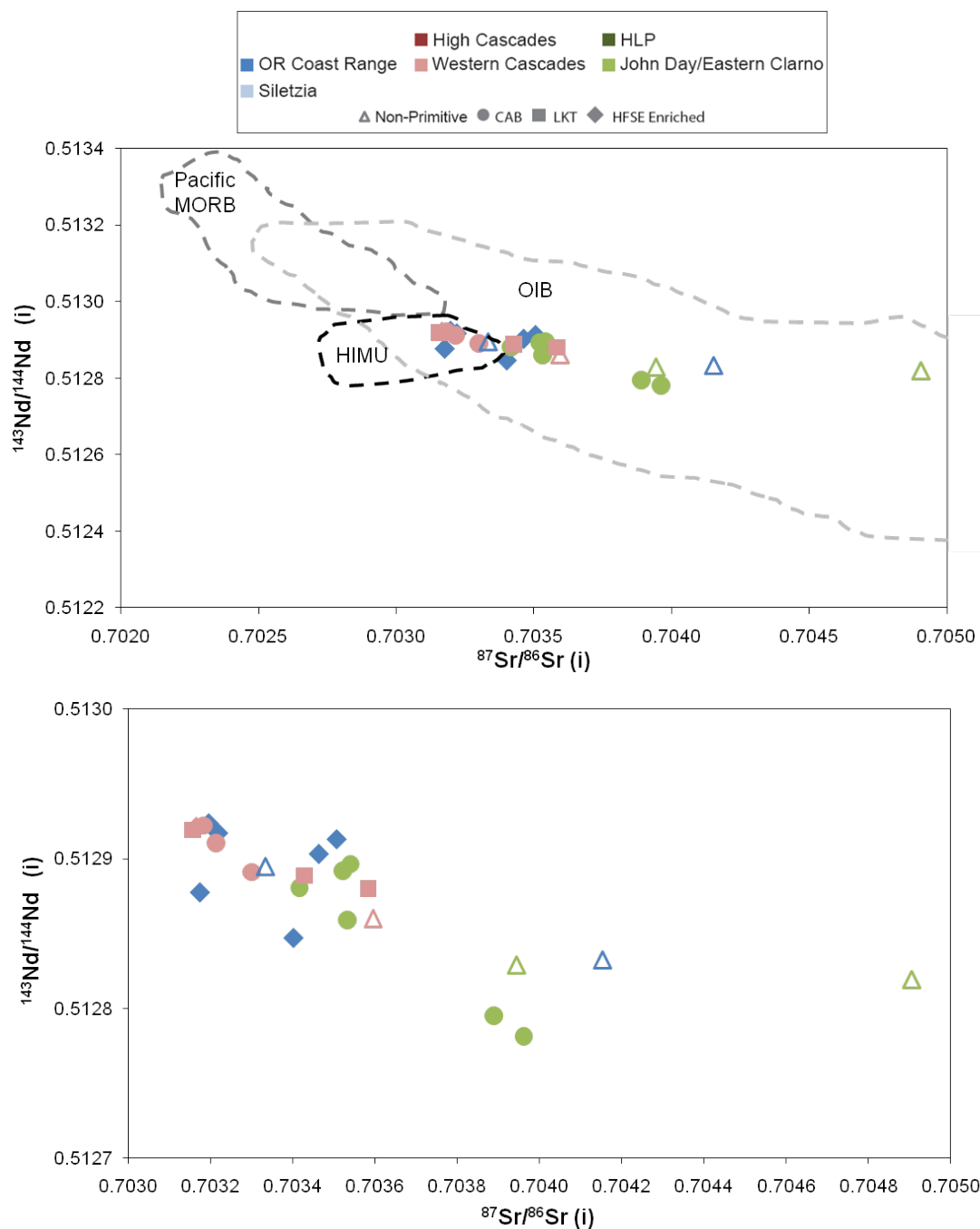


Figure 4.10: $^{143}\text{Nd}/^{144}\text{Nd}$ vs. $^{87}\text{Sr}/^{86}\text{Sr}$ for EOPC primitive magmas. A: Pacific MORB (compilation by Stracke et al., 2003), OIB (ibid.), HIMU (ibid.), and Cascadia sediment (Prytulak et al., 2006) fields shown for comparison. B: $^{143}\text{Nd}/^{144}\text{Nd}$ vs. $^{87}\text{Sr}/^{86}\text{Sr}$ for EOPC primitive magmas magnified.

Of the primitive samples, the backarc magmas are the most isotopically evolved despite appearing in major and trace element character to be among the most primitive samples from the transect. Any of the three inputs discussed in the paragraph above may explain the more evolved isotopic ratios for the backarc. The assimilation of a crustal melt would shift the isotopic character of the primitive melts to more evolved ratios but may also be apparent in the major and trace element chemistry. The addition of a subduction component may also be apparent in the trace element chemistry and would also be expected to shift isotopes to more evolved ratios, as slab fluids, sediments, or melt would carry crustal signatures. Additionally, the backarc may be influenced by the advection of distinct asthenosphere from beneath North America, thus tapping a more enriched source than is present in the arc or forearc.

Figure 4.11 supports an interpretation of the evolved isotopic signature of JD/EC primitive magmas as resulting from the addition of a subduction component. Sr concentration increases with $^{87}\text{Sr}/^{86}\text{Sr}$ as we might expect with the addition of a LILE (e.g. Sr) enriched and higher $^{87}\text{Sr}/^{86}\text{Sr}$ subduction component. In contrast, the non-primitive samples tend to have lower Sr concentrations at more evolved $^{87}\text{Sr}/^{86}\text{Sr}$. As Sr is generally less concentrated in crustal rocks and is compatible in felsic magmas, the assimilation of crustal melts may decrease the Sr content of the magma while increasing the $^{87}\text{Sr}/^{86}\text{Sr}$. So, while the non-primitive samples show evidence for crustal assimilation, the primitive backarc samples appear to acquire their higher $^{87}\text{Sr}/^{86}\text{Sr}$ from an added subduction component. This would also explain the less radiogenic $^{143}\text{Nd}/^{144}\text{Nd}$ as the subduction component can be expected to have a less radiogenic, more evolved Nd isotopic signature as well. While it appears that the backarc samples get their evolved isotopic signature from the subduction component, it is also possible that they are influenced by nearby, isotopically distinct North American lithospheric mantle. For the forearc OCR samples, data appear mostly scattered, arguing against a significant role for a subduction component in the formation of these magmas.

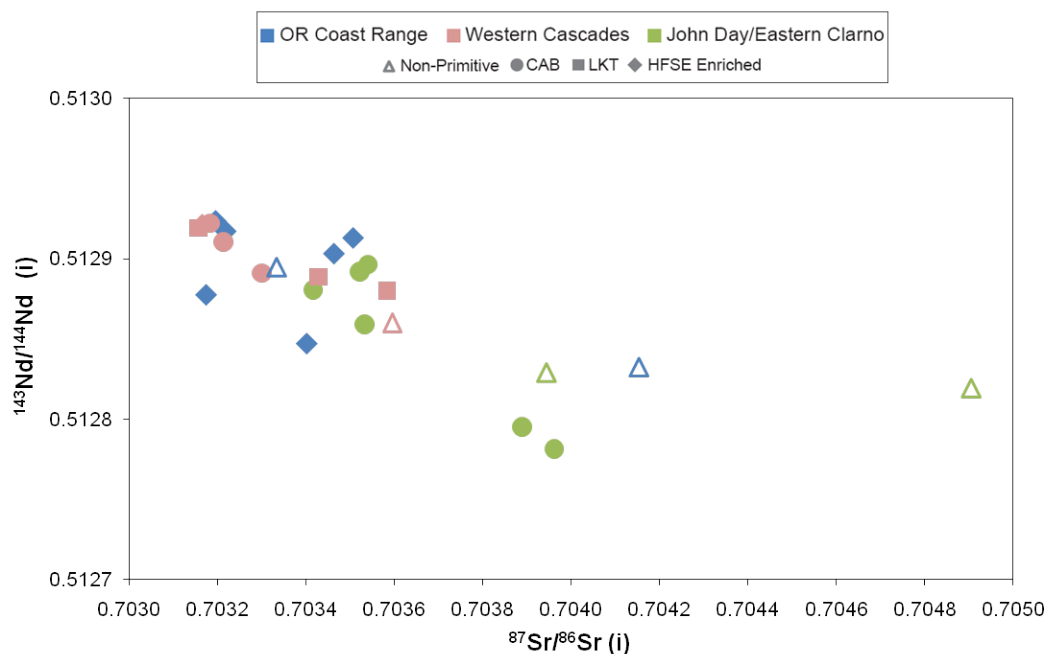


Figure 4.11: $^{87}\text{Sr}/^{86}\text{Sr}$ vs. Sr concentration for EOPC primitive magmas. Data are from this study and other sources where noted in Table 4.3.

Western Cascade arc magmas are more restricted in Sr than either the forearc or backarc but do have a general positive correlation between Sr concentration and $^{87}\text{Sr}/^{86}\text{Sr}$. However, one notable LKT sample trends toward higher $^{87}\text{Sr}/^{86}\text{Sr}$ at low Sr content. This may be a result of the isotopic heterogeneity of the source region or could indicate assimilation that is not apparent in the major or trace element chemistry of the sample. Schmidt et al. (2008) explain the range in $^{87}\text{Sr}/^{86}\text{Sr}$ for primitive LKTs as indicative of source variability. Thus the non-linearity of the WC trend does not necessarily require a crustal influence. The isotopic heterogeneity of the arc and forearc magmas is inferred to result more strongly from source characteristics while the addition of a subduction component appears to explain much of the isotopic variation in the backarc.

On a plot of $^{143}\text{Nd}/^{144}\text{Nd}$ vs. $^{206}\text{Pb}/^{204}\text{Pb}$ (Figure 4.12), the backarc samples form an array that extends toward and parallels the sub-vertical trend of the isotopic

range of Cascadia sediment, indicating that backarc magmas are a mixture between their mantle source and a subduction component. Samples from the arc generally follow the mantle array but also show an affinity for Cascadia sediment (though less pronounced) as they trend to lower $^{143}\text{Nd}/^{144}\text{Nd}$. In contrast, forearc samples have distinct $^{206}\text{Pb}/^{204}\text{Pb}$ enrichment. They plot in the OIB field in a trend that extends toward a HIMU-like component. While radiogenic Pb signatures may be interpreted as resulting from either a crustal or subduction contribution, forearc samples do not trend toward a Cascadia sediment source (Prytulak et al., 2006; Figure 4.13). Instead of extending from the mantle array toward a crustal or sediment source, the forearc samples appear to extend toward a HIMU-like component. In contrast, the arc and backarc samples extend from MORB values toward Cascadia sediment. The arc tends in general to have a lower $^{207}\text{Pb}/^{204}\text{Pb}$ at a given $^{206}\text{Pb}/^{204}\text{Pb}$ than does the backarc, perhaps suggesting a modest influence from the $^{206}\text{Pb}/^{204}\text{Pb}$ enriched component apparent in the forearc. As the Western Cascades are more proximal to this apparent forearc mantle source than are the JD/EC, some influence may be expected. One arc LKT in particular appears to be influenced by this signature. However, this is the same LKT sample with more evolved $^{87}\text{Sr}/^{86}\text{Sr}$ and $^{143}\text{Nd}/^{144}\text{Nd}$, perhaps suggesting a crustal influence.

All EOPC samples have less radiogenic $^{176}\text{Hf}/^{177}\text{Hf}$ than MORB but tend to fall along the mantle array (Figure 4.14). However, some backarc samples again demonstrate a Cascadia sediment influence, further suggesting the importance of a subduction component in their petrogenesis. While two of the forearc samples plot along the mantle array, one primitive and one non-primitive forearc sample plot at substantially lower $^{176}\text{Hf}/^{177}\text{Hf}$. These anomalous values may indicate a stronger subduction influence than is apparent in other isotope or trace element data sets. However, if $^{176}\text{Hf}/^{177}\text{Hf}$ is now plotted against $^{143}\text{Nd}/^{144}\text{Nd}$, these two forearc samples appear to plot in the HIMU field and do not trend toward the Cascadia sediment field (Figure 4.15). Therefore, the origin of these low $^{176}\text{Hf}/^{177}\text{Hf}$ values remains unconstrained, but they are considered unlikely to be the result of an otherwise

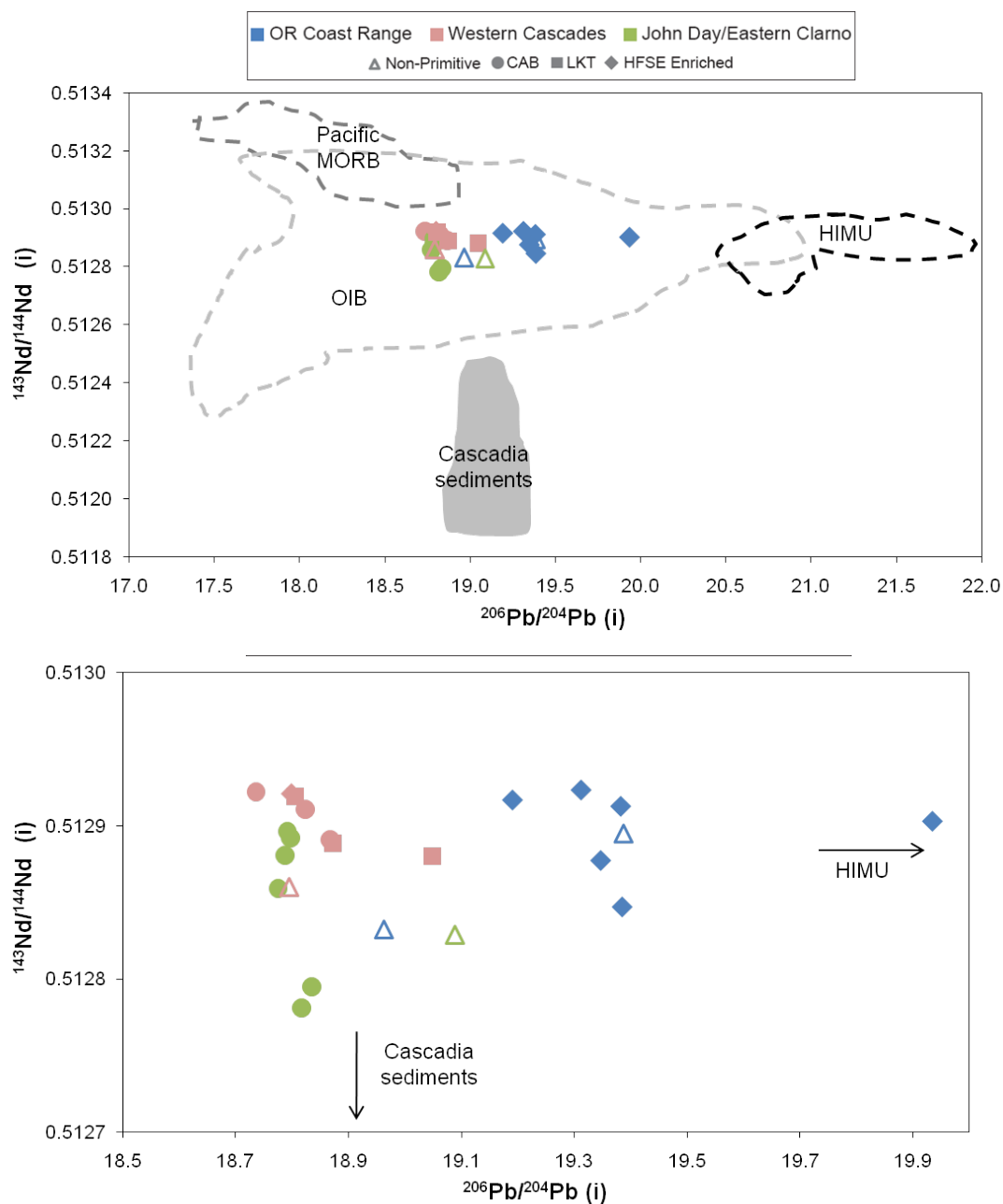


Figure 4.12: $^{143}\text{Nd}/^{144}\text{Nd}$ vs. $^{206}\text{Pb}/^{204}\text{Pb}$ for EOPC primitive magmas. A: Pacific MORB (compilation by Stracke et al., 2003), OIB (ibid.), HIMU (ibid.), and Cascadia sediment (Prytulak et al., 2006) fields shown for comparison. B: $^{143}\text{Nd}/^{144}\text{Nd}$ vs. $^{206}\text{Pb}/^{204}\text{Pb}$ for EOPC primitive magmas magnified.

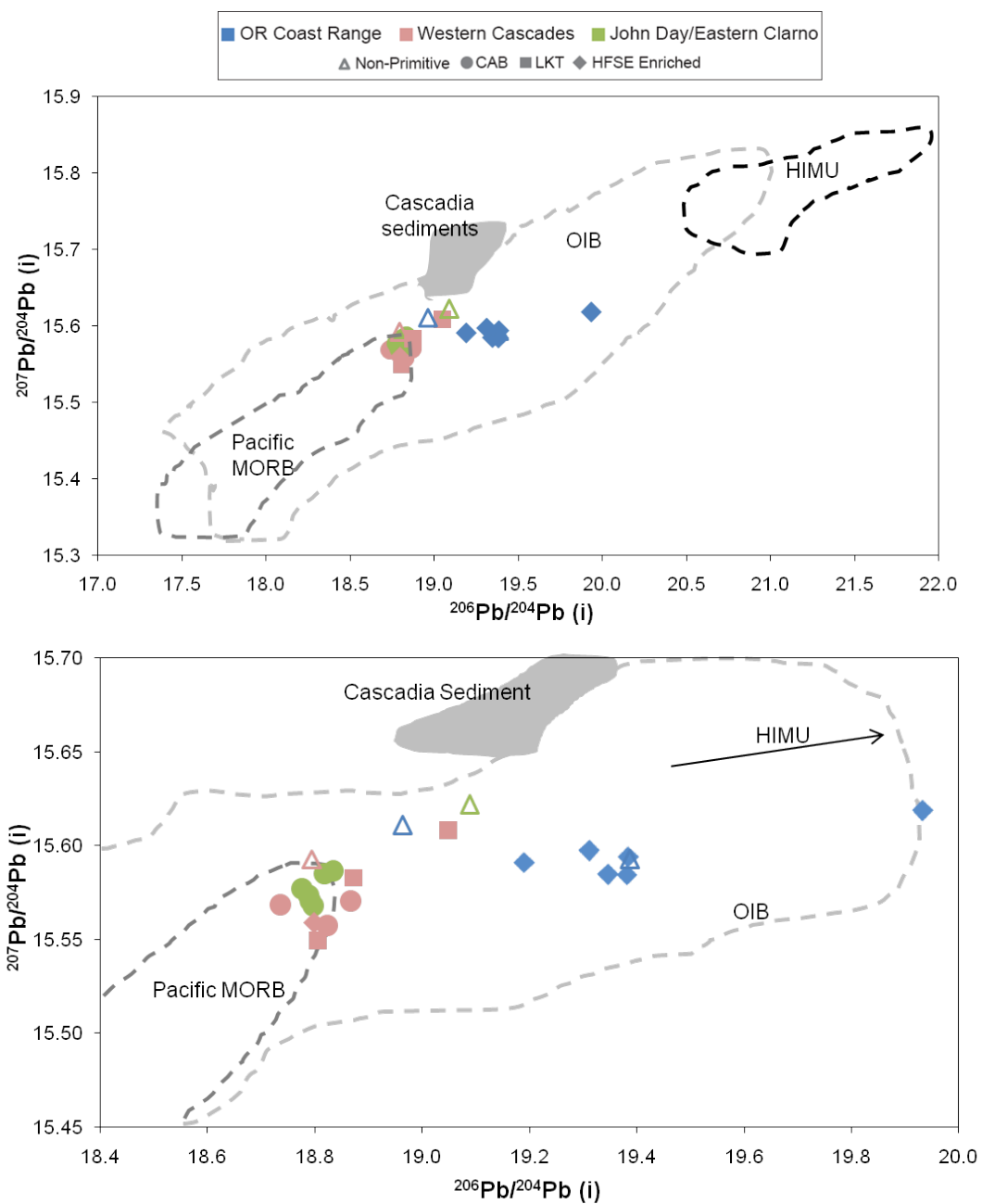


Figure 4.13: $^{207}\text{Pb}/^{204}\text{Pb}$ vs. $^{206}\text{Pb}/^{204}\text{Pb}$ for EOPC primitive magmas. A: Pacific MORB (compilation by Stracke et al., 2003), OIB (ibid.), HIMU (ibid.), and Cascadia sediment (Prytulak et al., 2006) fields shown for comparison. B: $^{207}\text{Pb}/^{204}\text{Pb}$ vs. $^{206}\text{Pb}/^{204}\text{Pb}$ for EOPC primitive magmas magnified.

obscured subduction influence. The remaining EOPC samples again fall along the mantle array and are more evolved than MORB, with the backarc magmas seemingly most strongly influenced by the sediment source.

The isotopic characterization of the EOPC agrees with major and trace element evidence suggesting distinct mantle sources across the arc that are variably influenced by subduction processes. The radiogenic isotope chemistry of the forearc samples is most notable for having a strong $^{206}\text{Pb}/^{204}\text{Pb}$ enrichment that is distinct from other EOPC magmas or from a hypothetical subduction component. Along the geographic arc, the Western Cascades appear to result from an isotopically variable mantle source that has been influenced by the addition of a subduction component. The WC may also be slightly influenced by the distinct $^{206}\text{Pb}/^{204}\text{Pb}$ enriched source of the forearc, but this effect may be exaggerated by the presence of one LKT sample that appears to have interacted with the crust. Backarc samples demonstrate the clearest subduction influence. In every plot they trend from the mantle array toward the field for Cascadia sediment and are therefore inferred to be mixes of their mantle source with subduction derived components. This observation does not rule out a paleo-enriched North American lithospheric mantle influence, but subduction input provides the most parsimonious explanation of the isotopically evolved nature of the backarc.

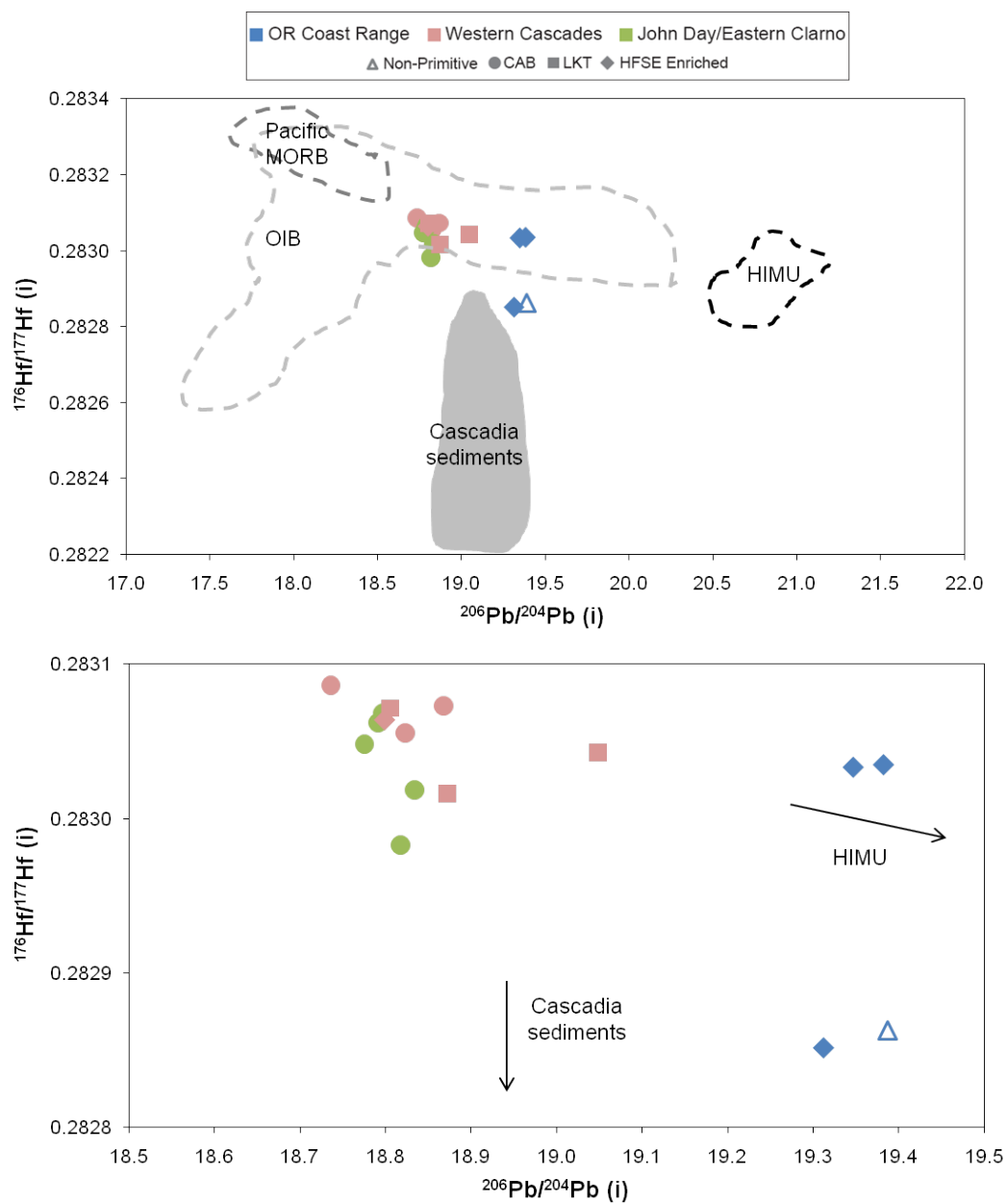


Figure 4.14: a) $^{176}\text{Hf}/^{177}\text{Hf}$ vs. $^{206}\text{Pb}/^{204}\text{Pb}$ for EOPC primitive magmas. A: Pacific MORB (compilation by Stracke et al., 2003), OIB (ibid.), HIMU (ibid.), and Cascadia sediment (Prytulak et al., 2006) fields shown for comparison. B: $^{176}\text{Hf}/^{177}\text{Hf}$ vs. $^{206}\text{Pb}/^{204}\text{Pb}$ for EOPC primitive magmas magnified.

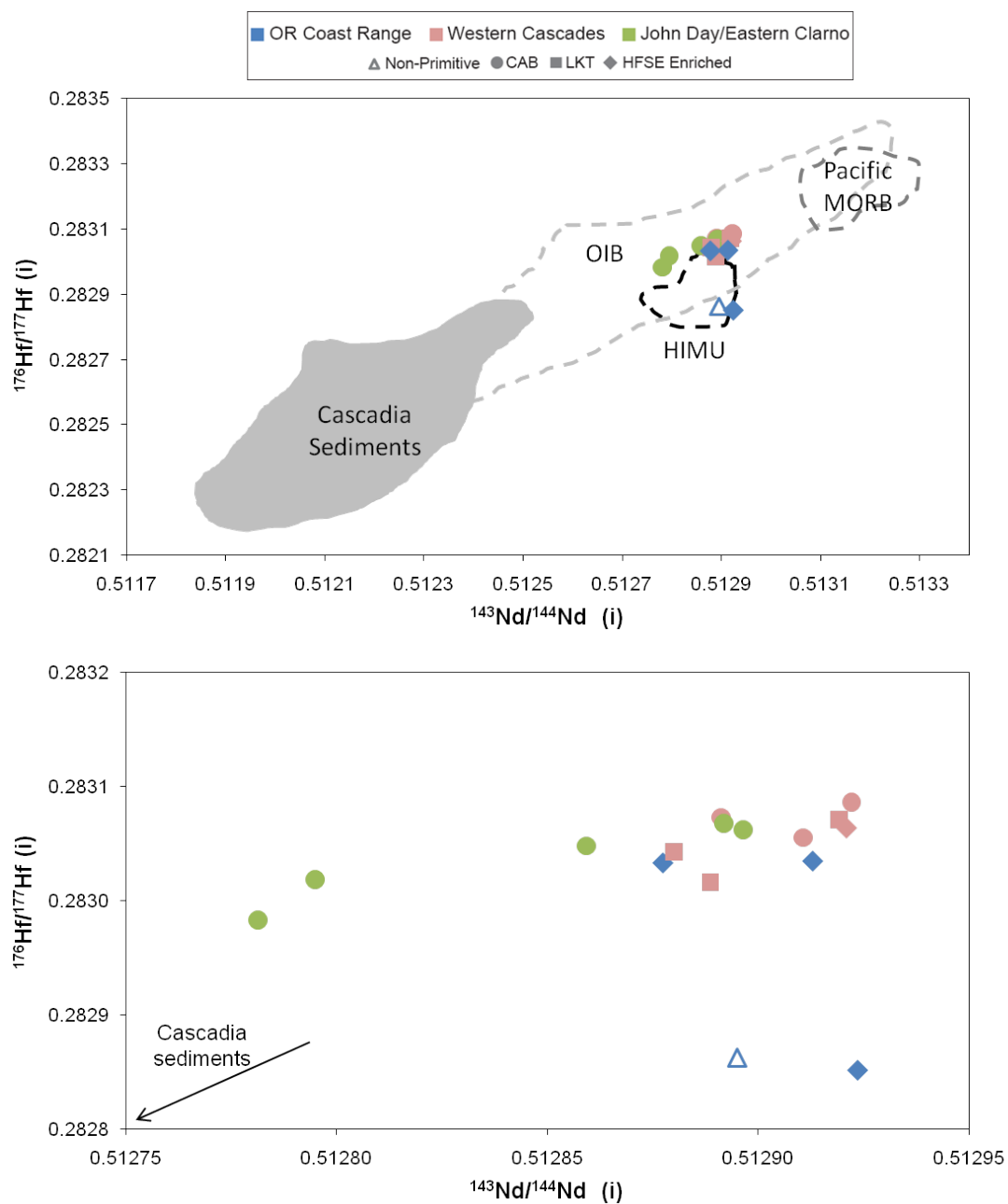


Figure 4.15: $^{176}\text{Hf}/^{177}\text{Hf}$ vs. $^{143}\text{Nd}/^{144}\text{Nd}$ for EOPC primitive magmas. A: Pacific MORB (compilation by Stracke et al., 2003), OIB (ibid.), HIMU (ibid.), and Cascadia sediment (Prytulak et al., 2006) fields shown for comparison. B: $^{176}\text{Hf}/^{177}\text{Hf}$ vs. $^{143}\text{Nd}/^{144}\text{Nd}$ for EOPC primitive magmas magnified.

4.5 Heterogeneity of the Eocene-Oligocene Proto-Cascadia Mantle

Major, trace element, and isotopic data from the Eocene-Oligocene Proto-Cascadia (EOPC) reveal a heterogeneous mantle source that was variably influenced by subduction processes. In the forearc, the HFSE-rich basalts of the Oregon Coast Range represent low degree partial melts of a relatively enriched mantle source. Evolved Sr, Nd, and Pb isotopic signatures from the Oregon Coast Range (OCR) samples further support the interpretation that they are derived from an enriched mantle source. Despite this enriched character, there is little evidence in the trace element or isotopic data to suggest that the OCR samples have been strongly influenced by either a crustal or subduction component. Their distinctive $^{206}\text{Pb}/^{204}\text{Pb}$ enrichment (as compared to $^{207}\text{Pb}/^{204}\text{Pb}$) distinguishes the forearc magmas from the arc and backarc magmas and also from the hypothetical subduction component. This feature is therefore interpreted as a characteristic of the mantle source of the forearc magmas. Borg et al. (2002) argued that an enriched Pb signature in the absence of other indicators of modern subduction influence may suggest an ancient subduction influence. Alternately, this $^{206}\text{Pb}/^{204}\text{Pb}$ enrichment may suggest that the forearc mantle has been influenced by a HIMU-like component. Such a component could be an inherited feature of exotic lithospheric mantle accreted as part of the Siletzia terrane or may be indigenous to the EOPC forearc mantle. Comparison with the Paleocene Siletzia terrane (see Section 5.1.1) will resolve the longevity of this mantle domain and inform its interpretation.

At the apparent arc axis, the Western Cascades produced CABs, LKTs, and HFSE-rich basalts that are interpreted to result from higher degrees of partial melting of a less enriched source. Trace element chemistry of HFSE-rich basalts tends to suggest a more enriched source. While the lone HFSE-rich basalt sample does not have a more evolved isotopic signature than the other WC samples, this is likely because it shows the least subduction influence (as surmised from trace element data).

While other arc samples are more heavily overprinted by the evolved signatures of the subduction component, the HFSE-rich basalt is less affected. The range in isotopic values among the LKTs suggests some source heterogeneity, consistent with a limited range of Nb/Zr if they experienced higher extents of partial melting. Fluid fluxing appears to have facilitated mantle melting beneath the Western Cascades. This influence is recorded in the LILE enrichment of the CABs and LKTs and also in the isotopic signatures of arc samples. Additionally, the mantle beneath the arc may be slightly influenced by the $^{206}\text{Pb}/^{204}\text{Pb}$ enriched source underlying the forearc. Though this effect is difficult to resolve, the WC samples appear to be slightly more variable in $^{206}\text{Pb}/^{204}\text{Pb}$ (and generally higher at a given $^{207}\text{Pb}/^{204}\text{Pb}$) than their backarc counterparts, perhaps suggesting such an influence. Comparison with the younger High Cascades where data are more complete may suggest whether there is a persistent influence from the $^{206}\text{Pb}/^{204}\text{Pb}$ enriched source. Such a comparison will also suggest the longevity of the mantle source between the Western Cascades and show whether the fluid and sediment flux has changed significantly through time.

Both trace element and isotopic data evidence a significant subduction contribution to backarc primitive magmas. It appears that the isotopic variation of the backarc may be largely controlled by the addition of the subduction component. The linearity of the $^{87}\text{Sr}/^{86}\text{Sr}$ vs. Sr concentration trend demonstrates this effect, as it suggests little initial source variability. However, as no HFSE-rich backarc basalts were selected for isotopic characterization, potential variability may be obscured in the isotopic data.

Taken together, these results demonstrate the heterogeneity of source and process across the Eocene-Oligocene arc. Apparent subduction contribution increases from geographic forearc to backarc, perhaps indicating a wider arc than is typically envisioned at the time. The distinct $^{206}\text{Pb}/^{204}\text{Pb}$ enrichment apparent in the forearc appears to wane in influence to the east, having at most a minor influence on the Western Cascade arc magmas. Despite a lower apparent subduction influence in Western Cascade magmas, they appear to result from larger degrees of partial melting.

5 –Temporal Evolution of Cascadia Mantle Reservoirs

5.1 Comparison of the Eocene-Oligocene to Older and Younger Mantle Domains

5.1.1 *Comparison with the Siletz River Volcanics*

Oxford (2006) noted that Eocene-Oligocene and younger forearc magmatism in Oregon is restricted to areas underlain by the Siletzia terrane (Figure 1.1). Drawing on this observation, Oxford (2006) hypothesized that the accreted oceanic mantle of the Siletzia terrane was a mantle source shared by the Siletz River Volcanics (SRV) and the subsequent EOPC forearc magmas. Trace element data alone can not definitively resolve a shared mantle source. New isotopic data collected on primitive EOPC forearc samples as part of this work allow for a more rigorous comparison with the SRV to test for the presence of a shared mantle source. As the Siletzia terrane is inferred to extend to beneath the Western Cascades—or possibly as far east as the axis of the High Cascades—the influence of this mantle domain may also be felt in EOPC Western Cascade lavas (Schmidt et al., 1998; Trehu et al., 1994). The following section evaluates the relationship between the mantle source of the SRV and those of primitive magmas from across the EOPC arc.

As trace element data are not available for the Siletz River Volcanics in Oregon, major and trace element data from the Crescent Basalts of Washington (also a member of the SRV) are used for comparison with EOPC (Glassley et al., 1974; Babcock et al., 1992). The SRV, like the EOPC forearc magmas, have lower MgO at a given SiO₂ than do EOPC arc or backarc magmas (Figure 5.1). As in the EOPC forearc, MgO and SiO₂ do not appear to closely vary together in the SRV magmas. While the SRV chemistry grossly mirrors that of the EOPC forearc magmas, the SRV are on average more silicic and less magnesian.

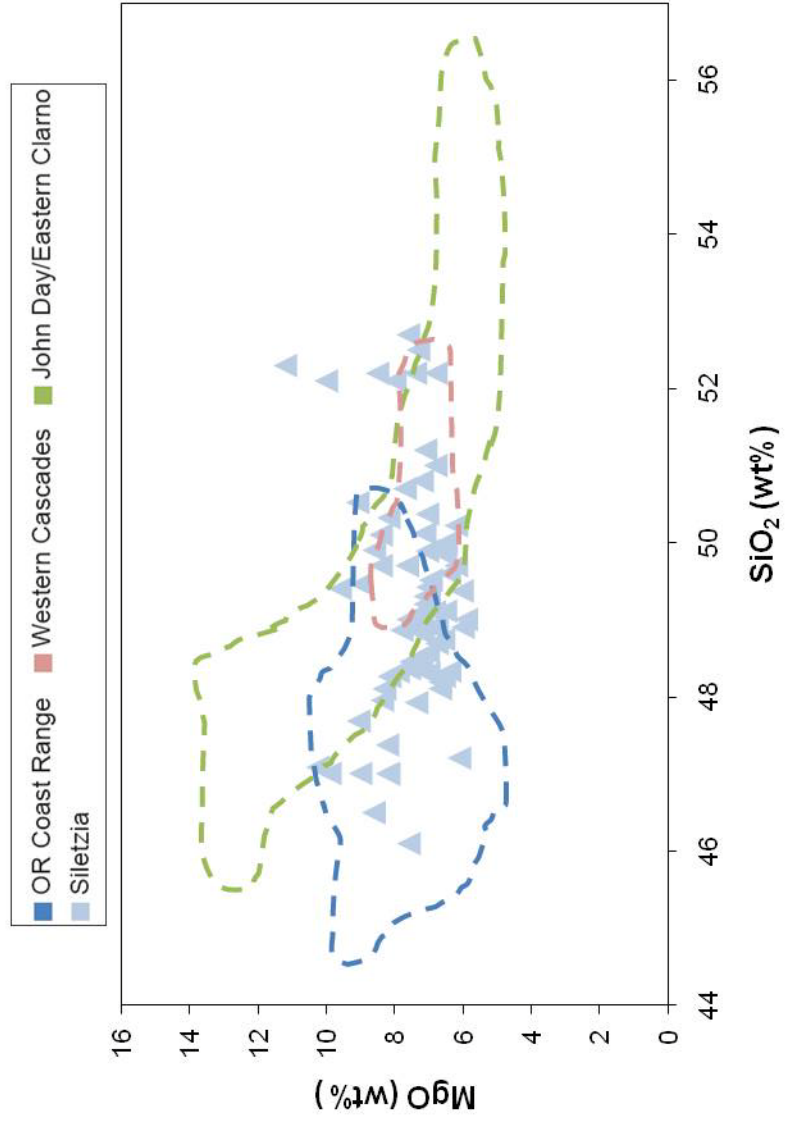


Figure 5.1: MgO vs. SiO₂ for primitive basalts from the Siletz River Volcanics. Siletzia data are from the Crescent Basalts of Washington, characterized by Glassley et al. (1974) and Babcock et al. (1992). Data from each region of the Eocene-Oligocene Proto-Cascadia arc are shown as fields for comparison.

EOPC forearc and SRV magmas have substantially different Nb/Zr, which is generally taken to indicate separate mantle sources (Figure 5.2). The lower Nb/Zr of the SRV may also be explained by higher degrees of partial melting. Zirconium is somewhat less incompatible than Nb and will thus increase relative to Nb with progressive melting. The SRV do overlap with, but are not restricted to, the Nb/Zr range of the WC arc. Both the EOPC forearc and SRV have a range of FeO*/MgO, indicating sources of variable fertility. However, the SRV range is somewhat displaced toward a more depleted source.

Unlike the EOPC forearc magmas, the SRV are not significantly enriched in the HFSE (Figure 5.3). Niobium values for the SRV are more similar to those of the EOPC arc and backarc than those of the forearc. However, the SRV also have low Ba concentrations, whereas the arc, backarc, and even forearc of the EOPC have higher Ba concentrations. The relatively low concentrations of both of these highly incompatible elements could also point to an origin from higher degrees of partial melting for the SRV.

Both the SRV and EOPC forearc magmas share low Ba/Zr values that fall below the mantle array (Figure 5.4), which suggests that their mantle sources must have either experienced leaching of fluid mobile elements or somehow been enriched in HFSE elements without attendant enrichment in LILEs. This similarity may argue for a common mantle source with differences in incompatible element ratios (e.g. Nb/Zr) explained by different degrees of partial melting. Oxford (2006) also considered variable degrees of partial melting to be a possible explanation for the discrepancies between their trace element compositions.

To test this hypothesis, La/Y was used as a proxy for degree of partial melting. Ce/Yb could not be used to investigate partial melting for the SRV, as trace element data are more limited for this suite. Oxford (2006) used La/Y to test for the presence of garnet in the source of OCR alkaline magmas and SRV magmas. He used the lower La/Y ratios of the SRV to suggest a shallower source for the SRV than for the OCR.

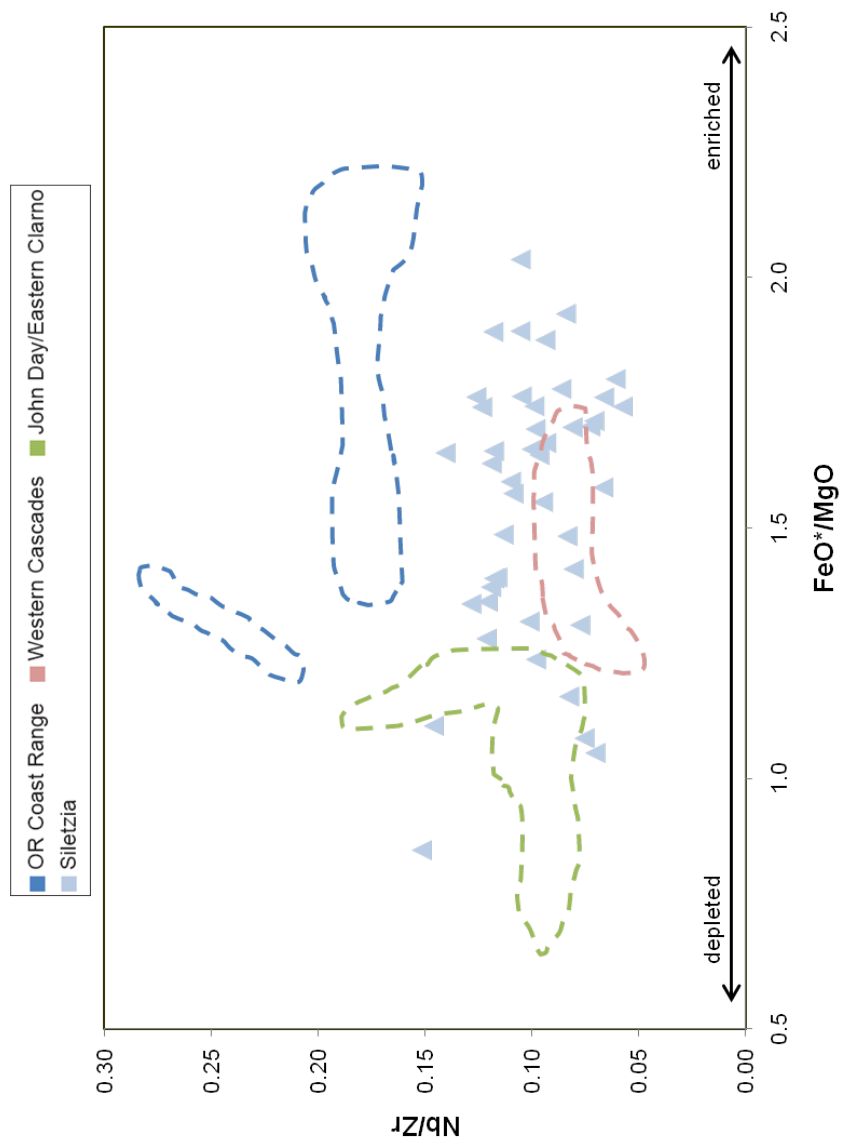


Figure 5.2: Nb/Zr vs. FeO*/MgO for primitive basalts from the Siletz River Volcanics. Siletzia data are from the Crescent Basalts of Washington, characterized by Glassley et al. (1974) and Babcock et al. (1992). Data from each region of the Eocene-Oligocene Proto-Cascadia arc are shown as fields for comparison.

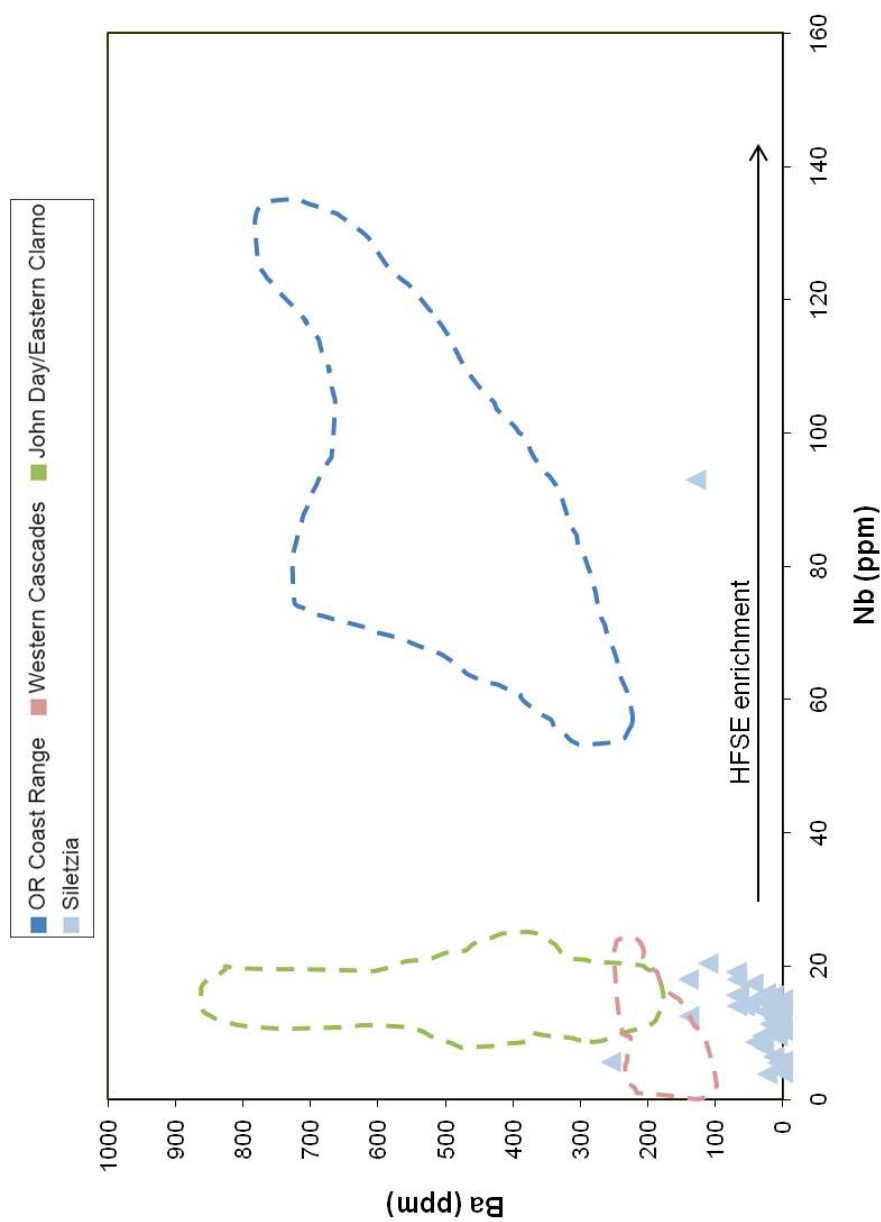


Figure 5.3: Ba vs. Nb for primitive basalts from the Siletz River Volcanics. Siletzia data are from the Crescent Basalts of Washington, characterized by Glassley et al. (1974) and Babcock et al. (1992). Data from each region of the Eocene-Oligocene Proto-Cascadia arc are shown as fields for comparison.

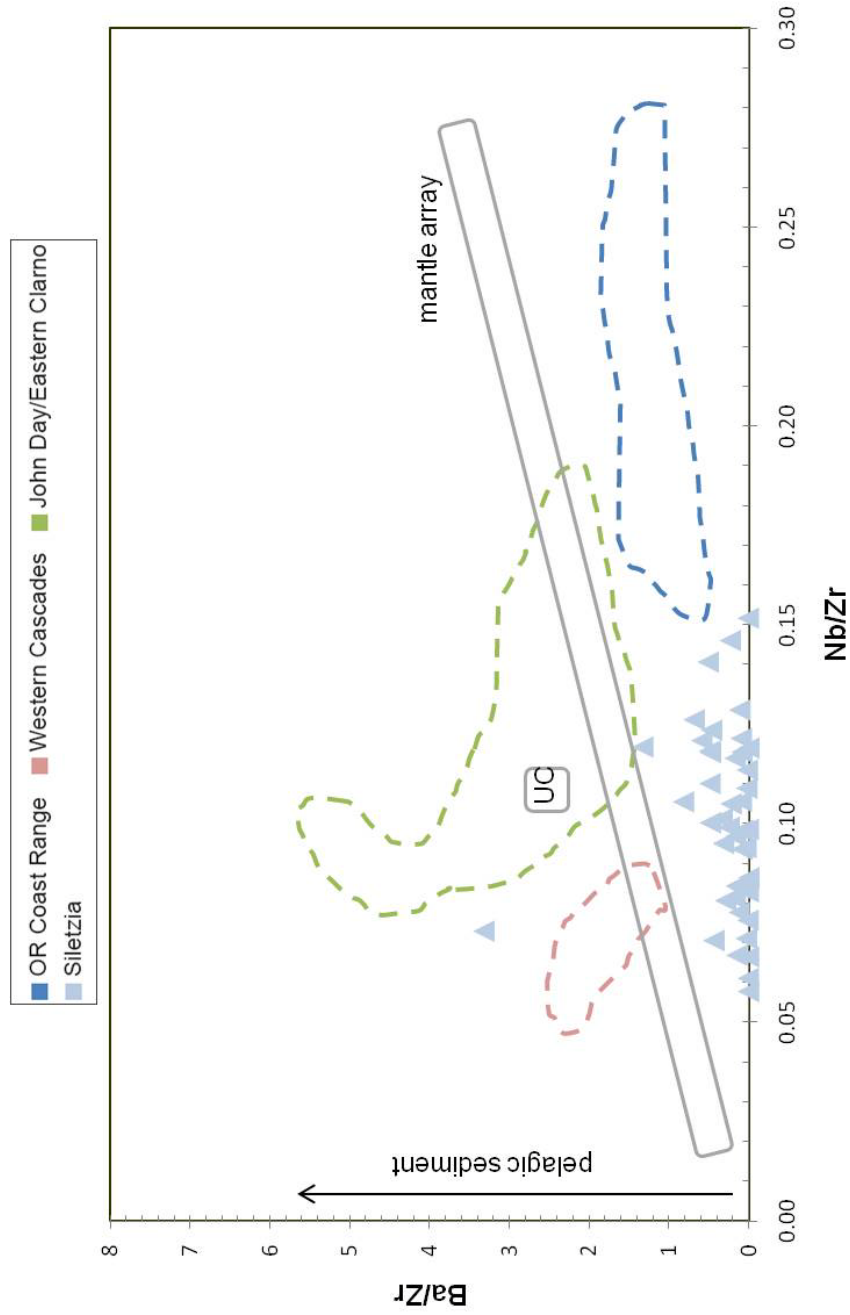


Figure 5.4: Ba/Zr vs. Nb/Zr for primitive basalts from the Siletz River Volcanics. Siletzia data are from the Crescent Basalts of Washington characterized by Glassley et al. (1974) and Babcock et al. (1992). Data from each region of the Eocene-Oligocene Proto-Cascadia arc are shown as fields for comparison. UC represents an average upper crustal composition and is reported by Taylor and McLennan, 1985. The mantle array is defined by Tristan de Cunha (Weaver et al., 1987), BHVO-1 Hawaiian tholeiite (Govindaraju, 1984), N-MORB (Le Roex et al., 1983) and the unpublished data and literature compilation of W.P. Leeman given as a field in Leeman et al., 1990). Pelagic sediment composition is from Hole et al. (1984).

However, La/Y may also be affected by partial melting. As LREEs tend to be more incompatible in basaltic liquids than HREE, progressive melting tends to lower LREE/HREE. Here Y is used as a proxy for a HREE. Garnet fractionation would be expected to deplete the melt of HREE, but the pattern is here interpreted as LREE enrichment due to low degree partial melting. The high La/Y of the EOPC forearc samples is taken to show that LREE have been enriched via low degrees of partial melting. In contrast, the comparably low La/Y in SRV magmas (Figure 5.5) suggests a greater degree of partial melting, a possibility also entertained by Oxford (2006). This conclusion suggests that the differences observed between the EOPC forearc and SRV do not rule out a shared mantle source, but that the characteristics of this source have been obscured by the effects of incompatible element decoupling at low degrees of partial melting. The notably low Ba/Zr and Ba/Ce of SRV and EOPC forearc magmas provide the strongest support for a shared source. Not only were these magmas little imprinted by subduction, they appear to show depletion relative to typical mantle values, suggesting they are likely to share a source that has been enriched in HFSE or depleted in LILE.

With the exception of one sample, the SRV are much more restricted and lower in Sr concentration than the EOPC forearc magmas (Figure 5.7). Sr isotopic ratios and Sr concentration do not show evidence for fluid flux melting as they do not increase together. The SRV do, however, have a considerable range in $^{87}\text{Sr}/^{86}\text{Sr}$ that attests to source variability largely unrelated to subduction fluxing.

The SRV share the distinctive $^{206}\text{Pb}/^{204}\text{Pb}$ enrichment of the primitive EOPC forearc magmas. Like the EOPC forearc, the SRV extend from the Nd-Pb isotopic values of evolved Pacific MORB toward a HIMU-like source (Figure 5.8). This $^{206}\text{Pb}/^{204}\text{Pb}$ enrichment signature strongly argues for a shared source as it is a feature exclusive to these forearc magmas that cannot be explained by a Cascadia sediment or fluid contribution.

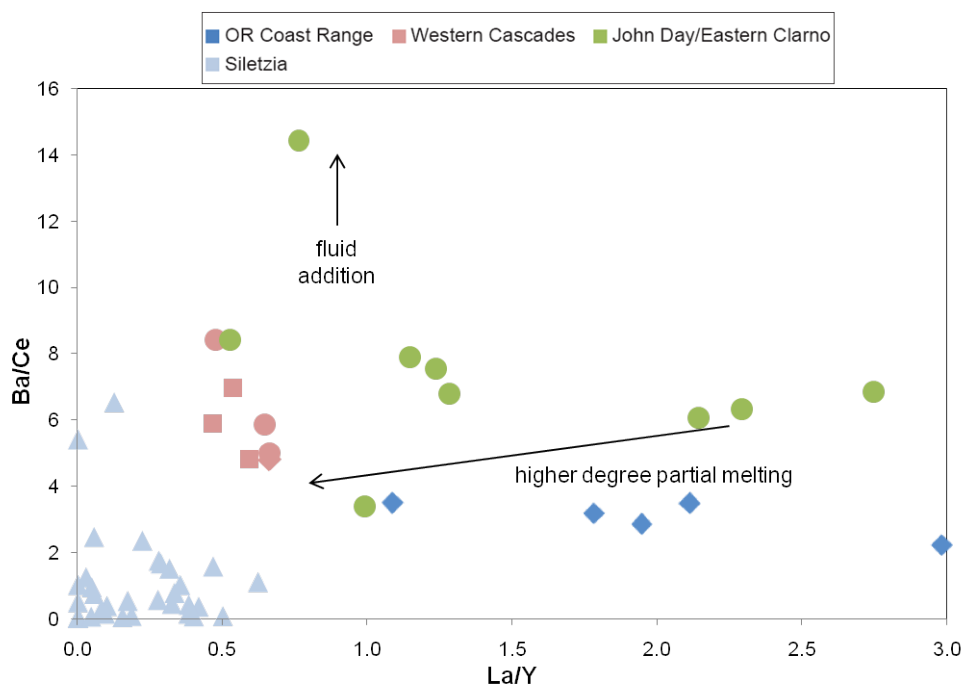


Figure 5.5: Ba/Ce vs. La/Y for primitive basalts from the Siletz River Volcanics. Siletzia data are from the Crescent Basalts of Washington, characterized by Glassley et al. (1974) and Babcock et al. (1992). Data from each region of the Eocene-Oligocene Proto-Cascadia arc are shown for comparison.

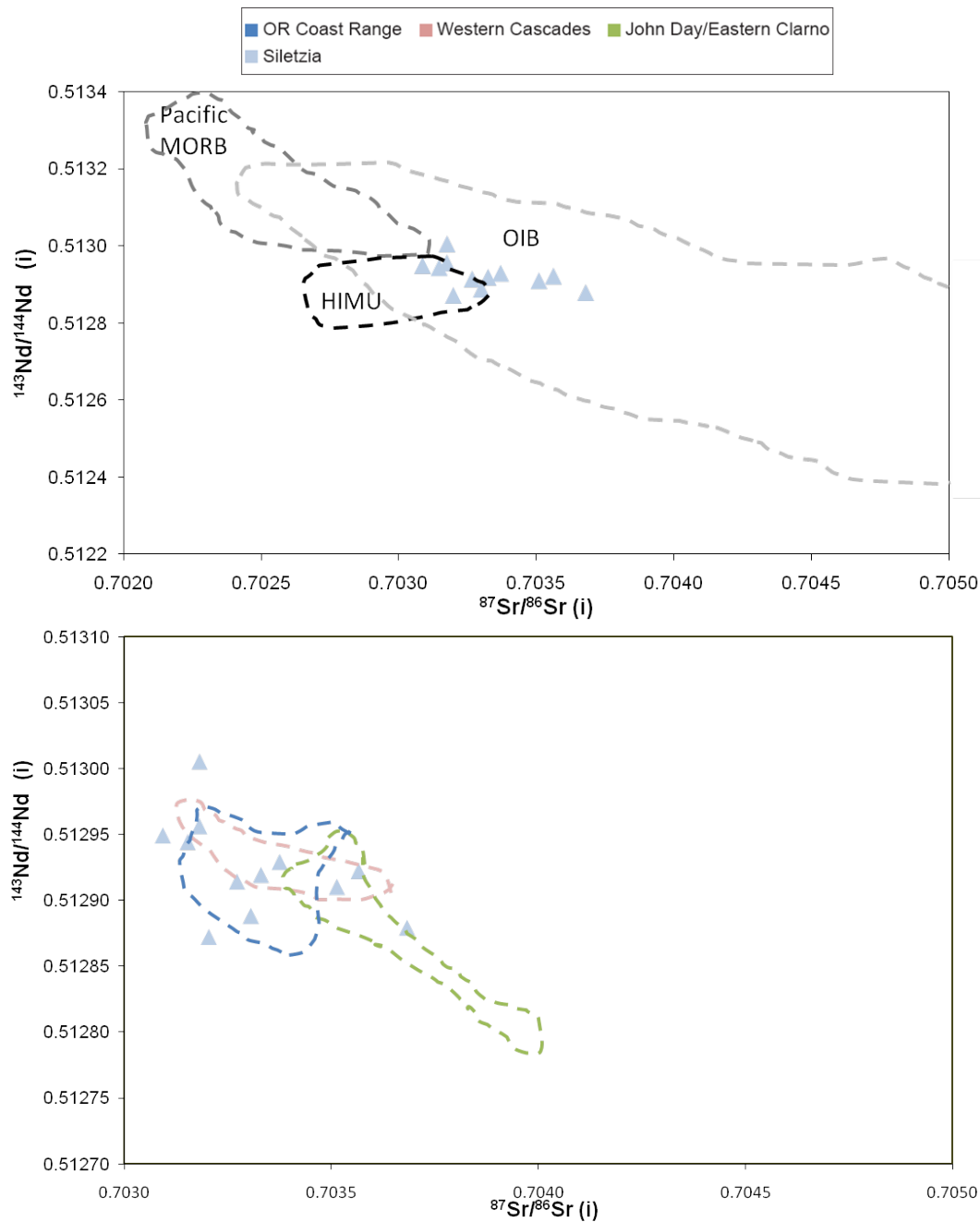


Figure 5.6: $^{143}\text{Nd}/^{144}\text{Nd}$ vs. $^{87}\text{Sr}/^{86}\text{Sr}$ for primitive magmas from the Siletz River Volcanics. Data are from Pyle et al. (2009; personal communication). A: Pacific MORB (compilation by Stracke et al., 2003), OIB (ibid.), and HIMU (ibid.) fields shown for comparison. B: $^{143}\text{Nd}/^{144}\text{Nd}$ vs. $^{87}\text{Sr}/^{86}\text{Sr}$ for EOPC primitive magmas from the Siletz River Volcanics magnified. Data from each region of the Eocene-Oligocene Proto-Cascadia arc are shown as fields for comparison.

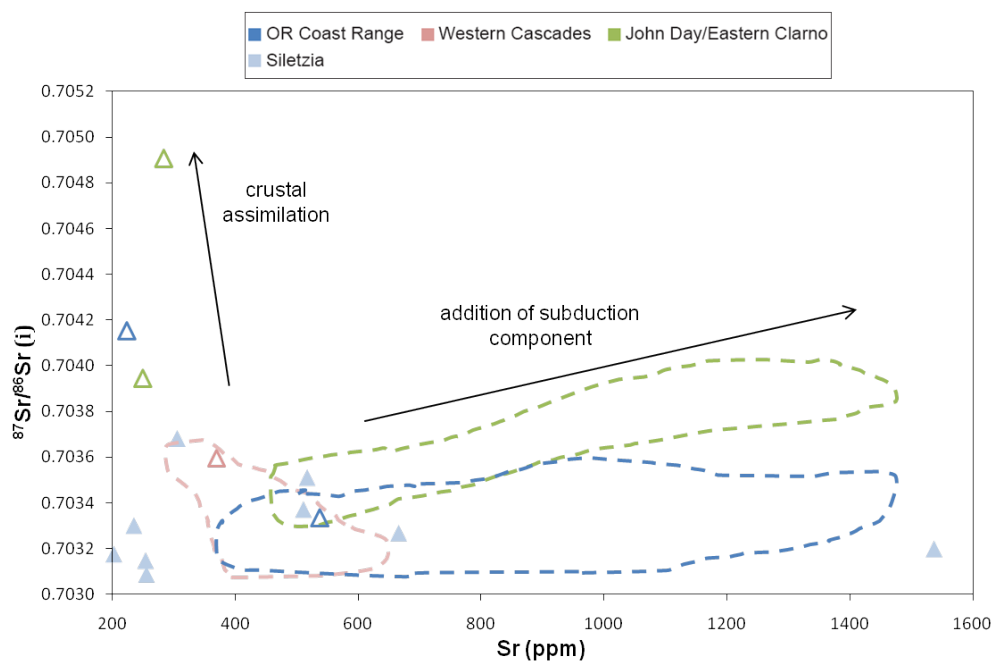


Figure 5.7: $^{87}\text{Sr}/^{86}\text{Sr}$ vs. Sr concentration for primitive magmas from the Siletz River Volcanics. Data are from Pyle et al. (2009; personal communication). Data from each region of the Eocene-Oligocene Proto-Cascadia arc are shown as fields for comparison. Non-primitive samples are shown as open symbols.

The majority of SRV samples have low $^{207}\text{Pb}/^{204}\text{Pb}$ at a given $^{206}\text{Pb}/^{204}\text{Pb}$ and do not appear to be influenced by the high $^{207}\text{Pb}/^{204}\text{Pb}$ Cascadia sediment source (Figure 5.9). However, a few samples of the SRV do have the higher $^{207}\text{Pb}/^{204}\text{Pb}$, suggesting a localized Cascadia sediment subduction influence.

The distinct $^{206}\text{Pb}/^{204}\text{Pb}$ signature of the SRV and OCR suggest a shared and persistent mantle source. The uniqueness of this mantle signature supports the hypothesis that the Siletz terrane is an accreted ocean island chain or oceanic plateau and represents a distinct mantle reservoir (Pyle et al., 1997; Duncan, 1982). The OCR and SRV share an accreted mantle source. However, the SRV appear to be larger degree partial melts of this source and show evidence that this source may have interacted with a MORB-like source and, in a few samples, show evidence for some subduction influence.

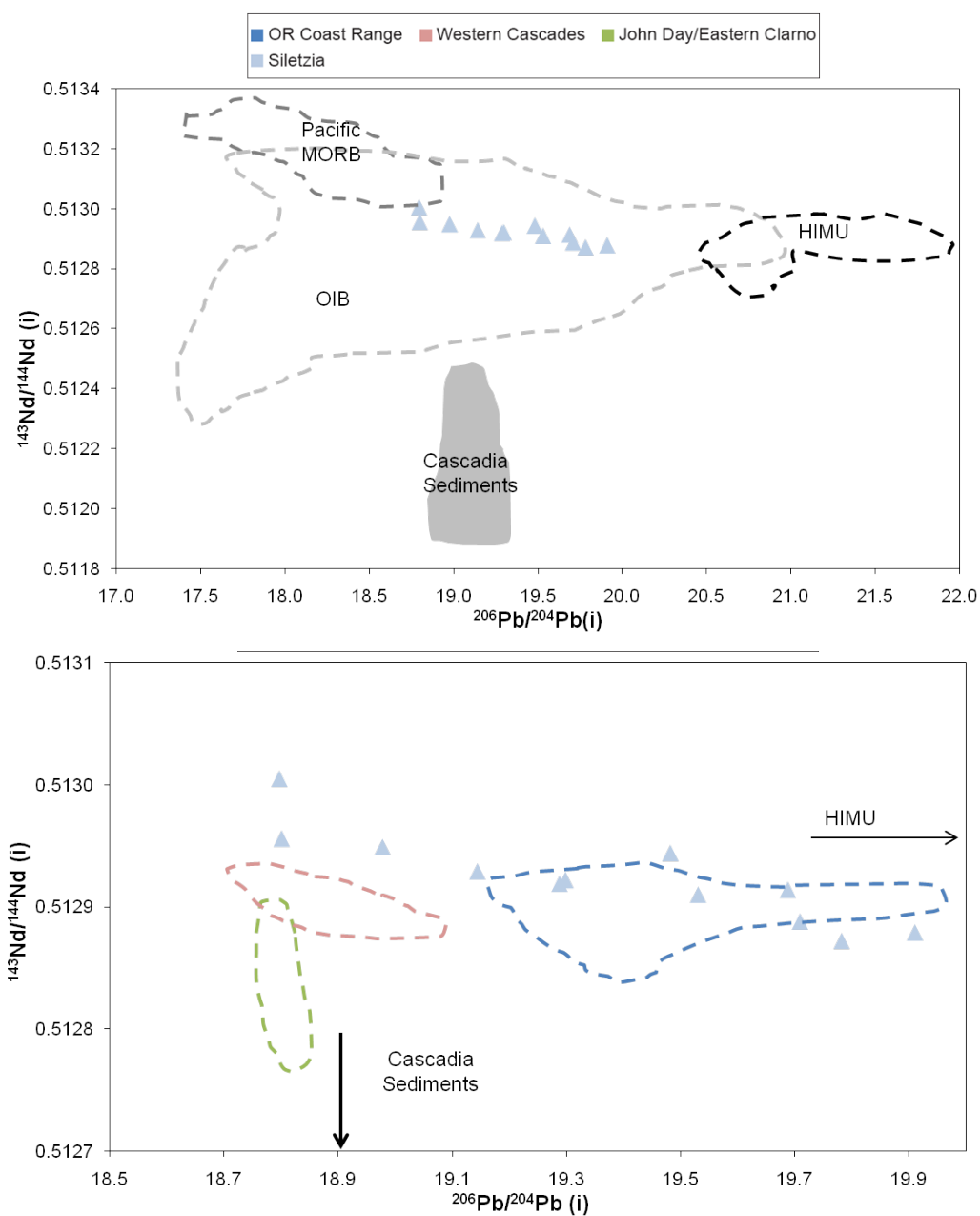


Figure 5.8: $^{143}\text{Nd}/^{144}\text{Nd}$ vs. $^{206}\text{Pb}/^{204}\text{Pb}$ for primitive magmas from the Siletz River Volcanics. Data are from Pyle et al. (2009; personal communication). A: Pacific MORB (compilation by Stracke et al., 2003), OIB (ibid.), HIMU (ibid.), and Cascadia sediment (Prytulak et al., 2006) fields shown for comparison. B: $^{143}\text{Nd}/^{144}\text{Nd}$ vs. $^{206}\text{Pb}/^{204}\text{Pb}$ for primitive magmas from the Siletz River Volcanics magnified. Data from the EOPC are shown as fields for comparison.

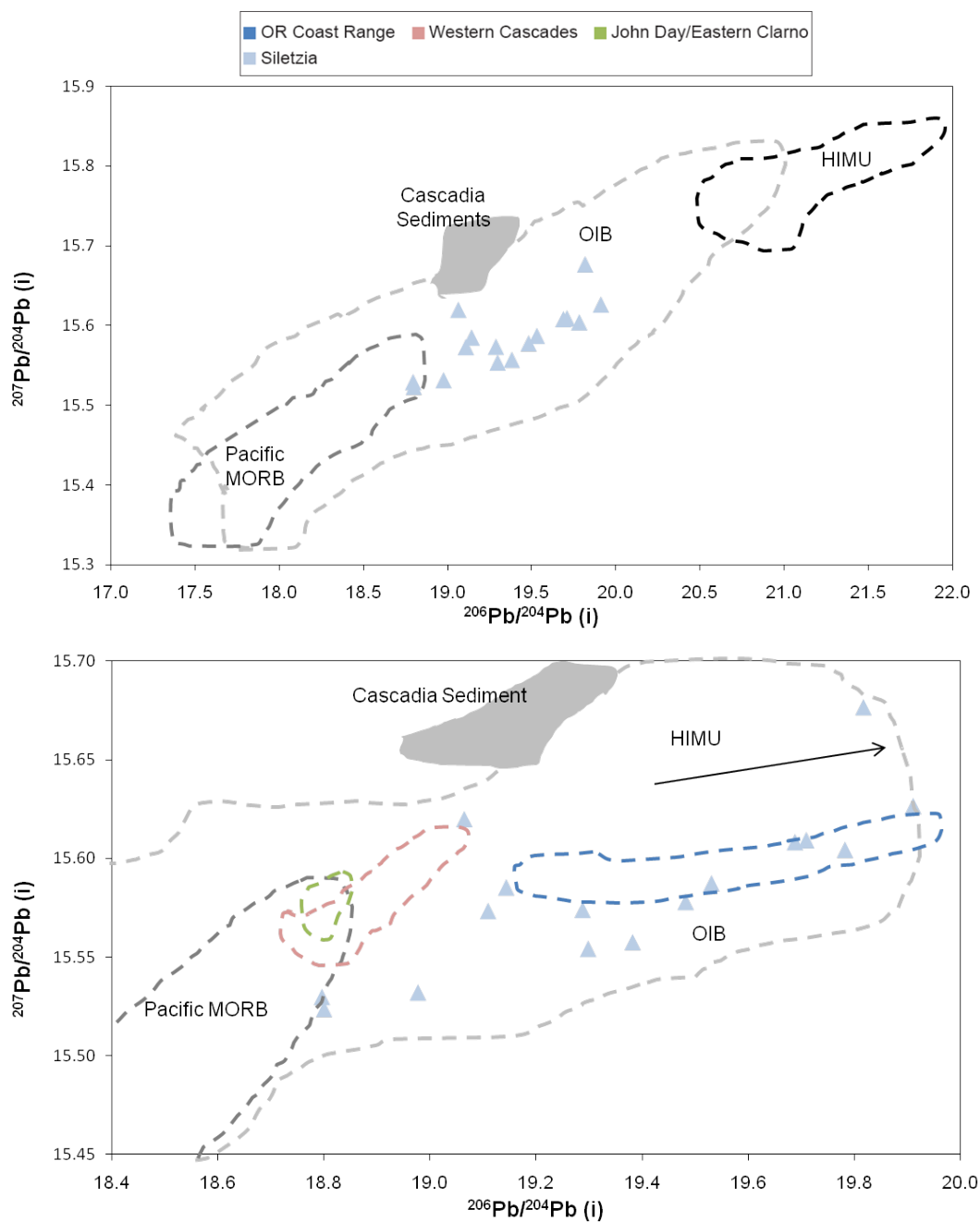


Figure 5.9: $^{207}\text{Pb}/^{204}\text{Pb}$ vs. $^{206}\text{Pb}/^{204}\text{Pb}$ for primitive magmas from the Siletz River Volcanics. Data are from Pyle et al. (2009; personal communication). A: Pacific MORB (compilation by Stracke et al., 2003), OIB (ibid.), HIMU (ibid.), and Cascadia sediment (Prytulak et al., 2006) fields shown for comparison. B: $^{143}\text{Nd}/^{144}\text{Nd}$ vs. $^{206}\text{Pb}/^{204}\text{Pb}$ for primitive magmas from the Siletz River Volcanics magnified. Data from the EOPC are shown as fields for comparison.

5.1.2 *Comparison with the High Cascades*

As a whole, the High Cascades extend to more primitive compositions than the Western Cascades and are more diverse (Figure 5.10). The HFSE-rich basalts of the High Cascades have lower MgO at a given SiO₂, extend to lower SiO₂ than other recent HLP and High Cascades basalt types, and form a relatively flat trend with respect to MgO vs. SiO₂. These characteristics are shared with the OCR and SRV (Figure 5.10). The LKTs and HFSE-rich basalts appear to have two distinct mantle sources, as indicated by their disparate ranges in Nb/Zr (Figure 5.11). Though this separation could also result from differing degrees of partial melting, a finding of discrete mantle sources for the LKTs and HFSE-rich basalts agrees with the findings of Schmidt et al. (2008) and others (e.g. Leeman et al., 2005). No Zr data are available for the primitive CABs of the Central or Columbia segments of the High Cascades, so they cannot be evaluated in comparison. The HFSE-rich basalts of the High Cascades are again similar to the Eocene-Oligocene Proto-Cascadia (EOPC) forearc with respect to Nb/Zr while the LKTs have Nb/Zr values typical of the WC.

The High Cascades tend to have relatively enriched sources, as evidenced by high FeO*/MgO. However, LKTs of the High Cascades tend to be lower in both Ba and Nb than the Western Cascades, suggesting either a higher degree of partial melting or a more depleted source (Figure 5.12). Schmidt et al. (2008) argue for a subduction modified depleted source for High Cascades LKTs that would account for their lower concentrations of incompatible elements. In contrast, CABs and HFSE-rich basalts of the High Cascades have high incompatible element concentrations consistent with a fertile source. CABs from the High Cascades are higher in Ba and Nb and extend past the Western Cascades in Ba concentration. The High Cascades HFSE-rich basalts are high in Nb and extend toward the OCR trend.

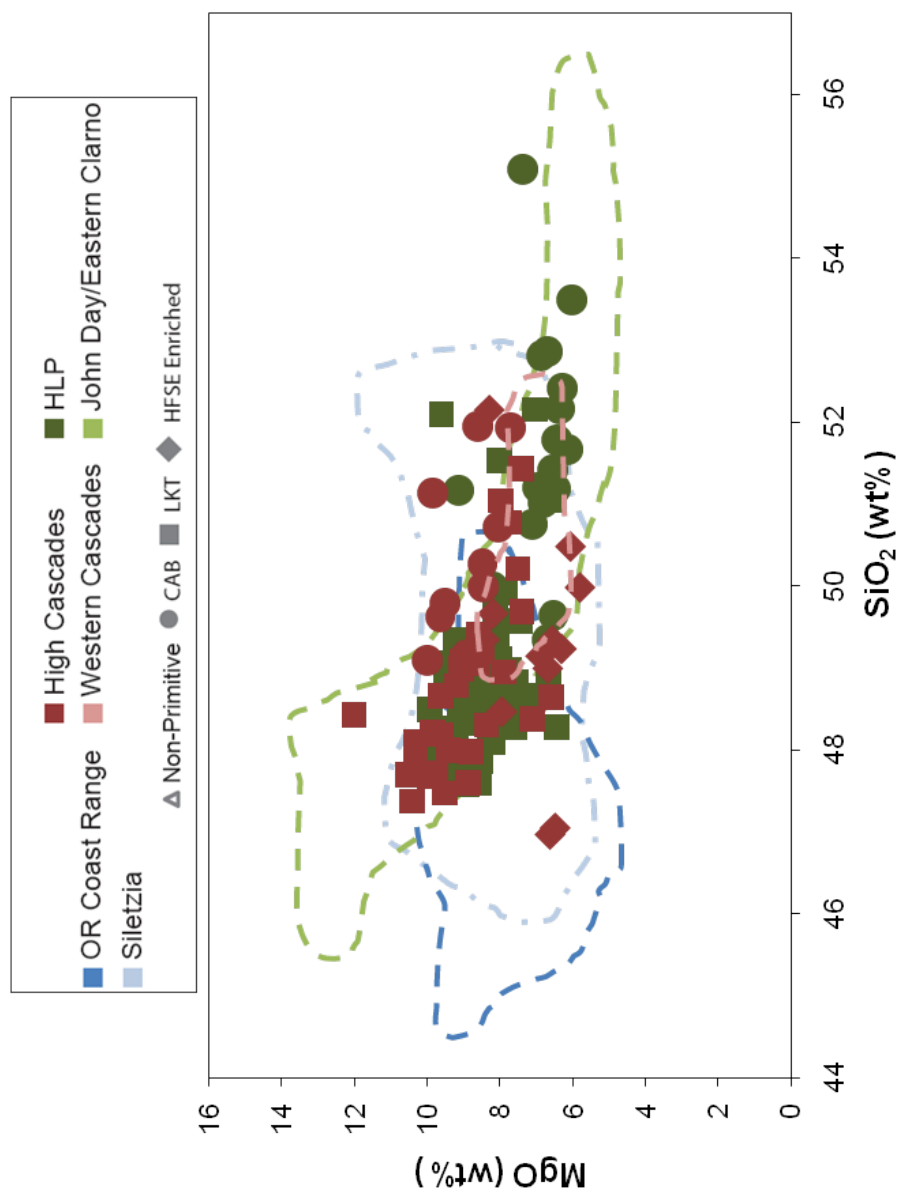


Figure 5.10: MgO vs. SiO₂ for primitive basalts from the High Cascades and High Lava Plains. High Cascades data are from the compilation of Schmidt et al. (2008). High Lava Plains data are from Jordan (2001). Data from Siletzia and each region of the Eocene-Oligocene Proto-Cascadia arc are shown as fields for comparison.

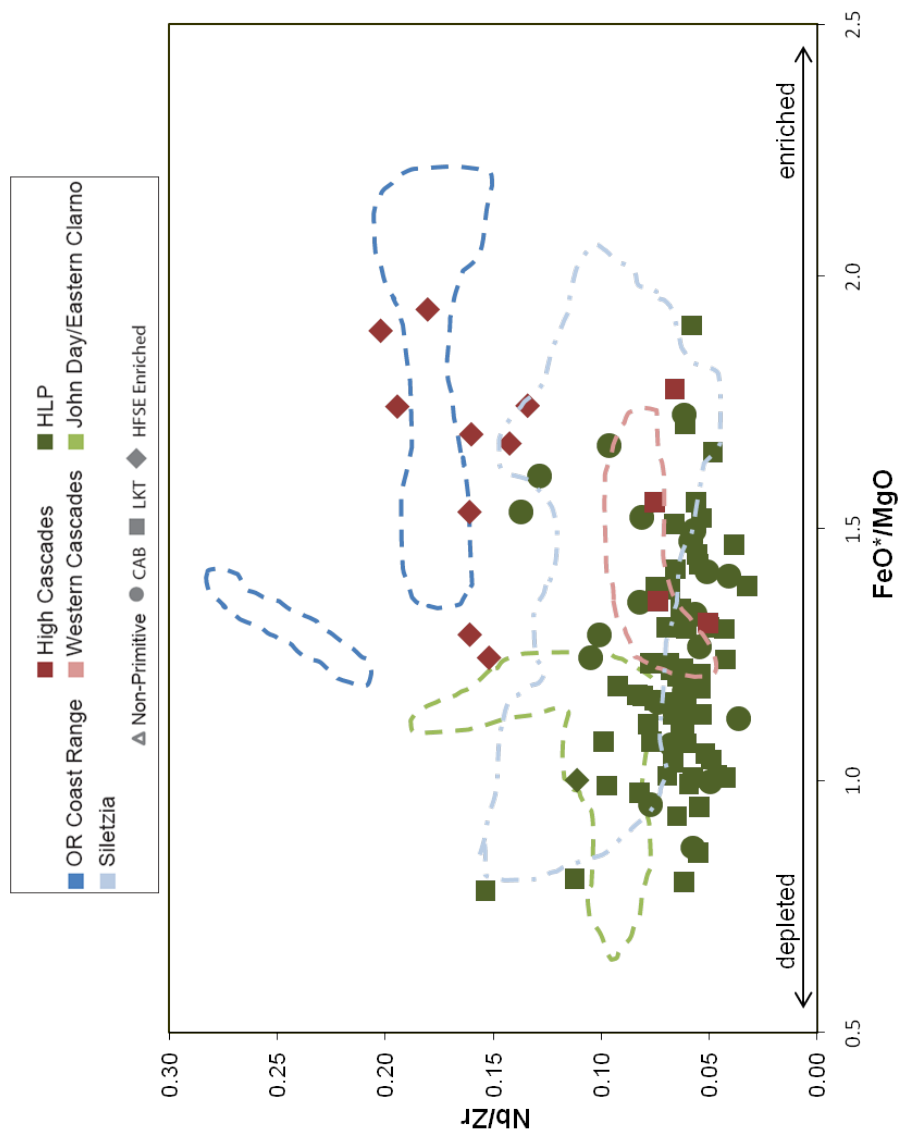


Figure 5.11: Nb/Zr vs. FeO*/MgO for primitive basalts from MgO vs. SiO₂ for primitive basalts from the High Cascades and High Lava Plains. High Cascades data are from the compilation of Schmidt et al. (2008). High Lava Plains data are from Jordan (2001). Data from Siletzia and each region of the Eocene-Oligocene Proto-Cascadia arc are shown as fields for comparison.

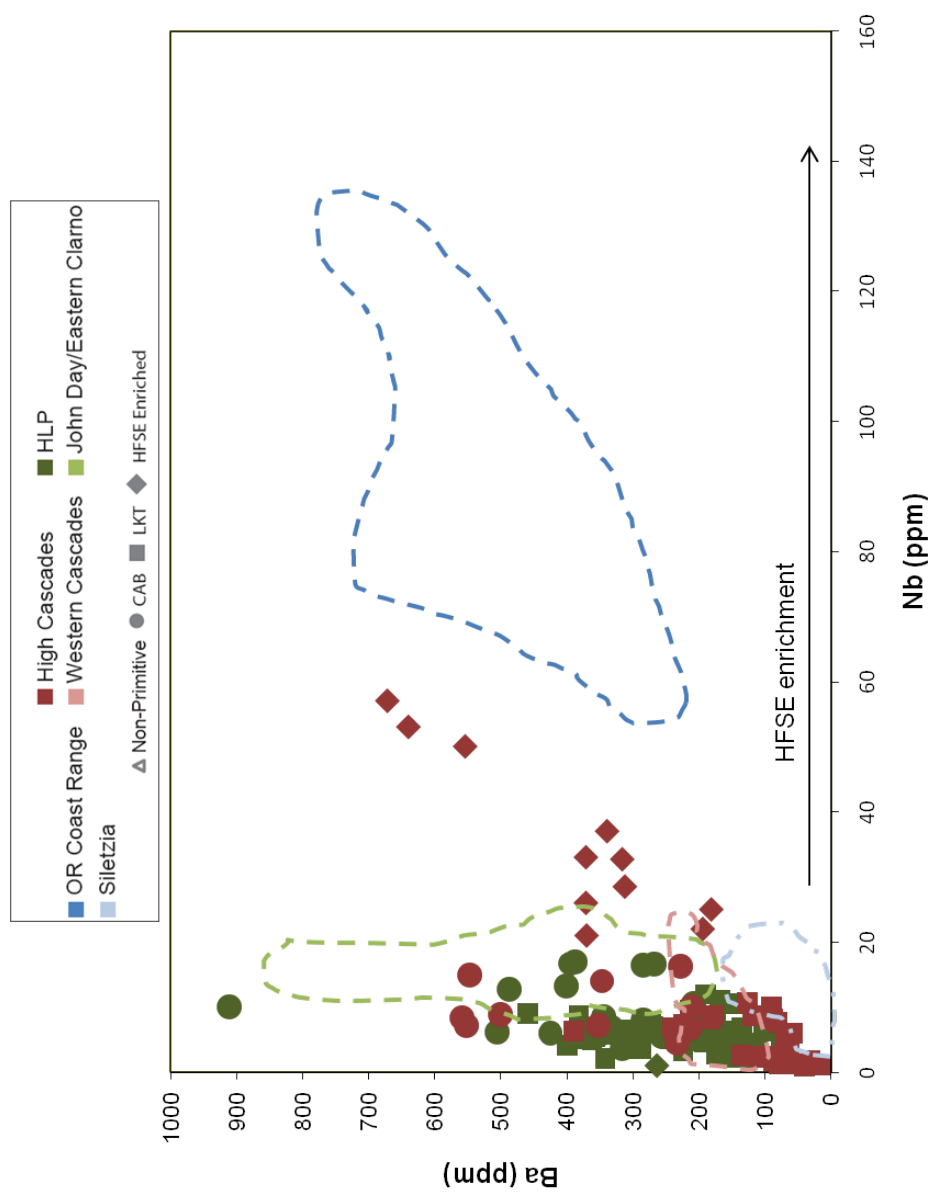


Figure 5.12: Ba vs. Nb for primitive basalts from the High Cascades and High Lava Plains. High Cascades data are from the compilation of Schmidt et al. (2008). High Lava Plains data are from Jordan (2001). Data from Siletzia and each region of the Eocene-Oligocene Proto-Cascadia arc are shown as fields for comparison.

LKTs from the High Cascades fall along the Ba/Zr-Nb/Zr mantle array, suggesting that they are mantle melts with little subduction fluid or sediment addition (Figure 5.13). No CABs from the High Cascades are shown on this figure, but they would be expected to extend toward values of sediment, as they demonstrate greater subduction influence. HFSE-rich basalts from the High Cascades mostly plot below the mantle array, like the OCR and SRV. This may suggest that they share a LILE-depleted/HFSE-enriched mantle source with the OCR and SRV.

The High Cascades CABs and HFSE-rich basalts are lower degree partial melts (higher Ce/Yb) than the LKTs from the High Cascades (Figure 5.14). High Cascades HFSE-rich basalts appear to have more fluid involvement (elevated Ba/Ce) and higher degrees of partial melting (lower Ce/Yb, La/Y) than the EOPC forearc magmas (Figures 5.14, 5.15). The Western Cascades appear to represent lower degree partial melts than most LKTs, but higher than most HFSE and CABs from the High Cascades. The High Cascades HFSE enriched basalts share a number of trace element characteristics with the EOPC forearc and SRV magmas and appear to represent an intermediate degree of partial melting between the two.

LKTs and HFSE-rich basalts of the High Cascades tend to be more primitive, while the CABs are more evolved, likely from a subduction component. The HFSE-rich basalts of the High Cascades have a wider, less linear spread of $^{87}\text{Sr}/^{86}\text{Sr}$ vs. $^{143}\text{Nd}/^{144}\text{Nd}$ that mimics that of the OCR and SRV, and like the SRV, some plot within the HIMU field (Figure 5.16). The High Cascades are much more isotopically diverse than the WC as well as in major and trace element chemistry. While the LKTs of the High Cascades appear similar to the WC in trace element space, the steep trend of LKTs is different than that of the WC and suggests a different source. The High Cascades CABs mostly form a trend with a positive slope of $^{87}\text{Sr}/^{86}\text{Sr}$ vs. Sr, suggesting an important role for fluid flux melting (Figure 5.17). The LKTs of th

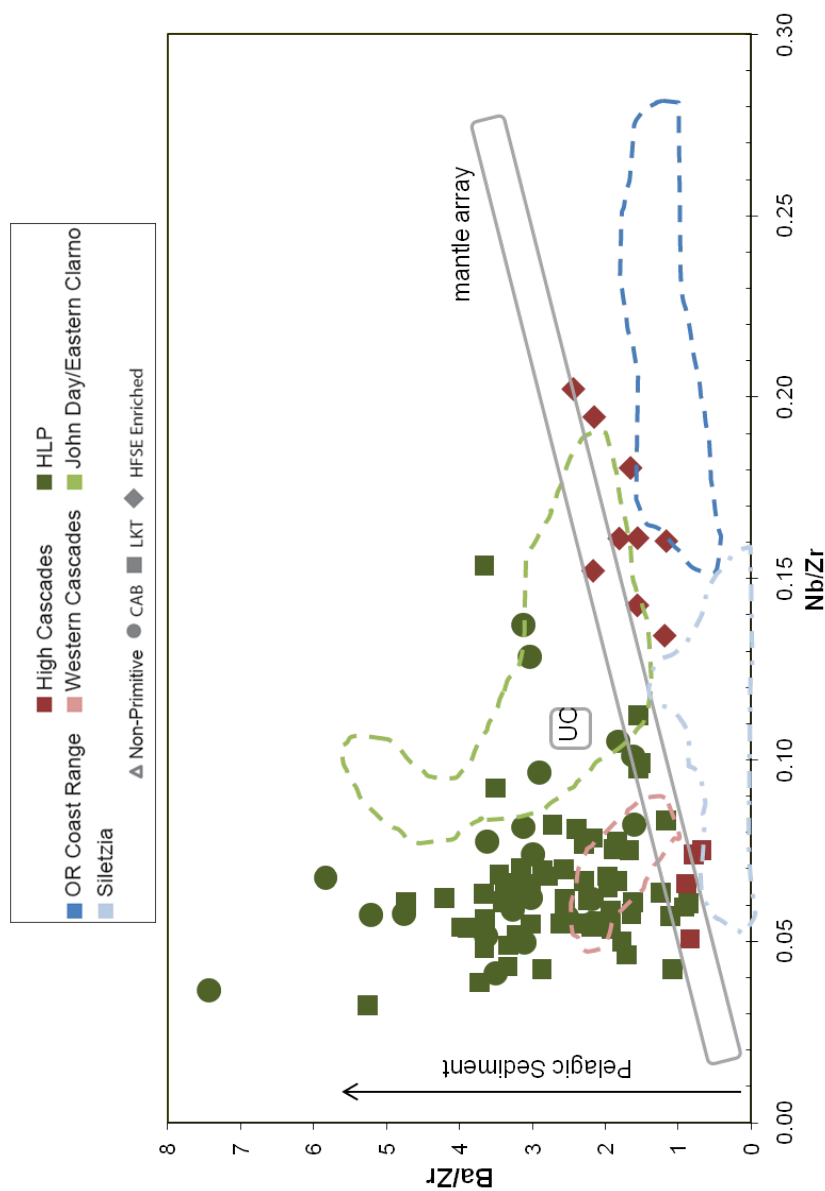


Figure 5.13: Ba/Zr vs. Nb/Zr for the High Cascades and High Lava Plains. High Cascades data are from the compilation of Schmidt et al. (2008). High Lava Plains data are from Jordan (2001). Data from Siletzia and each region of the Eocene-Oligocene Proto-Cascadia arc are shown as fields for comparison. UC represents an average upper crustal composition and is reported by Taylor and McLennan, 1985. The mantle array is defined by Tristan de Cunha (Weaver et al., 1987), BHVO-1 Hawaiian tholeiite (Govindaraju, 1984), N-MORB (Le Roex et al., 1983) and the unpublished data and literature compilation of W.P. Leeman given as a field in Leeman et al., 1990). Pelagic sediment composition is from Hole et al. (1984).

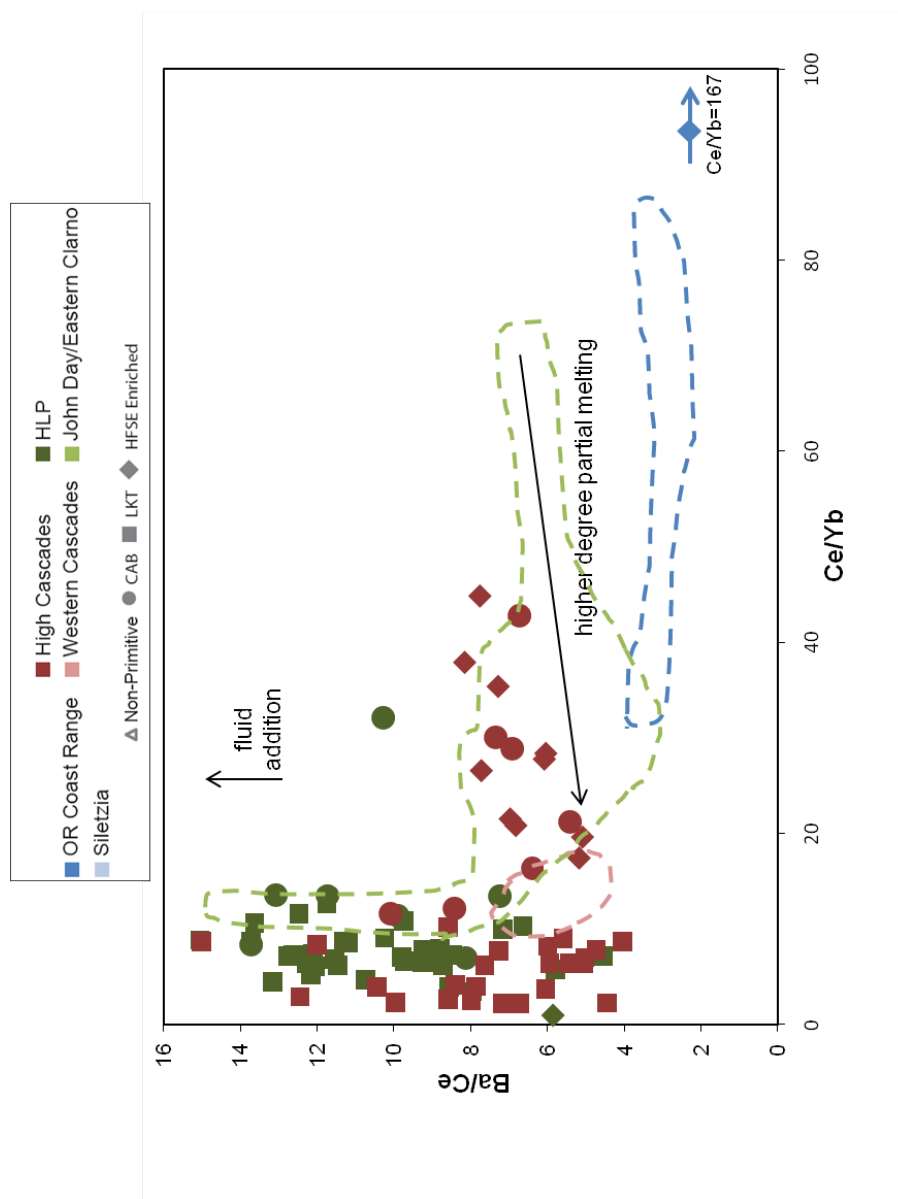


Figure 5.14: Ba/Ce vs. La/Y for primitive basalts from the High Cascades and High Lava Plains. High Cascades data are from the compilation of Schmidt et al. (2008). High Lava Plains data are from Jordan (2001). Data from each region of the Eocene-Oligocene Proto-Cascadia arc are shown as fields for comparison.

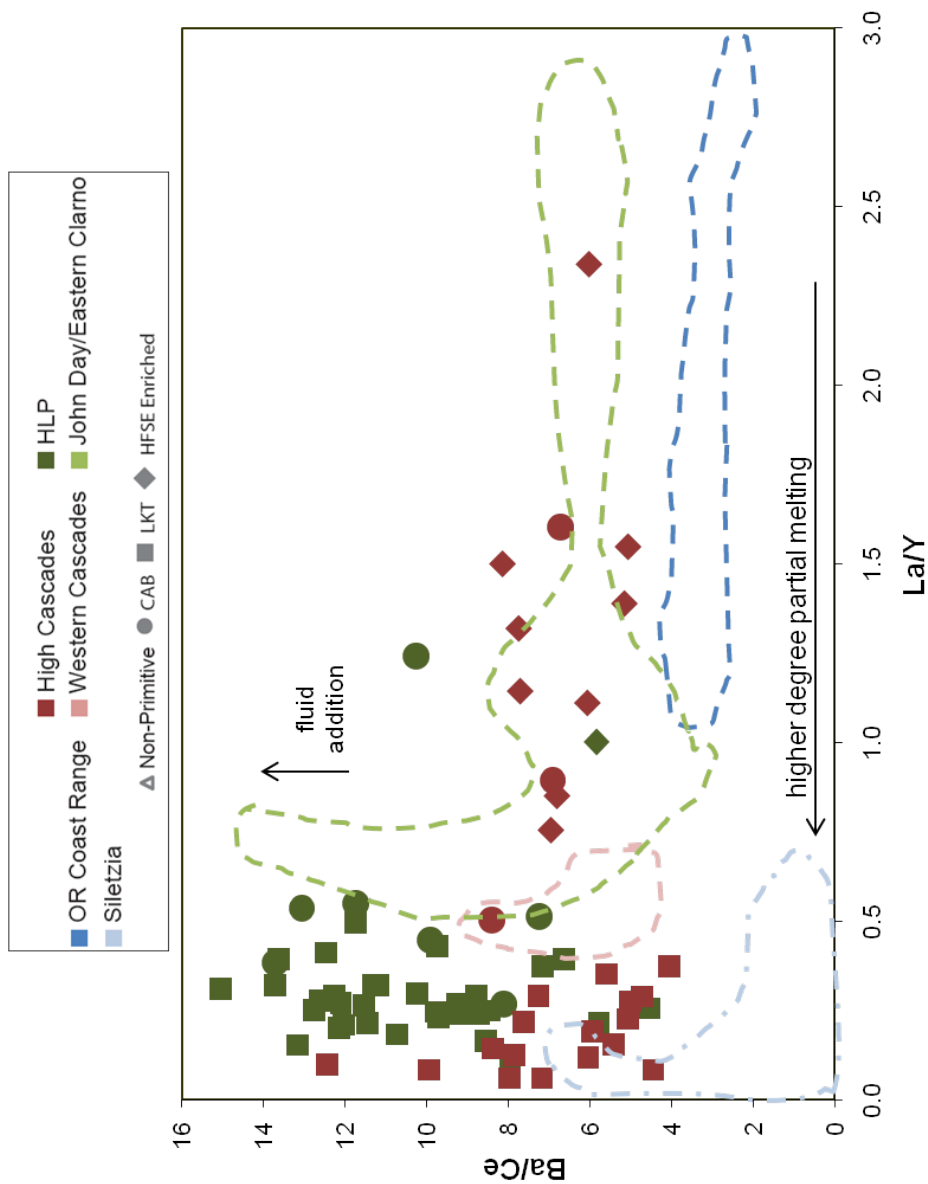
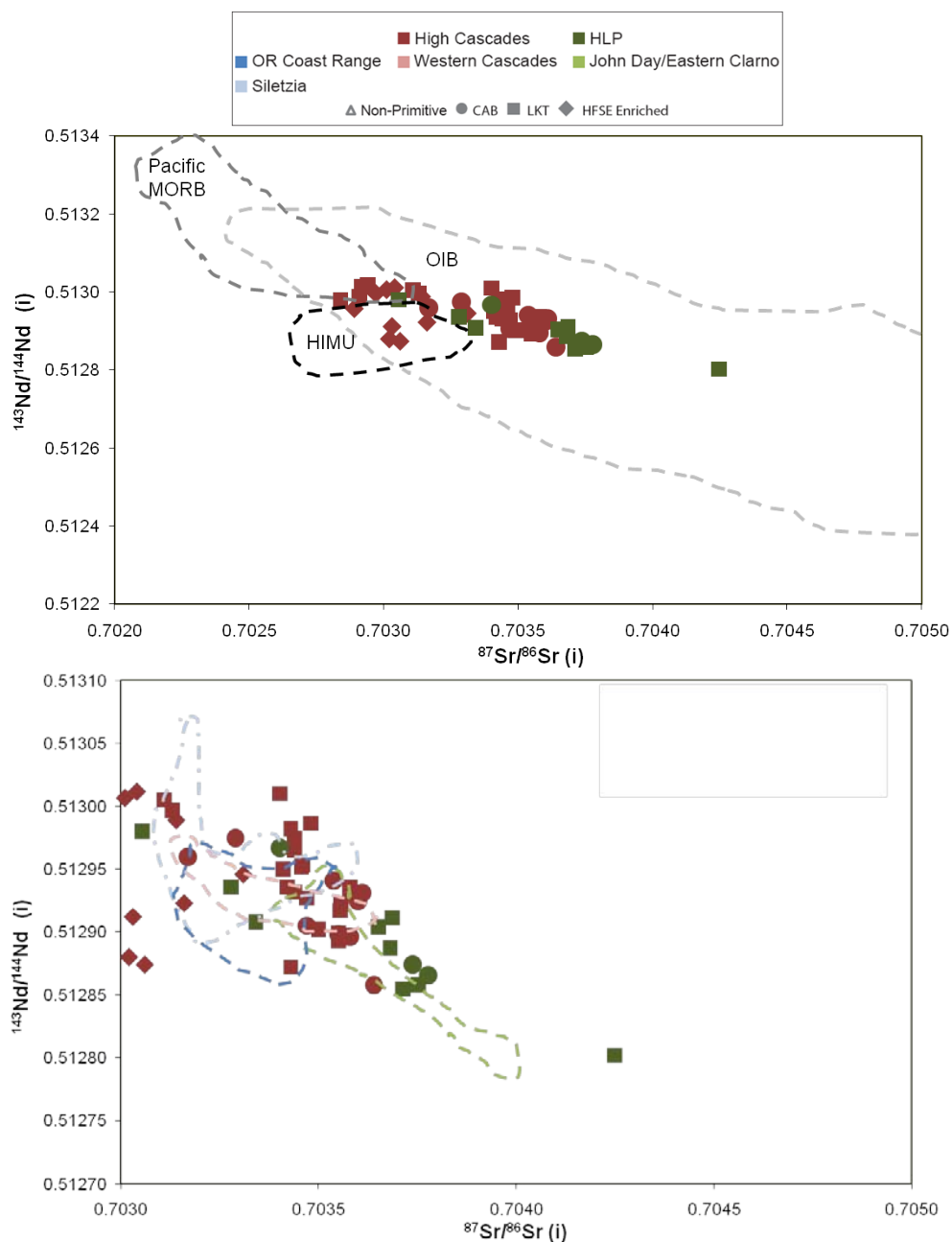


Figure 5.15: Ba/Ce vs. Ce/Yb for primitive basalts from the High Cascades and High Lava Plains. High Cascades data are from the compilation of Schmidt et al. (2008). High Lava Plains data are from Jordan (2001). Data from Siletzia and each region of the Eocene-Oligocene Proto-Cascadia arc are shown as fields for comparison.



5.16: $^{143}\text{Nd}/^{144}\text{Nd}$ vs. $^{87}\text{Sr}/^{86}\text{Sr}$ for primitive magmas from the High Cascades and High Lava Plains. High Cascades data are from the compilation of Schmidt et al. (2008). High Lava Plains data are from Jordan (2001). A: Pacific MORB (compilation by Stracke et al., 2003), OIB (ibid.), and HIMU (ibid.) fields shown for comparison. B: Data from Siletzia and each region of the Eocene-Oligocene Proto-Cascadia arc are shown as fields for comparison.

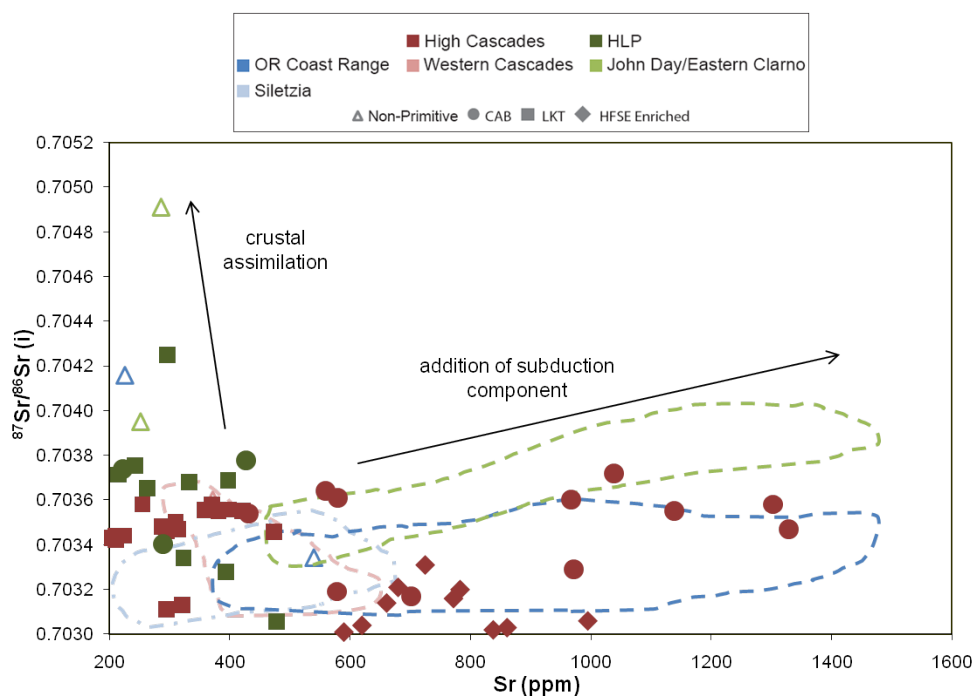


Figure 5.17: $^{87}\text{Sr}/^{86}\text{Sr}$ vs. Sr concentration for primitive magmas from the High Cascades and High Lava Plains. High Cascades data are from the compilation of Schmidt et al. (2008). High Lava Plains data are from Jordan (2001). Data from Siletzia and each region of the Eocene-Oligocene Proto-Cascadia arc are shown as fields for comparison. Non-primitive samples are shown as open symbols.

High Cascades tend to have lower Sr (suggesting a lower flux) and variable $^{87}\text{Sr}/^{86}\text{Sr}$ in a range that is similar to the Western Cascades, suggesting source variability. The High Cascades appear to be more strongly influenced by subduction than do the Western Cascades, as evidenced by the relationship between $^{87}\text{Sr}/^{86}\text{Sr}$ and Sr. The HFSE-rich High Cascades also have higher Sr. Some fall along a positive slope suggesting a fluid influence, but others do not. The CABs and most LKTs of the High Cascades appear to be influenced by the high $^{207}\text{Pb}/^{204}\text{Pb}$ signature of the Cascadia sediments (Figure 5.18). Some HFSE-rich basalts and some LKTs show high $^{206}\text{Pb}/^{204}\text{Pb}$, suggesting an affinity with EOPC forearc and SRV.

In $^{207}\text{Pb}/^{204}\text{Pb}$ vs. $^{206}\text{Pb}/^{204}\text{Pb}$ space, High Cascade samples trend from MORB toward a Cascadia sediment source (Figure 5.19). They are roughly similar to the WC, but are pulled more strongly toward sediments, having a higher $^{207}\text{Pb}/^{204}\text{Pb}$ at a given $^{206}\text{Pb}/^{204}\text{Pb}$. The High Cascades again appear more variable here with values ranging from true Pacific MORB well toward sediment. A few High Cascades seem influenced by the high $^{206}\text{Pb}/^{204}\text{Pb}$ Siletzia mantle source, but the sediment seems to be a bigger effect, even for the HFSE-rich basalts.

Although the Columbia Embayment is inferred to extend beneath the High Cascades arc, the Siletzia influence appears to be absent in nearly all samples from the High Cascades. Many HFSE basalts from the High Cascades share trace element characteristics with Siletzia and the EOPC forearc, but, with the exception of a single sample, they lack the distinctive $^{206}\text{Pb}/^{204}\text{Pb}$ enrichment. The HFSE enriched basalts of the High Cascades may result from similar processes as those forming HFSE enriched basalts of the EOPC forearc and Siletzia, but they do not share a mantle source.

Furthermore, the Western Cascades and High Cascades appear to have different mantle sources. Though the Western Cascades are grossly similar to the LKTs of the High Cascades, differences in isotopic signatures suggest that they originate from largely distinct sources. Both the Western Cascades and John Day and Eastern Clarno formations share some geochemical similarities with the High Cascades, but these appear to result largely from the overprinting of the subduction process, and do not suggest that Western Cascade or JD/EC mantle domains persisted through time. Though influences from Western Cascade, JD/EC, or Siletzia mantle may be suggested in some samples, there is no evidence that any of these mantle domains persist as coherent reservoirs beneath the active Cascade arc.

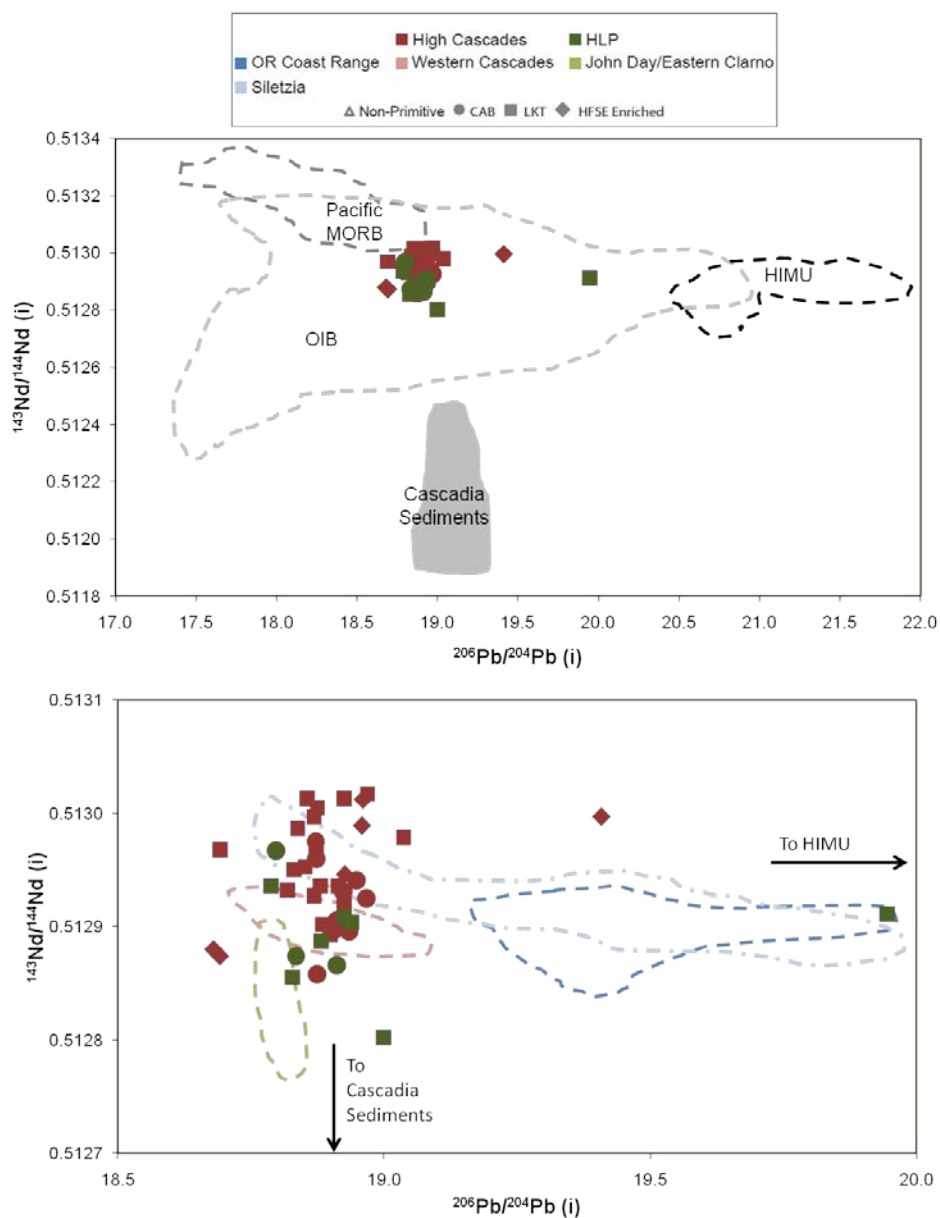


Figure 5.18: $^{143}\text{Nd}/^{144}\text{Nd}$ vs. $^{206}\text{Pb}/^{204}\text{Pb}$ for primitive magmas from the High Cascades and High Lava Plains. High Cascades data are from the compilation of Schmidt et al. (2008). High Lava Plains data are from Jordan (2001). A: Pacific MORB (compilation by Stracke et al., 2003), OIB (ibid.), HIMU (ibid.), and Cascadia sediment (Prytulak et al., 2006) fields shown for comparison. B: Data from Siletzia and each region of the Eocene-Oligocene Proto-Cascadia arc are shown as fields for comparison.

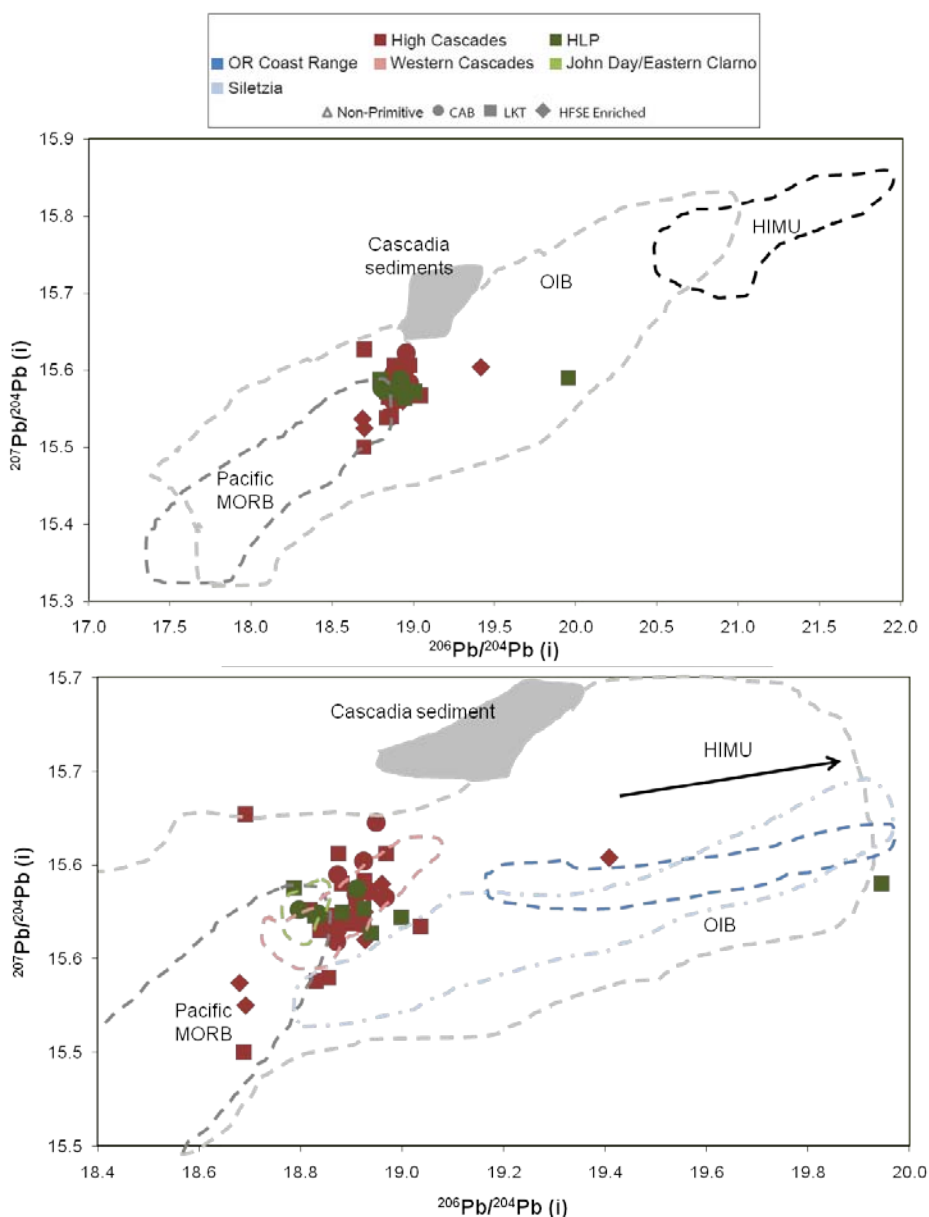


Figure 5.19: $^{207}\text{Pb}/^{204}\text{Pb}$ vs. $^{206}\text{Pb}/^{204}\text{Pb}$ for primitive magmas from the High Cascades and High Lava Plains. High Cascades data are from the compilation of Schmidt et al. (2008). High Lava Plains data are from Jordan (2001). A: Pacific MORB (compilation by Stracke et al., 2003), OIB (ibid.), HIMU (ibid.), and Cascadia sediment (Prytulak et al., 2006) fields shown for comparison. B: Data from the EOPC are shown as fields for comparison.

5.1.3 *Comparison with the High Lava Plains*

The High Lava Plains primitive magmas have a more restricted compositional range than do those of the Eocene-Oligocene Proto-Cascadia (EOPC) backarc (Figure 5.10). The HLP primitive magmas vary from more depleted to more enriched source characteristics (FeO^*/MgO), but extend to much more enriched values than the JD/EC (Figure 5.11). Additionally, they are displaced to lower Nb/Zr than are the JD/EC. The variable Nb/Zr for the HLP may suggest a heterogeneous source or one affected by varying degrees of partial melting. The HLP tend to be low in Nb, with variable Ba (Figure 5.12). They are generally lower in both Ba and Nb than the John Day and Eastern Clarno, which could suggest a higher degree of partial melting or melting from a less enriched source than the JD/EC. Taken together, higher Nb and Ba concentrations, higher Nb/Zr, and higher Ce/Yb and La/Y of the JD/EC confirm that the EOPC backarc magmas were lower degree partial melts than the HLP. A subset of CABs from the HLP is higher in Nb and fall along the JD/EC trend (Figure 5.12). As with the EOPC backarc magmas, the HLP extend from the Ba/Zr-Nb/Zr mantle array past an upper crustal composition and extend toward pelagic sediment, documenting the importance of subduction contributions in these magmas.

The HLP are displaced to more evolved ratios compared to the High Cascades, and the LKTs and CABs of the HLP are not distinguishable. The HLP extend to more isotopically primitive signatures than the JD/EC but within the range of overlap share a grossly similar trajectory.

The HLP have variable $^{87}\text{Sr}/^{86}\text{Sr}$ and don't form a clear trend, obscuring the evidence for a subduction component. Peaks in Pb and Sr concentrations relative to neighboring elements on basalt-normalize elemental plots are taken to reflect a subduction component, albeit potentially not from the present arc (Borg et al., 2002; Urbanczyk, 1994).

The HLP is more primitive than the JD/EC. One HLP shows significant $^{206}\text{Pb}/^{204}\text{Pb}$ enrichment that is difficult to explain as coming from Siletzia given the

distance. The HLP do not appear to be strongly pulled toward Cascadia sediment but trend nearly perpendicular to the High Cascades.

The JD/EC basalts are lower degree partial melts than the HLP, and they also appear to have a mantle source that is distinct from that of the HLP. Though magmatism of the JD/EC and HLP are broadly similar, distinct Nb/Zr and isotopic signatures suggest that they originated from different mantle domains. HLP magmas demonstrate a number of trace element characteristics that suggest an important role for subduction fluids and sediments in their production. However, they do not appear to have an affinity for Cascadia sediment (Figure 5.19). This observation may suggest that the apparent subduction influence recorded in the HLP is actually a paleo-enrichment, and thus not an indicator of active fluid fluxing in the HLP backarc. The observation that HLP basalts become slightly more isotopically evolved to the east (Jordan et al., 2004) could be explained by the greater influence of a paleo-enriched lithospheric mantle domain advected from beneath North America.

5.2 Implications for the Persistence and Modification of Sub-arc Mantle Domains

In the forearc, the Oregon Coast Range (OCR) basalts of the Eocene-Oligocene Proto-Cascadia (EOPC) have a strong geochemical affinity with the Siletz River Volcanics. The shared $^{206}\text{Pb}/^{204}\text{Pb}$ isotopic enrichment signature clearly demonstrates a Siletzia mantle source for the EOPC forearc magmas. Lithospheric mantle from the accreted Siletzia terrane has persisted beneath the forearc as a discrete mantle domain (Figure 5.20). This result suggests that mantle domains may endure for tens of millions of years, even in areas of active subduction.

However, the High Cascades appear to have mantle sources that are largely distinct from those of the Western Cascades, Oregon Coast Range, and John Day and Eastern Clarno basalts. There appears to be very little inheritance of mantle source

beneath the active arc axis. This suggests that while arc domains may be preserved through time, beneath the arc--where thermal erosion of the lithosphere is greatest and mantle flow is more pronounced—such domains may not survive. Such a result suggests that any arc signature in basalts from beneath the High Cascade arc is likely to be modern signatures, as modified lithosphere with a paleo-subduction signature would be unlikely to persist. (Figure 5.20)

The High Lava Plains have a mantle source distinct from the mantle domains of the EOPC basalts. Given the dynamic nature of the backarc, where slab rollback and attendant mantle flow redistributed material within the mantle wedge and heat flow may be high, it is unsurprising that mantle domains do not persist. HLP magmas demonstrate a number of trace element characteristics that suggest an important role for subducted sediments and slab derived fluids in their production. However, they do not appear to have an affinity for Cascadia sediment (Figure 5.19). This observation may suggest that the apparent subduction influence recorded in the HLP is actually a paleo-enrichment, and not an indicator of active fluid fluxing in the HLP backarc. Though it is unclear when this paleo-enrichment may have occurred, this appears to be an acquired mantle signature that suggests the persistence of some mantle domains, even in the active backarc region. In fact, this paleo-enriched source may be a reflection of distinct, previously enriched lithospheric mantle advected from beneath North America (Figure 5.20).

This work suggests that while mantle domains have the potential to be long-lived features, they are often largely or wholly replaced. This observation is especially true where melting and mantle flow are most active, as beneath the arc and backarc, and contribute greatly to the erosion of the mantle lithosphere and reworking of the mantle wedge. However, potentially paleo-enriched mantle appears to have been preserved in the backarc, suggesting that while mantle advection may compromise some mantle domains, it also allows the influence of others to be exhibited. The gross similarity of the mantle domains beneath the arc and backarc may also make it more difficult to trace the persistence of a single domain. Where subduction is most active,

mantle magmas appear to be the result of a highly heterogeneous mantle that may sample the remains of numerous formerly coherent mantle reservoirs.

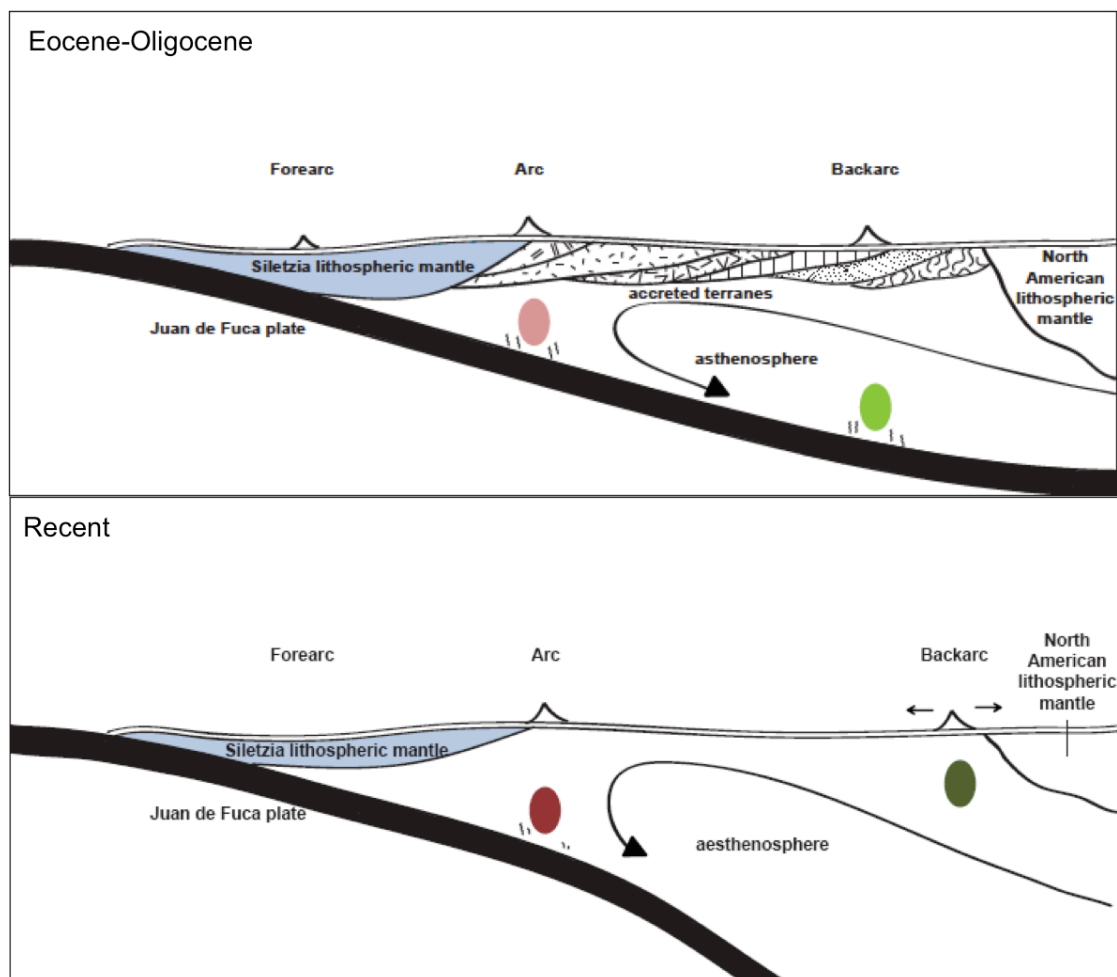


Figure 5.20: Schematic cartoon of Cascadia during the Eocene-Oligocene and Recent. In the Eocene-Oligocene, the forearc is underlain by thick Siletzia lithospheric mantle that extends beneath the arc. This mantle provides a source for the Eocene-Oligocene forearc magmas and may influence Western Cascades magmas slightly. Magmas in the Western Cascades and John Day and Eastern Clarno Formations result from fluid fluxing from the slab. Fluid is released over a distance because subduction is relatively flat at this time. Both the arc and backarc overlie accreted terranes. In the Recent panel, the Siletzia lithosphere has thinned. The mantle lithosphere of the accreted terranes beneath the arc and backarc has largely been eroded and replaced by a mantle reworked by protracted melting and mantle flow. North American lithospheric mantle from beneath the craton has been advected further west and is a component in the HLP magmas, which result from decompression related to slab rollback. Magmas beneath the arc continue to originate from fluxing from the subducting slab.

6 – Conclusions

The major element, trace element, and isotopic transect of the Eocene-Oligocene Proto-Cascadia mantle reveals a heterogeneous mantle source beneath the nascent Cascadia arc. In the forearc, the Siletzia terrane provides a mantle lithosphere source for the late Eocene- Oligocene alkaline intrusions and Tertiary volcanic centers. While gabbroic samples from the region may experience subduction influence, the alkaline intrusions and Yachats and Cascade Head basalts are little affected by subduction, but appear to be low degree partial melts of the enriched Siletzia mantle.

The Western Cascades demonstrate a clear subduction influence and appear to have a more depleted source than the forearc EOPC magmas. Although the Siletzia terrane extends beneath the Western Cascades, the Siletzia mantle domain does not appear to remain a coherent reservoir east of the forearc. Small influences of the Siletzia mantle may be seen in some Western Cascade samples, but they appear to have a mantle source largely distinct from the Siletzia mantle domain in the forearc. The Western Cascades are strongly influenced by a Cascadia sediment signature, suggesting they result from active subduction processes beneath the arc.

The John Day and Eastern Clarno basalts also have an affinity with Cascadia sediments and appear to have been overprinted by subduction. The JD/EC have a more diverse mantle source, but this source appears to be distinct from that of both the Western Cascades and EOPC forearc magmas. Although some authors have argued that the apparent subduction signature of the EC basalts results from a paleo-enrichment and they are merely the products of extension with little subduction overprint, this work suggests that subduction actively overprinted the JD and EC backarc mantle sources.

Although the Siletzia mantle domain persists in the forearc, domains from neither Western Cascades nor JD/EC are clearly preserved in the High Cascades or High Lava Plains. The High Cascades show a very minor influence of the Siletzia

mantle (as do the Western Cascades), but there does not appear to be a coherent Siletzia mantle domain beneath the modern High Cascades. Though the Western Cascade or JD/EC mantle domains may be partially reflected in younger magmatism, they do not appear to be directly tapped, suggesting they no longer exist as coherent reservoirs. However, an apparent paleo-enrichment signature in HLP basalts may attest to the persistence of a previously enriched mantle lithosphere. This lithospheric mantle may have been advected from beneath North America via slab counterflow, potentially explaining the more enriched signatures of eastern HLP basalts.

This work demonstrates that coherent mantle reservoirs may persist for tens of millions of years, but that such longevity is less likely in the more dynamic arc or backarc environment, where mantle domains appear to be largely replaced on shorter timescales. The contrasting examples of the High Lava Plains and John Day and Eastern Clarno basalts demonstrate that subduction signatures may be either actively acquired at the arc or inherited from earlier episodes of magmatism. However, mantle domains carrying such paleo-subduction signatures may or may not persist in more active regions of the arc. Mantle domains may both persist and be actively sampled by advection, creating a piecemeal mantle that may carry a history that is reflected in youthful magmas.

Bibliography

- Appel, M., 2001, Alkaline and peraluminous intrusives in the Clarno Formation around Mitchell, Oregon: Ramifications on magma genesis and subduction tectonics: [Masters Thesis]: Oregon State University, 222 p.
- Arai, S., 1994, Compositional variation of olivine-chromian spinel in Mg-rich magmas as a guide to their residual spinel peridotites: *Journal of Volcanology and Geothermal Research*, v. 59, p. 279-293.
- Babcock, R.S., Burmester, R.F., Engebretson, D.C., Warnock, A., and Clark, K.P., 1992, A rifted margin origin for the Crescent Basalts and related rocks in the Northern Coast Range Volcanic Province, Washington and British Columbia: *Journal of Geophysical Research*, v. 97, p. 6799-6821.
- Bacon, C.R., Bruggman, P.E., Christiansen, R.L., Clynne, M.A., Donnelly-Nolan, J.M., Hildreth, W., 1997, Primitive magmas at five Cascade volcanic fields: Melts from hot, heterogeneous sub-arc mantle: *Canadian Mineralogist*, v. 35, p.397-423.
- Barnes, M.A., and Barnes, C.G., 1992, Petrology of late Eocene basaltic lavas at Cascade Head, Oregon Coast Range: *Journal of Volcanology and Geothermal Research*, v. 52, p. 157-170.
- Bartels, K.S., Kenzler, R.J., Grove, T.L., 1991, High-pressure phase-relations of primitive high-alumina basalts from Medicine Lake Volcano, northern California: *Contributions to Mineralogy and Petrology*, v. 108, p. 253-270.
- Beck, Jr., M.E., and Burr, C.D., 1979, Paleomagnetism and tectonic significance of the Goble Volcanic Series, southwestern Washington: *Geology*, v. 7, p. 175-179.
- Bestland, E.A. and Retallack, G.J., 1994, Geology and paleoenvironments of the Painted Hills Unit, John Day Fossil Beds National Monument, Oregon, U.S. National Park Service Open-File Report, 211 p.
- Borg, L.E., Brandon, A.D., Clynne, M.A., and Walker, R.J., 2000, Re-Os isotopic systematic of primitive lavas from the Lassen region of the Cascade arc, California: *Earth and Planetary Science Letters*, v. 177, p. 301-317.
- Borg, L.E., Blichert-Toft, J., and Clynne, M.A., 2002, Ancient and modern subduction zone contributions to the mantle sources of lavas from the Lassen region of

- California inferred from Lu-Hf isotopic systematic: *Journal of Petrology*, v. 43, p. 705-723.
- Burchfiel, B.C., Cowan, D.S., Davis, G.A., 1992, Tectonic overview of the Cordilleran orogen in the western United States, in: Burchfiel, B.C., Lipman, P.W., Zoback, M.L. (Eds.), *The Geology of North America Vol. G-3, the Cordilleran Orogen: Conterminous U.S.: The Geological Society of America*, Boulder, CO, p. 407-479.
- Carlson, R.W., Czamanske, G., Fedorenko, V., and Ilupin, I., 2006, A comparison of the Siberian meimechites and kimberlites: Implications for the source of high-Mg alkali magmas and flood basalts: *Geochemistry, Geophysics, Geosystems*, v. 7.
- Christiansen, R.L. and McKee, E.H., 1978, Late Cenozoic volcanic and tectonic evolution of the Great Basin and the Columbia intermontane regions: in *Cenozoic Tectonics and Regional Geophysics of the Western Cordillera* (eds. Smith, R.B. and Eaton, G.P.)
- Christiansen, R.L., Yeats, R.S., Graham, S.A., Niem, W.A., Niem, A.R., and Snavely, Jr., P.D., 1992, Post-Laramide geology of the U.S. Cordilleran region: *The Geology of North America*, v. G-3, *The Cordilleran Orogen: Conterminous U.S.*, Geological Society of America, Chapter 7, p. 261-406.
- Conrey, R.M., Sherrod, D.R., Hooper, P.R., and Swanson, D.A., 1997, Diverse primitive magmas in the Cascade arc, Northern Oregon and Southern Washington: *The Canadian Mineralogist*, v. 35, p. 367-396.
- Couch, R.W. and Riddhough, R.P., 1989, The crustal structure of the western continental margin of North America, in: Pakiser, L.C., Mooney, W.D. (Eds.), *Geophysical Framework of the Continental United States: Boulder, Colorado. Geological Society of America Memoirs*, v. 172, p. 103-128.
- Davis, A.S., Snavely, Jr., P.D., Gray, L.B., and Minasian, D.L., 1995, Petrology of late Eocene lavas erupted in the forearc of Central Oregon: U.S. Geological Survey, Open File Report, 95-40.
- Dostal, J., Breitsprecher, K., Church, B. N., Thorkelson, D., and Hamilton, T.S., 2003, Eocene melting of Precambrian lithospheric mantle: Analcime-bearing volcanic rocks from the Challis-Kamloops belt of south central British Columbia: *Journal of Volcanology and Geothermal Research*, v. 126, p. 303-326.
- Draper, D.S. and Johnston, A.D., 1992, Anhydrous PT phase relations of an Aleutian

high-MgO basalt: an investigation of the role of olivine-liquid reaction in the generation of arc high-alumina basalts: *Contributions to Mineralogy and Petrology*, v. 112, p. 501-519.

Druken, K.A., Long, M.D., and Kincaid, C., *in submission*, Mantle flow driven by slab rollback beneath the High Lava Plains: *Geophysical Research Letters*.

du Bray, E.A., John, D.A., Sherrod, D.R., Evarts, R.C., Conrey, R.M., and Lexa, J., 2006, Geochemical Database for volcanic rocks of the Western Cascades, Oregon and California: U.S. Geological Survey Data Series, 155, 49 p.

Duncan, R.A., 1982, A captured island chain in the Coast Range, of Oregon and Washington: *Journal of Geophysical Research*, v. 87, p. 827–837.

Enlows, H.E. and Parker, D.J., 1972, Geochronology of the Clarno igneous activity in Mitchell Quadrangle, Wheeler County, Oregon: Oregon Department of Geology and Mineral Industries, v. 34, p. 104-110.

Ford, M.T., Carlson, R.W., and Grunder, A.L., 2009, Isotopic compositional changes across space, time, and bulk rock composition in the High Lava Plains and Northwest Basin and Range, Oregon: *Geological Society of America Abstracts with Programs*, v. 41, p. 571.

Gill, J.B., 1981, *Orogenic Andesites and Plate Tectonics*, New York: Springer-Verlag, 390 p.

Glassley, W., 1974, Geochemistry and tectonics of the Crescent Volcanic Rocks, Olympia Peninsula, Washington: *Geological Society of America Bulletin*, v. 85, p. 785–794.

Govindaraju, K., 1984, Compilation of working values and sample description for 170 international reference samples of mainly silicate rocks and minerals, *Geostandards Newsletter*, special issue, v. 8, p. 3-16.

Grove, T.L., Gerlach, D.C., and Sando, T.W., 1982, Origin of calc-alkaline series lavas at Medicine Lake Volcano by fractionation, assimilation, and mixing: *Contributions to Mineralogy and Petrology*, v. 80, p. 160-182.

Gunn, S.H., Conrey, R.M., Sherrod, D.R., 1996, Sr, Pb, and Nd isotopic study of Cascade Range basalts in northern Oregon: Constraints on mantle heterogeneity in a subduction zone: *Abstracts with Programs—Geological Society of America Cordilleran Section*, v. 28, p. 71.

- Hauessler, P.J., Wells, R.E., and Miller, M.L., 2003, Life and death of the Resurrection plate: Evidence for its existence and subduction in the northeastern Pacific in Paleocene-Eocene time: *Geologic Society of America Bulletin*, v. 115, 867-880.
- Hart, S.R., 1984, A large-scale isotope anomaly in the Southern Hemisphere mantle: *Nature*, v. 309, p. 717-733.
- Hart, W.K., Carlson, R.W., and Shirey, S.B., 1997, Radiogenic Os in primitive basalts from the northwestern U.S.A.: Implications for petrogenesis: *Earth and Planetary Science Letters*, v. 150, p. 103-116.
- Hatfield, A., 2009, Snow Peak, OR: Late Miocene to Early Pliocene volcanism in the central Cascadia forearc: [Masters Thesis]: Oregon State University, 155 p.
- Hildreth, W., 2007, Quaternary magmatism in the Cascades--geologic perspectives: U.S. Geological Survey Professional Paper 1744, 125 p.
- Hiza, M.M., 1999, The geochemistry and geochronology of the Eocene Absaroka volcanic province, northern Wyoming and southwest Montana, USA: [PhD Dissertation]: Oregon State University, 243 p.
- Hole, M.J., Kempton, P.D., and Millar, I.L., 1993, Trace-element and isotopic characteristics of small-degree melts of the asthenosphere: Evidence from the alkali basalts of the Antarctic Peninsula: *Chemical Geology*, v. 109, p. 51-68.
- Hooper, P.R., Bailey, D.G., and Holder, G.A., 1995, Tertiary calc-alkaline magmatism associated with lithospheric extension in the Pacific Northwest: *Journal of Geophysical Research*, v. 100, p. 10303-10319.
- Hughes, S.S. and Taylor, E.M., 1986, Geochemistry, petrogenesis, and tectonic implications of central High Cascade mafic platform lavas: *Geological Society of America Bulletin*, v. 97, p. 1024-1036.
- Humphreys, E.D., Dueker, K.G., Schutt, D.L., and Smith, R.B., 2000, Beneath Yellowstone: Evaluating plume and nonplume models using teleseismic images of the upper mantle: *GSA Today*, v. 10, p. 1-7.
- Jicha, B.R., Hart, G.L., Johnson, C.M., Hildreth, W., Beard, B.L., Shirey, S.B., and Valley, J.W., 2009, Isotopic and trace element constraints on the petrogenesis of lavas from the Mount Adams volcanic field, Washington: *Contributions to Mineralogy and Petrology*, v. 157, p.189-207.

- Johnson, D.M., Hooper, P.R., and Conrey, R.M., 1999, XRF analysis of rocks and minerals for major and trace elements on a single low dilution Li-tetraborate fused bead: *Advances in X-ray Analysis*, v. 41, p. 843-867.
- Jordan, B.T., 2001, Basaltic volcanism and tectonics of the High Lava Plains, Southeastern Oregon: [PhD Dissertation]: Oregon State University, 218 p.
- Jordan, B.T., Grunder, A.L., Duncan, R.A., and Deino, A.L., 2004, Geochronology of age-progressive volcanism of the Oregon High Lava Plains: Implications for the plume interpretation of Yellowstone, *Journal of Geophysical Research*, v. 109, p. 1-19.
- Keiko, H.H., Guillot, S., Saumur, B., Tubrett, M.N., Vidal, O., and Morfin, S., 2010, Corundum-bearing garnet peridotite from northern Dominican Republic: A metamorphic product of an arc cumulate in the Caribbean subduction zone: *Lithos*, v. 114, p. 437-450.
- Kinzler, R.J. and Grove, T.L., 1992, Primary magmas of mid-ocean ridge basalts 1. Experiments and methods: *Journal of Geophysical Research*, v. 97, p. 6885-6906.
- Koppers, A., 2002, ArArCALC: <http://earthref.org/tools/ararc>.
- Koppers, A., Staudigel, H., and Duncan, R., 2003, High-resolution $^{40}\text{Ar}/^{39}\text{Ar}$ dating of the oldest oceanic basement basalts in the western Pacific basin: *Geochemistry, Geophysics, Geosystems*, v.4.
- Knaack, C., Cornelius, S.B., and Hooper, P.R., 1994, Trace Element Analyses of Rocks and Minerals by ICP-MS, GeoAnalytical Lab, Washington State University.
- Lawrence, R.D., 1976, Strike-slip faulting terminates the Basin and Range province in Oregon: *GSA Bulletin*, v. 87, p. 846-850.
- Leeman, W.P., Lewis, J.F., Evarts, R.C., Conrey, R.M., and Streck, M.J., 2005, Petrologic constraints on the thermal structure of the Cascades arc: *Journal of Volcanology and Geothermal Research*, v.140, p. 67-105.
- Leeman, W.P., Smith, D.R., Hildreth, W., Palacz, Z., and Rogers, N., 1990, Compositional diversity of Late Cenozoic basalts in a transect across the Southern Washington Cascades: Implications for subduction zone magmatism: *Journal of Geophysical Research*, v. 95 (B12), p. 19,561-19,582.

- Loewen, Matthew. Petrology of Eocene Intrusive Rocks in Northeast Washington: Evidence for Widespread Deep Crustal Melting: [Senior Thesis] University of Puget Sound, 96 p.
- Long, M.D., Gao, H., Klaus, A., Wagner, L.S., Fouch, M.J., James, D.E., and Humphreys, E., 2009, Shear wave splitting and the pattern of mantle flow beneath eastern Oregon: *Earth and Planetary Science Letters*, v. 288, p. 359-369.
- Lux, D.R., 1981, Geochronology, geochemistry, and petrogenesis of basaltic rocks from the western Cascades, Oregon: [Dissertation]: Columbus, Ohio State University, 182 p.
- Madsen, J.K., Thorkleson, D.J., Friedman, R.M., and Marshall, D.D., 2006, Cenozoic to Recent plate configurations in the Pacific Basin: Ridge subduction and slab window magmatism in western North America: *Geosphere*, v. 2, p. 11–34.
- MacLeod, N.S., Walker, G.W., and McKee, E.H., 1975, Geothermal significance of eastward increase in age of Upper Cenozoic rhyolitic domes in southeastern Oregon, U.S. Geologic Survey Open File Report, 75-348, 21 p.
- Magill, J., Cox, A., and Duncan, R., 1981, Tillamook Volcanic Series: Further evidence for tectonic rotation of the Oregon Coast Range: *Journal of Geophysical Research*, v. 86, p. 2953–2970.
- McBirney, A.R., Sutter, J.F., Naslund, H.R., Sutton, K.G., and White, C.M., 1974, Episodic volcanism in the central Oregon Cascade Range: *Geology*, v. 2, p. 585-589.
- McClaughry, J.D., Ferns, M.L., Caroline, L.G., and Partridge, K.A., 2009, Field trip guide to the Oligocene Crooked River caldera: Central Oregon's Supervolcano, Crook, Deschutes, and Jefferson Counties, Oregon: *Oregon Geology*, v. 69, p. 25-44.
- McKee, E.H. and Walker, G.W., 1976, Potassium-argon ages of late Cenozoic silicic volcanic rocks, southeastern Oregon: *Isochron West*, v. 15, p. 37-41.
- Miller, R.B., 1989, the Mesozoic Rimrock Lake inlier, southern Washington Cascades: Implications for the basement to the Columbia Embayment: *Geological Society of America Bulletin*, v. 101, p. 1289-1305.
- Min, K., Mundil, R., Renne, P.R., and Ludwig, K.R., 2000, A test for systematic errors in ^{40}Ar - ^{39}Ar geochronology through comparison with U-Pb analysis of a

- 1.1 Ga rhyolite: *Geochim Cosmochim Acta*, v. 64, p. 73-98.
- Miyashiro, A., 1974, Volcanic rock series in island arcs and active continental margins: *American Journal of Science*, v. 274, p. 321-355.
- Neal, C.R., Mahoney, J.J., Kroenke, L.W., Dunacn, R.A., and Petterson, M.G., 1997, The Ontong Java Plateau: in *Large Igneous Provinces; Continental, Oceanic, and Planetary Flood Volcanism* (eds. Mahoney, J.J. and Coffin, M.F.), p. 183-216.
- Noblett, J.B., 1981, Subduction-related origin of the volcanic rocks of the Eocene Clarno Formation near Cherry Creek, Oregon: *Oregon Geology*, v. 43, p. 91-98.
- Oxford, J., 2006, Early Oligocene Intrusions in the Central Coast Range of Oregon: Petrography, Geochemistry, Geochronology, and Implications for the Tertiary Magmatic Evolution of the Cascadia Forearc: [Masters Thesis]: Oregon State University, 237 p.
- Plank, T. and Langmuir, C.H., 1993, Tracing trace elements from sediment input to volcanic output at subduction zones: *Nature*, v. 326, p. 739-742.
- Plumley, P.W., Beck, Jr., M.E., 1977, Tectonic rotation of Oligocene intrusive rocks in the Coast Range of Oregon: a constant rate of rotation for the period 50-30 M.Y.B.P.: *EOS, Transactions, American Geophysical Union*, v. 58, No. 12, p. 183.
- Priest, G.R., 1990, Volcanic and tectonic evolution of the Cascade volcanic arc, Central Oregon: *Journal of Geophysical Research*, v. 95, p. 19,583-19,599.
- Prytulak, J., Vervoort, J.D., Plank, T., and Chunjiang, Y., 2006, Astoria Fan sediments, DSDP site 174, Cascadia Basin: Hf-Nd-Pb constraints on provenance and outburst flooding: *Chemical Geology*, v. 233, p. 276-292.
- Pyle, D.G., Hanan, B.B., Graham, D.W., and Duncan, R.A., 1997, Siletzia; geochemistry and geochronology of the Yellow Stone Hot Spot volcanism in a suboceanic setting: *Geological Society of America, Abstracts with Programs*, v. 29, p. 298.
- Pyle, D.G., Duncan, R., Wells, R.E., Graham, D.W., Harrison, B., and Hanan, B., 2009. Siletzia: An oceanic large igneous province in the Pacific Northwest: *Geological Society of America Abstracts with Programs*, v. 41, p. 369.
- Reiners, P.W., Hammond, P.E., McKenna, J.M., and Duncan, R.A., 2000, Young

basalts of the central Washington Cascades, flux melting of the mantle, and trace element signatures of primary arc magmas: *Contributions to Mineralogy and Petrology*, v. 138, p. 249-264.

Renne, P.R., Deino, A.L., Walter, R.C., Turrin, B.D., Swisher, C.C., Becker, T.A., Curtis, G.H., Sharp, W.D., and Jaouni, A., 1994, Intercalibration of astronomical and radioisotopic time: *Geology*, v. 22, p. 783-786.

Robinson, P.T., Brem, G.F., and McKee, E.H., 1984, John Day Formation of Oregon: A distal record of early Cascade volcanism: *Geology*, v. 12, p. 229–232.

Rowe, M.C., Kent, A.J.R., and Nielsen, R.L., 2009, Subduction influence on oxygen fugacity and trace and volatile elements in basalts across the Cascade volcanic arc, *Journal of Petrology*, v. 50, p. 61-91.

Rowe, M.C., 2006, The role of subduction fluids in generating compositionally diverse basalts in the Cascadia subduction zone [Ph.D. Thesis]: Oregon State University, 441 p.

Saunders, A.D., Norry, M.J., and Tarney, J., 1991, Fluid influence on the trace element compositions of subduction zone magmas: *Philosophical Transactions: Physical Sciences and Engineering*, v. 335, p. 377-392.

Scarberry, K.C., Meigs, A.J., and Grunder, A.L., 2010, Faulting in a propagating continental rift: Insight from the late Miocene structural development of the Abert Rim fault, southern Oregon, USA: *Tectonophysics*, v. 488, p. 71-86.

Schmidt, M.E., Grunder, A.L., and Rowe, M.C., 2008, Segmentation of the Cascade Arc as indicated by Sr and Nd isotopic variation among diverse primitive basalts: *Earth and Planetary Science Letters*, v. 266, p. 166-181.

Sherrod, D.R., Mastin, L.G., Scott, W.E., and Schilling, S.P., 1997, Volcano hazards at Newberry Volcano, Oregon: U.S. Geological Survey Open File Report 97-513.

Sherrod, D.R. and Smith, J.G., 2000, Geologic map of Upper Eocene to Holocene volcanic and related rocks of the Cascade Range, Oregon, U.S. Geological Survey Geological Investigations Series Map I-2569.

Sherrod, D.R. and Smith, J.G., 1990, Quaternary extrusion rates of the Cascade Range, northwestern United States and southern British Columbia, *Journal of Geophysical Research*, v. 95, p. 19,465-19,474.

- Snively, Jr., P.D. and Wagoner, H.C., 1961, Differentiated gabbroic sills and associated alkaline rocks in the central part of the Oregon Coast Range, Oregon: Geological Survey Research, D-156-D-160.
- Stanley, W.D., Mooney, W.D., and Fuis, G.S., 1990, Deep crustal structure of the Cascade Range and surrounding regions from seismic refraction and magnetotelluric data: *Journal of Geophysical Research*, v. 95, p. 19,419-19,438.
- Stracke, A., Zindler, A., Salters, V.J.M., McKenzie, D., Blichert-Toft, J., Albarede, F., and Gronvold, K., 2003, Theistrareykir revisited, *Geochemistry, Geophysics, Geosystems*, v. 4.
- Sun, S.S., 1980, Lead isotopic study of young volcanic rocks from mid-ocean ridges, ocean islands, and island arcs: *Phil. Trans. R. Soc.*, v. A297, p. 409-455.
- Takahashi, E., 1986, Origin of basaltic magmas: Implication from peridotite melting experiments and an olivine fractionation model: *Bulletin of the Volcanological Society of Japan*, v. 30, p. S17-S40.
- Taylor, E.M., 1981, A mafic dike system in the vicinity of Mitchell, Oregon, and its bearing on the timing of Clarno-John Day volcanism and early Oligocene deformation in central Oregon: *Oregon Geology*, v. 43, p. 107-112.
- Taylor, E. M., 1990, Volcanic history and tectonic development of the central high Cascade Range, Oregon, *Journal of Geophysical Research*, v. 95, p. 19,611–19,622.
- Taylor, S.R. and McLennan, S.M., 1985, *The continental crust; its composition and evolution*: Blackwell Scientific, Oxford, 312 p.
- Till, C.B., Elkins-Tanton, L.T., and Fischer, K.M., 2010, A mechanism for low-extent melts at the lithosphere-asthenosphere boundary: *Geochemistry, Geophysics, Geosystems*, v. 11.
- Todt, W., Cliff, R.A., Hanser, A., and Hofmann, A.W., 1996, Evaluation of a ^{202}Pb - ^{205}Pb double spike for high precision lead isotope analysis: *American Geophysical Union Monographs* (eds. Basu, A. and Hart, S.), v. 95.
- Trehu, A.M., Asudeh, I., Brocher, T.M., Luetgert, J.H., Mooney, W.D., Nabelek, J.L., and Nakamura, Y., 1994, Crustal architecture of the Cascadia forearc: *Science*, v. 266, p. 237-243.
- Urbanczyk, K.M., 1994, *Geology of the eastern part of the Clarno Formation*,

- northeast Oregon, [Ph.D. Dissertation]: Washington State University, 129 p.
- Verplanck, E.P. and Duncan, R.A., 1987, Temporal variations in plate convergence and eruption rates in the western Cascades, Oregon: *Tectonics*, v. 6, p. 197–209.
- Verplanck, E.P., 1985, Temporal variations in volume and geochemistry of volcanism in the Western Cascades, Oregon: [Masters Thesis]: Oregon State University, 115 p.
- Walker, G.W. and Robinson, P.T., 1990, Paleocene (?), Eocene, and Oligocene (?) rocks of the Blue Mountains region: in *Geology of the Blue Mountains region of Oregon, Idaho, and Washington*: US Geological Survey Professional Paper 1437, p. 29-62.
- Walker, G.W., 1974, Some implications of Late Cenozoic volcanism to geothermal potential in the High Lava Plains or south-central Oregon: *Ore Bin*, v. 36, p. 109-119.
- Weaver, B.L., Wood, D.A., Tarney, J., and Joron, J.L., 1987, Geochemistry of ocean island basalts from the South Atlantic: Ascension, Bouvet, St. Helena, Gough, and Tristan da Cunha, in *Alkalkine Igneous Rocks*, edited by J.G. Fitton and B.J. Upton, Special Publication of the Geological Society of London, v. 30, p. 253-267.
- Wells, R.E., Weaver, C.S., and Blakely, R.J., 1998, Fore-arc migration in Cascadia and its neotectonic significance: *Geology*, v. 26, p. 759–762.
- Wells, R.E., Engebretson, D.C., Snavely, Jr., P.D., and Coe, R.S., 1984, Cenozoic plate motions and the volcano-tectonic evolution of western Oregon and Washington: *Tectonics*, v. 3, p. 275–294.
- Yogodzinski, G.M., and Kelemen, P.B., 2007, Trace elements in clinopyroxenes from Aleutian xenoliths: Implications for primitive subduction magmatism in an island arc: *Earth and Planetary Science Letters*, v. 256, p. 617-632.

APPENDIX A

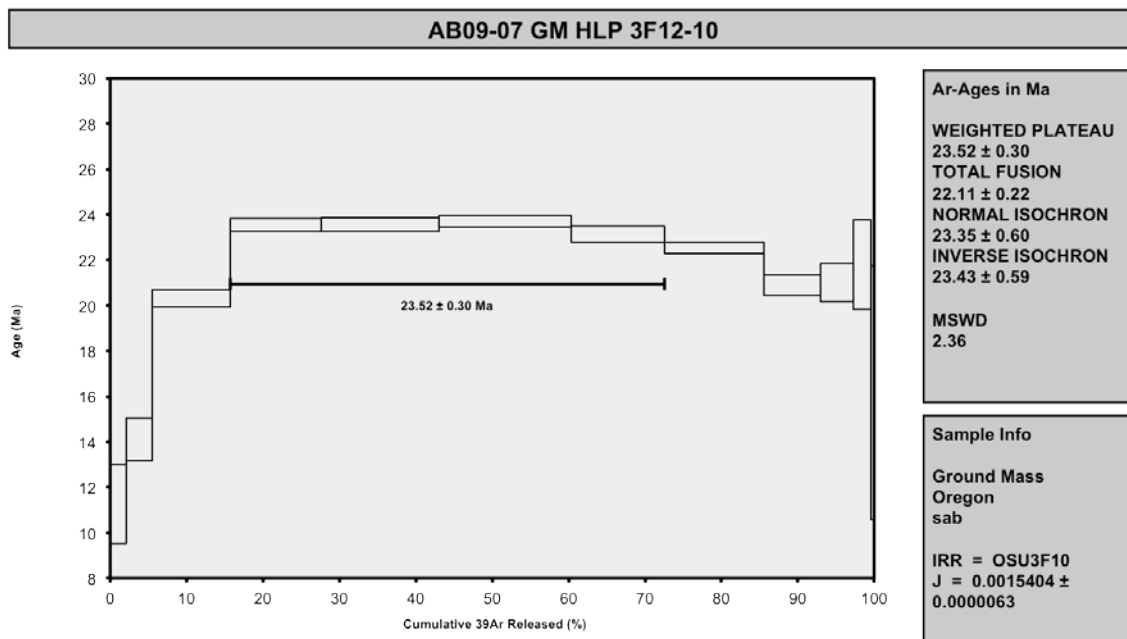
⁴⁰Ar/³⁹Ar Dating

Details for each $^{40}\text{Ar}/^{39}\text{Ar}$ age determination, including heating steps and plateau, total fusion, and isochron ages are presented in the following pages. Sample preparation, analytical techniques, and input parameters are given in the methods sections of this text. A summary of results and interpretation of age spectra is given in section 5.1. Data reduction was accomplished using ArArCalc v2.2 (Koppers, 2002). For both normal and inverse isochron plots, solid lines represent the calculated isochron while the dashed line represents the reference line that passes through the composition of atmospheric argon; solid black symbols are plateau heating steps while blue dots are steps that are not included in the plateau.

AB09-07

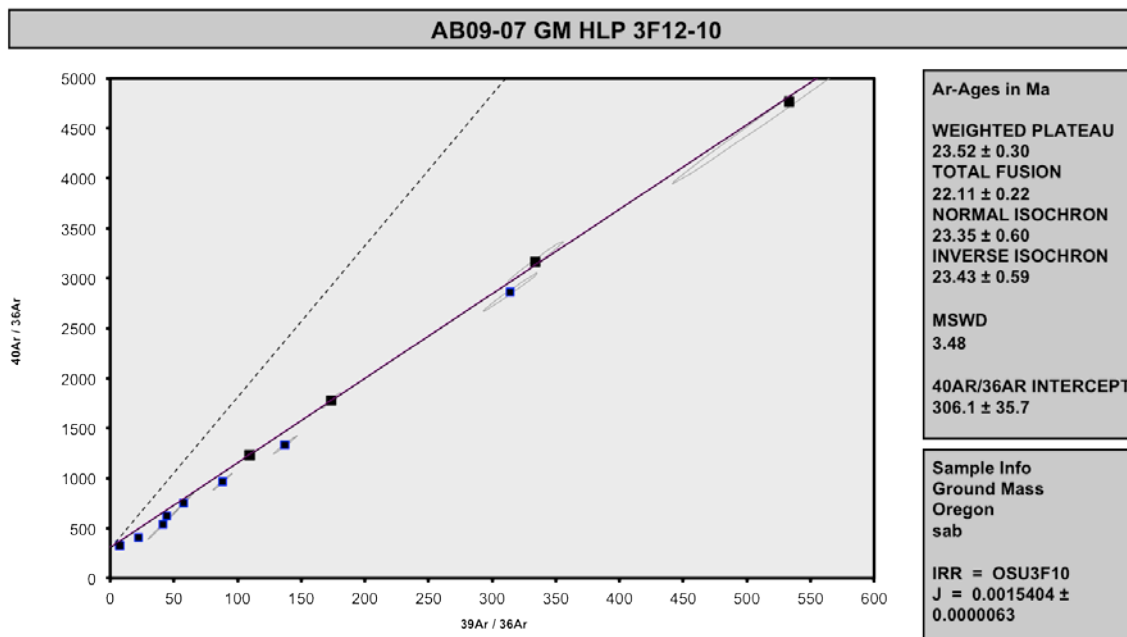
Incremental Heating		36Ar(a)	37Ar(ca)	38Ar(cl)	39Ar(k)	40Ar(r)	Age $\pm 2\sigma$ (Ma)	40Ar(r) (%)	39Ar(k) (%)	K/Ca $\pm 2\sigma$
10C3596	400 °C	0.000427	0.006907	0.000023	0.003251	0.013203	11.25 \pm 1.72	9.48	2.09	0.202 \pm 0.008
10C3597	500 °C	0.000243	0.006920	0.000041	0.005371	0.027369	14.11 \pm 0.95	27.59	3.46	0.334 \pm 0.013
10C3600	600 °C	0.000356	0.029653	0.000051	0.015757	0.115839	20.32 \pm 0.39	52.41	10.15	0.228 \pm 0.009
10C3601	675 °C ✓	0.000169	0.047785	0.000020	0.018527	0.158012	23.55 \pm 0.28	75.97	11.93	0.167 \pm 0.006
10C3602	750 °C ✓	0.000138	0.098256	0.000013	0.023914	0.204006	23.55 \pm 0.30	83.36	15.41	0.105 \pm 0.004
10C3605	825 °C ✓	0.000080	0.163349	0.000036	0.026850	0.230570	23.71 \pm 0.26	90.65	17.30	0.071 \pm 0.003
10C3606	900 °C ✓	0.000036	0.129913	0.000068	0.018977	0.159005	23.14 \pm 0.34	93.78	12.22	0.063 \pm 0.002
10C3607	1000 °C	0.000064	0.134990	0.000147	0.020154	0.164526	22.55 \pm 0.25	89.66	12.98	0.064 \pm 0.002
10C3609	1100 °C	0.000083	0.081039	0.000094	0.011457	0.086571	20.88 \pm 0.46	77.82	7.38	0.061 \pm 0.002
10C3610	1200 °C	0.000076	0.066354	0.000061	0.006716	0.051071	21.01 \pm 0.83	69.39	4.33	0.044 \pm 0.002
10C3611	1300 °C	0.000063	0.048556	0.000040	0.003626	0.028609	21.79 \pm 1.98	60.64	2.34	0.032 \pm 0.001
10C3613	1400 °C	0.000015	0.008313	0.000014	0.000637	0.003722	16.16 \pm 5.60	45.03	0.41	0.033 \pm 0.001
Σ		0.001750	0.822035	0.000607	0.155235	1.242503				

Information on Analysis	Results	40(r)/39(k) $\pm 2\sigma$	Age $\pm 2\sigma$ (Ma)	MSWD	39Ar(k) (% _n)	K/Ca $\pm 2\sigma$
AB09-07 WR HLP 3F12-10 Ground Mass Oregon sab	Weighted Plateau	8.5203 \pm 0.0819 $\pm 0.96\%$	23.52 \pm 0.30 $\pm 1.26\%$ External Error ± 0.48 Analytical Error ± 0.22	2.36	56.86 4	0.079 \pm 0.031 Statistical T Ratio Error Magnification
Project = HLP Irradiation = OSU3F10 J = 0.0015404 \pm 0.0000063 FCT-3 = 28.030 \pm 0.003 Ma	Total Fusion Age	8.0040 \pm 0.0474 $\pm 0.59\%$	22.11 \pm 0.22 $\pm 1.01\%$ External Error ± 0.42 Analytical Error ± 0.13		12	0.081 \pm 0.001



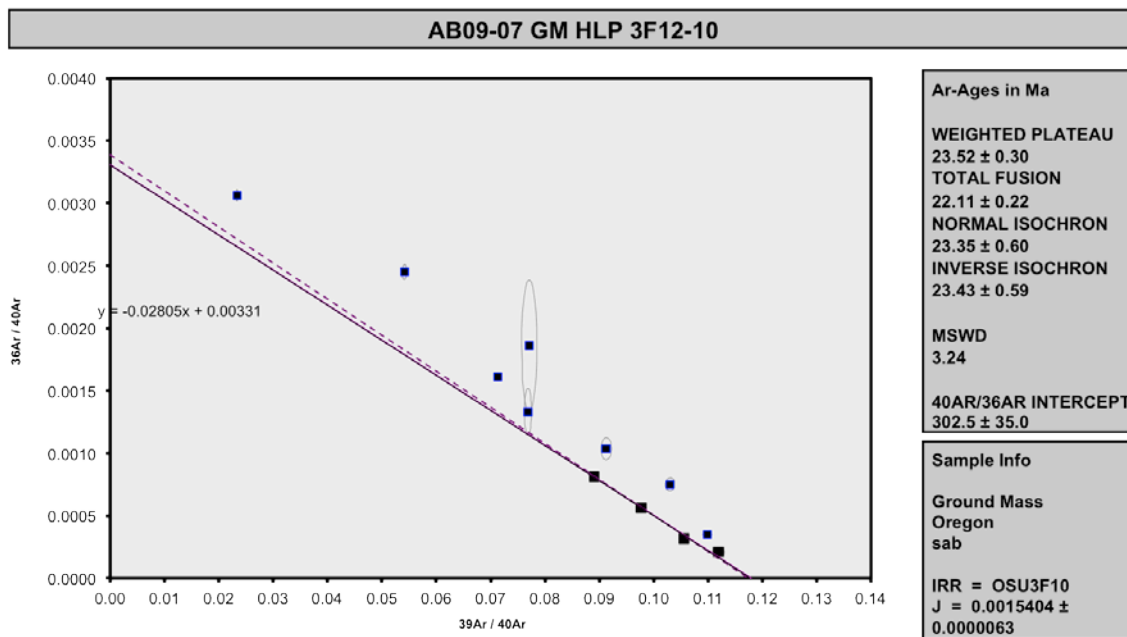
Normal Isochron		39(k)/36(a) ± 2σ	40(a+r)/36(a) ± 2σ	r.i.
10C3596	400 °C	7.6 ± 0.1	326.5 ± 5.2	0.9307
10C3597	500 °C	22.1 ± 0.6	408.1 ± 10.3	0.9554
10C3600	600 °C	44.3 ± 0.9	621.0 ± 12.1	0.9318
10C3601	675 °C ✓	109.5 ± 3.6	1229.8 ± 40.1	0.9832
10C3602	750 °C ✓	173.6 ± 7.5	1776.6 ± 76.3	0.9799
10C3605	825 °C ✓	334.0 ± 22.0	3163.3 ± 206.6	0.9909
10C3606	900 °C ✓	533.2 ± 92.0	4762.7 ± 820.4	0.9984
10C3607	1000 °C	314.1 ± 21.2	2860.0 ± 193.2	0.9939
10C3609	1100 °C	137.3 ± 9.7	1332.6 ± 93.6	0.9925
10C3610	1200 °C	88.1 ± 7.7	965.5 ± 83.4	0.9921
10C3611	1300 °C	57.7 ± 8.1	750.9 ± 105.3	0.9982
10C3613	1400 °C	41.5 ± 11.8	537.6 ± 153.1	0.9980

Results	40(a)/36(a) ± 2σ	40(r)/39(k) ± 2σ	Age ± 2σ (Ma)	MSWD
No Convergence	306.0907 ± 35.6949 ± 11.66%	8.4574 ± 0.2058 ± 2.43%	23.35 ± 0.60 ± 2.55% External Error ± 0.70 Analytical Error ± 0.56	3.48
Statistics	Statistical F Ratio Error Magnification n	3.00 1.8649 4	Convergence Number of Iterations Calculated Line	0.0000018111 500 Weighted York-2



Inverse Isochron		$39(k)/40(a+r) \pm 2\sigma$	$36(a)/40(a+r) \pm 2\sigma$	r.i.
10C3596	400 °C	0.023343 ± 0.000147	0.003063 ± 0.000049	0.0191
10C3597	500 °C	0.054138 ± 0.000408	0.002450 ± 0.000062	0.1370
10C3600	600 °C	0.071292 ± 0.000537	0.001610 ± 0.000031	0.0178
10C3601	675 °C ✓	0.089076 ± 0.000538	0.000813 ± 0.000026	0.0166
10C3602	750 °C ✓	0.097726 ± 0.000843	0.000563 ± 0.000024	0.0921
10C3605	825 °C ✓	0.105571 ± 0.000935	0.000316 ± 0.000021	0.0150
10C3606	900 °C ✓	0.111944 ± 0.001091	0.000210 ± 0.000036	0.0010
10C3607	1000 °C	0.109838 ± 0.000822	0.000350 ± 0.000024	0.0545
10C3609	1100 °C	0.102998 ± 0.000887	0.000750 ± 0.000053	0.0491
10C3610	1200 °C	0.091252 ± 0.000996	0.001036 ± 0.000090	0.0215
10C3611	1300 °C	0.076867 ± 0.000639	0.001332 ± 0.000187	0.0040
10C3613	1400 °C	0.077100 ± 0.001391	0.001860 ± 0.000530	0.0050

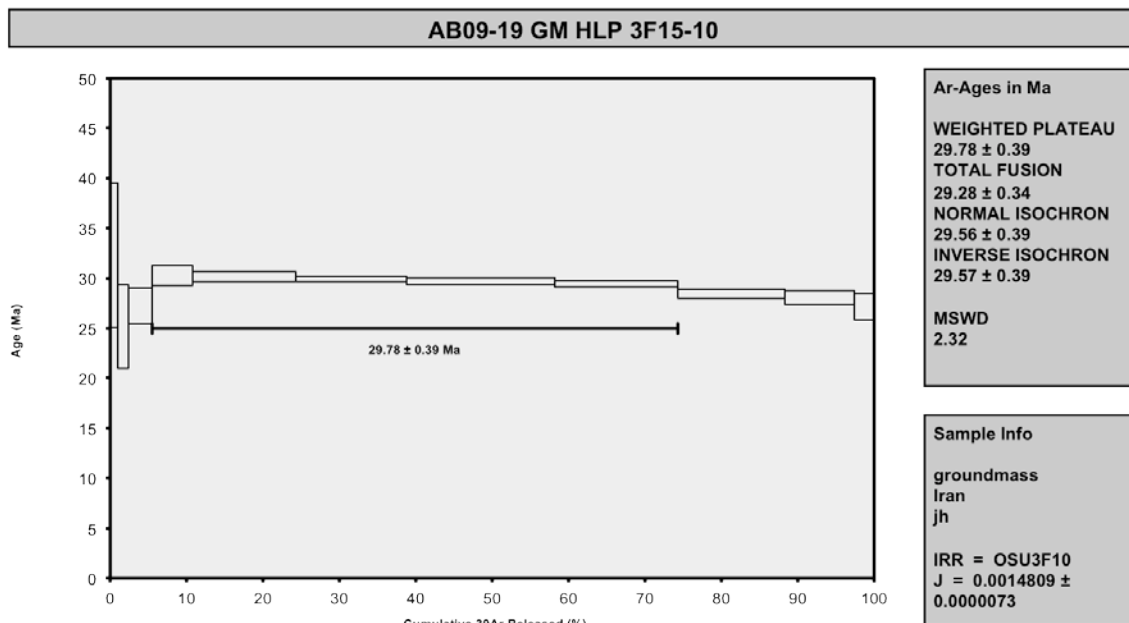
Results	$40(a)/36(a) \pm 2\sigma$	$40(r)/39(k) \pm 2\sigma$	Age ± 2σ (Ma)	MSWD
Error Chron	302.5199 ± 35.0226 ± 11.58%	8.4855 ± 0.2035 ± 2.40%	23.43 ± 0.59 ± 2.52%	3.24
			External Error ± 0.70 Analytical Error ± 0.56	
Statistics	Statistical F Ratio Error Magnification n	3.00 1.8008 4	Convergence Number of Iterations Calculated Line	0.000000430 5 Weighted York-2



AB09-19

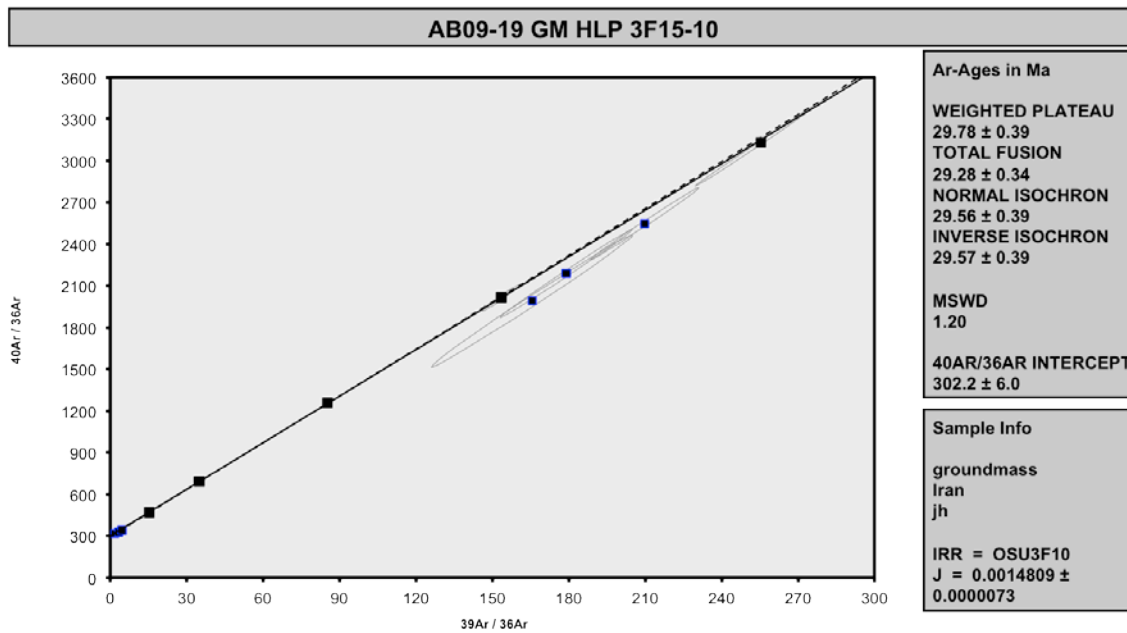
Incremental Heating		36Ar(a)	37Ar(ca)	38Ar(cl)	39Ar(k)	40Ar(r)	Age ± 2σ (Ma)	40Ar(r) (%)	39Ar(k) (%)	K/Ca ± 2σ
10C3665	400 °C	0.000589	0.004939	0.000012	0.001070	0.013059	32.32 ± 7.23	6.98	1.04	0.093 ± 0.004
10C3666	500 °C	0.000431	0.008291	0.000007	0.001401	0.013286	25.16 ± 4.18	9.46	1.36	0.073 ± 0.003
10C3668	600 °C	0.000677	0.022177	0.000003	0.003142	0.032270	27.23 ± 1.81	13.89	3.06	0.061 ± 0.002
10C3669	700 °C ✓	0.000362	0.045674	0.000000	0.005519	0.063090	30.28 ± 0.98	37.09	5.37	0.052 ± 0.002
10C3670	800 °C ✓	0.000398	0.111027	0.000004	0.013893	0.158227	30.17 ± 0.49	57.39	13.51	0.054 ± 0.002
10C3672	875 °C ✓	0.000174	0.105084	0.000012	0.014844	0.167672	29.93 ± 0.29	76.51	14.44	0.061 ± 0.002
10C3673	950 °C ✓	0.000130	0.133931	0.000022	0.019973	0.223741	29.68 ± 0.34	85.33	19.43	0.064 ± 0.002
10C3674	1025 °C ✓	0.000065	0.102769	0.000059	0.016548	0.183783	29.43 ± 0.34	90.55	16.10	0.069 ± 0.003
10C3676	1125 °C	0.000068	0.089908	0.000129	0.014353	0.154052	28.45 ± 0.46	88.39	13.96	0.069 ± 0.003
10C3677	1250 °C	0.000052	0.102111	0.000135	0.009374	0.099163	28.04 ± 0.71	86.50	9.12	0.039 ± 0.002
10C3678	1400 °C	0.000016	0.043236	0.000055	0.002686	0.027503	27.15 ± 1.30	85.15	2.61	0.027 ± 0.001
Σ		0.002963	0.769145	0.000439	0.102804	1.135846				

Information on Analysis	Results	40(r)/39(k) ± 2σ	Age ± 2σ (Ma)	MSWD	39Ar(k) (%),n	K/Ca ± 2σ
AB09-19 GM HLP 3F15-10 groundmass Iran jh	Weighted Plateau	11.2388 ± 0.0987 ± 0.88%	29.78 ± 0.39 ± 1.31% External Error ± 0.61 Analytical Error ± 0.26	2.32	68.85 5	0.059 ± 0.006 Statistical T Ratio Error Magnification
Project = HLP Irradiation = OSU3F10 J = 0.0014809 ± 0.0000073 FCT-3 = 28.030 ± 0.003 Ma	Total Fusion Age	11.0487 ± 0.0737 ± 0.67%	29.28 ± 0.34 ± 1.18% External Error ± 0.58 Analytical Error ± 0.19		11	0.057 ± 0.001



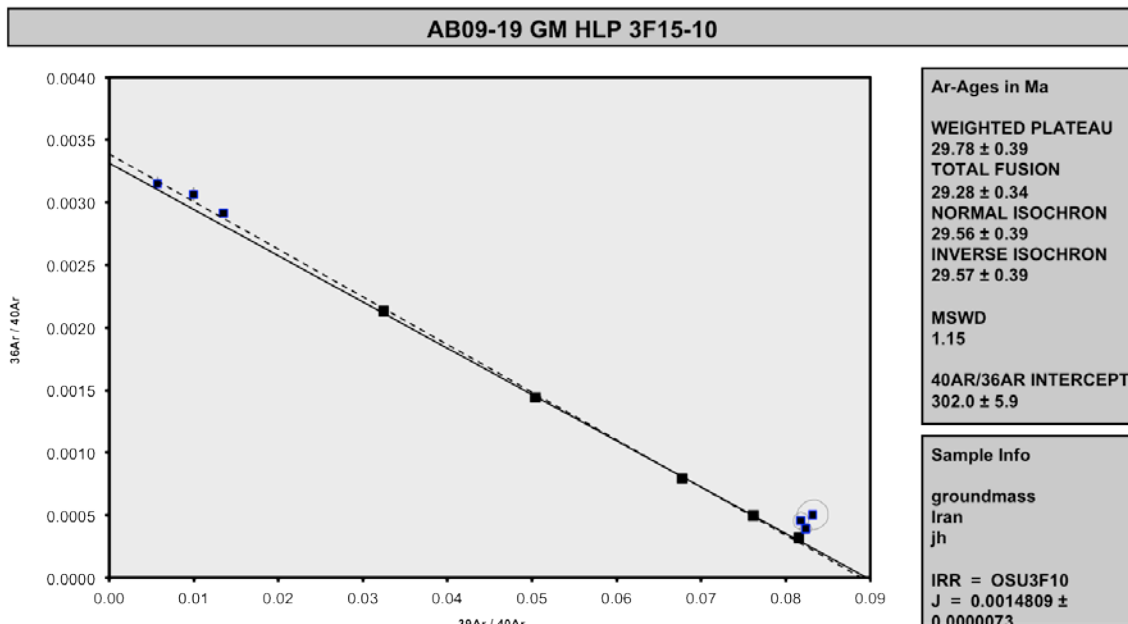
Normal Isochron		$39(k)/36(a) \pm 2\sigma$	$40(a+r)/36(a) \pm 2\sigma$	r.i.
10C3665	400 °C	1.8 ± 0.0	317.7 ± 5.3	0.6032
10C3666	500 °C	3.3 ± 0.1	326.4 ± 5.7	0.8063
10C3668	600 °C	4.6 ± 0.1	343.1 ± 3.6	0.6536
10C3669	700 °C ✓	15.2 ± 0.3	469.7 ± 8.9	0.9796
10C3670	800 °C ✓	35.0 ± 0.7	693.5 ± 14.1	0.9616
10C3672	875 °C ✓	85.2 ± 2.5	1258.3 ± 36.5	0.9901
10C3673	950 °C ✓	153.5 ± 7.4	2015.0 ± 96.6	0.9867
10C3674	1025 °C ✓	255.3 ± 25.8	3130.9 ± 316.0	0.9989
10C3676	1125 °C	209.8 ± 21.4	2547.3 ± 259.8	0.9966
10C3677	1250 °C	179.0 ± 26.1	2189.6 ± 319.0	0.9971
10C3678	1400 °C	165.6 ± 39.6	1990.7 ± 476.3	0.9958

Results	$40(a)/36(a) \pm 2\sigma$	$40(r)/39(k) \pm 2\sigma$	Age ± 2σ (Ma)	MSWD
Isochron	302.1677 ± 5.9503 $\pm 1.97\%$	11.1541 ± 0.1002 $\pm 0.90\%$	29.56 ± 0.39 $\pm 1.32\%$ External Error ± 0.61 Analytical Error ± 0.26	1.20
Statistics	Statistical F Ratio Error Magnification n	2.60 1.0936 5	Convergence Number of Iterations Calculated Line	0.0000001102 376 Weighted York-2



Normal Isochron		39(k)/36(a) ± 2σ	40(a+r)/36(a) ± 2σ	r.i.
10C3665	400 °C	1.8 ± 0.0	317.7 ± 5.3	0.6032
10C3666	500 °C	3.3 ± 0.1	326.4 ± 5.7	0.8063
10C3668	600 °C	4.6 ± 0.1	343.1 ± 3.6	0.6536
10C3669	700 °C ✓	15.2 ± 0.3	469.7 ± 8.9	0.9796
10C3670	800 °C ✓	35.0 ± 0.7	693.5 ± 14.1	0.9616
10C3672	875 °C ✓	85.2 ± 2.5	1258.3 ± 36.5	0.9901
10C3673	950 °C ✓	153.5 ± 7.4	2015.0 ± 96.6	0.9867
10C3674	1025 °C ✓	255.3 ± 25.8	3130.9 ± 316.0	0.9989
10C3676	1125 °C	209.8 ± 21.4	2547.3 ± 259.8	0.9966
10C3677	1250 °C	179.0 ± 26.1	2189.6 ± 319.0	0.9971
10C3678	1400 °C	165.6 ± 39.6	1990.7 ± 476.3	0.9958

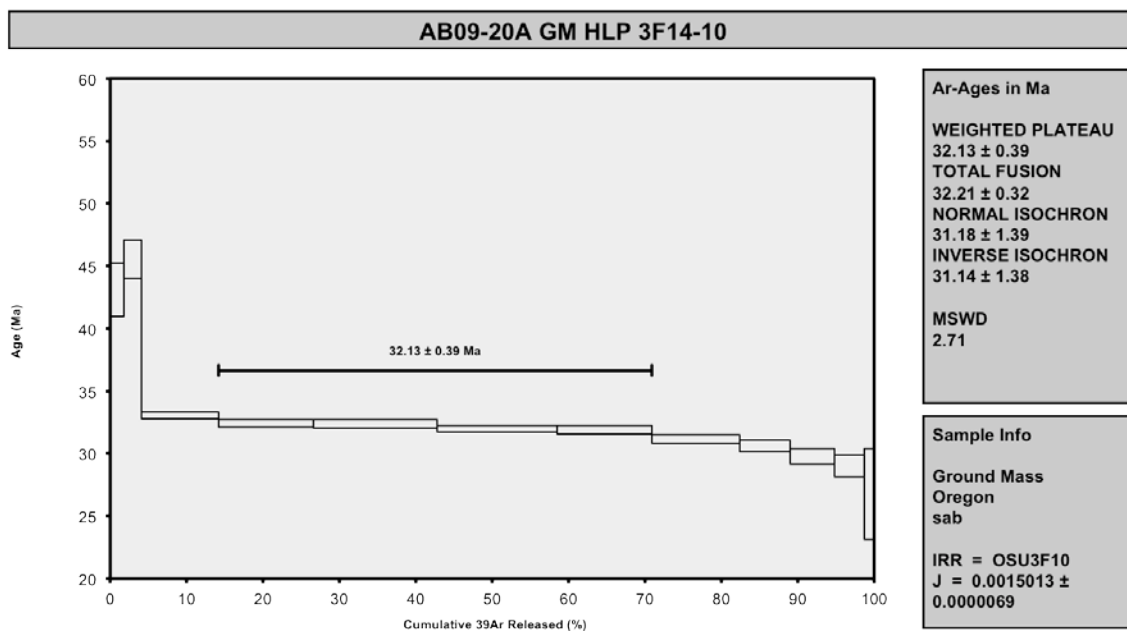
Results	40(a)/36(a) ± 2σ	40(r)/39(k) ± 2σ	Age ± 2σ (Ma)	MSWD
Isochron	302.1677 ± 5.9503 ± 1.97%	11.1541 ± 0.1002 ± 0.90%	29.56 ± 0.39 ± 1.32% External Error ± 0.61 Analytical Error ± 0.26	1.20
Statistics	Statistical F Ratio Error Magnification n	2.60 1.0936 5	Convergence Number of Iterations Calculated Line	0.0000001102 376 Weighted York-2



AB09-20A

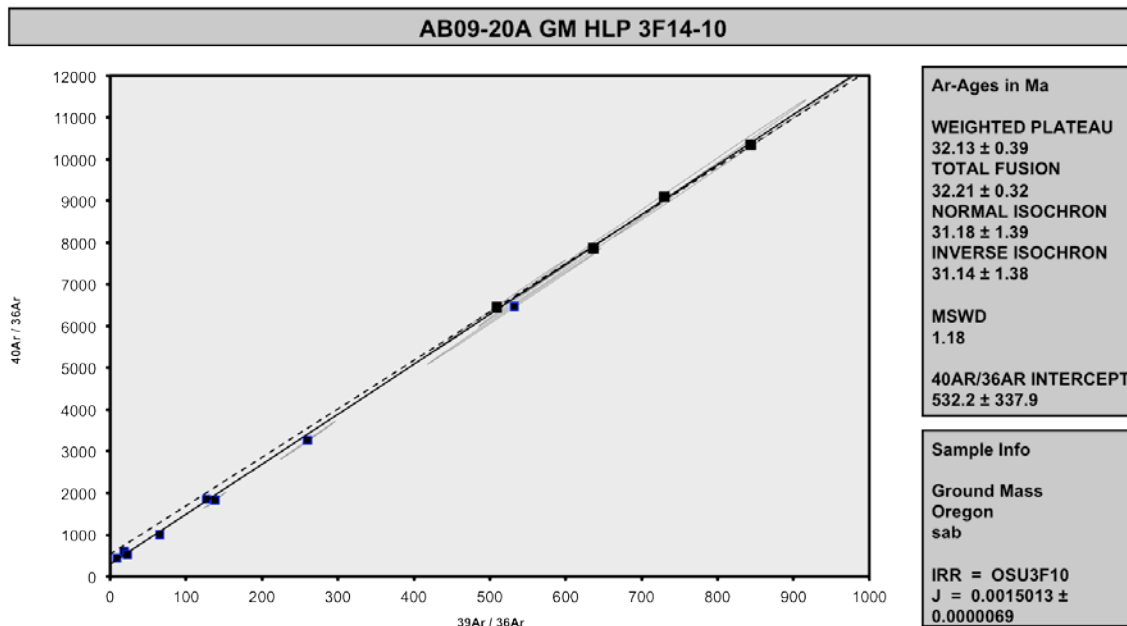
Incremental Heating		36Ar(a)	37Ar(ca)	38Ar(cl)	39Ar(k)	40Ar(r)	Age ± 2σ (Ma)	40Ar(r) (%)	39Ar(k) (%)	K/Ca ± 2σ
10C3632	400 °C	0.000288	0.006629	0.000010	0.002605	0.041961	43.10 ± 2.12	33.03	1.82	0.169 ± 0.007
10C3634	500 °C	0.000174	0.010633	0.000009	0.003218	0.054841	45.58 ± 1.53	51.65	2.25	0.130 ± 0.005
10C3635	600 °C	0.000115	0.073398	0.000006	0.014566	0.179437	33.06 ± 0.28	84.09	10.16	0.085 ± 0.003
10C3636	675 °C ✓	0.000035	0.098469	0.000005	0.017754	0.214422	32.42 ± 0.33	95.41	12.39	0.078 ± 0.003
10C3638	750 °C ✓	0.000032	0.115500	0.000025	0.023165	0.279382	32.37 ± 0.36	96.74	16.16	0.086 ± 0.003
10C3639	825 °C ✓	0.000027	0.095891	0.000045	0.022579	0.268991	31.98 ± 0.25	97.14	15.76	0.101 ± 0.004
10C3640	900 °C ✓	0.000028	0.066405	0.000082	0.017764	0.211100	31.90 ± 0.34	96.23	12.40	0.115 ± 0.004
10C3642	975 °C	0.000031	0.061145	0.000138	0.016500	0.191400	31.15 ± 0.34	95.42	11.51	0.116 ± 0.005
10C3643	1050 °C	0.000036	0.040166	0.000113	0.009371	0.106835	30.62 ± 0.45	90.93	6.54	0.100 ± 0.004
10C3644	1150 °C	0.000060	0.054238	0.000136	0.008265	0.091649	29.79 ± 0.61	83.83	5.77	0.066 ± 0.003
10C3646	1275 °C	0.000086	0.075846	0.000105	0.005615	0.060622	29.01 ± 0.88	70.45	3.92	0.032 ± 0.001
10C3647	1400 °C	0.000084	0.057015	0.000035	0.001907	0.018987	26.77 ± 3.64	43.37	1.33	0.014 ± 0.001
Σ		0.000994	0.755335	0.000710	0.143309	1.719628				

Information on Analysis	Results	40(r)/39(k) ± 2σ	Age ± 2σ (Ma)	MSWD	39Ar(k) (% , n)	K/Ca ± 2σ
AB09-20A GM HLP 3F14-10 Ground Mass Oregon sab	Weighted Plateau	11.9706 ± 0.0954 ± 0.80%	32.13 ± 0.39 ± 1.21% External Error ± 0.64 Analytical Error ± 0.25	2.71	56.70 / 4	0.091 ± 0.016
	Total Fusion Age	11.9994 ± 0.0518 ± 0.43%	32.21 ± 0.32 ± 1.01% External Error ± 0.61 Analytical Error ± 0.14	1.6455	12	0.082 ± 0.001



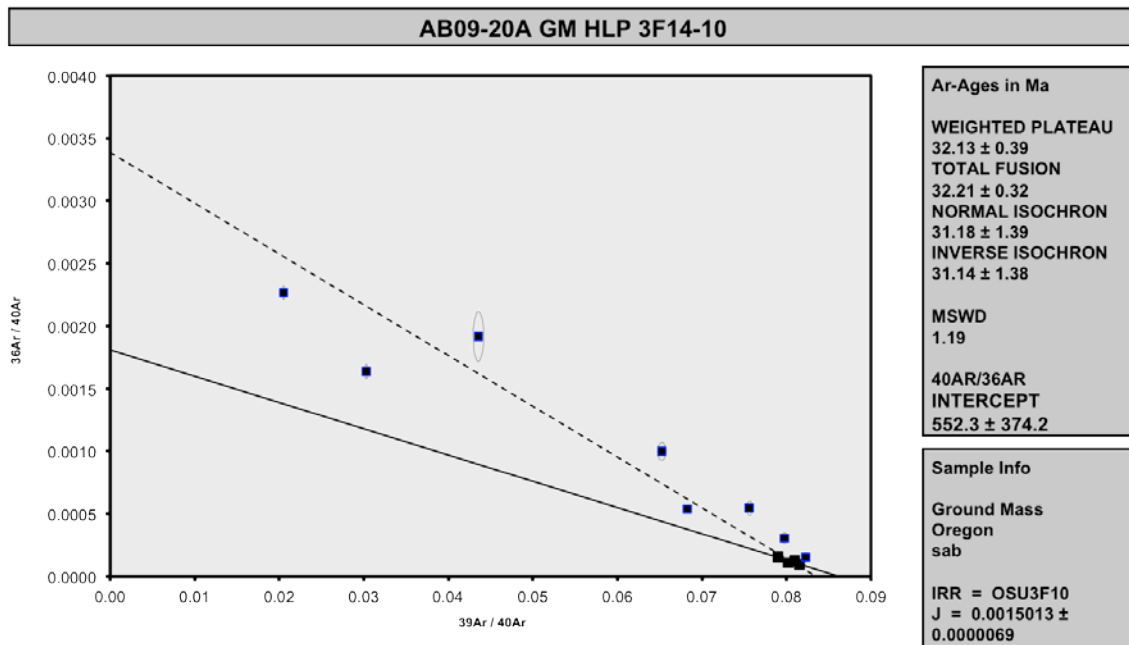
Normal Isochron		39(k)/36(a) ± 2σ	40(a+r)/36(a) ± 2σ	r.i.
10C3632	400 °C	9.0 ± 0.2	441.2 ± 10.6	0.9341
10C3634	500 °C	18.5 ± 0.7	611.2 ± 21.9	0.9892
10C3635	600 °C	126.9 ± 4.2	1858.4 ± 62.3	0.9891
10C3636	675 °C ✓	509.2 ± 90.1	6445.3 ± 1139.9	0.9995
10C3638	750 °C ✓	729.9 ± 186.9	9098.4 ± 2329.8	0.9996
10C3639	825 °C ✓	843.7 ± 179.6	10346.7 ± 2201.9	0.9998
10C3640	900 °C ✓	636.5 ± 152.0	7859.3 ± 1877.2	0.9998
10C3642	975 °C	532.1 ± 114.7	6467.5 ± 1393.6	0.9998
10C3643	1050 °C	260.2 ± 36.2	3262.3 ± 453.7	0.9993
10C3644	1150 °C	138.3 ± 14.5	1828.5 ± 191.2	0.9990
10C3646	1275 °C	65.3 ± 4.6	1000.2 ± 70.2	0.9936
10C3647	1400 °C	22.7 ± 2.4	521.8 ± 54.4	0.9910

Results	40(a)/36(a) ± 2σ	40(r)/39(k) ± 2σ	Age ± 2σ (Ma)	MSWD
No Convergence	532.2371 ± 337.8867 ± 63.48%	11.6103 ± 0.5095 ± 4.39%	31.18 ± 1.39 ± 4.45% External Error ± 1.47 Analytical Error ± 1.36	1.18
Statistics	Statistical F Ratio Error Magnification n	3.00 1.0879 4	Convergence Number of Iterations Calculated Line	0.0001355754 500 Weighted York-2



Inverse Isochron		$39(k)/40(a+r) \pm 2\sigma$	$36(a)/40(a+r) \pm 2\sigma$	r.i.
10C3632	400 °C	0.020509 ± 0.000188	0.002266 ± 0.000055	0.0063
10C3634	500 °C	0.030306 ± 0.000161	0.001636 ± 0.000059	0.0065
10C3635	600 °C	0.068267 ± 0.000337	0.000538 ± 0.000018	0.1131
10C3636	675 °C ✓	0.079003 ± 0.000459	0.000155 ± 0.000027	0.0021
10C3638	750 °C ✓	0.080223 ± 0.000555	0.000110 ± 0.000028	0.0064
10C3639	825 °C ✓	0.081541 ± 0.000376	0.000097 ± 0.000021	0.0082
10C3640	900 °C ✓	0.080988 ± 0.000430	0.000127 ± 0.000030	0.0094
10C3642	975 °C	0.082267 ± 0.000344	0.000155 ± 0.000033	0.0016
10C3643	1050 °C	0.079773 ± 0.000413	0.000307 ± 0.000043	0.0042
10C3644	1150 °C	0.075608 ± 0.000356	0.000547 ± 0.000057	0.0065
10C3646	1275 °C	0.065257 ± 0.000518	0.001000 ± 0.000070	0.0094
10C3647	1400 °C	0.043560 ± 0.000612	0.001916 ± 0.000200	0.0229

Results	$40(a)/36(a) \pm 2\sigma$	$40(r)/39(k) \pm 2\sigma$	Age ± 2σ (Ma)	MSWD
Isochron	552.2685 ± 374.1563 ± 67.75%	11.5971 ± 0.5091 ± 4.39%	31.14 ± 1.38 ± 4.45% External Error ± 1.47 Analytical Error ± 1.36	1.19
Statistics	Statistical F Ratio Error Magnification n	3.00 1.0897 4	Convergence Number of Iterations Calculated Line	0.0000001057 6 Weighted York-2

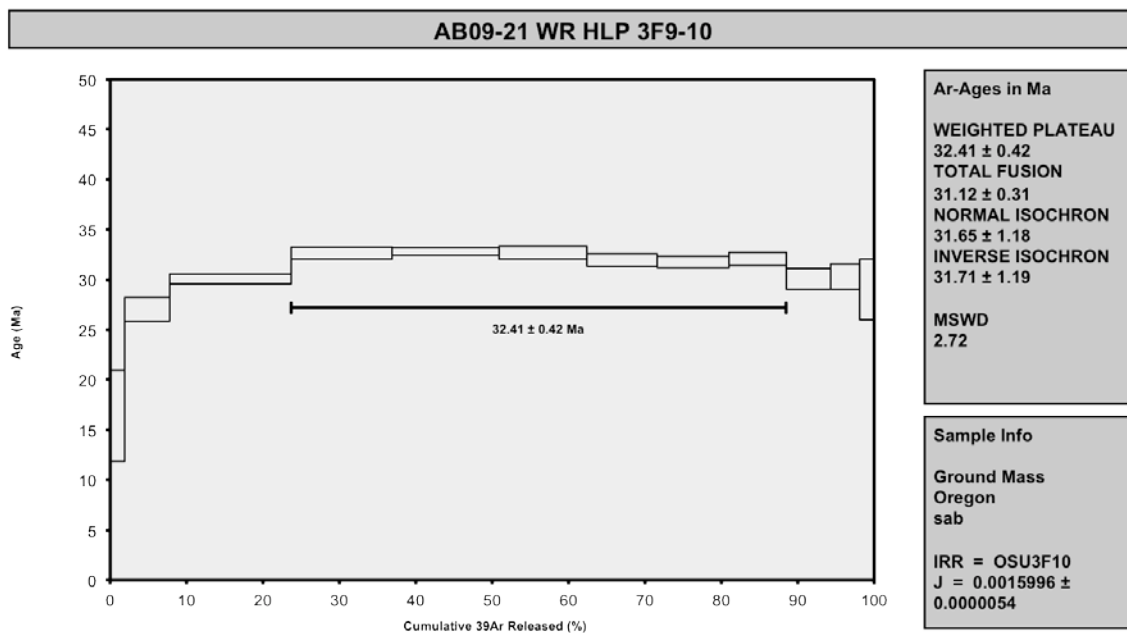


AB09-21

Incremental Heating		36Ar(a)	37Ar(ca)	38Ar(cl)	39Ar(k)	40Ar(r)	Age ± 2σ (Ma)	40Ar(r) (%)	39Ar(k) (%)	K/Ca ± 2σ
10C3580	400 °C	0.000567	0.003112	0.000035	0.001746	0.009969	16.40 ± 4.56	5.61	1.92	0.241 ± 0.012
10C3581	500 °C	0.000696	0.012782	0.000104	0.005370	0.050651	27.02 ± 1.18	19.77	5.91	0.181 ± 0.007
10C3582	600 °C	0.000897	0.064905	0.000234	0.014433	0.151721	30.08 ± 0.50	36.41	15.88	0.096 ± 0.003
10C3584	675 °C ✓	0.000327	0.081573	0.000168	0.012010	0.137077	32.64 ± 0.58	58.67	13.22	0.063 ± 0.002
10C3585	750 °C ✓	0.000220	0.111202	0.000123	0.012640	0.144862	32.77 ± 0.37	68.99	13.91	0.049 ± 0.002
10C3586	825 °C ✓	0.000121	0.113961	0.000078	0.010530	0.120357	32.69 ± 0.65	77.15	11.59	0.040 ± 0.001
10C3588	900 °C ✓	0.000088	0.101679	0.000048	0.008363	0.093383	31.94 ± 0.61	78.28	9.20	0.035 ± 0.001
10C3589	1000 °C ✓	0.000103	0.116114	0.000032	0.008534	0.094833	31.79 ± 0.57	75.69	9.39	0.032 ± 0.001
10C3590	1100 °C ✓	0.000118	0.104122	0.000032	0.006753	0.075668	32.05 ± 0.65	68.38	7.43	0.028 ± 0.001
10C3592	1200 °C	0.000164	0.110788	0.000027	0.005296	0.055645	30.07 ± 1.01	53.45	5.83	0.021 ± 0.001
10C3593	1300 °C	0.000176	0.128157	0.000016	0.003486	0.036894	30.29 ± 1.26	41.53	3.84	0.012 ± 0.000
10C3594	1400 °C	0.000144	0.064614	0.000014	0.001700	0.017229	29.01 ± 3.02	28.76	1.87	0.011 ± 0.000
Σ		0.003620	1.013010	0.000911	0.090860	0.988290				

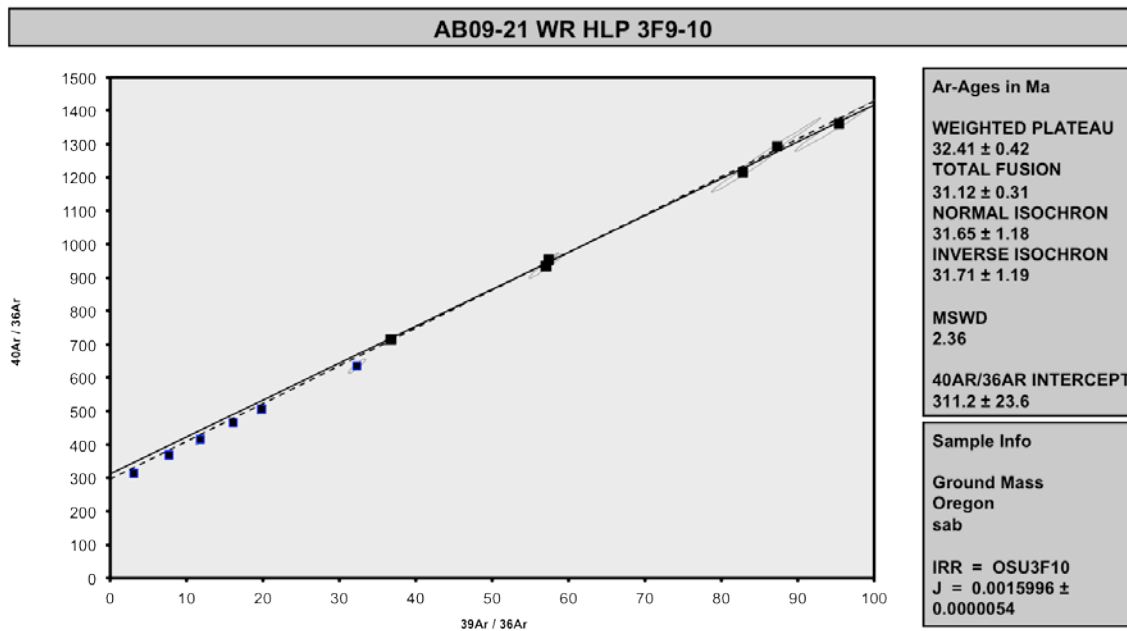
Information on Analysis
AB09-21 WR HLP 3F9-10 Ground Mass Oregon sab
Project = HLP Irradiation = OSU3F10 J = 0.0015996 ± 0.0000054 FCT-3 = 28.030 ± 0.003 Ma

Results	40(r)/39(k) ± 2σ	Age ± 2σ (Ma)	MSWD	39Ar(k) (% , n)	K/Ca ± 2σ
Error Plateau	11.3330 ± 0.1274 ± 1.12%	32.41 ± 0.42 ± 1.30%	2.72	64.75 6	0.036 ± 0.008
		External Error ± 0.67	2.57	Statistical T Ratio	
		Analytical Error ± 0.36	1.6503	Error Magnification	
Total Fusion Age	10.8770 ± 0.0793 ± 0.73%	31.12 ± 0.31 ± 0.99%		12	0.039 ± 0.000
		External Error ± 0.58			
		Analytical Error ± 0.22			



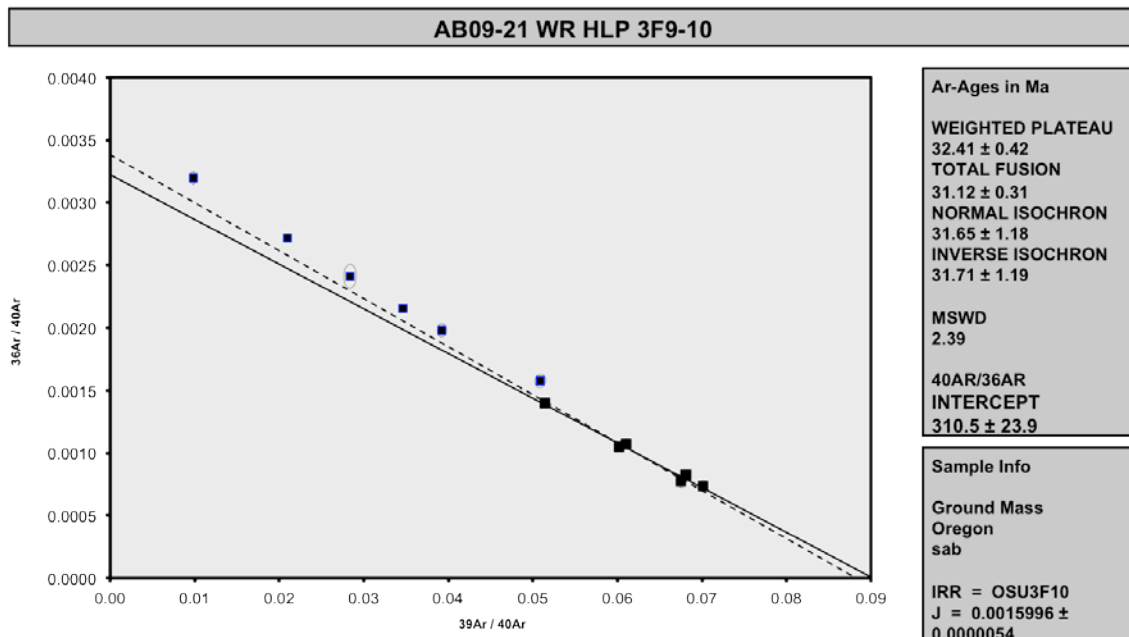
Normal Isochron		39(k)/36(a) ± 2σ	40(a+r)/36(a) ± 2σ	r.i.
10C3580	400 °C	3.1 ± 0.1	313.1 ± 5.2	0.5270
10C3581	500 °C	7.7 ± 0.1	368.3 ± 3.8	0.6641
10C3582	600 °C	16.1 ± 0.2	464.7 ± 4.2	0.9013
10C3584	675 °C ✓	36.8 ± 0.9	715.0 ± 17.0	0.9752
10C3585	750 °C ✓	57.4 ± 1.3	953.1 ± 22.1	0.9849
10C3586	825 °C ✓	87.3 ± 5.7	1293.4 ± 84.2	0.9968
10C3588	900 °C ✓	95.4 ± 5.9	1360.8 ± 83.7	0.9913
10C3589	1000 °C ✓	82.8 ± 4.2	1215.7 ± 60.9	0.9879
10C3590	1100 °C ✓	57.0 ± 2.2	934.7 ± 36.2	0.9719
10C3592	1200 °C	32.3 ± 1.2	634.8 ± 22.0	0.9322
10C3593	1300 °C	19.8 ± 0.6	505.4 ± 13.9	0.8910
10C3594	1400 °C	11.8 ± 0.6	414.8 ± 16.8	0.8326

Results	40(a)/36(a) ± 2σ	40(r)/39(k) ± 2σ	Age ± 2σ (Ma)	MSWD
Isochron	311.2018 ± 23.6444 ± 7.60%	11.0653 ± 0.4088 ± 3.69%	31.65 ± 1.18 ± 3.72% External Error ± 1.28 Analytical Error ± 1.16	2.36
Statistics	Statistical F Ratio	2.37	Convergence	0.0000001062
	Error Magnification	1.5373	Number of Iterations	86
	n	6	Calculated Line	Weighted York-2



Inverse Isochron		39(k)/40(a+r) ± 2σ	36(a)/40(a+r) ± 2σ	r.i.
10C3580	400 °C	0.009833 ± 0.000257	0.003194 ± 0.000053	0.0120
10C3581	500 °C	0.020959 ± 0.000227	0.002715 ± 0.000028	0.0701
10C3582	600 °C	0.034636 ± 0.000144	0.002152 ± 0.000019	0.1054
10C3584	675 °C ✓	0.051406 ± 0.000274	0.001399 ± 0.000033	0.0671
10C3585	750 °C ✓	0.060203 ± 0.000245	0.001049 ± 0.000024	0.0146
10C3586	825 °C ✓	0.067502 ± 0.000354	0.000773 ± 0.000050	0.0286
10C3588	900 °C ✓	0.070106 ± 0.000571	0.000735 ± 0.000045	0.0463
10C3589	1000 °C ✓	0.068113 ± 0.000534	0.000823 ± 0.000041	0.0397
10C3590	1100 °C ✓	0.061032 ± 0.000567	0.001070 ± 0.000041	0.0468
10C3592	1200 °C	0.050871 ± 0.000663	0.001575 ± 0.000055	0.0940
10C3593	1300 °C	0.039239 ± 0.000535	0.001979 ± 0.000055	0.0644
10C3594	1400 °C	0.028389 ± 0.000745	0.002411 ± 0.000098	0.0445

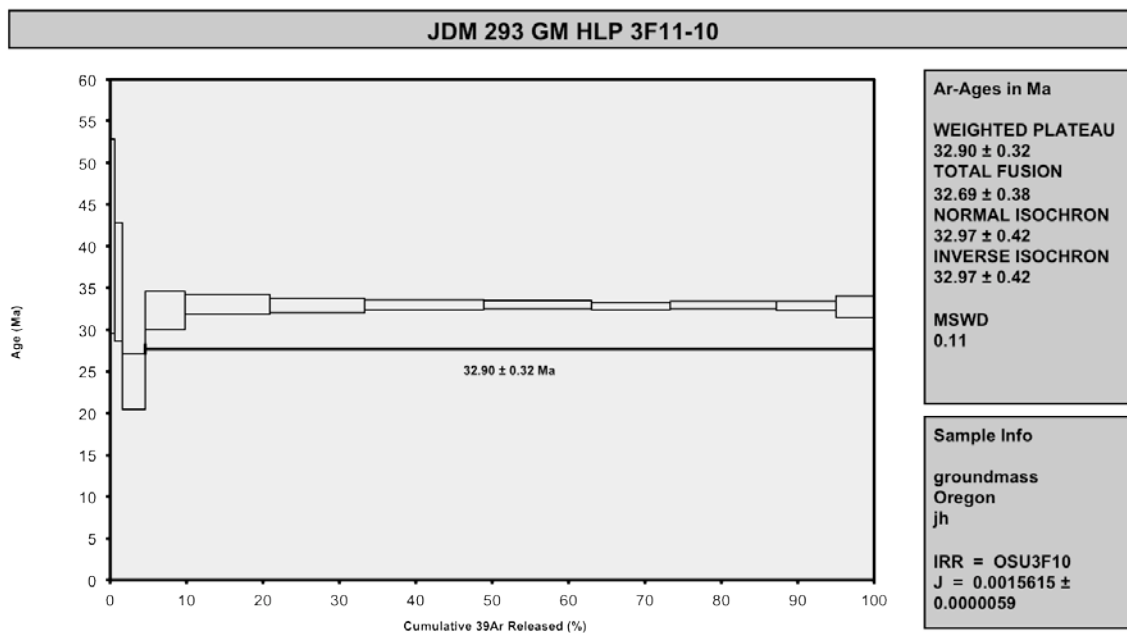
Results	40(a)/36(a) ± 2σ	40(r)/39(k) ± 2σ	Age ± 2σ (Ma)	MSWD
Error Chron	310.5235 ± 23.9157 ± 7.70%	11.0854 ± 0.4113 ± 3.71%	31.71 ± 1.19 ± 3.74% External Error ± 1.29 Analytical Error ± 1.17	2.39
Statistics	Statistical F Ratio Error Magnification n	2.37 1.5448 6	Convergence Number of Iterations Calculated Line	0.000000285 4 Weighted York-2



JDM-293

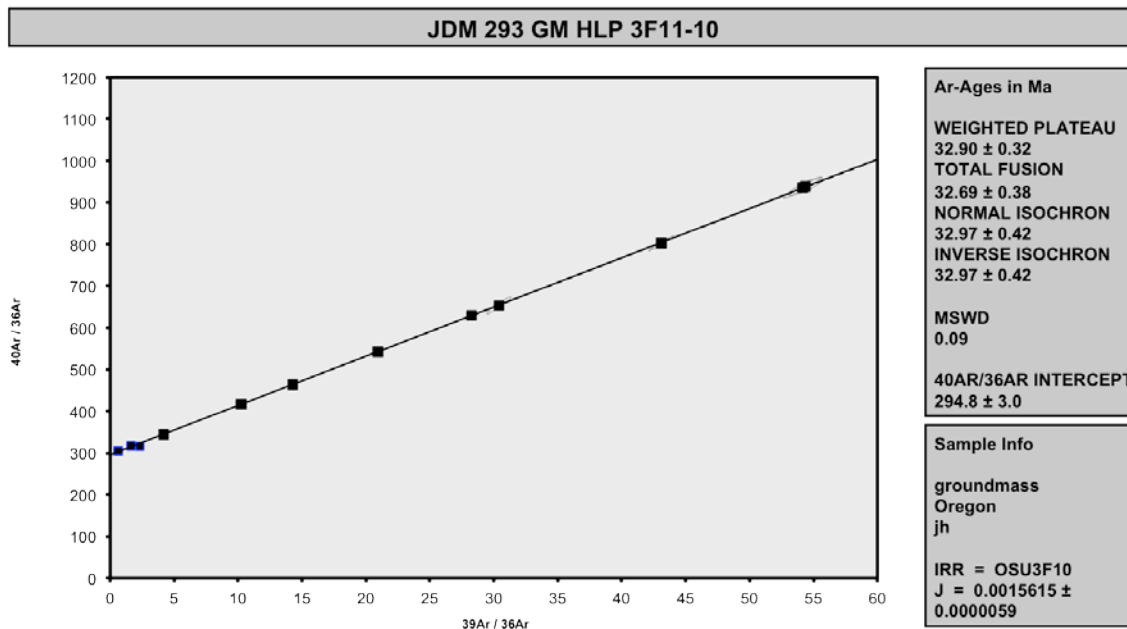
Incremental Heating		36Ar(a)	37Ar(ca)	38Ar(cl)	39Ar(k)	40Ar(r)	Age ± 2σ (Ma)	40Ar(r) (%)	39Ar(k) (%)	K/Ca ± 2σ
10C3721	400 °C	0.001185	0.002171	0.000009	0.000750	0.011094	41.21 ± 11.63	3.07	0.58	0.148 ± 0.007
10C3722	500 °C	0.000797	0.004981	0.000005	0.001301	0.016661	35.73 ± 7.12	6.61	1.00	0.112 ± 0.005
10C3723	600 °C	0.001688	0.019397	0.000016	0.003919	0.033280	23.76 ± 3.32	6.26	3.03	0.087 ± 0.003
10C3725	700 °C ✓	0.001608	0.062368	0.000014	0.006736	0.077882	32.28 ± 2.27	14.08	5.20	0.046 ± 0.002
10C3726	800 °C ✓	0.001397	0.159996	0.000017	0.014329	0.169460	33.01 ± 1.20	29.10	11.07	0.039 ± 0.002
10C3728	875 °C ✓	0.000529	0.114630	0.000013	0.016075	0.189213	32.86 ± 0.88	54.77	12.42	0.060 ± 0.002
10C3729	950 °C ✓	0.000371	0.080179	0.000014	0.020189	0.238523	32.98 ± 0.56	68.49	15.59	0.108 ± 0.005
10C3730	1025 °C ✓	0.000336	0.052365	0.000029	0.018221	0.215222	32.97 ± 0.47	68.40	14.08	0.150 ± 0.006
10C3732	1100 °C ✓	0.000311	0.037053	0.000024	0.013392	0.157382	32.81 ± 0.45	63.16	10.34	0.155 ± 0.006
10C3733	1200 °C ✓	0.000638	0.055339	0.000025	0.018021	0.212845	32.97 ± 0.46	53.03	13.92	0.140 ± 0.005
10C3734	1300 °C ✓	0.000483	0.031080	0.000013	0.010109	0.118924	32.84 ± 0.53	45.46	7.81	0.140 ± 0.005
10C3735	1400 °C ✓	0.000449	0.020391	0.000005	0.006416	0.075282	32.76 ± 1.30	36.19	4.96	0.135 ± 0.005
Σ		0.009791	0.639950	0.000185	0.129459	1.515770				

Information on Analysis	Results	40(r)/39(k) ± 2σ	Age ± 2σ (Ma)	MSWD	39Ar(k) (% , n)	K/Ca ± 2σ
JDM 293 gm HLP 3F11-10 groundmass Oregon jh	Weighted Plateau	11.7865 ± 0.0740 ± 0.63%	32.90 ± 0.32 ± 0.98% External Error ± 0.61 Analytical Error ± 0.20	0.11	95.39 9	0.062 ± 0.026
Project = HLP Irradiation = OSU3F10 J = 0.0015615 ± 0.0000059 FCT-3 = 28.030 ± 0.003 Ma	Total Fusion Age	11.7085 ± 0.1068 ± 0.91%	32.69 ± 0.38 ± 1.18% External Error ± 0.65 Analytical Error ± 0.30	1.0000	Statistical T Ratio Error Magnification	12 0.087 ± 0.001



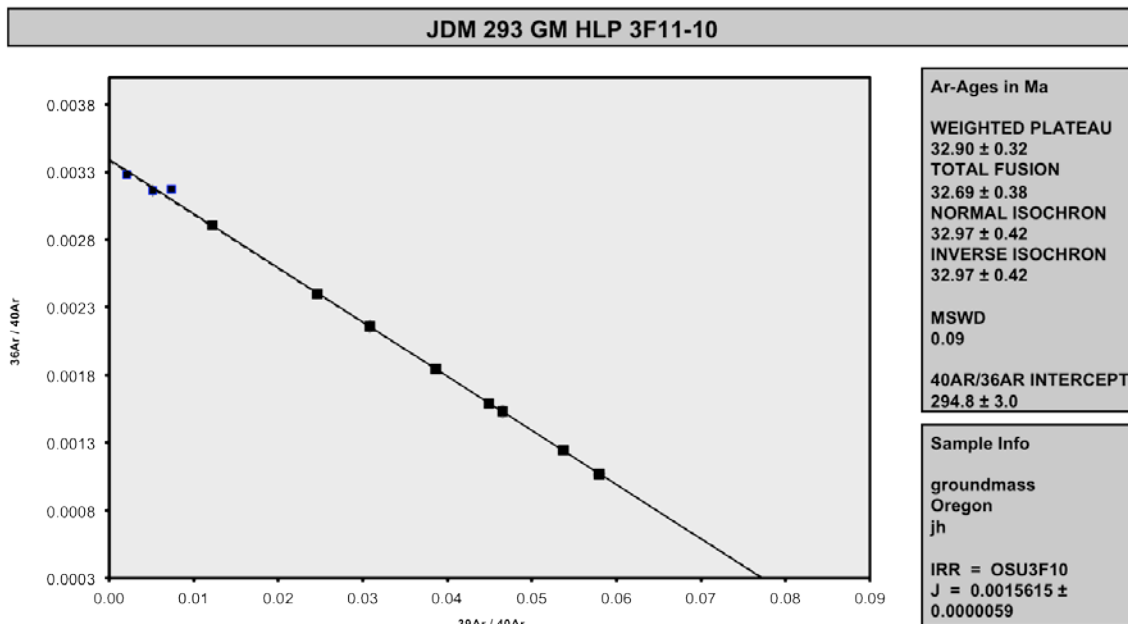
Normal Isochron		39(k)/36(a) ± 2σ	40(a+r)/36(a) ± 2σ	r.i.
10C3721	400 °C	0.6 ± 0.0	304.9 ± 2.7	0.4006
10C3722	500 °C	1.6 ± 0.0	316.4 ± 4.5	0.7835
10C3723	600 °C	2.3 ± 0.0	315.2 ± 3.0	0.9009
10C3725	700 °C ✓	4.2 ± 0.1	343.9 ± 3.9	0.7387
10C3726	800 °C ✓	10.3 ± 0.1	416.8 ± 5.8	0.8505
10C3728	875 °C ✓	30.4 ± 1.0	653.3 ± 20.3	0.9704
10C3729	950 °C ✓	54.4 ± 1.4	938.0 ± 21.5	0.8686
10C3730	1025 °C ✓	54.2 ± 1.5	935.1 ± 25.5	0.9761
10C3732	1100 °C ✓	43.1 ± 1.0	802.2 ± 18.0	0.9860
10C3733	1200 °C ✓	28.2 ± 0.4	629.2 ± 9.1	0.9477
10C3734	1300 °C ✓	20.9 ± 0.3	541.8 ± 7.2	0.9591
10C3735	1400 °C ✓	14.3 ± 0.3	463.1 ± 10.2	0.9492

Results	40(a)/36(a) ± 2σ	40(r)/39(k) ± 2σ	Age ± 2σ (Ma)	MSWD
Isochron	294.7933 ± 2.9643 ± 1.01%	11.8098 ± 0.1232 ± 1.04%	32.97 ± 0.42 ± 1.28% External Error ± 0.67 Analytical Error ± 0.34	0.09
Statistics	Statistical F Ratio Error Magnification n	2.01 1.0000 9	Convergence Number of Iterations Calculated Line	0.000000983 31 Weighted York-2



Inverse Isochron		$39(k)/40(a+r) \pm 2\sigma$	$36(a)/40(a+r) \pm 2\sigma$	r.i.
10C3721	400 °C	0.002076 ± 0.000040	0.003280 ± 0.000030	0.0350
10C3722	500 °C	0.005159 ± 0.000055	0.003160 ± 0.000045	0.0656
10C3723	600 °C	0.007367 ± 0.000033	0.003172 ± 0.000030	0.0335
10C3725	700 °C ✓	0.012181 ± 0.000123	0.002907 ± 0.000033	0.0392
10C3726	800 °C ✓	0.024608 ± 0.000186	0.002399 ± 0.000033	0.2932
10C3728	875 °C ✓	0.046530 ± 0.000358	0.001531 ± 0.000048	0.0370
10C3729	950 °C ✓	0.057977 ± 0.000717	0.001066 ± 0.000024	0.1060
10C3730	1025 °C ✓	0.057910 ± 0.000348	0.001069 ± 0.000029	0.0557
10C3732	1100 °C ✓	0.053745 ± 0.000204	0.001247 ± 0.000028	0.0136
10C3733	1200 °C ✓	0.044901 ± 0.000212	0.001589 ± 0.000023	0.1036
10C3734	1300 °C ✓	0.038648 ± 0.000150	0.001846 ± 0.000024	0.0296
10C3735	1400 °C ✓	0.030842 ± 0.000221	0.002159 ± 0.000048	0.0606

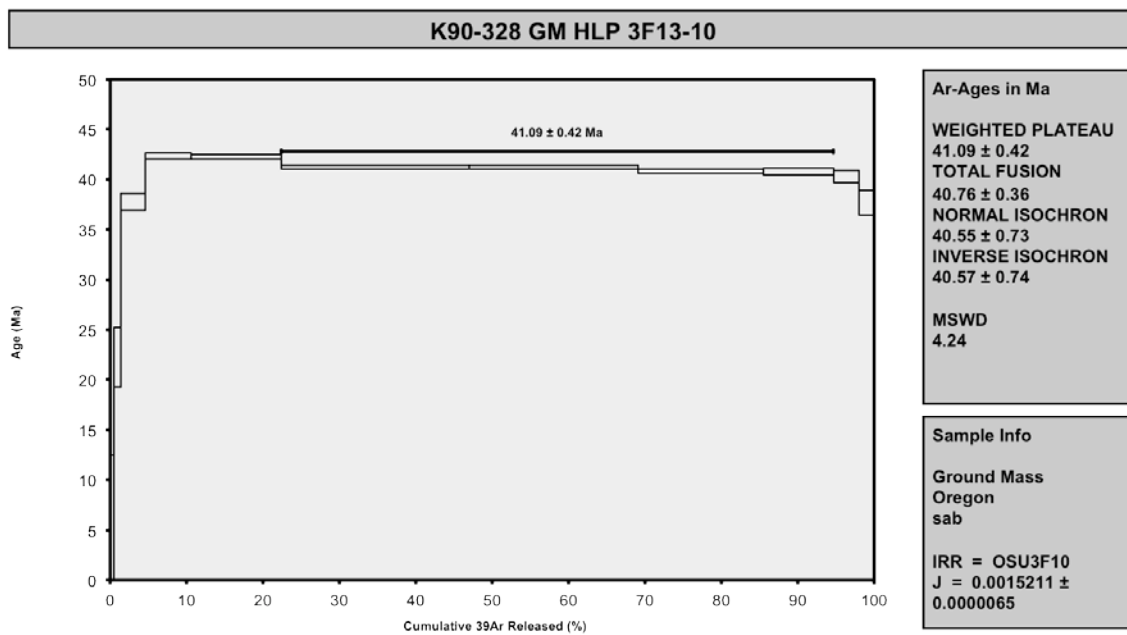
Results	$40(a)/36(a) \pm 2\sigma$	$40(r)/39(k) \pm 2\sigma$	Age ± 2σ (Ma)	MSWD
Isochron	294.7933 ± 2.9648 ± 1.01%	11.8100 ± 0.1232 ± 1.04%	32.97 ± 0.42 ± 1.28% External Error ± 0.67 Analytical Error ± 0.34	0.09
Statistics	Statistical F Ratio Error Magnification n	2.01 1.0000 9	Convergence Number of Iterations Calculated Line	0.000000709 4 Weighted York-2



K90-328

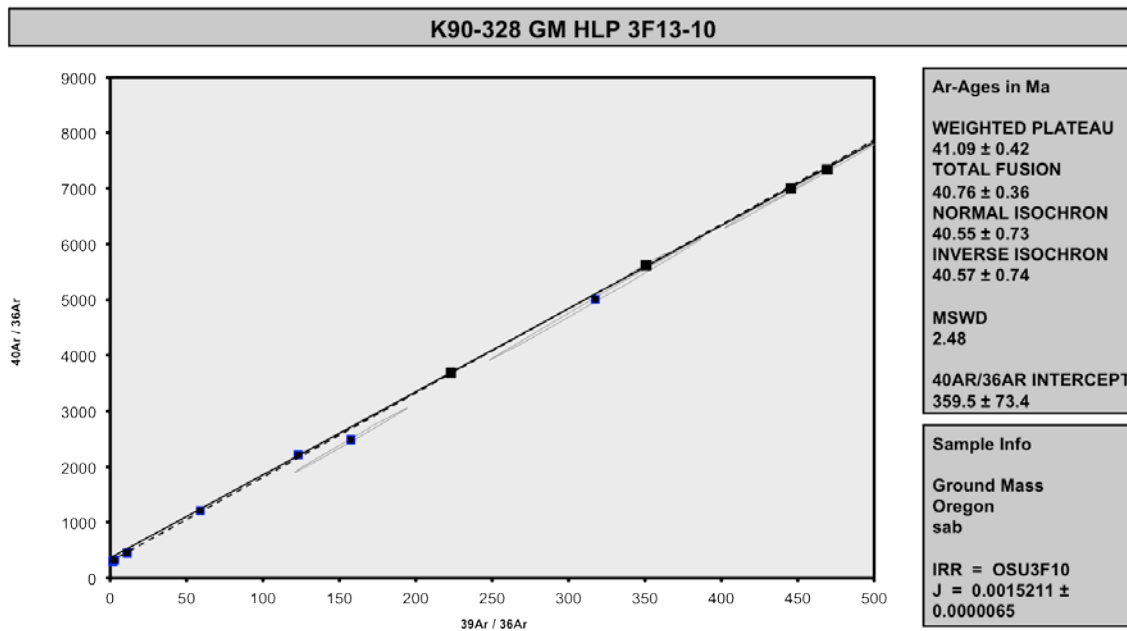
Incremental Heating		36Ar(a)	37Ar(ca)	38Ar(cl)	39Ar(k)	40Ar(r)	Age ± 2σ (Ma)	40Ar(r) (%)	39Ar(k) (%)	K/Ca ± 2σ
10C3649	400 °C	0.000754	0.004469	0.000042	0.001279	0.002541	5.44 ± 7.04	1.13	0.50	0.123 ± 0.005
10C3650	500 °C	0.000748	0.007366	0.000103	0.002188	0.017852	22.26 ± 2.95	7.48	0.85	0.128 ± 0.005
10C3651	600 °C	0.000732	0.022124	0.000289	0.008164	0.113605	37.79 ± 0.84	34.45	3.19	0.159 ± 0.006
10C3653	700 °C	0.000263	0.028829	0.000118	0.015509	0.242309	42.37 ± 0.31	75.71	6.06	0.231 ± 0.009
10C3654	775 °C	0.000246	0.048437	0.000051	0.030252	0.471481	42.27 ± 0.26	86.65	11.82	0.269 ± 0.010
10C3655	850 °C	✓ 0.000282	0.094630	0.000023	0.062811	0.955143	41.25 ± 0.21	91.98	24.53	0.285 ± 0.011
10C3657	925 °C	✓ 0.000161	0.090214	0.000012	0.056636	0.860257	41.21 ± 0.18	94.74	22.12	0.270 ± 0.010
10C3658	1000 °C	✓ 0.000094	0.084345	0.000027	0.041946	0.631146	40.83 ± 0.23	95.77	16.38	0.214 ± 0.008
10C3659	1075 °C	✓ 0.000050	0.059853	0.000009	0.023539	0.353681	40.77 ± 0.35	95.97	9.19	0.169 ± 0.006
10C3662	1275 °C	0.000027	0.067957	0.000005	0.008653	0.128353	40.25 ± 0.62	94.09	3.38	0.055 ± 0.002
10C3664	1400 °C	0.000032	0.052068	0.000010	0.005049	0.070065	37.69 ± 1.25	88.09	1.97	0.042 ± 0.002
Σ		0.003388	0.560294	0.000690	0.256024	3.846432				

Information on Analysis	Results	40(r)/39(k) ± 2σ	Age ± 2σ (Ma)	MSWD	39Ar(k) (% ,n)	K/Ca ± 2σ
K90-328 GM HLP 3F13-10 Ground Mass Oregon sab	Error Plateau	15.1448 ± 0.0858 ± 0.57%	41.09 ± 0.42 ± 1.02%	4.24	72.23 4	0.214 ± 0.053
			External Error ± 0.78 Analytical Error ± 0.23	3.18 2.0601	Statistical T Ratio Error Magnification	
Project = HLP Irradiation = OSU3F10 J = 0.0015211 ± 0.0000065 FCT-3 = 28.030 ± 0.003 Ma	Total Fusion Age	15.0237 ± 0.0401 ± 0.27%	40.76 ± 0.36 ± 0.89%		11	0.196 ± 0.003
			External Error ± 0.74 Analytical Error ± 0.11			



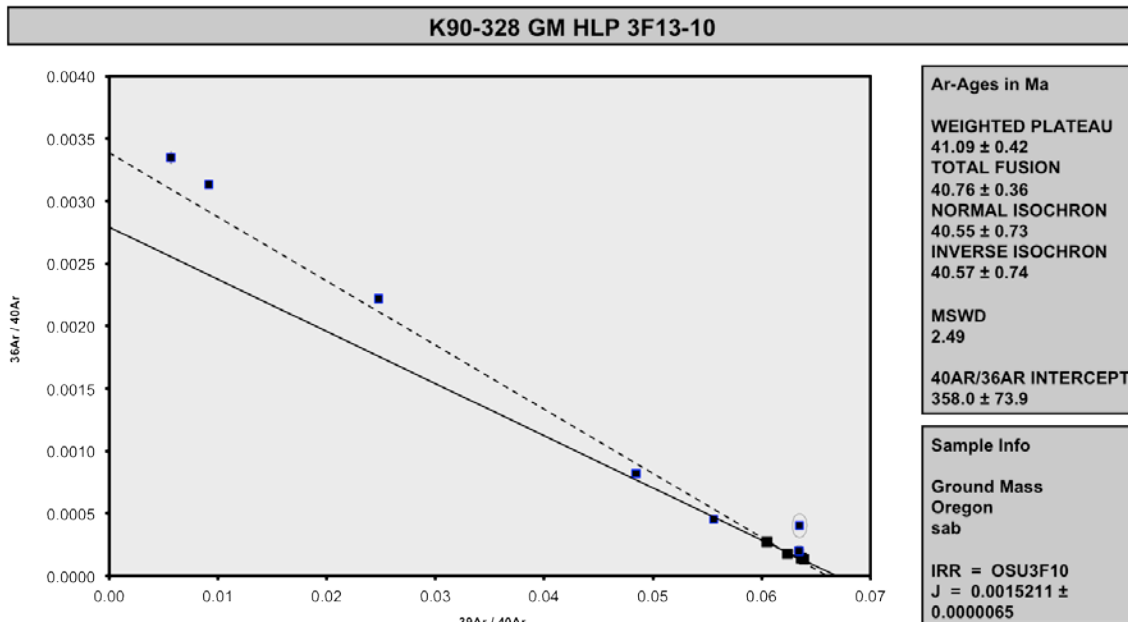
Normal Isochron		39(k)/36(a) ± 2σ	40(a+r)/36(a) ± 2σ	r.i.
10C3649	400 °C	1.7 ± 0.0	298.9 ± 4.4	0.6844
10C3650	500 °C	2.9 ± 0.0	319.4 ± 3.4	0.6560
10C3651	600 °C	11.2 ± 0.1	450.8 ± 5.0	0.8767
10C3653	700 °C	59.0 ± 1.2	1216.6 ± 24.4	0.9846
10C3654	775 °C	123.1 ± 3.9	2214.4 ± 70.5	0.9933
10C3655	850 °C ✓	223.0 ± 4.8	3685.9 ± 77.9	0.9755
10C3657	925 °C ✓	350.7 ± 13.0	5622.7 ± 207.6	0.9946
10C3658	1000 °C ✓	445.6 ± 22.2	7000.2 ± 346.8	0.9942
10C3659	1075 °C ✓	469.4 ± 67.7	7347.7 ± 1060.0	0.9992
10C3662	1275 °C	317.6 ± 69.6	5006.6 ± 1096.9	0.9995
10C3664	1400 °C	157.6 ± 37.0	2482.1 ± 583.1	0.9990

Results	40(a)/36(a) ± 2σ	40(r)/39(k) ± 2σ	Age ± 2σ (Ma)	MSWD
No Convergence	359.4933 ± 73.4363 ± 20.43%	14.9440 ± 0.2393 ± 1.60%	40.55 ± 0.73 ± 1.80% External Error ± 0.97 Analytical Error ± 0.64	2.48
Statistics	Statistical F Ratio Error Magnification n	3.00 1.5741 4	Convergence Number of Iterations Calculated Line	0.0000018366 500 Weighted York-2



Inverse Isochron		$39(k)/40(a+r) \pm 2\sigma$	$36(a)/40(a+r) \pm 2\sigma$	r.i.
10C3649	400 °C	0.005680 ± 0.000088	0.003346 ± 0.000049	0.0164
10C3650	500 °C	0.009162 ± 0.000086	0.003131 ± 0.000033	0.2838
10C3651	600 °C	0.024754 ± 0.000148	0.002218 ± 0.000025	0.0544
10C3653	700 °C	0.048459 ± 0.000170	0.000822 ± 0.000016	0.0590
10C3654	775 °C	0.055601 ± 0.000206	0.000452 ± 0.000014	0.0325
10C3655	850 °C ✓	0.060488 ± 0.000286	0.000271 ± 0.000006	0.0302
10C3657	925 °C ✓	0.062376 ± 0.000239	0.000178 ± 0.000007	0.0475
10C3658	1000 °C ✓	0.063654 ± 0.000342	0.000143 ± 0.000007	0.0094
10C3659	1075 °C ✓	0.063878 ± 0.000375	0.000136 ± 0.000020	0.0360
10C3662	1275 °C	0.063438 ± 0.000451	0.000200 ± 0.000044	0.0115
10C3664	1400 °C	0.063478 ± 0.000677	0.000403 ± 0.000095	0.0036

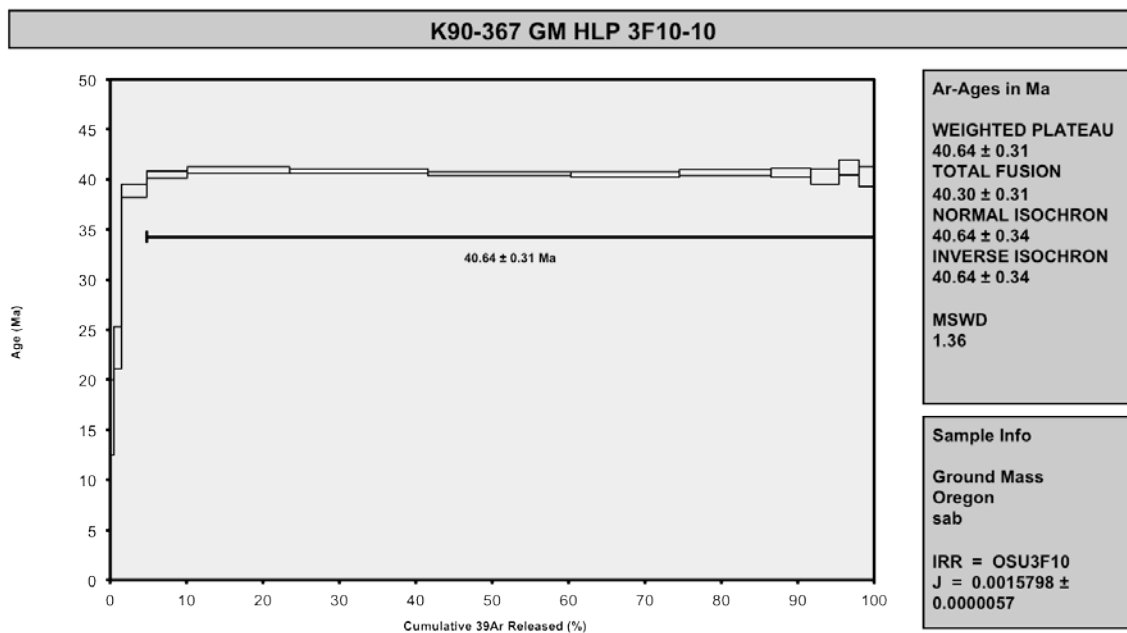
Results	$40(a)/36(a) \pm 2\sigma$	$40(r)/39(k) \pm 2\sigma$	Age ± 2σ (Ma)	MSWD
Isochron	357.9525 ± 73.8682 ± 20.64%	14.9512 ± 0.2420 ± 1.62%	40.57 ± 0.74 ± 1.81% External Error ± 0.98 Analytical Error ± 0.65	2.49
Statistics	Statistical F Ratio Error Magnification n	3.00 1.5792 4	Convergence Number of Iterations Calculated Line	0.000000085 6 Weighted York-2



K90-367

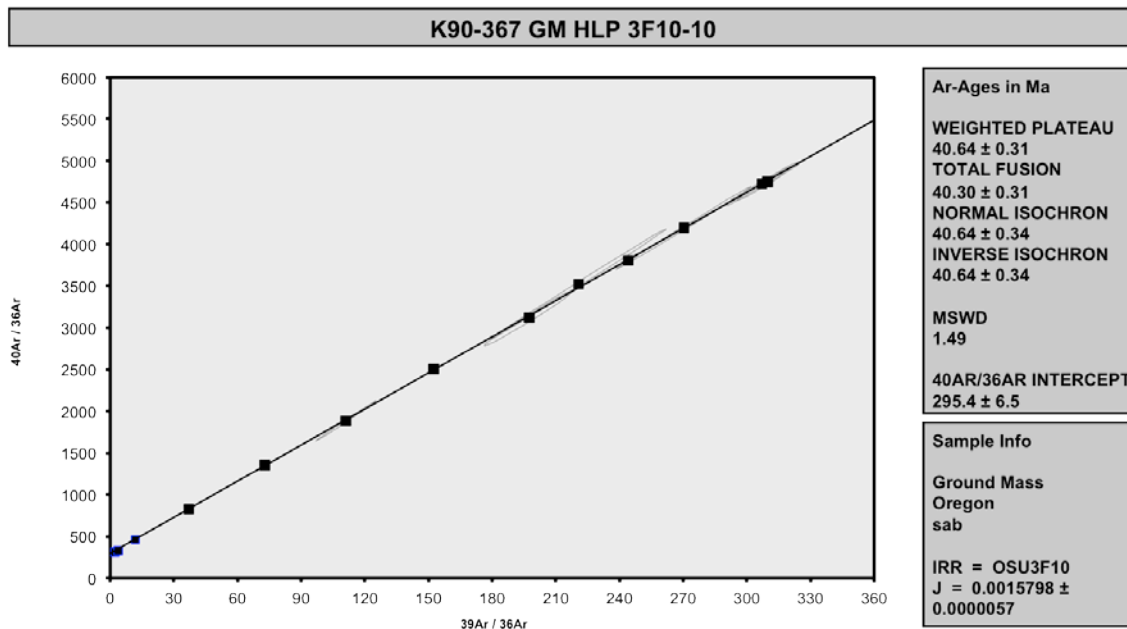
Incremental Heating		36Ar(a)	37Ar(ca)	38Ar(cl)	39Ar(k)	40Ar(r)	Age ± 2σ (Ma)	40Ar(r) (%)	39Ar(k) (%)	K/Ca ± 2σ
10C3614	400 °C	0.000640	0.006743	0.000012	0.001465	0.008387	16.24 ± 3.75	4.25	0.54	0.093 ± 0.004
10C3615	500 °C	0.000671	0.010632	0.000012	0.002566	0.021010	23.19 ± 2.09	9.59	0.94	0.104 ± 0.004
10C3617	600 °C	0.000766	0.032224	0.000012	0.009146	0.126108	38.88 ± 0.62	35.79	3.35	0.122 ± 0.005
10C3618	675 °C ✓	0.000388	0.042778	0.000007	0.014380	0.206479	40.47 ± 0.34	64.31	5.26	0.145 ± 0.005
10C3619	750 °C ✓	0.000502	0.111668	0.000000	0.036602	0.531353	40.91 ± 0.34	78.16	13.40	0.141 ± 0.005
10C3621	825 °C ✓	0.000325	0.128701	0.000037	0.049623	0.718789	40.82 ± 0.21	88.20	18.16	0.166 ± 0.006
10C3622	900 °C ✓	0.000209	0.117460	0.000058	0.051039	0.734065	40.53 ± 0.20	92.23	18.68	0.187 ± 0.007
10C3623	975 °C ✓	0.000125	0.085461	0.000056	0.038773	0.556978	40.48 ± 0.27	93.77	14.19	0.195 ± 0.007
10C3626	1050 °C ✓	0.000107	0.082169	0.000076	0.032852	0.473633	40.63 ± 0.30	93.74	12.02	0.172 ± 0.007
10C3627	1150 °C ✓	0.000052	0.055349	0.000032	0.014036	0.202539	40.67 ± 0.43	92.95	5.14	0.109 ± 0.004
10C3628	1250 °C ✓	0.000052	0.043636	0.000023	0.010259	0.146657	40.29 ± 0.75	90.52	3.75	0.101 ± 0.004
10C3630	1350 °C ✓	0.000032	0.036365	0.000026	0.007113	0.104033	41.21 ± 0.78	91.61	2.60	0.084 ± 0.003
10C3631	1400 °C ✓	0.000049	0.031402	0.000021	0.005390	0.077009	40.27 ± 1.01	84.30	1.97	0.074 ± 0.003
Σ		0.003917	0.784586	0.000372	0.273245	3.907040				

Information on Analysis	Results	40(r)/39(k) ± 2σ	Age ± 2σ (Ma)	MSWD	39Ar(k) (% , n)	K/Ca ± 2σ
K90-367 GM HLP 3F10-10 Ground Mass Oregon sab	Weighted Plateau	14.4206 ± 0.0424 ± 0.29%	40.64 ± 0.31 ± 0.77%	1.36	95.18 10	0.111 ± 0.026
			External Error ± 0.72 Analytical Error ± 0.12	2.26 1.1672	Statistical T Ratio Error Magnification	
Project = HLP Irradiation = OSU3F10 J = 0.0015798 ± 0.0000057 FCT-3 = 28.030 ± 0.003 Ma	Total Fusion Age	14.2986 ± 0.0383 ± 0.27%	40.30 ± 0.31 ± 0.76%		13	0.150 ± 0.002
			External Error ± 0.71 Analytical Error ± 0.11			



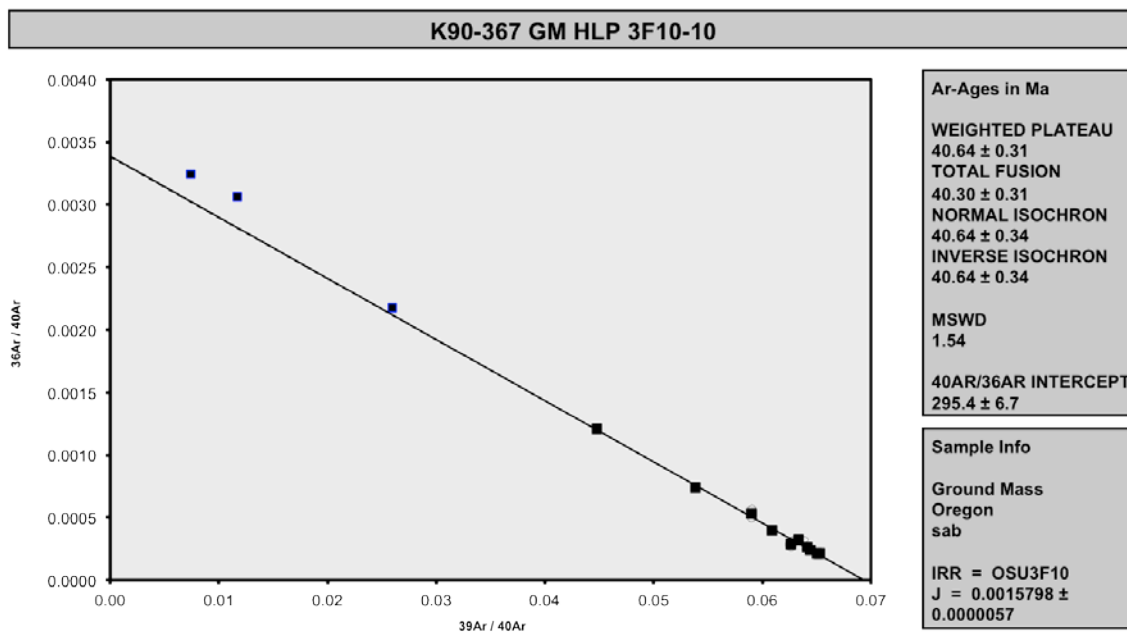
Normal Isochron		39(k)/36(a) ± 2σ	40(a+r)/36(a) ± 2σ	r.i.
10C3614	400 °C	2.3 ± 0.0	308.6 ± 3.2	0.7136
10C3615	500 °C	3.8 ± 0.1	326.8 ± 3.1	0.6402
10C3617	600 °C	11.9 ± 0.1	460.2 ± 3.8	0.8263
10C3618	675 °C ✓	37.1 ± 0.5	827.9 ± 8.8	0.8702
10C3619	750 °C ✓	72.9 ± 1.0	1353.6 ± 16.9	0.8486
10C3621	825 °C ✓	152.5 ± 2.3	2504.5 ± 35.4	0.9438
10C3622	900 °C ✓	244.1 ± 4.6	3806.2 ± 71.9	0.9700
10C3623	975 °C ✓	309.8 ± 14.6	4745.8 ± 222.5	0.9918
10C3626	1050 °C ✓	307.1 ± 17.0	4722.8 ± 260.3	0.9931
10C3627	1150 °C ✓	270.3 ± 31.9	4195.6 ± 495.1	0.9988
10C3628	1250 °C ✓	197.5 ± 21.3	3118.7 ± 336.3	0.9911
10C3630	1350 °C ✓	220.7 ± 41.5	3523.6 ± 662.4	0.9991
10C3631	1400 °C ✓	111.1 ± 14.3	1882.2 ± 242.6	0.9982

Results	40(a)/36(a) ± 2σ	40(r)/39(k) ± 2σ	Age ± 2σ (Ma)	MSWD
Isochron	295.4245 ± 6.5414 ± 2.21%	14.4195 ± 0.0655 ± 0.45%	40.64 ± 0.34 ± 0.84% External Error ± 0.73 Analytical Error ± 0.18	1.49
Statistics	Statistical F Ratio Error Magnification n	1.94 1.2212 10	Convergence Number of Iterations Calculated Line	0.0000001407 255 Weighted York-2



Inverse Isochron		39(k)/40(a+r) ± 2σ	36(a)/40(a+r) ± 2σ	r.i.
10C3614	400 °C	0.007423 ± 0.000067	0.003240 ± 0.000033	0.1301
10C3615	500 °C	0.011705 ± 0.000120	0.003060 ± 0.000029	0.0904
10C3617	600 °C	0.025957 ± 0.000135	0.002173 ± 0.000018	0.1255
10C3618	675 °C ✓	0.044787 ± 0.000268	0.001208 ± 0.000013	0.0132
10C3619	750 °C ✓	0.053847 ± 0.000386	0.000739 ± 0.000009	0.1552
10C3621	825 °C ✓	0.060892 ± 0.000299	0.000399 ± 0.000006	0.0247
10C3622	900 °C ✓	0.064131 ± 0.000298	0.000263 ± 0.000005	0.0964
10C3623	975 °C ✓	0.065279 ± 0.000394	0.000211 ± 0.000010	0.0030
10C3626	1050 °C ✓	0.065022 ± 0.000421	0.000212 ± 0.000012	0.0230
10C3627	1150 °C ✓	0.064418 ± 0.000371	0.000238 ± 0.000028	0.0102
10C3628	1250 °C ✓	0.063323 ± 0.000914	0.000321 ± 0.000035	0.0537
10C3630	1350 °C ✓	0.062641 ± 0.000504	0.000284 ± 0.000053	0.0238
10C3631	1400 °C ✓	0.059005 ± 0.000462	0.000531 ± 0.000068	0.0313

Results	40(a)/36(a) ± 2σ	40(r)/39(k) ± 2σ	Age ± 2σ (Ma)	MSWD
Isochron	295.3722 ± 6.6557 ± 2.25%	14.4221 ± 0.0665 ± 0.46%	40.64 ± 0.34 ± 0.85% External Error ± 0.73 Analytical Error ± 0.19	1.54
Statistics	Statistical F Ratio Error Magnification n	1.94 1.2393 10	Convergence Number of Iterations Calculated Line	0.000000008 4 Weighted York-2



APPENDIX B

Phenocryst Compositions from Electron Microprobe (EMP) Analysis

Table B.1: Electron Microprobe results for olivines from the Western Cascades. All oxides are reported as wt. %.

Sample Name-Grain	SiO ₂	Al ₂ O ₃	K ₂ O	MnO	FeO	NiO	Na ₂ O	MgO	CaO	TiO ₂	Cr ₂ O ₃	Total
ABO9_21-OL1	38.65	0.04	0.00	0.21	17.72	0.17	-0.01	41.81	0.15	0.01	0.03	98.79
ABO9_21-OL1	38.03	0.04	-0.02	0.32	21.99	0.15	0.00	38.69	0.19	0.01	0.03	99.44
ABO9_21-OL2	37.62	0.03	0.00	0.36	25.45	0.05	0.02	36.26	0.18	0.01	0.01	100.00
ABO9_21-OL2	36.79	0.00	0.00	0.42	28.13	0.09	0.02	33.86	0.20	0.03	0.01	99.55
ABO9_21-OL3	37.38	0.02	0.02	0.32	21.67	0.16	0.02	38.51	0.19	0.01	0.02	98.32
ABO9_21-OL3	37.94	0.01	-0.01	0.27	19.60	0.13	0.00	40.21	0.19	0.01	0.01	98.40
ABO9_21-OL3	37.58	0.02	0.00	0.35	21.98	0.16	0.00	38.34	0.17	0.02	0.02	98.62
ABO9_21-OL4	36.79	0.01	-0.01	0.43	29.35	0.07	0.00	32.76	0.22	0.02	0.00	99.66
ABO9_21-OL4	38.22	0.03	0.00	0.37	23.65	0.12	0.00	37.71	0.22	0.02	0.00	100.35
ABO9_21-OL4	37.51	0.00	0.01	0.33	24.63	0.09	0.00	36.66	0.18	0.01	0.01	99.43
ABO9_21-OL6	38.61	0.02	0.00	0.32	20.73	0.12	0.01	40.06	0.19	0.02	-0.02	100.08
ABO9_21-OL6	38.42	0.01	0.00	0.31	20.96	0.12	0.01	39.75	0.19	0.01	0.01	99.79
ABO9_21-OL6	37.84	0.08	0.01	0.34	23.81	0.09	0.02	36.49	0.24	0.01	-0.01	98.93
ABO9_21-OL7	38.38	0.03	0.00	0.29	20.95	0.17	0.00	39.90	0.16	0.01	0.01	99.89
ABO9_21-OL7	37.58	0.02	0.00	0.35	24.80	0.12	0.00	36.20	0.17	0.01	0.03	99.27
ABO9_21-OL8	37.64	0.04	0.00	0.34	24.90	0.07	-0.01	37.05	0.19	0.02	0.02	100.26
ABO9_21-OL8	37.95	0.02	0.01	0.33	23.26	0.07	-0.01	37.80	0.19	0.01	0.01	99.66
ABO9_21-OL5	38.63	0.01	0.01	0.27	19.56	0.15	0.00	40.69	0.20	0.01	-0.01	99.53
ABO9_21-OL5	38.54	0.02	0.02	0.26	19.62	0.11	0.00	40.54	0.19	0.02	0.01	99.32
ABO9_21-OL5	38.48	0.03	-0.02	0.26	20.54	0.15	0.00	39.79	0.18	0.01	0.00	99.44
ABO9_21-OL5	38.70	0.02	0.00	0.26	19.55	0.15	0.02	40.51	0.19	0.01	0.02	99.43
ABO9_21-OL9	37.65	0.01	-0.01	0.34	24.80	0.14	0.00	36.33	0.17	0.01	0.01	99.46

Sample Name-Grain	SiO ₂	Al ₂ O ₃	K ₂ O	MnO	FeO	NiO	Na ₂ O	MgO	CaO	TiO ₂	Cr ₂ O ₃	Total
ABO9_21-OL9	37.07	0.03	0.01	0.40	26.70	0.14	-0.01	34.63	0.18	0.01	0.01	99.18
ABO9_21-OL10	38.71	0.03	-0.01	0.27	18.83	0.19	0.02	41.32	0.18	0.01	0.02	99.60
ABO9_21-OL10	38.20	0.03	-0.01	0.33	21.91	0.11	-0.01	38.36	0.16	0.02	0.01	99.13
ABO9_21-OL11	45.15	33.33	0.04	0.00	0.60	0.02	1.40	0.07	17.67	0.03	0.00	98.33
ABO9_21-OL11	38.20	0.03	0.00	0.38	21.99	0.07	-0.01	38.56	0.19	0.02	0.00	99.44
ABO9_21-OL11	38.04	0.01	-0.01	0.31	21.79	0.08	0.02	38.68	0.19	0.01	0.02	99.15
ABO9_21-OL11	38.02	-0.02	0.00	0.35	22.14	0.08	0.02	38.80	0.19	0.02	0.00	99.62
ABO9_21-OL12	38.76	0.00	-0.01	0.27	20.06	0.14	0.02	40.70	0.17	0.01	0.01	100.13
ABO9_21-OL12	38.71	0.00	0.02	0.27	21.11	0.08	0.01	40.17	0.18	0.01	0.02	100.58
ABO9_21-OL13	38.44	-0.01	0.02	0.32	21.07	0.10	-0.02	39.92	0.17	0.02	0.02	100.07
ABO9_21-OL13	38.13	0.03	0.00	0.30	22.13	0.10	0.02	39.17	0.17	0.00	0.03	100.10
ABO9_14-OL14	35.93	0.02	0.01	0.50	32.70	0.08	0.01	30.08	0.20	0.02	0.01	99.55
ABO9_14-OL14	36.38	0.02	-0.01	0.48	31.33	0.09	-0.01	31.21	0.20	0.02	-0.01	99.74
ABO9_14-OL14	36.42	0.01	0.01	0.48	30.14	0.04	-0.01	31.85	0.21	0.02	0.00	99.17
ABO9_14-OL15	36.31	0.01	0.00	0.53	32.28	0.05	0.01	31.00	0.22	0.02	0.00	100.42
ABO9_14-OL15	35.99	0.01	0.00	0.55	33.16	0.07	0.00	30.47	0.19	0.03	0.02	100.49
ABO9_14-OL15	36.35	0.00	0.00	0.48	32.29	0.07	0.01	31.07	0.20	0.03	0.01	100.50
ABO9_14-OL16	36.81	0.01	0.01	0.47	30.44	0.09	0.01	32.66	0.22	0.02	0.01	100.75
ABO9_14-OL16	36.56	0.00	0.01	0.45	30.36	0.11	0.01	32.32	0.22	0.02	0.02	100.07
ABO9_14-OL16	36.47	0.01	0.01	0.50	30.39	0.09	0.00	32.32	0.21	0.01	-0.02	100.00
ABO9_14-OL17	36.53	0.03	0.00	0.47	30.85	0.12	0.02	31.47	0.22	0.01	0.01	99.71
ABO9_14-OL17	36.39	0.01	0.01	0.53	32.00	0.04	0.02	31.40	0.22	0.00	0.00	100.62
ABO9_14-OL17	35.99	0.01	0.02	0.54	33.51	0.06	0.00	29.96	0.19	0.01	-0.01	100.29
ABO9_14-OL18	35.85	0.02	0.01	0.50	32.27	0.06	0.08	30.28	0.18	0.04	0.02	99.32
ABO9_14-OL18	35.88	0.02	0.01	0.51	32.86	0.07	0.08	30.25	0.19	0.02	-0.01	99.90

Sample Name-Grain	SiO ₂	Al ₂ O ₃	K ₂ O	MnO	FeO	NiO	Na ₂ O	MgO	CaO	TiO ₂	Cr ₂ O ₃	Total
ABO9_14-OL19	36.04	0.02	-0.01	0.54	32.39	0.04	0.01	30.48	0.20	0.01	0.01	99.75
ABO9_14-OL19	35.77	0.01	0.01	0.53	33.65	0.08	-0.01	29.89	0.20	0.00	0.01	100.16
ABO9_14-OL19	35.79	0.07	-0.01	0.49	33.16	0.08	0.01	29.40	0.19	0.04	-0.01	99.25
ABO9_14-OL20	37.38	0.01	0.00	0.39	27.74	0.09	-0.01	34.58	0.24	0.01	0.01	100.47
ABO9_14-OL20	36.10	0.01	0.00	0.49	32.99	0.06	-0.01	30.23	0.19	0.03	-0.01	100.08
ABO9_14-OL20	36.71	0.03	0.01	0.42	29.35	0.10	0.00	32.98	0.23	0.02	0.00	99.85
ABO9_14-OL21	36.99	0.01	0.00	0.50	28.19	0.09	0.00	33.86	0.24	0.01	0.01	99.90
ABO9_14-OL21	36.32	0.05	0.00	0.51	29.69	0.07	0.01	32.06	0.23	0.03	0.00	98.97
ABO9_14-OL21	37.06	0.02	-0.01	0.43	27.71	0.15	0.01	34.06	0.25	0.01	0.01	99.71
ABO9_14-OL22	36.15	0.00	0.01	0.52	32.58	0.05	0.00	30.55	0.24	0.01	0.01	100.13
ABO9_14-OL22	36.09	0.02	0.00	0.50	32.85	0.09	0.00	29.86	0.16	0.03	0.00	99.61
ABO9_14-OL22	36.05	0.01	0.00	0.42	32.90	0.10	0.01	30.58	0.22	0.01	0.00	100.31
ABO9_14-OL23	36.72	-0.01	0.01	0.49	29.73	0.07	0.01	32.73	0.22	0.02	0.00	100.00
ABO9_14-OL23	36.80	0.02	-0.01	0.43	29.14	0.12	0.00	33.36	0.24	0.01	0.02	100.14
ABO9_14-OL23	36.24	-0.01	-0.01	0.49	31.53	0.07	-0.01	31.36	0.17	0.03	-0.01	99.88
ABO9_14-OL24	36.22	0.01	0.01	0.47	30.91	0.06	0.01	31.48	0.24	0.01	0.00	99.43
ABO9_14-OL24	35.99	0.01	0.00	0.50	32.54	0.03	0.01	30.46	0.17	0.04	0.01	99.77
ABO9_14-OL24	36.35	0.02	0.00	0.47	29.98	0.09	0.02	31.85	0.23	0.01	0.00	99.04
ABO9_14-OL25	35.75	0.02	0.00	0.55	33.26	0.09	0.02	30.01	0.19	0.04	0.00	99.92
ABO9_14-OL25	35.57	0.02	0.00	0.56	33.54	0.09	0.00	29.89	0.19	0.03	0.01	99.90
ABO9_14-OL26	36.14	0.00	0.02	0.50	30.52	0.09	0.21	31.29	0.22	0.03	0.01	99.03
ABO9_14-OL26	36.25	0.03	0.02	0.49	30.98	0.04	0.07	31.29	0.23	0.02	0.01	99.43
ABO9_14-OL26	36.18	0.02	0.03	0.53	31.24	0.04	0.01	31.28	0.16	0.03	0.02	99.54
ABO9-17OL1	51.92	3.09	0.18	0.02	5.53	0.06	0.24	24.10	0.88	0.00	-0.01	86.03
ABO9-17OL1	51.54	3.09	0.18	0.06	5.32	0.05	0.25	24.36	0.96	0.01	0.00	85.82

Sample Name-Grain	SiO ₂	Al ₂ O ₃	K ₂ O	MnO	FeO	NiO	Na ₂ O	MgO	CaO	TiO ₂	Cr ₂ O ₃	Total
AB09-17OL1	51.16	3.03	0.21	-0.01	5.35	0.05	0.22	23.72	0.91	0.01	0.01	84.66
AB09-17OL2	49.03	2.87	0.14	0.04	5.68	0.06	0.17	22.48	0.99	0.00	0.01	81.46
AB09-17OL2	50.70	3.54	0.19	0.04	6.76	0.03	0.24	23.54	1.25	0.01	0.00	86.32
AB09-17OL2	15.93	1.06	0.07	0.01	1.69	0.02	0.06	6.97	0.29	0.00	-0.01	26.11
AB09-17OL3	50.70	3.27	0.19	0.08	5.81	0.07	0.21	23.46	1.15	0.00	0.01	84.96
AB09-17OL3	50.93	3.51	0.18	0.07	5.70	0.09	0.16	23.74	1.34	0.01	0.00	85.73
AB09-17OL3	48.93	3.50	0.23	0.09	5.87	-0.01	0.19	22.83	1.25	0.03	0.00	82.93
AB09-17OL4	50.09	8.17	0.34	0.08	10.45	0.05	0.14	16.21	1.52	0.03	0.02	87.11
AB09-17OL4	50.20	2.93	0.23	0.12	7.80	0.04	0.13	22.90	1.08	0.02	0.04	85.50
AB09-17OL4	52.34	2.57	0.17	0.06	6.10	0.09	0.10	23.99	0.94	0.00	0.01	86.37
AB09-17OL5	49.81	3.74	0.17	0.07	6.83	0.04	0.20	22.90	1.13	-0.01	-0.01	84.88
AB09-17OL5	51.06	2.90	0.16	0.07	5.62	0.03	0.14	23.77	0.82	0.00	0.02	84.59
AB09-17OL5	49.84	3.18	0.13	0.11	8.49	0.07	0.15	22.17	1.07	0.02	0.02	85.24
AB09-17OL6	51.29	3.33	0.13	0.15	6.85	0.08	0.17	23.61	1.22	0.00	-0.01	86.83
AB09-17OL6	51.14	3.60	0.19	0.07	6.62	0.00	0.20	22.87	1.14	0.02	-0.02	85.87
AB09-17OL6	48.82	5.52	0.21	0.10	11.07	0.09	0.15	19.87	1.46	0.03	0.03	87.33
AB09-19OL7	36.53	0.01	0.00	0.42	31.05	0.07	0.00	31.78	0.24	0.02	0.02	100.16
AB09-19OL7	36.32	0.00	0.01	0.41	29.91	0.05	0.02	31.96	0.23	0.03	0.00	98.94
AB09-19OL7	35.80	0.04	0.00	0.42	28.54	0.10	0.03	31.64	0.26	0.02	0.01	96.84
AB09-19OL7	36.08	0.02	0.02	0.40	28.11	0.12	0.04	31.25	0.23	0.02	0.00	96.28
AB09-19OL7	34.72	0.01	-0.01	0.49	32.29	0.04	0.01	27.67	0.20	0.02	0.00	95.45
AB09-19OL8	36.95	0.04	0.01	0.42	28.07	0.11	0.01	33.75	0.22	0.01	0.02	99.61
AB09-19OL8	36.78	0.03	-0.01	0.44	29.07	0.10	-0.01	32.59	0.24	0.00	0.03	99.28
AB09-19OL8	36.76	-0.02	0.00	0.45	29.54	0.08	0.01	32.87	0.25	0.00	0.05	100.00
AB09-19OL8	36.50	0.02	0.00	0.45	29.74	0.09	-0.02	32.47	0.23	0.02	0.00	99.53

Sample Name-Grain	SiO ₂	Al ₂ O ₃	K ₂ O	MnO	FeO	NiO	Na ₂ O	MgO	CaO	TiO ₂	Cr ₂ O ₃	Total
AB09-19OL9	36.80	0.03	0.00	0.39	27.60	0.07	0.01	34.17	0.25	0.00	0.02	99.34
AB09-19OL9	36.88	0.04	0.00	0.40	28.21	0.07	0.00	33.32	0.25	0.00	0.04	99.22
AB09-19OL9	36.65	0.03	-0.01	0.41	28.83	0.10	0.00	33.51	0.24	0.01	0.02	99.78
AB09-19OL9	36.86	0.02	-0.01	0.46	28.43	0.06	0.02	33.42	0.24	-0.01	0.02	99.53
AB09-19OL9	37.02	0.03	0.01	0.39	27.87	0.07	0.00	33.84	0.24	0.01	-0.02	99.49
AB09-19OL9	36.46	0.00	-0.01	0.44	29.33	0.08	0.02	32.38	0.24	0.02	0.02	98.98
AB09-19OL10	36.89	0.03	-0.02	0.41	28.90	0.13	0.01	33.45	0.25	0.02	0.00	100.10
AB09-19OL10	37.12	0.02	0.01	0.37	25.95	0.16	-0.01	35.88	0.22	0.01	0.02	99.76
AB09-19OL10	35.83	0.02	0.01	0.47	33.40	0.04	0.02	29.76	0.24	0.02	0.02	99.82
AB09-19OL11	36.41	0.02	0.01	0.46	31.72	0.06	0.01	30.49	0.25	0.00	0.02	99.46
AB09-19OL11	36.66	0.01	-0.01	0.42	29.35	0.09	0.01	32.73	0.25	0.01	0.01	99.52
AB09-19OL11	36.05	-0.02	0.01	0.45	33.25	0.09	-0.03	29.82	0.17	0.03	-0.01	99.87
AB09-19OL11	36.28	0.00	0.01	0.48	32.94	0.05	-0.01	29.51	0.22	0.04	-0.01	99.52
AB09-19OL12	36.39	0.01	0.00	0.44	31.32	0.10	0.00	31.73	0.25	0.01	0.00	100.25
AB09-19OL12	36.09	0.03	0.00	0.42	31.48	0.05	0.00	30.98	0.24	0.02	0.00	99.32
AB09-19OL13	36.85	0.03	0.00	0.45	29.76	0.15	0.01	32.31	0.25	0.02	0.02	99.84
AB09-19OL13	36.50	0.05	0.01	0.46	30.66	0.04	0.01	32.09	0.26	0.02	0.02	100.10
AB09-19OL13	36.03	0.01	0.01	0.43	32.59	0.08	-0.02	30.68	0.25	0.02	0.01	100.11
AB09-19OL14	37.14	0.02	0.01	0.42	29.19	0.08	0.01	32.83	0.24	0.01	-0.01	99.95
AB09-19OL14	36.98	0.02	0.00	0.40	29.57	0.05	-0.01	32.73	0.26	0.00	0.01	100.03
AB09-19OL14	36.63	0.01	0.00	0.46	31.14	0.13	0.00	31.54	0.23	0.02	0.02	100.19
AB09-19OL15	37.75	0.02	0.00	0.40	26.06	0.15	0.00	35.58	0.20	0.01	0.02	100.19
AB09-19OL15	37.27	0.05	0.00	0.40	26.30	0.10	-0.02	35.28	0.24	0.00	0.01	99.65
AB09-19OL15	36.53	0.01	0.00	0.48	31.83	0.10	0.00	31.38	0.25	0.02	0.03	100.64
AB09-19OL15	37.22	0.01	0.00	0.40	28.66	0.07	0.00	33.14	0.24	0.01	0.01	99.77

Sample Name-Grain	SiO ₂	Al ₂ O ₃	K ₂ O	MnO	FeO	NiO	Na ₂ O	MgO	CaO	TiO ₂	Cr ₂ O ₃	Total
AB09-19OL16	36.68	0.02	-0.01	0.46	29.67	0.07	-0.01	32.89	0.25	0.02	0.02	100.07
AB09-19OL16	36.44	0.04	0.01	0.46	29.63	0.09	0.00	32.73	0.26	0.01	0.03	99.70
AB09-19OL16	35.89	0.03	0.01	0.46	31.64	0.08	0.00	31.21	0.26	0.01	0.01	99.60
AB09-19OL17	37.30	0.02	0.00	0.38	26.91	0.12	0.01	34.91	0.26	0.01	0.02	99.94
AB09-19OL17	36.54	0.01	0.01	0.45	29.78	0.06	0.01	32.44	0.23	0.01	0.03	99.59
AB09-19OL17	36.60	0.02	0.01	0.43	30.59	0.10	0.03	32.34	0.25	0.02	0.03	100.40
AB09-19OL18	36.23	0.03	0.01	0.45	31.22	0.02	0.03	31.22	0.24	0.02	0.01	99.49
AB09-19OL18	43.97	4.04	0.29	0.15	13.04	-0.03	0.07	17.42	1.37	0.01	0.04	80.40
AB09-19OL18	36.47	0.03	0.00	0.50	30.51	0.11	0.01	31.91	0.25	0.02	0.00	99.81
AB09-19OL18	36.50	0.03	0.00	0.42	28.74	0.10	-0.02	33.44	0.24	0.00	0.03	99.50
AB09-19OL19	36.81	0.04	-0.01	0.43	29.73	0.07	0.00	32.43	0.25	0.01	0.00	99.79
AB09-19OL19	36.24	0.02	0.00	0.47	31.23	0.08	0.00	31.20	0.24	0.02	0.01	99.52
AB09-19OL20	36.99	0.06	0.02	0.42	29.48	0.03	0.00	33.30	0.23	0.03	0.04	100.59
AB09-19OL20	36.02	0.03	0.00	0.46	32.94	0.05	0.00	30.67	0.24	0.02	0.01	100.44
AB09-19OL20	36.29	0.03	0.01	0.48	31.22	0.15	0.01	31.85	0.22	0.03	0.02	100.30
AB09-19OL21	37.11	0.00	-0.01	0.39	27.37	0.17	0.01	34.73	0.23	0.02	0.02	100.05
AB09-19OL21	37.18	0.03	-0.01	0.47	27.80	0.10	0.00	34.78	0.22	0.01	0.02	100.62
AB09-19OL21	36.74	0.03	0.00	0.47	31.36	0.10	-0.01	32.03	0.25	0.01	0.01	101.00
AB09-19OL21	36.96	0.01	-0.01	0.43	28.49	0.13	0.00	33.96	0.23	0.00	-0.01	100.22
AB09-19OL22	36.68	0.02	-0.01	0.44	29.94	0.11	0.01	32.43	0.26	0.00	-0.01	99.89
AB09-19OL22	43.33	4.98	0.10	0.19	16.02	0.04	0.05	16.58	1.71	0.06	0.04	83.10
AB09-19OL22	36.50	0.03	0.00	0.44	29.77	0.06	-0.01	32.92	0.25	0.00	0.03	100.00
AB09-19OL22	36.51	0.04	0.00	0.46	32.20	0.12	0.01	31.05	0.23	0.02	0.01	100.65
AB09-19OL23	36.25	0.01	0.01	0.46	31.24	0.04	0.01	31.54	0.24	0.03	0.02	99.85
AB09-19OL23	36.33	0.01	-0.01	0.42	30.19	0.08	-0.01	32.71	0.26	0.02	0.00	100.02

Sample Name-Grain	SiO ₂	Al ₂ O ₃	K ₂ O	MnO	FeO	NiO	Na ₂ O	MgO	CaO	TiO ₂	Cr ₂ O ₃	Total
AB09-19OL23	36.97	-0.01	-0.01	0.41	29.49	0.14	0.00	33.74	0.24	0.01	0.03	101.02

Table B.2: Electron Microprobe results for clinopyroxenes from the Western Cascades. All oxides are reported as wt. %.

Sample Name-Grain	SiO ₂	Al ₂ O ₃	K ₂ O	FeO	Na ₂ O	MgO	TiO ₂	CaO	MnO	Cr ₂ O ₃	NiO	Total
AB09-22_PYX1	51.72	3.71	0.01	9.02	0.32	17.16	0.64	16.96	0.21	0.35	-0.05	100.10
AB09-22_PYX1	51.84	2.98	0.00	9.56	0.26	17.66	0.58	16.06	0.21	0.35	0.02	99.52
AB09-22_PYX1	52.27	2.93	-0.01	10.26	0.27	17.87	0.51	16.17	0.24	0.11	0.07	100.71
AB09-22_PYX2	51.77	3.34	-0.01	9.34	0.31	16.88	0.62	16.92	0.27	0.33	0.05	99.83
AB09-22_PYX2	51.21	3.39	0.00	10.41	0.28	17.23	0.73	15.61	0.22	0.30	0.09	99.46
AB09-22_PYX2	52.06	3.08	0.00	9.47	0.26	17.14	0.57	16.71	0.23	0.34	0.02	99.89
AB09-22_PYX3	52.44	3.23	0.00	9.36	0.28	17.79	0.53	15.94	0.28	0.23	0.05	100.14
AB09-22_PYX3	51.82	3.22	0.00	9.22	0.26	16.90	0.59	17.08	0.21	0.34	-0.03	99.63
AB09-22_PYX3	52.47	16.73	0.45	8.64	3.31	8.03	0.76	7.86	0.19	0.02	0.02	98.49
AB09-22_PYX4	52.51	2.86	0.01	9.47	0.28	17.99	0.53	16.59	0.17	0.30	0.01	100.71
AB09-22_PYX4	51.68	3.38	-0.01	9.80	0.29	17.63	0.59	17.06	0.22	0.34	-0.01	101.00
AB09-22_PYX4	52.07	3.13	0.01	9.45	0.28	18.02	0.56	16.32	0.22	0.30	-0.01	100.36
AB09-22_PYX5	53.07	2.44	0.01	9.99	0.26	18.37	0.49	16.16	0.31	0.19	-0.05	101.27
AB09-22_PYX5	52.07	3.16	0.00	9.41	0.28	17.33	0.57	17.14	0.21	0.29	0.07	100.52
AB09-22_PYX6	52.03	3.42	-0.01	9.89	0.28	17.14	0.64	17.19	0.22	0.28	0.00	101.07
AB09-22_PYX6	51.38	3.62	0.00	10.32	0.28	16.98	0.70	16.98	0.27	0.30	-0.11	100.83
AB09-22_PYX6	51.19	2.08	-0.01	9.37	0.22	17.56	0.42	15.08	0.22	0.14	-0.08	96.30
AB09-22_PYX7	51.07	2.10	0.01	9.01	0.24	17.62	0.44	15.50	0.21	0.15	0.03	96.37

Sample Name-Grain	SiO ₂	Al ₂ O ₃	K ₂ O	FeO	Na ₂ O	MgO	TiO ₂	CaO	MnO	Cr ₂ O ₃	NiO	Total
AB09-22_PYX8	51.49	3.77	0.00	10.07	0.31	16.96	0.72	16.90	0.17	0.30	0.00	100.71
AB09-22_PYX8	55.45	2.18	-0.01	14.69	0.05	28.84	0.26	1.96	0.30	0.06	0.02	103.82
AB09-22_PYX8	55.69	1.96	-0.01	14.38	0.05	28.72	0.27	2.04	0.28	0.08	0.01	103.48
AB09-22_PYX9	51.66	3.40	-0.01	9.55	0.32	17.29	0.62	16.98	0.29	0.25	0.01	100.38
AB09-22_PYX9	52.65	3.23	0.01	9.44	0.29	17.47	0.55	16.94	0.20	0.27	0.08	101.15
AB09-22_PYX9	52.96	2.62	0.01	9.85	0.29	18.11	0.48	16.33	0.27	0.26	-0.02	101.18
AB09-22_PYX10	53.03	2.78	0.00	9.10	0.29	18.09	0.44	16.92	0.24	0.17	0.09	101.15
AB09-22_PYX10	50.74	2.37	0.00	9.20	0.25	17.23	0.43	15.28	0.17	0.13	0.02	95.82
AB09-22_PYX10	52.36	3.31	0.00	9.07	0.29	17.19	0.56	17.48	0.17	0.35	-0.01	100.78
AB09-22_PYX11	40.06	0.02	0.00	21.51	0.02	42.52	0.02	0.22	0.35	0.02	-0.06	104.74
AB09-22_PYX11	51.85	3.57	-0.01	9.61	0.32	17.09	0.63	16.89	0.20	0.15	-0.14	100.31
AB09-22_PYX11	53.02	2.31	0.01	10.98	0.23	19.28	0.47	14.04	0.31	0.20	-0.05	100.85
AB09-18_PYX12	53.60	2.12	0.02	8.69	0.19	17.91	0.35	17.27	0.20	0.17	-0.07	100.50
AB09-18_PYX12	53.02	2.59	0.01	8.62	0.23	17.47	0.37	17.57	0.14	0.10	-0.07	100.12
AB09-18_PYX12	52.81	2.79	0.00	8.92	0.23	17.47	0.39	17.29	0.25	0.22	0.02	100.37
AB09-18_PYX13	52.93	2.50	-0.01	8.84	0.22	17.73	0.37	17.23	0.16	0.23	-0.02	100.21
AB09-18_PYX13	52.63	2.94	-0.01	9.55	0.24	17.46	0.42	16.73	0.26	0.18	0.04	100.45
AB09-18_PYX13	51.98	3.34	0.02	9.42	0.26	16.99	0.48	17.85	0.23	0.19	-0.03	100.75
AB09-18_PYX14	52.05	3.18	0.00	9.57	0.21	16.80	0.55	17.72	0.26	0.22	0.04	100.61
AB09-18_PYX14	52.59	3.04	0.01	9.28	0.27	17.52	0.43	16.85	0.21	0.18	-0.05	100.39
AB09-18_PYX14	52.90	2.44	0.00	8.78	0.21	17.79	0.36	17.38	0.23	0.11	0.02	100.24
AB09-18_PYX15	53.23	2.34	-0.01	9.37	0.20	18.14	0.36	16.61	0.27	0.14	0.15	100.82
AB09-18_PYX15	53.31	1.94	0.01	9.58	0.22	18.33	0.37	16.32	0.22	0.13	-0.04	100.41
AB09-18_PYX16	52.88	2.11	-0.01	8.20	0.20	17.84	0.34	17.95	0.23	0.21	-0.03	99.95
AB09-18_PYX16	52.87	2.36	0.01	8.00	0.19	17.72	0.33	18.01	0.17	0.28	0.00	99.95

Sample Name-Grain	SiO ₂	Al ₂ O ₃	K ₂ O	FeO	Na ₂ O	MgO	TiO ₂	CaO	MnO	Cr ₂ O ₃	NiO	Total
AB09-18_PYX16	52.66	2.55	0.03	7.87	0.22	17.60	0.34	18.39	0.24	0.26	0.11	100.26
AB09-18_PYX17	53.43	2.25	0.01	7.89	0.22	17.82	0.33	17.79	0.21	0.24	-0.04	100.21
AB09-18_PYX17	49.68	3.43	0.00	8.08	0.22	15.78	0.48	16.54	0.14	0.38	0.00	94.72
AB09-18_PYX17	52.99	2.94	0.01	8.36	0.21	17.53	0.37	18.11	0.16	0.30	0.05	101.05
AB09-22_PYX18	52.33	3.19	0.00	8.88	0.26	17.45	0.46	17.59	0.25	0.23	-0.01	100.62
AB09-22_PYX18	50.68	2.41	0.03	7.28	0.19	16.45	0.33	16.91	0.18	0.26	0.02	94.72
AB09-22_PYX18	53.15	2.13	-0.01	7.89	0.19	17.94	0.34	18.16	0.18	0.20	0.04	100.21
AB09-22_PYX19	52.14	3.04	0.00	8.16	0.25	17.38	0.39	18.30	0.13	0.29	0.04	100.12
AB09-22_PYX19	51.24	2.75	0.00	11.90	0.26	16.93	0.57	16.30	0.36	0.13	-0.05	100.44
AB09-22_PYX19	51.98	3.41	0.00	8.55	0.22	17.31	0.45	17.80	0.21	0.35	-0.02	100.29
AB09-22_PYX20	52.71	3.31	0.01	8.78	0.25	16.96	0.48	17.94	0.23	0.19	-0.01	100.85
AB09-22_PYX20	51.32	3.53	0.03	8.84	0.23	16.56	0.47	17.66	0.18	0.29	0.07	99.19
AB09-22_PYX20	52.96	3.08	-0.01	9.11	0.25	17.25	0.44	17.40	0.24	0.22	-0.09	100.96
AB09-22_PYX21	52.80	2.63	0.00	8.92	0.24	17.95	0.35	17.49	0.23	0.20	-0.03	100.81
AB09-22_PYX21	51.92	3.98	-0.02	7.72	0.25	16.45	0.49	18.84	0.19	0.41	-0.08	100.25
AB09-22_PYX21	53.60	2.16	0.01	8.40	0.19	17.78	0.34	17.55	0.27	0.15	-0.04	100.45
AB09-22_PYX21	53.37	2.22	0.00	8.72	0.23	17.72	0.35	17.71	0.18	0.15	-0.08	100.64

Table B.3: Electron Microprobe results for orthopyroxenes from the Western Cascades. All oxides are reported as wt. %.

Sample Name-Grain	SiO ₂	Al ₂ O ₃	K ₂ O	FeO	Na ₂ O	MgO	TiO ₂	CaO	MnO	Cr ₂ O ₃	NiO	Total
AB09-20APYX1	1.49	0.13	0.03	0.03	0.54	0.07	-0.01	-0.52	0.03	0.02	116.28	118.62
AB09-20APYX1	49.22	5.97	0.02	9.90	0.30	14.43	1.38	17.73	0.19	0.21	-0.07	99.34
AB09-20APYX1	50.95	3.04	0.20	12.62	0.26	14.84	0.76	16.30	0.29	0.03	0.05	99.32
AB09-20APYX1	51.35	2.83	0.00	13.05	0.28	15.16	0.83	16.88	0.27	0.06	-0.02	100.70
AB09-20APYX2	55.01	28.46	0.49	1.34	5.05	0.15	0.13	9.94	-0.04	-0.01	0.05	100.61
AB09-20APYX3	52.10	2.37	0.04	12.35	0.24	16.75	0.66	15.04	0.27	0.01	0.06	99.89
AB09-20APYX4	37.13	1.63	0.05	38.20	0.12	11.27	6.67	4.10	0.53	0.01	0.02	99.72
AB09-20APYX6	49.18	5.13	0.07	10.06	0.29	14.94	1.25	18.14	0.20	0.21	-0.06	99.46
AB09-20APYX6	51.71	30.80	0.19	1.32	3.62	0.08	0.07	12.41	0.07	-0.01	-0.04	100.26
AB09-20APYX7	51.02	3.34	0.00	10.81	0.30	15.96	0.89	17.51	0.22	0.07	0.01	100.13
AB09-20APYX7	53.17	19.41	0.37	5.42	4.54	4.04	0.35	11.54	0.17	0.01	0.00	99.01
AB09-20APYX8	52.09	1.76	0.01	13.02	0.29	15.93	0.74	15.98	0.33	0.01	-0.02	100.15
AB09-20APYX9	45.54	0.41	0.02	31.28	0.02	25.45	0.22	2.09	0.51	0.00	-0.01	105.54
AB09-20APYX10	51.61	2.08	0.00	11.17	0.20	17.77	0.58	15.84	0.25	0.08	0.09	99.67
AB09-20APYX11	50.75	2.62	0.03	13.12	0.30	15.52	0.87	16.33	0.34	0.02	0.02	99.91
AB09-20APYX11	51.31	2.65	0.01	11.31	0.28	16.82	0.68	15.81	0.27	0.05	-0.05	99.19
AB09-20APYX12	51.16	1.72	0.11	20.65	0.16	16.56	0.63	8.61	0.51	0.01	0.06	100.18
AB09-20APYX13	51.09	2.09	0.02	14.40	0.29	15.75	0.88	15.39	0.37	0.01	-0.03	100.30
AB09-20APYX14	53.55	14.15	0.36	7.51	3.44	8.03	0.48	11.83	0.17	-0.01	0.02	99.54
AB09-20APYX15	51.68	1.19	0.01	19.85	0.15	18.13	0.58	8.32	0.52	0.02	0.02	100.48
AB09-20APYX16	50.53	3.81	0.01	10.33	0.26	16.22	0.90	17.50	0.19	0.20	-0.06	99.95
AB09-20APYX17	52.85	1.72	0.01	11.16	0.19	18.12	0.53	15.68	0.23	0.05	0.03	100.58
AB09-20APYX17	51.29	2.77	0.01	10.86	0.29	16.10	0.82	17.68	0.29	0.03	-0.03	100.13
AB09-20APYX18	49.04	8.41	0.14	15.54	1.33	11.42	0.54	9.19	0.31	0.00	-0.01	95.92

Sample Name-Grain	SiO ₂	Al ₂ O ₃	K ₂ O	FeO	Na ₂ O	MgO	TiO ₂	CaO	MnO	Cr ₂ O ₃	NiO	Total
AB09-20APYX19	51.28	3.47	0.01	11.01	0.25	15.88	0.88	17.20	0.24	0.08	-0.05	100.29
AB09-20APYX20	51.57	2.10	0.04	13.31	0.29	15.55	0.77	16.30	0.34	0.00	0.02	100.30
AB09-20APYX20	51.30	7.05	0.11	9.79	0.84	13.02	0.86	16.08	0.27	0.06	-0.04	99.38
AB09-20APYX21	51.83	2.53	0.00	12.23	0.28	15.27	0.82	17.59	0.27	0.02	0.01	100.84
AB09-20APYX21	49.43	4.00	0.03	11.03	0.27	13.80	1.09	18.15	0.19	0.11	-0.03	98.11
AB09-20APYX22	51.24	3.28	0.00	11.35	0.27	16.02	0.94	17.31	0.18	0.03	-0.01	100.62
AB09-20APYX22	51.33	2.51	0.00	11.74	0.29	16.00	0.77	17.23	0.21	0.02	-0.03	100.11
AB09-20APYX23	43.01	2.00	0.00	21.21	0.11	29.43	0.39	7.04	0.32	0.08	-0.04	103.60
AB09-20APYX23	52.31	1.95	0.01	11.72	0.26	16.77	0.66	16.44	0.35	0.01	0.05	100.53
AB09-20APYX24	51.70	2.79	0.19	11.36	0.28	15.81	0.70	16.52	0.34	0.02	-0.05	99.72
AB09-20APYX24	52.94	1.13	0.03	25.24	0.25	19.73	0.42	3.82	0.58	0.00	0.05	104.21
AB09-20APYX24	51.00	2.69	0.07	11.72	0.29	15.51	0.88	17.10	0.26	0.02	-0.05	99.54
AB09-20APYX25	51.22	2.47	0.00	12.51	0.30	16.17	0.77	16.71	0.29	0.03	-0.10	100.47
AB09-20APYX25	51.59	2.34	-0.01	13.28	0.28	15.76	0.77	16.67	0.40	0.00	-0.02	101.09
AB09-20APYX25	48.13	1.43	0.02	16.05	0.25	14.05	0.72	16.25	0.44	0.00	0.05	97.39
AB09-20APYX25	50.44	1.77	0.04	18.23	0.36	13.34	0.81	14.82	0.47	0.01	0.03	100.32
AB09-20APYX26	51.73	1.94	0.00	12.87	0.28	16.06	0.76	16.52	0.26	0.01	0.06	100.49
AB09-20APYX26	51.37	1.92	0.01	13.58	0.29	15.51	0.81	16.25	0.37	0.01	0.00	100.13
AB09-20APYX27	52.12	1.80	-0.01	12.94	0.30	16.19	0.70	15.96	0.39	0.01	-0.01	100.41
AB09-20APYX28	50.50	2.97	0.01	12.75	0.28	15.46	0.87	16.89	0.30	0.04	-0.10	100.08
AB09-07PYX29	51.22	1.86	-0.01	17.36	0.34	14.23	1.22	14.71	0.46	0.01	0.00	101.41
AB09-07PYX29	54.34	1.08	0.00	18.65	0.05	25.67	0.41	2.30	0.30	0.11	0.18	103.09
AB09-07PYX30	48.61	1.67	0.02	20.36	0.31	13.00	2.63	13.48	0.48	0.03	0.04	100.64
AB09-07PYX31	54.70	1.05	0.01	18.33	0.05	26.24	0.35	2.04	0.42	0.15	0.13	103.47
AB09-07PYX31	53.09	1.76	0.02	14.28	0.22	20.17	0.49	10.24	0.24	0.21	0.03	100.76

Sample Name-Grain	SiO ₂	Al ₂ O ₃	K ₂ O	FeO	Na ₂ O	MgO	TiO ₂	CaO	MnO	Cr ₂ O ₃	NiO	Total
AB09-07PYX32	52.34	2.05	-0.01	11.96	0.34	16.09	0.75	16.72	0.23	0.19	-0.04	100.68
AB09-07PYX32	50.81	2.61	0.02	15.32	0.46	14.02	1.20	15.69	0.32	0.03	0.06	100.56
AB09-07PYX33	54.58	1.21	0.01	17.92	0.05	26.50	0.37	1.96	0.38	0.14	-0.02	103.12
AB09-07PYX33	54.76	1.17	-0.01	18.08	0.07	26.34	0.35	2.01	0.38	0.13	-0.01	103.29
AB09-07PYX34	54.74	1.03	0.00	18.44	0.04	26.31	0.34	2.02	0.32	0.12	0.11	103.48
AB09-07PYX34	54.79	1.04	0.01	18.59	0.03	26.13	0.37	1.96	0.32	0.11	0.02	103.37
AB09-07PYX35	54.86	1.01	0.01	17.90	0.04	26.57	0.28	1.93	0.31	0.14	0.03	103.08
AB09-07PYX35	52.29	1.94	0.00	13.35	0.33	16.56	0.77	14.81	0.30	0.13	-0.04	100.47
AB09-07PYX36	52.41	30.81	0.08	1.19	3.78	0.10	0.05	12.11	0.00	0.01	0.00	100.53
AB09-07PYX37	54.52	1.16	0.01	18.33	0.04	26.25	0.37	2.04	0.28	0.16	0.08	103.24
AB09-07PYX37	53.44	1.02	-0.01	23.06	0.02	23.57	0.49	2.02	0.40	0.03	0.11	104.18
AB09-07PYX37	57.72	26.94	0.19	1.44	6.09	0.10	0.12	8.51	0.01	0.01	0.04	101.16
AB09-07PYX38	54.92	1.02	-0.01	19.00	0.04	26.30	0.38	2.01	0.29	0.12	0.16	104.25
AB09-07PYX38	54.58	1.16	-0.01	18.39	0.04	26.16	0.38	2.08	0.36	0.12	0.12	103.40
AB09-07PYX38	50.78	1.62	0.00	19.26	0.29	14.01	1.15	13.68	0.50	0.04	-0.05	101.33
AB09-07PYX39	52.22	30.92	0.09	1.36	3.74	0.09	0.05	12.40	-0.01	0.01	0.02	100.90
AB09-07PYX39	53.35	30.27	0.14	1.24	4.19	0.17	0.06	11.73	0.00	0.01	-0.03	101.15
AB09-07PYX40	54.37	1.04	0.01	18.25	0.04	26.55	0.33	2.03	0.32	0.13	0.02	103.08
AB09-07PYX40	54.52	1.32	0.00	17.97	0.05	26.76	0.34	1.98	0.40	0.17	-0.02	103.50
AB09-07PYX41	51.76	1.92	-0.01	11.34	0.32	16.58	0.68	16.25	0.18	0.25	0.14	99.40
AB09-07PYX42	52.75	1.76	-0.01	11.96	0.30	17.14	0.63	15.82	0.33	0.24	-0.05	100.94
AB09-07PYX43	54.75	1.05	0.00	18.06	0.04	26.53	0.36	2.03	0.40	0.12	0.06	103.41
AB09-07PYX43	58.60	20.38	0.27	4.96	6.13	3.31	0.27	8.51	0.07	-0.01	0.01	102.50
AB09-07PYX44	55.83	28.31	0.14	1.57	5.31	0.11	0.10	9.98	-0.01	-0.01	-0.01	101.34
AB09-07PYX45	55.01	0.77	-0.01	18.12	0.04	26.36	0.27	2.05	0.41	0.10	0.12	103.24

Sample Name-Grain	SiO ₂	Al ₂ O ₃	K ₂ O	FeO	Na ₂ O	MgO	TiO ₂	CaO	MnO	Cr ₂ O ₃	NiO	Total
AB09-07PYX46	52.22	2.11	0.59	20.15	0.17	19.57	0.54	4.30	0.37	0.05	0.06	100.14
AB09-07PYX47	54.10	1.16	0.00	18.38	0.05	26.45	0.36	2.20	0.29	0.15	0.09	103.22
AB09-07PYX47	52.64	1.56	0.03	20.06	0.11	24.26	0.40	2.15	0.42	0.09	-0.03	101.72
AB09-07PYX48	54.00	1.08	0.01	18.14	0.05	26.28	0.37	2.01	0.31	0.14	-0.05	102.40
AB09-07PYX49	53.68	1.08	0.01	18.32	0.04	26.30	0.38	2.01	0.40	0.14	0.09	102.46
AB09-07PYX50	50.35	2.26	0.02	17.86	0.40	14.92	1.16	13.80	0.39	0.03	0.00	101.19
AB09-07PYX50	52.18	1.86	0.00	11.26	0.32	16.84	0.64	16.71	0.21	0.23	0.14	100.39
AB09-07PYX51	44.72	3.50	0.33	27.03	0.15	10.61	0.49	5.95	0.36	0.00	0.07	93.22
AB09-17PYX52	53.80	5.81	0.04	16.79	0.89	21.72	0.41	2.88	0.43	0.00	0.00	102.77
AB09-17PYX52	54.34	1.30	0.02	19.12	0.03	26.08	0.48	2.03	0.51	0.02	0.04	103.97
AB09-17PYX54	52.26	2.08	-0.01	11.43	0.39	15.82	0.81	17.42	0.37	0.03	-0.03	100.60
AB09-17PYX54	67.50	5.14	0.36	7.64	0.29	7.61	1.18	5.94	0.20	0.00	0.05	95.91
AB09-17PYX55	50.57	4.23	0.01	10.73	0.31	15.40	1.01	18.03	0.25	0.17	0.01	100.72
AB09-17PYX55	49.74	4.40	0.02	11.79	0.33	14.79	1.11	17.85	0.33	0.13	-0.01	100.48
AB09-17PYX55	51.44	2.88	0.01	10.93	0.38	15.60	0.78	17.19	0.23	0.14	0.07	99.67
AB09-17PYX56	52.22	2.43	0.01	10.45	0.33	16.16	0.40	17.33	0.30	0.39	0.08	100.10
AB09-17PYX56	50.80	2.98	0.04	11.42	0.43	14.79	1.08	17.82	0.35	0.05	-0.01	99.76
AB09-17PYX57	47.01	13.38	0.16	11.01	2.05	10.80	0.22	12.61	0.26	-0.01	-0.03	97.51
AB09-17PYX59	54.23	1.24	0.01	19.50	0.07	26.04	0.45	1.81	0.44	0.01	0.15	103.95
AB09-17PYX60	54.62	13.10	0.10	11.81	2.06	15.60	0.29	5.25	0.39	0.00	-0.04	103.21
AB09-17PYX60	58.30	2.31	0.04	18.17	0.37	23.64	0.36	1.69	0.50	0.01	-0.07	105.39
AB09-17PYX60	55.23	0.99	0.01	19.10	0.01	25.94	0.39	1.87	0.44	0.01	-0.01	103.99
AB09-17PYX61	54.72	4.52	0.06	17.53	0.66	22.77	0.41	2.52	0.38	0.01	-0.05	103.56
AB09-17PYX62	55.09	13.93	0.14	11.81	2.48	14.79	0.26	5.07	0.33	0.00	0.01	103.90
AB09-17PYX63	55.09	22.79	0.45	5.94	3.93	4.94	0.16	7.87	0.19	0.00	0.02	101.37

Sample Name-Grain	SiO ₂	Al ₂ O ₃	K ₂ O	FeO	Na ₂ O	MgO	TiO ₂	CaO	MnO	Cr ₂ O ₃	NiO	Total
AB09-17PYX63	55.01	15.69	0.19	10.97	2.53	13.85	0.28	5.51	0.36	0.01	0.03	104.41
AB09-17PYX63	52.56	19.70	0.21	8.43	2.07	11.43	0.17	7.03	0.30	0.00	0.01	101.92
AB09-17PYX64	54.05	1.77	0.02	18.78	0.04	25.65	0.44	1.76	0.53	-0.02	0.13	103.18
AB09-17PYX64	54.39	1.07	0.01	19.75	0.03	25.47	0.43	1.78	0.48	0.01	-0.06	103.43
AB09-17PYX65	53.96	1.03	0.01	19.13	0.03	25.80	0.45	1.86	0.55	0.00	-0.12	102.82
AB09-17PYX66	53.59	16.52	0.23	5.81	3.14	7.89	0.41	13.45	0.21	0.00	0.06	101.30
AB09-17PYX66	53.81	28.57	0.36	1.61	4.63	0.39	0.09	10.25	-0.02	0.00	0.03	99.75

APPENDIX C

Complete Geochemistry of Samples Analyzed for This Study

Table C.1: Whole-rock geochemistry by XRF analysis for all samples collected and analyzed for this study. All oxides are in weight percent, and all trace elements are in ppm.

	AB09-01	AB09-02	AB09-03	AB09-04	AB09-05	AB09-06	AB09-07
SiO₂	58.56	62.53	52.63	51.71	52.81	48.35	54.68
TiO₂	0.905	1.219	1.959	1.583	1.962	1.635	1.171
Al₂O₃	16.54	18.95	15.64	18.97	15.66	19.93	17.00
FeO*	7.98	4.67	12.89	10.84	12.75	11.42	8.27
MnO	0.372	0.150	0.287	0.193	0.224	0.192	0.139
MgO	1.41	0.46	4.18	3.33	3.97	4.35	6.12
CaO	8.60	7.32	8.24	9.36	8.39	11.17	8.59
Na₂O	4.25	3.72	3.28	3.23	3.33	2.58	3.30
K₂O	0.91	0.69	0.62	0.56	0.62	0.18	0.50
P₂O₅	0.482	0.300	0.267	0.227	0.268	0.180	0.237
Pre-norm Total	93.78	95.69	99.52	98.85	99.44	97.49	99.32
Ni	4	32	10	11	11	21	105
Cr	0	132	0	2	0	23	238
Sc	21	18	44	32	43	36	22
V	30	158	337	251	337	310	191
Ba	213	264	179	156	173	103	189
Rb	19	15	12	11	13	3	9
Sr	294	561	260	297	257	282	464
Zr	125	122	126	107	127	85	92
Y	43	20	39	32	38	29	17
Nb	7.2	8.3	10.7	8.9	9.9	6.9	7.5
Ga	21	21	22	21	23	22	20
Cu	43	51	361	231	257	230	58
Zn	81	65	120	102	123	99	88
Pb	6	4	4	4	4	2	4
La	15	16	11	11	9	14	11
Ce	32	32	28	22	25	20	24
Th	2	2	1	2	2	1	1
Nd	18	18	18	19	18	12	14
U	2	1	2	2	1	0	0

Table C.1 (cont.): Whole-rock geochemistry by XRF analysis for all samples collected and analyzed for this study. All oxides are in weight percent, and all trace elements are in ppm.

	AB09-08	AB09-09	AB09-10	AB09-11	AB09-12	AB09-13	AB09-14
SiO₂	53.37	51.08	65.50	53.68	54.62	50.05	51.06
TiO₂	1.855	1.554	0.735	1.196	1.834	1.791	1.271
Al₂O₃	15.55	19.50	16.53	17.39	15.37	18.28	17.55
FeO*	12.20	9.65	5.97	8.28	11.82	12.02	8.93
MnO	0.222	0.174	0.105	0.216	0.201	0.206	0.156
MgO	4.09	3.67	0.55	4.23	3.76	3.84	7.22
CaO	8.60	10.71	5.02	10.90	7.83	10.24	9.91
Na₂O	3.38	2.89	4.42	3.33	3.57	2.83	3.17
K₂O	0.56	0.52	0.96	0.51	0.76	0.42	0.46
P₂O₅	0.188	0.250	0.215	0.271	0.232	0.329	0.283
Pre-norm	99.44	99.03	95.67	95.03	98.64	100.38	100.47
Total							
Ni	8	16	3	89	5	23	93
Cr	0	31	3	170	0	24	210
Sc	42	33	20	22	42	36	31
V	393	286	25	171	279	287	222
Ba	162	188	266	219	207	180	213
Rb	12	17	9	7	17	14	5
Sr	273	365	245	494	280	317	618
Zr	94	100	147	108	111	142	97
Y	33	26	32	17	34	37	25
Nb	6.5	7.2	7.3	7.3	7.7	11.2	6.1
Ga	21	20	22	19	20	21	19
Cu	317	83	44	48	193	276	31
Zn	117	87	103	87	124	117	80
Pb	6	3	7	5	6	5	2
La	12	11	13	9	9	13	11
Ce	21	28	29	27	26	30	27
Th	1	2	2	2	2	0	0
Nd	14	17	18	15	18	19	18
U	3	2	1	1	2	1	0

Table C.1 (cont.): Whole-rock geochemistry by XRF analysis for all samples collected and analyzed for this study. All oxides are in weight percent, and all trace elements are in ppm.

	AB09-15	AB09-16	AB09-17	AB09-18	AB09-19	AB09-20A	AB09-20B
SiO₂	54.25	54.42	51.85	50.08	49.46	49.79	50.16
TiO₂	1.786	1.835	1.147	1.688	1.586	1.586	1.658
Al₂O₃	15.63	15.58	16.84	16.40	16.87	16.55	16.51
FeO*	11.17	11.03	9.10	11.14	10.77	10.45	10.57
MnO	0.197	0.198	0.158	0.208	0.185	0.179	0.182
MgO	4.32	4.21	6.89	6.49	8.13	6.68	6.20
CaO	8.14	7.96	10.62	10.00	9.92	11.36	10.85
Na₂O	3.42	3.49	2.49	2.71	2.47	2.47	2.68
K₂O	0.80	0.95	0.67	0.75	0.38	0.53	0.73
P₂O₅	0.279	0.321	0.233	0.544	0.226	0.408	0.454
Pre-norm	98.84	99.47	99.71	99.26	98.70	98.30	99.33
Total							
Ni	26	25	52	68	100	46	42
Cr	28	26	124	147	340	132	102
Sc	37	33	35	32	33	38	36
V	317	295	262	245	261	293	280
Ba	208	233	163	221	112	205	213
Rb	16	23	10	13	7	4	9
Sr	310	305	491	468	316	450	441
Zr	174	205	102	210	82	175	195
Y	36	38	21	32	19	29	31
Nb	12.2	14.3	9.4	21.5	8.2	16.2	17.5
Ga	20	20	18	20	18	20	19
Cu	170	167	157	54	34	83	114
Zn	108	108	84	111	84	95	100
Pb	3	4	3	4	2	3	3
La	13	23	11	23	5	18	17
Ce	37	48	32	53	20	41	51
Th	2	2	3	2	0	1	2
Nd	21	27	17	30	11	24	27
U	3	1	0	2	2	1	1

Table C.1 (cont.): Whole-rock geochemistry by XRF analysis for all samples collected and analyzed for this study. All oxides are in weight percent, and all trace elements are in ppm.

	AB09-21	AB09-22	AB09-23	AB10-24	AB10-25	AB10-26	AB10-27
SiO₂	51.98	49.30	58.15	46.77	48.62	48.76	52.65
TiO₂	0.984	1.339	0.974	3.373	3.274	3.311	3.146
Al₂O₃	17.19	17.23	17.89	14.76	16.03	15.64	14.40
FeO*	9.04	10.11	6.90	13.46	12.42	14.80	13.67
MnO	0.163	0.169	0.146	0.177	0.140	0.260	0.213
MgO	6.97	8.04	3.56	8.01	5.35	3.80	2.94
CaO	11.02	10.94	7.79	9.34	10.36	6.98	8.60
Na₂O	2.27	2.32	3.46	2.67	2.92	4.08	2.77
K₂O	0.27	0.32	0.97	0.95	0.43	1.49	1.16
P₂O₅	0.121	0.226	0.168	0.491	0.454	0.878	0.467
Pre-norm	99.21	97.43	98.86	96.62	96.06	95.82	95.82
Total							
Ni	40	56	28	131	99	15	8
Cr	122	153	30	67	96	0	12
Sc	37	35	19	23	25	20	37
V	279	285	165	266	300	195	341
Ba	116	129	269	251	178	388	329
Rb	3	5	19		2	24	31
Sr	465	407	578	483	517	401	240
Zr	54	95	106	251	240	381	298
Y	15	22	18	29	29	43	46
Nb	4.7	8.9	8.3	44.6	41.8	39.5	23.0
Ga	18	19	21	23	23	28	24
Cu	125	103	91	68	100	27	27
Zn	77	84	85	128	113	177	140
Pb	5	1	8	2	2	5	5
La	6	11	13	32	35	36	26
Ce	17	23	29	76	72	84	55
Th	1	1	1	2	2	2	4
Nd	11	12	16	38	38	47	34
U	1	2	2	1	3	1	3

Table C.1 (cont.): Whole-rock geochemistry by XRF analysis for all samples collected and analyzed for this study. All oxides are in weight percent, and all trace elements are in ppm.

	AB10-28	AB10-29	EMT-117	K89-130
SiO₂	52.60	49.95	52.95	48.22
TiO₂	2.939	3.166	3.024	1.307
Al₂O₃	13.78	14.64	13.96	13.85
FeO*	14.11	14.72	13.81	9.32
MnO	0.233	0.231	0.226	0.160
MgO	3.91	4.75	3.78	13.51
CaO	8.08	8.39	8.02	10.24
Na₂O	2.91	2.72	3.18	2.14
K₂O	1.08	1.08	0.66	0.82
P₂O₅	0.351	0.360	0.386	0.422
Pre-norm	94.71	94.71	100.06	96.55
Total				
Ni	9	10	11	317
Cr	21	23	23	749
Sc	38	40	40	31
V	329	360	337	237
Ba	322	262	346	345
Rb	29	29	37	
Sr	241	219	250	548
Zr	214	220	224	119
Y	40	41	44	20
Nb	18.4	18.6	19.1	12.3
Ga	23	27	23	18
Cu	29	29	35	91
Zn	130	128	139	76
Pb	3	3	5	4
La	19	21	22	24
Ce	44	45	50	57
Th	2	2	4	5
Nd	27	27	27	30
U	0	3	2	1

Table C.2: Whole-rock geochemistry by ICP-MS analysis for all samples collected and analyzed for this study. All trace elements are in ppm.

	AB09-01	AB09-02	AB09-03	AB09-04	AB09-05	AB09-06	AB09-07
La	15.25	14.12	11.12	9.75	11.01	7.92	9.44
Ce	32.06	30.71	27.08	23.26	26.67	18.65	21.46
Pr	4.40	4.13	3.95	3.39	3.94	2.84	2.99
Nd	20.00	17.78	18.93	16.30	18.69	13.52	13.69
Sm	5.48	4.16	5.43	4.70	5.37	4.01	3.39
Eu	1.82	1.52	1.87	1.63	1.85	1.44	1.34
Gd	6.40	4.15	6.41	5.53	6.38	4.75	3.40
Tb	1.12	0.65	1.14	0.97	1.10	0.84	0.53
Dy	7.05	3.72	7.21	6.18	7.04	5.27	3.10
Ho	1.50	0.72	1.49	1.26	1.45	1.09	0.59
Er	4.19	1.83	4.08	3.45	3.90	2.90	1.55
Tm	0.62	0.25	0.59	0.49	0.56	0.42	0.21
Yb	3.87	1.45	3.59	3.13	3.45	2.59	1.35
Lu	0.62	0.23	0.56	0.49	0.54	0.39	0.21
Ba	212	268	173	154	172	99	188
Th	1.76	1.11	1.23	1.03	1.22	0.92	0.56
Nb	6.29	7.50	8.78	7.40	8.68	5.74	6.04
Y	40.59	18.58	36.64	31.26	35.19	27.27	14.85
Hf	3.50	3.02	3.54	2.94	3.50	2.45	2.38
Ta	0.43	0.48	0.57	0.47	0.57	0.37	0.40
U	0.69	0.38	0.47	0.39	0.46	0.15	0.26
Pb	6.72	4.12	3.96	3.32	3.66	4.06	3.88
Rb	16.9	13.8	10.7	10.1	11.7	2.8	7.5
Cs	1.12	1.77	0.26	0.36	0.39	0.76	0.43
Sr	285	547	256	297	254	279	453
Sc	19.4	17.0	42.7	30.7	42.4	35.7	22.9
Zr	121	120	124	105	123	84	90

Table C.2 (cont.): Whole-rock geochemistry by ICP-MS analysis for all samples collected and analyzed for this study. All trace elements are in ppm.

	AB09-08	AB09-09	AB09-10	AB09-11	AB09-12	AB09-13	AB09-14
La	8.71	11.77	13.39	11.38	10.75	13.14	11.59
Ce	20.35	26.03	30.35	25.56	25.04	30.64	24.86
Pr	3.09	3.61	4.20	3.49	3.65	4.44	3.81
Nd	14.68	16.34	18.91	15.29	16.89	20.44	17.25
Sm	4.38	4.37	5.14	3.66	5.00	5.70	4.23
Eu	1.60	1.61	1.60	1.38	1.78	1.85	1.62
Gd	5.31	4.73	5.61	3.64	5.76	6.47	4.61
Tb	0.94	0.80	0.96	0.56	1.02	1.12	0.76
Dy	5.85	4.96	5.94	3.45	6.59	7.07	4.62
Ho	1.26	1.01	1.19	0.67	1.35	1.46	0.96
Er	3.40	2.69	3.20	1.74	3.65	3.92	2.56
Tm	0.49	0.38	0.46	0.24	0.53	0.56	0.37
Yb	3.02	2.41	2.83	1.49	3.29	3.50	2.25
Lu	0.47	0.37	0.43	0.23	0.51	0.54	0.36
Ba	160	185	262	216	204	180	209
Th	1.19	2.03	2.82	0.88	1.63	1.41	0.71
Nb	5.75	6.49	7.07	6.50	6.61	9.27	5.00
Y	31.66	25.11	29.19	16.60	33.40	36.13	24.28
Hf	2.73	2.69	4.18	2.70	3.23	3.73	2.51
Ta	0.39	0.42	0.52	0.41	0.46	0.59	0.31
U	0.47	0.60	0.93	0.35	0.64	0.55	0.23
Pb	5.45	3.14	6.60	3.79	5.95	6.24	2.10
Rb	10.2	15.3	9.1	5.5	16.3	12.8	4.9
Cs	0.39	0.60	0.14	0.10	0.23	1.01	0.05
Sr	266	365	241	496	287	321	619
Sc	42.6	31.0	18.6	19.7	36.7	31.4	28.0
Zr	91	99	144	108	110	140	96

Table C.2 (cont.): Whole-rock geochemistry by ICP-MS analysis for all samples collected and analyzed for this study. All trace elements are in ppm.

	AB09-15	AB09-16	AB09-17	AB09-18	AB09-19	AB09-20A	AB09-20B
La	15.97	18.86	12.42	19.47	8.22	17.82	19.34
Ce	36.57	42.95	27.58	44.24	19.01	40.26	43.85
Pr	5.00	5.81	3.76	6.01	2.68	5.44	5.94
Nd	22.61	25.42	16.41	25.89	12.28	23.46	25.70
Sm	5.94	6.56	3.92	6.18	3.19	5.57	6.07
Eu	1.87	2.00	1.34	1.96	1.30	1.81	1.96
Gd	6.44	6.94	3.91	6.23	3.46	5.60	6.08
Tb	1.09	1.16	0.64	1.00	0.58	0.90	0.98
Dy	6.66	7.07	3.90	5.94	3.59	5.47	5.91
Ho	1.37	1.43	0.77	1.20	0.72	1.09	1.16
Er	3.69	3.79	2.05	3.11	1.91	2.81	3.10
Tm	0.53	0.54	0.29	0.44	0.27	0.40	0.43
Yb	3.30	3.33	1.76	2.68	1.67	2.45	2.64
Lu	0.53	0.51	0.27	0.41	0.26	0.38	0.41
Ba	208	231	162	212	112	201	211
Th	2.22	2.57	1.52	1.53	0.69	1.65	1.51
Nb	10.99	12.97	7.68	15.89	7.00	14.02	15.72
Y	34.50	35.58	19.20	29.46	17.59	26.85	29.04
Hf	4.54	5.33	2.59	4.34	2.11	3.85	4.27
Ta	0.73	0.87	0.47	0.93	0.46	0.82	0.92
U	0.77	0.88	0.47	0.54	0.24	0.51	0.52
Pb	4.19	4.55	3.32	3.27	1.51	3.32	3.27
Rb	15.0	22.0	9.4	8.4	6.5	3.2	8.3
Cs	0.32	0.41	0.33	0.10	0.22	0.06	0.09
Sr	314	306	494	444	319	441	441
Sc	33.5	31.8	32.1	34.3	32.3	37.2	35.9
Zr	172	204	101	193	81	170	191

Table C.2 (cont.): Whole-rock geochemistry by ICP-MS analysis for all samples collected and analyzed for this study. All trace elements are in ppm.

	AB09-21	AB09-22	AB09-23	AB10-24	AB10-26	AB10-27	AB10-28
La	7.32	11.81	13.28	32.99	31.99	37.70	24.74
Ce	16.03	25.87	26.51	70.28	69.01	83.46	56.63
Pr	2.20	3.51	3.49	8.97	8.84	11.08	7.68
Nd	9.78	15.50	14.28	37.79	36.38	47.36	33.91
Sm	2.55	3.85	3.40	8.74	8.14	11.12	8.82
Eu	0.96	1.34	1.24	2.91	2.71	3.61	2.80
Gd	2.61	3.95	3.34	8.27	7.47	10.79	9.33
Tb	0.44	0.65	0.54	1.23	1.14	1.66	1.55
Dy	2.69	3.97	3.21	6.88	6.36	9.56	9.59
Ho	0.55	0.80	0.63	1.24	1.19	1.81	1.91
Er	1.48	2.09	1.70	2.96	2.90	4.61	5.06
Tm	0.21	0.29	0.24	0.38	0.38	0.62	0.71
Yb	1.26	1.77	1.48	2.14	2.21	3.64	4.34
Lu	0.20	0.27	0.24	0.31	0.32	0.55	0.67
Ba	112	124	261	245	172	390	336
Th	1.62	1.09	2.37	3.42	3.21	2.97	4.06
Nb	3.54	7.63	6.80	43.20	40.86	38.46	21.63
Y	13.61	19.86	15.93	30.20	28.85	45.28	47.60
Hf	1.51	2.44	2.83	6.09	5.78	8.85	7.22
Ta	0.22	0.46	0.45	2.81	2.66	2.47	1.45
U	0.77	0.25	1.07	0.82	0.94	1.01	1.32
Pb	5.83	2.42	7.74	1.81	1.65	3.71	5.02
Rb	2.9	4.0	17.8	19.5	2.3	23.0	30.4
Cs	0.31	0.34	0.74	0.28	0.01	0.13	0.80
Sr	465	406	559	499	537	416	249
Sc	36.3	36.7	18.2	23.4	24.4	21.8	37.7
Zr	53	94	103	248	235	399	299

Table C.2 (cont.): Whole-rock geochemistry by ICP-MS analysis for all samples collected and analyzed for this study. All trace elements are in ppm.

	AB10-29	AB10-30	EMT-117	K90-251	K90-266	K90-328	K90-366
La	19.29	19.75	21.04	50.86	61.37	28.33	25.97
Ce	43.64	44.70	47.56	104.47	127.17	58.28	55.29
Pr	5.98	6.07	6.49	12.56	15.25	7.64	7.30
Nd	26.52	26.94	28.53	49.10	59.75	31.43	30.55
Sm	7.13	7.29	7.60	9.14	10.95	6.43	6.52
Eu	2.33	2.43	2.38	2.45	2.92	1.90	2.01
Gd	7.68	7.94	8.21	6.76	7.70	5.22	5.61
Tb	1.30	1.33	1.40	0.89	0.99	0.74	0.84
Dy	8.09	8.34	8.51	4.80	5.08	4.09	4.77
Ho	1.62	1.69	1.71	0.89	0.88	0.75	0.91
Er	4.30	4.55	4.54	2.29	2.22	1.94	2.38
Tm	0.62	0.63	0.64	0.32	0.30	0.25	0.32
Yb	3.79	3.90	3.89	1.95	1.79	1.55	1.96
Lu	0.59	0.61	0.60	0.30	0.29	0.23	0.30
Ba	319	257	341	660	870	463	440
Th	3.24	3.23	3.52	10.24	11.30	5.80	4.68
Nb	16.57	17.39	17.15	12.91	15.97	8.38	10.79
Y	40.63	41.81	42.66	22.18	22.33	18.83	22.87
Hf	5.50	5.68	5.64	3.63	3.97	2.83	3.17
Ta	1.13	1.17	1.17	0.73	0.90	0.48	0.65
U	1.03	1.05	1.13	2.28	2.57	1.34	1.15
Pb	4.33	4.30	4.95	7.36	7.76	4.84	3.94
Rb	29.2	27.9	35.0	19.6	26.9	20.1	21.1
Cs	0.99	0.38	2.09	0.74	0.81	0.54	0.25
Sr	252	227	249	1151	1451	826	717
Sc	40.2	43.0	40.4	39.6	35.9	37.2	32.8
Zr	214	219	217	144	161	105	119

Table C.2 (cont.): Whole-rock geochemistry by ICP-MS analysis for all samples collected and analyzed for this study. All trace elements are in ppm.

	K90-367	8_31_08
La	25.76	90.42
Ce	54.78	196.98
Pr	7.20	23.84
Nd	30.04	95.82
Sm	6.33	19.71
Eu	2.00	6.31
Gd	5.50	15.68
Tb	0.83	1.99
Dy	4.70	9.02
Ho	0.91	1.25
Er	2.39	2.35
Tm	0.32	0.24
Yb	1.93	1.18
Lu	0.30	0.14
Ba	437	441
Th	4.60	9.63
Nb	10.88	106.22
Y	22.62	30.32
Hf	3.16	13.94
Ta	0.66	6.75
U	1.19	2.68
Pb	3.82	5.49
Rb	20.9	13.6
Cs	0.26	0.13
Sr	715	1092
Sc	32.1	8.5
Zr	118	664